NANOCARBON BLACK-BASED ULTRA-HIGH-PERFORMANCE CONCRETE WITH SELF-SENSING CAPABILITY: DEVELOPMENT AND DURABILITY

ABASAL HUSSAIN

PhD

The Hong Kong Polytechnic University

2025

The Hong Kong Polytechnic University

Department of Civil and Environmental Engineering

Nanocarbon Black-based Ultra-High-Performance Concrete with Self-Sensing Capability: Development and Durability

Abasal Hussain

A thesis submitted in partial fulfilment of the requirement for the degree of

Doctor of Philosophy

October 2024

CERTIFICATE OF ORIGINALITY

I hereby declare that this thesis is my own work and that, to the best of my knowledge and belief, it reproduces no material previously published or written, nor material that has been accepted for the award of any other degree or diploma except where due acknowledgement has been made in the text.

________________________ (Signed)

Abasal Hussain (Name of student)

To my family

Abstract

Concrete structures are inevitably affected by different loads and environmental conditions during their service life, and the resulting structural cracks and damage significantly reduce the durability and serviceability of the structures. Therefore, there is an increasing demand for real-time monitoring of the stress state and deformation in concrete structures. Smart cementitious composites (SCCs) have emerged as a promising technology that aims to develop an intrinsic sensing system to replace conventional sensors which are generally expensive, often incompatible with concrete structures, and may suffer from durability issues. However, the existing SCCs still face many challenges, including their relatively high costs, dispersion issues of piezoresistive materials, inferior mechanical properties, durability and/or serviceability.

Against this background, this PhD study aims to develop a new type of SCC with ultra-high strength, excellent durability, and an incredible strain sensing capability while being highly cost-effective. Ultra-high-performance concrete (UHPC) has exceptional mechanical and durability properties due to its dense and well-compacted microstructure. The dense microstructure of UHPC, however, makes it challenging for the development of sensing capability as it hinders the mobility of piezoresistive materials. In this study, UHPC with sensing capability was developed by incorporating nanocarbon black (nCB) in the cement matrix. Nanocarbon black is a highly conductive and low-cost material, with its unit cost being less than 1% of that of carbon nanotubes, and the use of nCB makes the cement matrix conductive by its branched structure through a quantum tunnelling mechanism. The resulting UHPC is termed herein nCB-UHPC.

This study started with investigations on the effect of the structures of nCB on the mechanical and piezoresistive properties of cementitious matrix. Three different nCB structures were investigated, and nCB with the most suitable structure was identified. The selected nCB was then used for a comprehensive experimental programme, in which it was incorporated into UHPC by up to 2.0% of the binder mass. The experimental programme included the formulation of proper mix designs and evaluation of the fresh, hardened mechanical properties and microstructure of nCB-UHPC under different curing environments. In addition, the piezoresistive properties of the nCB-UHPC, including the percolation threshold, strain sensitivity and conductive mechanism, were examined. The test results show that by incorporating nCB of a proper content (e.g., 1.0-1.5%), the resulting nCB-UHPC can have an ultrahigh 28-day compressive strength (>140 MPa), sufficiently good workability (slump spread ≥170 mm) and excellent strain-sensing capability (gauge factor >130) at the same time.

Moreover, UHPC with 1.50% nCB was further investigated for its durability under different working conditions. The effects of multiple curing conditions and long-term aggressive environmental exposure on the mechanical, piezoresistive and microstructural properties of the UHPC were examined. The test results showed that the nCB-UPBC developed in this study possesses a highly durable and well-synchronized response and is less influenced by the aggressive environment.

Furthermore, nCB was incorporated into UHPC with seawater and sea-sand (i.e., ultra-high-performance seawater sea-sand concrete or UHPSSC), leading to the so-called nCB-UHPSSC. The use of seawater and sea-sand offers significant benefits, especially for construction of coastal/marine infrastructure; by replacing river sand with sea-sand, the environmental impact caused by excessive sand mining in riverbeds can also be mitigated. A comprehensive experimental programme was conducted, involving the development of new mix designs of UHPSSC with varying concentrations of nCB (up to 1.80% by binder mass) as well as investigations of its mechanical, microstructural and piezoresistive properties with different curing conditions. In addition, the piezoresistive behaviour was studied in a fully saturated state and after drying treatment. The test results indicated that the nCB-UHPSSC has comparable mechanical properties to nCB-UHPC. The piezoresistive behaviour of nCB-UHPSSC is characterized by a precisely synchronized response with a low percolation zone, and the nCB-UHPSSC in a saturated state has a higher sensitivity than that in a dry state due to the dissolved ions in the former.

While the initial findings were incredibly promising, the durability performance of nCB-UHPSSC considering practical applications was further evaluated. A comprehensive experimental programme was conducted on UHPSSC with 1.40% nCB by binder mass, which is the percolation threshold of nCB-UHPSSC. The investigations encompassed electromechanical properties under various curing conditions and exposure durations, as well as the microstructure analysis. Besides, the impact of different in-situ temperatures on the piezoresistive properties was also explored to gain insights into the sensitivity and reliability of the self-sensing UHPSSC. The result indicated that the strain sensitivity of nCB-UHPSSC increases with the temperature due to the thermal energy which allows more charge carriers to flow easily within a system.

In summary, this PhD study has successfully developed two new types of UHPCs with self-sensing capability (i.e., nCB-UHPC and nCB-UHPSSC) and has systematically investigated their mechanical, piezoresistive properties and durability. The two types of

UHPCs, with their demonstrated excellent properties, can be used as high-performance constructional materials as well as a real-time monitoring measure for civil infrastructure.

List of Publications

Journal Papers

Hussain, A., Yu, T., & Zou, F. (2024). Nanocarbon black based ultra-high-performance seawater sea-sand concrete (UHPSSC) with self-strain sensing capability. *Cement and Concrete Composites,* 105895.

Hussain, A., Xiang, Y., Yu, T., & Zou, F. (2022). Nanocarbon black-based ultra-high-performance concrete (UHPC) with self-strain sensing capability. *Construction and Building Materials*, 359, 129496.

Hussain, A., Yu, T., & Zou, F. (2024). Effects of moisture content and sea-salt solution exposure on the properties of nanocarbon black (nCB)-based self-sensing ultrahigh-performance concrete (UHPC). *Construction and Building Materials*, (Under review).

Hussain, A., Yu, T., & Zou, F. Effects of temperature and sea-salt solution exposure on the durability of self-sensing ultra-high-performance seawater sea-sand concrete. (*Under preparation*).

Hussain, A., Yu, T., & Zou, F. Effects of nanocarbon black structure on the self-sensing performance of cementitious composites. (*Under preparation*).

Conference Presentations/Publications

Hussain, A., Yu, T., & Zou, F. (2024). "Development and durability analysis of self-strain sensing ultra-high-performance concrete enabled by nanocarbon black", *International Congress and Expo on Civil and Structural Engineering*, 13-15 June 2024, Edinburgh, Scotland.

Hussain, A., Yu, T., & Zou, F. (2023). "Development of nanocarbon black-enabled self-strain sensing ultra-high-performance cementitious composites", *Proceedings of the 14th International Workshop on Structural Health Monitoring (IWSHM),* 12-14 September 2023, California, United States.

Hussain, A., Yu, T., & Zou, F. (2023). "Nanocarbon black-enabled self-strain sensing ultra-high-performance concrete: development and durability analysis", *PolyU Research Student Conference (PRSC),* 8-9 May 2023, Hong Kong.

Acknowledgements

In the name of ALLAH, The Most Gracious and The Most Merciful.

I would like to extend my profound gratitude and appreciation to Prof. Tao Yu, my chief supervisor, for his exceptional support and guidance during my PhD degree. Prof. Yu has been an invaluable source of knowledge and inspiration to me and many others worldwide. I am very grateful for his firm dedication and mentorship throughout my journey. I am truly fortunate to have had an opportunity to work with him and to benefit from his wisdom and leadership.

I extended my deepest gratitude to my co-supervisor and mentor, Dr. Fangxin Zou, who has played a crucial role in my decision to join PolyU. I immensely admire him for his unwavering guidance, cooperation, and mentorship, which have vigorously shaped my academic journey. From the beginning to the final stages of my degree, he has been a constant source of support and encouragement. I am grateful for his understanding and willingness to help and his commitment to assisting me in any situation. I have entrusted Dr. Zou with both my research and personal problems, as he has created an environment of trust and confidence.

Moreover, I am profoundly grateful to my supervisors, Prof. Yu Tao and Dr. Fangxin Zou, for their outstanding mentorship and insightful discussions throughout my PhD journey. Their firm dedication, guidance and provision of the best possible resources have had a sincere and lasting impact on my research. Their guidance and unconditional support will forever be cherished and remembered. They have mentored me and shaped my approach and attitude toward research despite my limited experience.

Furthermore, I truly admire Dr Xiang Yu, Dr Mehran Khan, Dr Hafiz Asad Ali, and all my lab fellows, colleagues, lab assistants, and technicians for their invaluable guidance, cooperation, support, and discussions throughout my PhD journey. Their expertise, encouragement, and insightful feedback have played a crucial role in the accomplishment of my research and PhD journey. I am genuinely grateful for their dedication and commitment.

I would like to express my appreciation to the Student Affairs Office for providing me with the opportunity to serve as a tutor at Student Hall. This experience has been invaluable in my personal and professional growth. As a Hall Tutor, I have participated in various trainings and workshops, which further enrich my knowledge and skills. I am grateful for the support and guidance I have received as a tutor.

Additionally, I am very grateful to the Research Institute for Sustainable Urban Development (RISUD), The Hong Kong Polytechnic University for their generous financial support of my PhD study.

Last but not least, I would also like to extend my heartfelt gratitude to my friends and family, especially my mother, my late father Ghulam Haider, my brother, my sister, and my sweet wife, for supporting me morally and spiritually far away from home throughout my studies and my life in general. Ammi, your love, encouragement, and belief in me have been a constant source of motivation and strength. Moreover, the understanding and support of my wife during the ups and downs of my life and this journey have been immeasurable.

I am truly fortunate to have such a remarkable support system in my life, and I am indebted to each one of them for their contributions to my success.

May ALLAH bless you all.

Table of Contents

List of Figures

List of Tables

List of Abbreviations

AC	Alternating current
AFm	Monosulfoaluminate
AFt	Ettringite
BSE	Backscattered electron
C_2S	Belite
C_3A	Aluminate
C_3S	Alite
$Ca(OH)_2$	Portlandite
CaO	Calcium oxides
$CaSO_4 \cdot 2H_2O$	Gypsum
CCSF	Copper-coated steel fibres
CF	Carbon fibre
CF-CNT	Carbon nanotube on carbon fibre
CH	Calcium hydroxide
CNF	Carbon nanofibers
CNT	Carbon nanotube
C-S-H	Calcium silicate hydrate
DBP	Dibutyl phthalate oil
DC	Direct current
ECC	Engineered Cementitious Composites
EDX	Energy dispersive X-ray spectroscopy
EFA	Epoxidized Fatty Acid Ester

EIS	Electrochemical impedance spectroscopy
FCR	Fractional change in electrical resistance/resistivity
FESEM	Field emission scanning electron microscope
FRP	Fibre-reinforced polymer
GF	Gauge factor
GNF	Graphene nanofiber
GNP	Graphene nanoplatelets
GO	Graphene Oxide
GONP	Graphene Oxide Nanoplatelets
GP	Graphene Platelets
IC	Ion chromatography
$Mg(OH)_2$	Magnesium hydroxide
MgO	Magnesium oxide
MIP	Mercury intrusion porosimetry
MLG	Multi-layer graphene
MWCNT	Multi-walled carbon nanotube
NaCl	Sodium chloride
NaDDBS	Sodium dodecyl benzenesulfonate
nCB	Nanocarbon black
NGPs	Nano graphite platelets
NWC	Normal water curing
OAN	Oil absorption number
OPC	Ordinary Portland cement
PAN	Polyacrylonitrile

PC	Plain concrete
PNS	Polynaphthalene sulfonate superplasticiser
PP	Polypropylene
PVA	Polyvinyl alcohol
PSD	Particle size distribution
QP	Quartz powder
RCF	Recycled carbon fibers
RPC	Reactive power concrete
SCC	Smart cementitious composite
SEM	Scanning electron microscope
SF	Silica Fume
SFs	Steel Fibers
SHM	Structural health monitoring
SiO2	Quartz
SP	Superplasticiser
SSA	Specific surface area
SSAs	Steel slag aggregates
SSC	Seawater sea-sand concrete
SSFs	Stainless-steel fibres
SSSW	Short-cut super-fine stainless-steel wire
SWC	Seawater immersion curing
SWCNT	Single-walled carbon nanotube
TEM	Transmission electron microscope
UHPC	Ultra-high-performance concrete

UHPFRC	Ultra-high-performance fibre-reinforced concrete
UHPSSC	Ultra-high-performance seawater sea-sand concrete
VCF	Virgin carbon fibers
WHO	World Health Organization
XRD	X-ray diffraction
XRF	X-ray Fluorescence

Chapter 1.

Introduction

1.1 Background and Significance

Concrete is the second most-consumed resource in the world after water (Gagg, 2014; Han et al., 2015). Most of the infrastructure around the world is built using concrete. During the service life, concrete structures such as dams, airports, tunnels, bridges and building structures are susceptible to unfavourable environmental factors. The cumulative impacts of fatigue, corrosion, and material aging inevitably cause damage to accumulate over time. This leads to reduced resistance to applied loads and the widening of existing cracks, which ultimately result in unexpected and potentially catastrophic accidents. In general, cracks in reinforced concrete structures provide a route to penetrate harmful ions, such as chloride ions, to reach steel rebars. Thus, it can lead to corrosion in steel, which affects the durability of the structure. The structure degradation process is often accompanied by increased porosity of concrete, micro-cracks, and crack expansion. Therefore, the timely monitoring of stresses, strains, cracks, and damage in the structures would considerably reduce the risk of unanticipated accidents, saving human life, resources and maintenance costs in the later stage.

For instance, more than half of annual construction spending in Europe is now allocated to repairing and maintaining existing structures. Bridge and building maintenance costs in Europe alone exceed up to 20 billion Euros per year, with a considerable portion used to repair cementitious composite infrastructure (Han et al., 2019). American Society of Civil Engineers estimated in 2015 that the infrastructure repair cost would be $3.6 trillion by 2020 (Wille & Boisvert-Cotulio, 2015). It is due to this fact that the industry has spent much effort and resources developing real-time structural health monitoring to minimize the occurrence of adverse scenarios. Early detection of cracks and damages in concrete infrastructure can save billions of dollars to the economy, human lives, and resources, and it can be considered a safety and durability measure. Thus, it is necessary to produce a real-time monitoring system for stress-strain, cracks, and damage sensing of the structure.

Structural Health Monitoring (SHM) in civil infrastructure is a promising technology that refers to the implementation of damage diagnosing and identification strategy, which will be helpful in evaluating the structure health and residual strength by performance-based analysis. In current structural health monitoring systems, different sensing systems are embedded or attached to enable the continuous monitoring and assessment of the damages caused by different loading processes (Chong et al., 2003; Kong et al., 2016; Taheri, 2019). The data are utilized to assess the health condition of the civil infrastructures, which eventually helped in making any decision to optimize the maintenance and retrofitting of the structure. Different types of traditional sensors are being used to sense stresses, strains, cracks, damages, humidity, temperature, and other physical parameters (Moyo et al., 2005; Sikarwar & Yadav, 2015; Taheri, 2019). Although some of these sensors can perform well, their incompatibility with concrete infrastructures, low operational life, demand for skilled labour and high installation and maintenance costs limit their large-scale implementation in concrete infrastructure (Ou, 2006).

Smart cementitious composites (SCC) are a new development in concrete technology that aims to replace the traditional sensors in concrete infrastructure by making cementitious composites themselves a sensor. The research on SSCs started with the findings of the self-sensing property of cementitious composites with short carbon fibres (Chen & Chung, 1993). The basic phenomenon is the insulator-to-conductor transition. The resistivity of insulators (concrete in the dry stage (Xu et al., 2010)) is reduced by adding different conductive fillers into a cementitious matrix. The distance between the fillers decreases when a compressive load is applied, which leads to the construction of the conductive path in a matrix and the decrease of the overall resistivity of the material. With this breakthrough, cementitious materials could be used as structural materials that can intrinsically sense their stresses, strains, damage and cracks. SCCs are fabricated by incorporating various micro and nano conductive materials, including carbon fibres (Azhari & Banthia, 2012; Chen et al., 2004; Chen & Chung, 1993; Hoheneder et al., 2015), nanocarbon black (Ding et al., 2013; Dong et al., 2019; Li et al., 2008; Monteiro et al., 2017; Wu et al., 2005), carbon nanotubes (D'Alessandro et al., 2016; Ding et al., 2022; Materazzi et al., 2013; Naqi et al., 2019; Zhang et al., 2018), steel fibres (Ahmed et al., 2021; Ding et al., 2019; Hussain et al., 2022; Kim et al., 2018; Nguyen et al., 2015) and other hybrid materials into the cementitious matrix (Ding et al., 2016; Ding et al., 2012; Ding et al., 2019; Hussain et al., 2019; Lee et al., 2018; Luo et al., 2010; Sasmal et al., 2017). Thus, cementitious composites can be used to monitor stresses, strains, damage, and cracks in bridges and offshore structures. Additionally, it can also be used for traffic monitoring, energy storage devices, border/military security and the snow melting process (Chanut et al., 2023; Han et al., 2009; Han et al., 2014; Monteiro et al., 2017; Ou, 2006; Sassani et al., 2018).

Nevertheless, this technology is still under development and faces many challenges, which need to be addressed before it can be used as a field-deployable solution in the construction industry. A large number of studies have been conducted to investigate the self-sensing capabilities of cement paste, mortar, and concrete with the addition of various conductive materials. However, it is essential to consider several vital aspects to facilitate the continued improvement of this technology. The relatively low strength of the SCC and inconsistencies in test results are real challenges, particularly as the sensor's working principle relies on an elastic range of materials, which limits the maximum strain that can be monitored. Furthermore, a significant practical concern pertains to the durability and serviceability of the existing sensors. The impact of harsh environmental conditions, as well as external factors like temperature, moisture content, aggressive environment exposure and other parameters, on the continuous real-time monitoring and long-term functionality of the cementitious sensors needs to be carefully evaluated. Additionally, substantial challenges include the considerable dispersion issues and high costs associated with piezoresistive materials, which hinders their large-scale field applications. Therefore, exploring cost-effective materials with easy fabrication processes as well as improved electromechanical properties and durability is crucial. By utilizing such materials, the implementation of large-scale infrastructure monitoring systems becomes more feasible and viable.

1.2 Research Aim and Objectives

Driven by the identified key challenges and limitations, this thesis aims to develop a novel smart cementitious composite that offers higher mechanical and durability performance while being cost-effective and easy to fabricate. To achieve this, ultra-high-performance concrete (UHPC) is utilized as the matrix that ensures long-term, feasible, and sustainable construction due to its exceptional mechanical properties and high durability by improving porosity and resistance to aggressive environments. On the other hand, nanocarbon black (nCB) is a highly conductive and cost-effective material (<1% of carbon nanotubes), making it the most promising candidate as a conductive filler. This newly developed multifunctional nCB-based UHPC composite would have the potential to revolutionize the construction industry by offering sustainability, cost-effectiveness, and significant advancements in real-time monitoring of concrete infrastructures.

This thesis involves comprehensive investigations on the development of nCB-based UHPC composites and their durability, with focuses on addressing the following challenges and objectives.

1) The structure of nCB is a key factor influencing the electromechanical properties and cost, so the first objective of the PhD study is to identify the most suitable nCB structure for use in SCCs.
2) Given the lower mechanical performance and durability of existing SCCs, the development of the intrinsic strain-sensing capability of UHPC by incorporation of the cost-effective nCB would be a significant contribution to the construction industry, and this is the second objective of the PhD study.
3) The mechanical and piezoresistive behaviour of nCB-UHPC under various working conditions including aggressive environmental exposure is important for their practical applications, so the third objective of the PhD study is to assess its performance under various working conditions.
4) The fourth objective of the PhD study is to develop nCB-UHPC using seawater and sea-sand, so as to address the global challenges of scarcity of fresh water and river sand in construction; this development is particularly important for offshore projects by offering cost-effective solutions for real-time performance monitoring while reducing the carbon footprint of marine infrastructure.
5) The fifth objective of the PhD study is to investigate the effects of different temperatures and accelerated exposure on the performance of nCB-UHPSSC to ensure confident use of the material in field applications. Additionally, the durability and long-term assessment of the composite's performance under

aggressive environmental conditions will be conducted through various materials characterization techniques.

1.3 Outline of Thesis

This thesis develops two new materials and investigates their durability parameters by considering their field applicability. The framework of the thesis can be seen in Figure 1.1 and the outline of the PhD thesis is as follows:

Chapter 1 includes the background and general concept of structural health monitoring of concrete structures, identifying the key challenges faced by self-sensing concrete technology and the investigation methodology. The problem statement and the key objectives of this study are also stated.

Chapter 2 systematically reviews the progress of research on self-sensing cementitious composites, including different conductive materials and matrixes, and their applications, especially in nCB-employed studies. It further reviews the existing studies on UHPC, including its principles, fabrication, new functionalities and durability.

Chapter 3 examines different nCB structures to assess their effects on the mechanical properties and piezoresistive behaviour of SCCs, including the percolation threshold, repeatability, and strain sensing capabilities, in order to identify the most suitable nCB for use as a functional filler in further studies.

Chapter 4 systematically investigates the feasibility of developing a multifunctional UHPC for the desired fresh and hardened mechanical properties and piezoresistive properties by incorporation of branched-structured nCB (nCB-UHPC).

Chapter 5 investigates the performance of nCB-UHPC under various working conditions and explores the relationship between the mechanical and microstructural properties and the piezoresistive behaviour of nCB-UHPC with its moisture content and sea-salt solution exposure.

Chapter 6 focuses on the development of seawater sea-sand nCB-UHPC with an intrinsic sensing capability through a systematic experimental investigation.

Chapter 7 investigates the durability of nCB-UHPSSC by exploring their mechanical microstructural properties and piezoresistive behaviour at different temperatures and after accelerated exposure.

Chapter 8 contains the main contributions of this study and recommendations for future research.

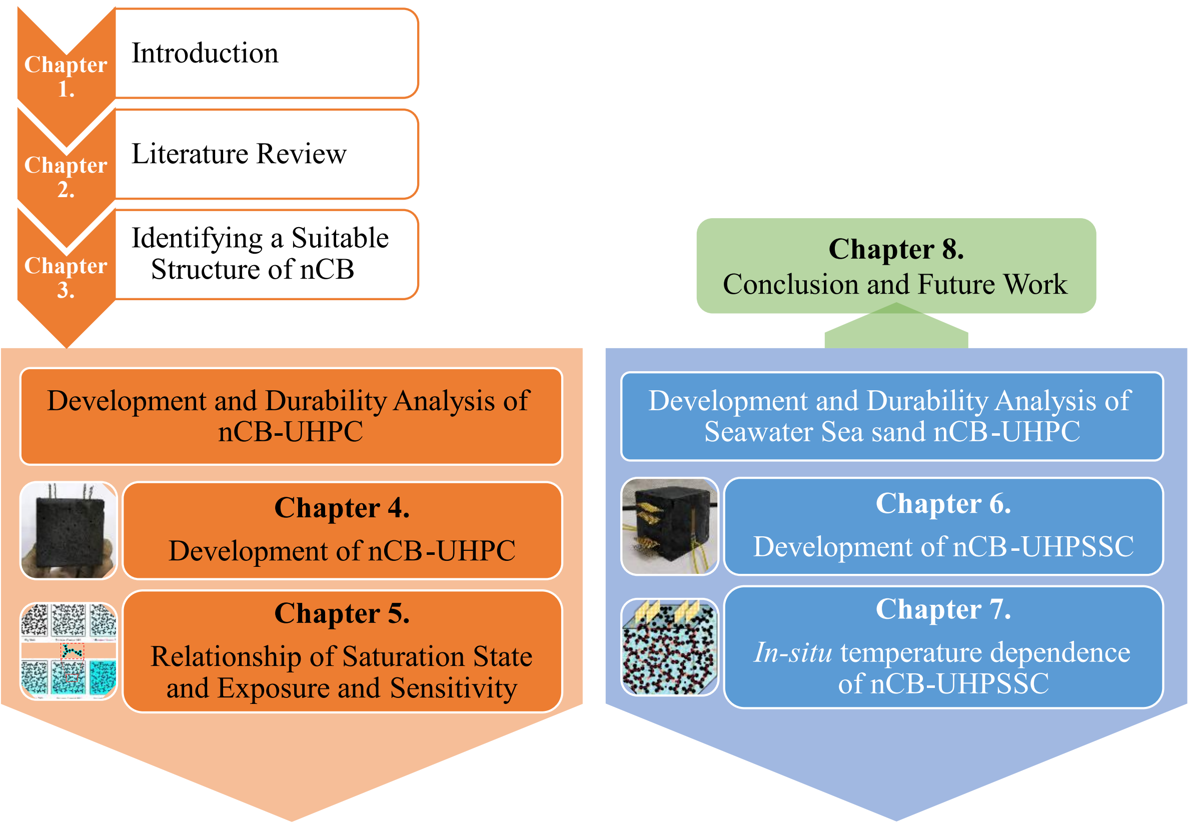

Figure 1.1. Thesis Framework

Chapter 2.

Literature Review

2.1 Introduction

In the past three to four decades, there has been a significant focus on Structural Health Monitoring (SHM) due to its ability to monitor the real-time health of structures and enhance safety by optimizing maintenance approaches. In civil infrastructure, damage diagnosis and identification refer to the implementation of strategies to assess and identify damage within a structure on time. This approach aims to evaluate the overall health and residual strength of the infrastructure through performance-based analysis.

Currently, SHM systems generally involve embedding or attaching different sensing systems to enable continuous monitoring and assessment of damages caused by different loading conditions. The data collected from the sensing systems was then used to assess the condition and health of the civil infrastructure, which ultimately assisted in making decisions to optimize the maintenance and retrofitting required for the structure. At present, different types of sensors are used to monitor the various physical properties of the structures, including stresses, strains, cracks, damage, and other physical properties; the commonly used sensors include strain gauges (Choi et al., 2008), fibre optic sensors (Robins et al., 2001), piezoelectric sensors (Taheri, 2019), piezoceramic transducers (Zhao et al., 2016; Zhao et al., 2008) and fibre brag grating sensors (Kersey, 1996; Moyo et al., 2005). Moreover, vision-based displacement measurement systems and sensors are also used in SHM (He et al., 2022). **Figure 2.1** describes the evolution of the SHM throughout history. Although these sensors normally show reasonable performance, however, their incompatibility with concrete infrastructures, low operational life, skilled labour demand, and high installation and maintenance cost limit their large-scale civil infrastructure applications (Ou, 2006). Additionally, embedding it in a concrete structure may affect the strength of the structure.

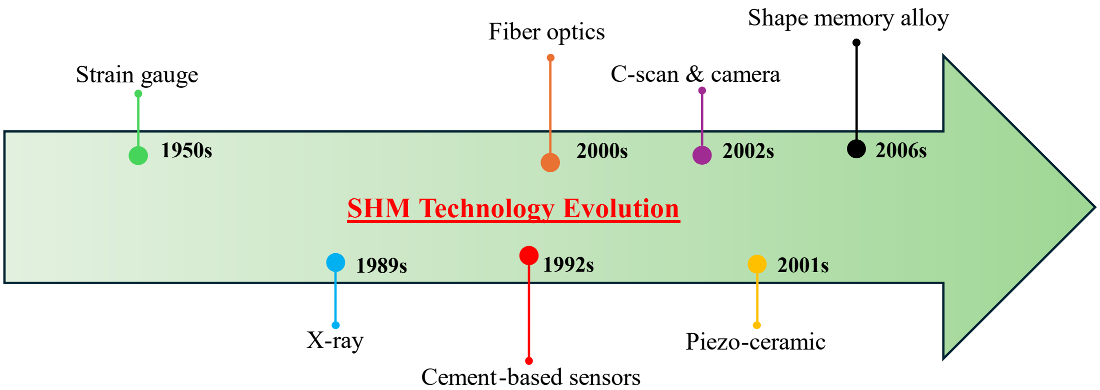

Figure 2.1. The history of applying sensing techniques by SHM (Dong et al., 2019).

Therefore, smart cementitious composites are gaining attention from scientists and engineers, who potentially aim to replace the traditional sensors in concrete structures.

2.2 Smart Cementitious Composites (SCCs)

Concrete is an insulator of electric current in its dry condition (Xu et al., 2010). Back in the 1990s, the introduction of SCCs or cement-based smart sensors (piezoresistive behaviour of concrete) was reported for the first time to address the issues of conventional sensors (Chen & Chung, 1993). The preparation of cement-based sensors provides better compatibility with concrete structures and better durability than conventional sensors. Piezoresistivity is a phenomenon in which the electrical resistivity changes with strain (Chen & Chung, 1993; Chung, 2002, 2018). SCCs are a type of cement-based material that incorporates various types of macro-scale fibres (such as steel or carbon fibres) and nano-scale fibres/fillers (such as carbon nanotubes, nCB, or graphite powder). These additives enable the concrete to sense and respond to stresses, strains, cracks, and damage through changes in its electrical resistance. By monitoring the electrical properties of the SCC, it is possible to detect and locate structural issues within the concrete, allowing for proactive maintenance and repair (Azenha et al., 2016; Dai et al., 2010; Danoglidis et al., 2016; Ding et al., 2019; Jiang et al., 2017; Li et al., 2006; Li et al., 2008; Wang et al., 2018; Zhang et al., 2011). Since the initial development of SCC, extensive research has been conducted to understand this technology and to improve it. Researchers have investigated the piezoresistive behaviours while incorporating different electrically conductive materials and testing them under various loading conditions and environmental actions. This extensive research has aimed to optimize the sensing capabilities of SCC and expand the understanding of the underlying principles and conductive mechanisms that enable concrete to detect and respond to structural changes and damage.

2.2.1 Conductive Mechanisms of SCCs

SCCs are fabricated by incorporating conductive materials in a concrete matrix, which can make a conducive network through different conductive mechanisms. The fundamental conduction mechanisms are ionic (which comes from cement base matrix by ions movement) and electronic conduction (quantum tunnelling, field emission, and direct contact, which comes from conductive fillers by the movement of electrons) (Al-Dahawi et al., 2016). **Figure 2.2** describes the different conduction mechanisms. The ionic conduction mainly depends upon a substantial number of free ions present in pores and voids of cementitious composite, while in a dry state, concrete or cement matrix is approximately an insulator due to the lower number of ions. On the other hand, electronic conduction involves tunnelling conduction (electrons jump through the energy barriers between conductive materials in a concrete matrix) (Han & Ou, 2007) and contacting conduction, which involves the direct contact of neighbouring functional fillers (Chiarello & Zinno, 2005).

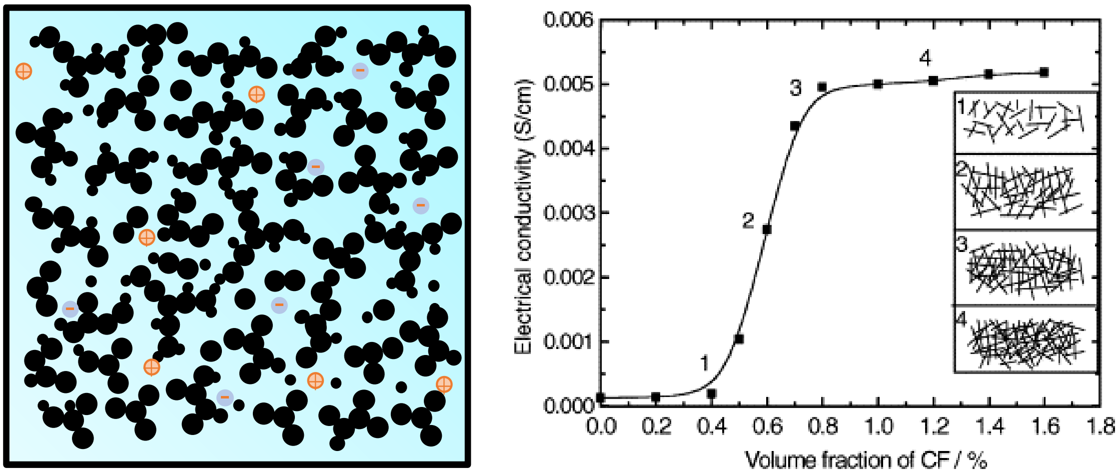

Ionic Conduction | Contacting Conduction

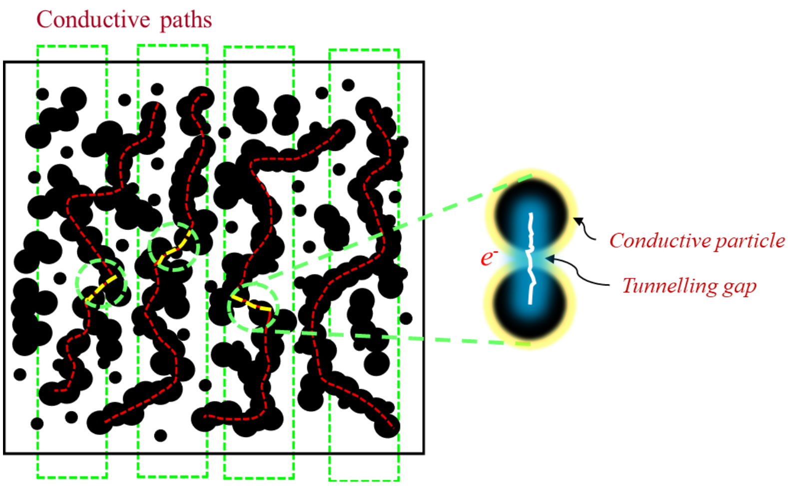

Figure 2.2. Conduction mechanisms of the SCCs (Chen et al., 2004; Hussain et al., 2022).

SCCs may be categorized into three zones, each with a different mechanism, as seen in **Figure 2.3**. *Zone-1*, the insulation zone, contains a minimal number of conductive materials, showing their impact is insignificant. The sole conductive mechanism in this zone is ionic conduction. *Zone-2*, known as the percolation zone, is where the conductive materials reach a critical level, resulting in a combination of ionic and electronic conduction that contributes to the system's conductivity. Finally, *Zone-3*, the conduction zone, is demonstrated by the conductive material attaining a threshold level, facilitating the establishment of a conductive network through direct connections between fibres or fillers.

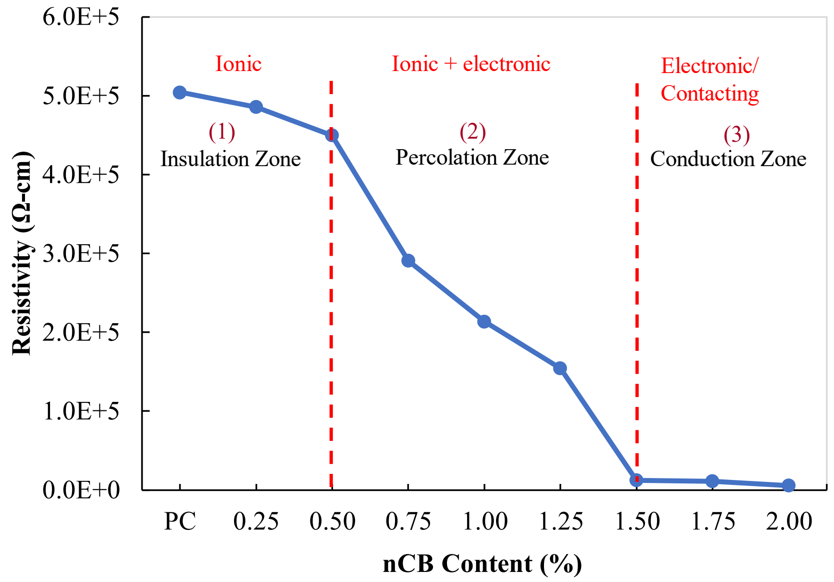

Figure 2.3. Electrical resistivities of nCB-UHPC specimens (Hussain et al., 2022).

Taking into consideration that concrete is a heterogenous material, its conductivity depends on several factors simultaneously, including the hydration process, pore solution composition and concentration, tortuosity of the pore network, moisture content and temperature (Rajabipour & Weiss, 2007; Spragg et al., 2013). It is also important to note that the conduction processes mentioned above occur simultaneously and are interrelated. When an external load is applied to the conductive composite, the internal structure undergoes deformation, resulting in changes to the conduction process and conductive pathways.

2.2.2 Sensing Behaviour at Different Loading Conditions

It is worth noting that various types of loads exert distinct influences on the conduction mechanism. Under compressive loads, the composite specimen experiences compression, causing a reduction in the distance between fibre-fibre, fibre-filler, and filler-filler contacts. Even if the conductive admixture content is below the percolation threshold, the compressive load can facilitate the formation of a few conductive paths. In the percolation zone, tunnelling conduction is dominant, where particles come close to each other to enable tunnelling, and some are even in direct contact. On the other hand, the composites are subjected to tensile stresses, and the distance between adjacent fibres and fillers increases, which may lead to the disconnection of some conductive pathways. Hence, during the loading, the resistance change can be easily measured.

Figure 2.4 provides a schematic representation of the redistribution of the electrically conductive path by compression (below the percolation) and tension-stressed (above percolation) specimens. Additionally, flexural loading has both compression and tensile effects. On the tensile side, the fibres stretch, while on the compression side, they come closer together before cracking. Once cracking occurs, the fibres may pull out, leading to disconnection of the conductive path.

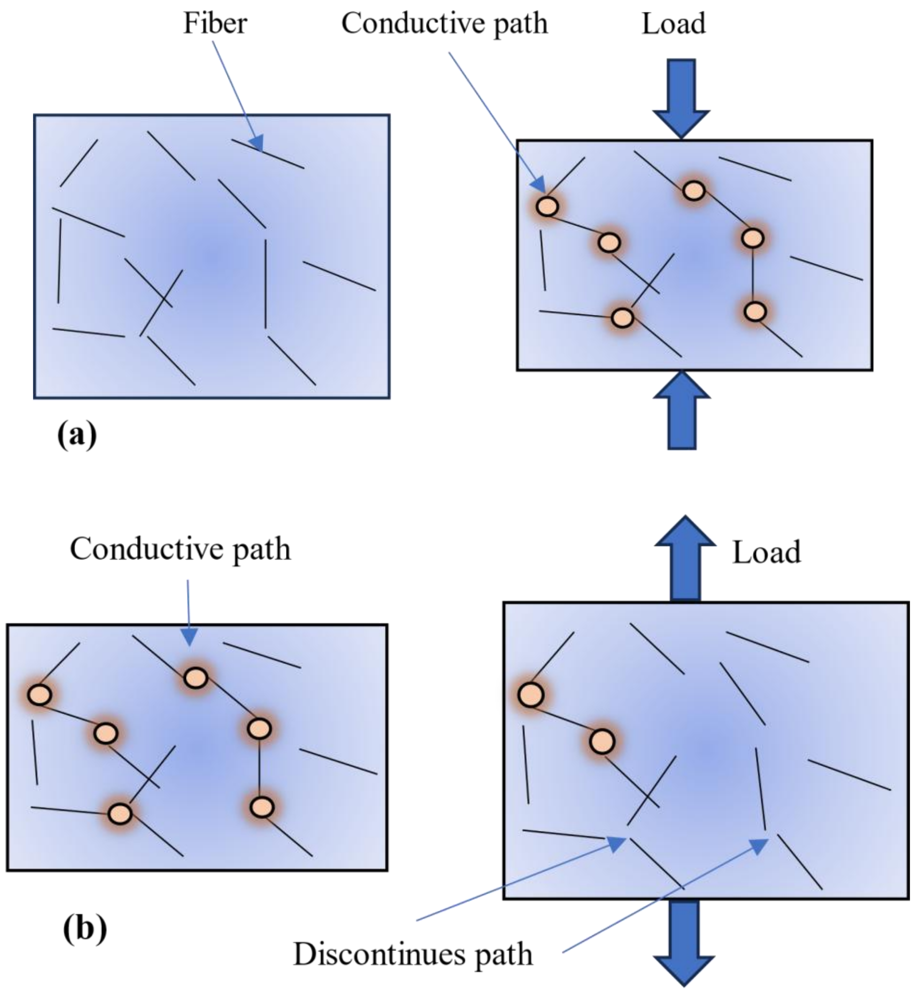

Figure 2.4. Redistribution of conductive network by compressive and tensile loading.

2.2.3 Polarization

Free ions act as electrolytes in concrete with a high moisture content (Demircilioğlu et al., 2019), particularly at low concentrations of conductive materials. In the percolation zone, ionic conduction has a substantial effect on conductivity. In the case of ion conduction, when an electric field is applied, ions present in cementitious composites (K+, Na^{+}, Ca^{2+}, OH^{-}, and SO_4^{2-} undergo the influence of an electrical force (Dehghani & Aslani, 2021). Consequently, they migrate towards the oppositely charged electrodes, forming a thin film on the electrode walls, as can be seen in **Figure 2.5**; this phenomenon is known as polarization (Banthia et al., 1992). However, when measuring the electrical conductivity of the material, it is important to understand the effect of polarization.

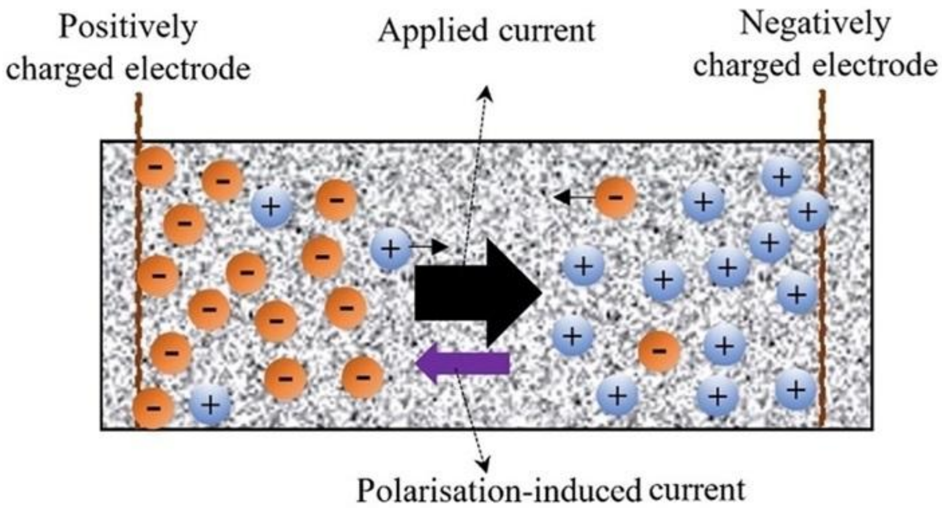

Figure 2.5. Polarization phenomena in cementitious composites (Dehghani & Aslani, 2021).

There are several methods reported in the literature to mitigate polarization and measure the actual conductivity. One approach is to dry out the samples, reducing the ionic activity in the system. By removing moisture, the ions have less mobility and are less likely to form the polarized film on the electrodes. Another method involves applying a direct current (DC) for a specific duration before conducting the conductivity measurement. This pre-conditioning process, typically lasting around 20 minutes, helps to eliminate the polarization effect and stabilize the conductivity (Hussain et al., 2019).

Additionally, alternating current (AC) is commonly employed for conductivity measurements. AC continuously changes direction, preventing the accumulation of ions at the electrodes and minimizing polarization effects. This approach allows for accurate and reliable electrical conductivity measurements in cementitious smart materials. By employing these techniques, researchers can effectively address the polarization issue to obtain precise electrical conductivity measurements, facilitating a better understanding of the conduction mechanisms in SCCs.

2.3 Piezoresistive Materials

A large number of conductive materials are being used, including carbon fibres (CFs), carbon nanotubes (CNTs), nCB, graphite-based materials, steel fibres, nickel powder, and many more.

CFs appear to be the first material to develop this technology. Due to the growing popularity of self-sensing concrete, many new materials are employed to develop cementitious strain sensors. Because of advances in nanotechnology, researchers have been increasingly interested in CNTs, nCB, nickel powder, and graphene as supplementary fillers. This section summarizes the main conductive materials that have been used in previous studies.

2.3.1 Carbon Fibres

For the first time, (Chen & Chung, 1993) employed CFs in concrete as a conductive material that lowers the volume resistivity of concrete. It states that increasing the pressure from 0 - 0.05 MPa was enough to reduce the resistivity of the samples. Since then, much research has been done on developing new types of self-sensing concrete. Furthermore, different studies were conducted to further explore the mechanical and sensing properties of fibre-reinforced cementitious material to study the feasibility as a field-deployable solution (Zhang et al., 2024). A study explored self-sensing capabilities of concrete through a hybrid combination of CFs and CNTs (Azhari & Banthia, 2012). The findings indicated that the hybrid approach yielded superior output signal quality, enhanced repeatability, and increased sensitivity compared to CFs alone. The integration of CNTs played a critical role in bridging the gap between carbon fibres and establishing a continuous conductive pathway.

The degree of fibre dispersion, including carbon nanofibers (CNFs), influences the efficiency of composites in enhancing their structural or functional properties. It is essential to achieve a high degree of fibre dispersion to satisfy the piezoresistive behaviour at a low fibre volume fraction. A lower fibre volume percentage is generally preferred in composites due to the material cost, workability and compressive strength (Chen & Chung, 1996). The degree of dispersion dramatically influences the functional properties of SCCs. The higher the degree of fibre dispersion, the higher the conductivity of the composite. Fibre dispersion, especially in high-volume fractions, is very difficult without any proper dispersion agent (Chung, 2005). Therefore, the mixing methods and the dispersion agents are among the most critical parameters that need special attention. (Chung, 2005) conducted a study about the dispersion of short fibres in the cementitious composite. Many dispersion agents (namely acrylic particle dispersion, silane, and methylcellulose solution) and fibre surface treatment (like ozone treatment) were applied, and the results were measured by electrical resistivity measurement. The degree of fibre dispersion is also enhanced by using fibre surface treatment, such as ozone treatment, which explains the impact of fibre size, fibre volume fraction and hydration on the percolation threshold phenomena (Chiarello & Zinno, 2005). It is stated that the CFs with a higher fibre length leads to a lower threshold value than those with a lower fibre length. It also mentions that the addition of fibre content above the threshold value does not show any significance in electrical conductivity.

Moreover, the economic consideration of using fibres in the cementitious composite is crucial. For instance, the hybrid use of the low-cost filler with CFs is employed to reduce the cost of the cementitious sensor without diminishing the piezoresistive behaviour. A study employed partial (50%) replacement of CFs by nCB to investigate the piezoresistive behaviour (Wen & Chung, 2007). As a result, it lowered the cost and increased the workability while maintaining the electrical conductivity. Therefore, it would be an attractive alternative for a field-deployable solution. Although carbon fibres have superior electrical properties, the high cost and poor dispersion are the main problems that are vital to the practical applications of cement-based materials (Wen & Chung, 2007).

2.3.2 Carbon Nanotubes

CNTs have attracted considerable research interest because of their remarkable mechanical, electrical, piezoresistive, and physical properties (Hong et al., 2024; Jackson et al., 2016; Lau & Hui, 2002; Shah et al., 2009). It is anticipated that incorporating CNTs into cement-based materials would enable the development of a new class of multifunctional cement-based materials (Han et al., 2015; Han et al., 2017). Cement-based materials incorporating CNTs and exhibiting piezoresistive properties offer a significant advancement for structural health monitoring applications

CNTs have been used in many studies to investigate the self-sensing behaviour of concrete. CNTs were used with a concentration of 0.1%, 0.5%, 1.5%, 1%, and 2% by weight (Parvaneh & Khiabani, 2019). However, extensive dispersion materials and techniques were used to avoid significant agglomeration. Sodium dodecyl benzenesulfonate (NaDDBS) was used as the surfactant to disperse the CNTs, modify their surface, and then an ultrasonic bath was used to disperse the CNTs. It was observed that 1% was the optimum concentration of the CNTs which led to the best piezoresistive behaviour.

A study was conducted on cement pastes containing 1% by weight multiwall CNTs (MWCNT) (Yoo et al., 2018). Cyclic loading with varying amplitudes and frequencies was applied to the specimens. Simultaneously, strain gauges were used to detect the strains on the specimen surface. Resistance changes were found to be exceptionally well correlated with strain changes recorded during cyclic loading throughout a wide range of amplitudes. The pressure-sensitivity of treated and untreated CNTs in cement-based composites under cyclic compressive loading was investigated (Li et al., 2007). The authors discovered a significant increase in compressive sensitivity when treated or untreated CNTs were added to cement-based materials. The piezoresistive properties of cement-based composites containing CNTs under various loading conditions, including tension and compression, were investigated (Andrawes & Chan, 2012). They observed that tensile stresses increased the electrical resistance, whereas compression stresses did the opposite. This finding demonstrates that cement-based composites containing CNTs can sense the two types of loading.

CNTs are considered one of the exceptional conductive fillers for cementitious composites compared to other carbon conductive fillers. It may fill pores and enhance the flexural properties, compressive strength, ultimate strain, and other mechanical properties of composites as a nanomaterial (Li et al., 2007). The use of CNTs fulfils the conductivity requirement and improves the mechanical properties of a cementitious composite. However, agglomeration is more likely due to the large specific surface area of CNTs and the Van der Waals force. It has also been demonstrated that adding CNTs to cement-based composites produces poor fluidity. As a result, most research has concentrated on specific dispersion strategies to increase the workability and performance of CNT-based SCCs.

Furthermore, its high cost limits its wide application, which is the most important field application factor (Han et al., 2020). Similarly, replacing some parts of these expensive materials could be the solution for large-scale implementation. The CNTs was replaced by 60% of nCBs in a study (Zhang et al., 2018), and the CNT-nCB-based cementitious composite fillers exhibited acceptable mechanical properties, high conductivity, and stable piezoresistive properties at a low filler content. The addition of CNT-nCB composite fillers with 1.41 vol.% can significantly improve electrical resistivity, stress sensitivity and strain sensitivity with a substantial reduction in cost (Zhang et al., 2018). Similar to CFs, the CNTs have a high dispersion problem, as seen in **Figure 2.6**; they also suffer from their high cost, which hinders their use as field-applicable solutions.

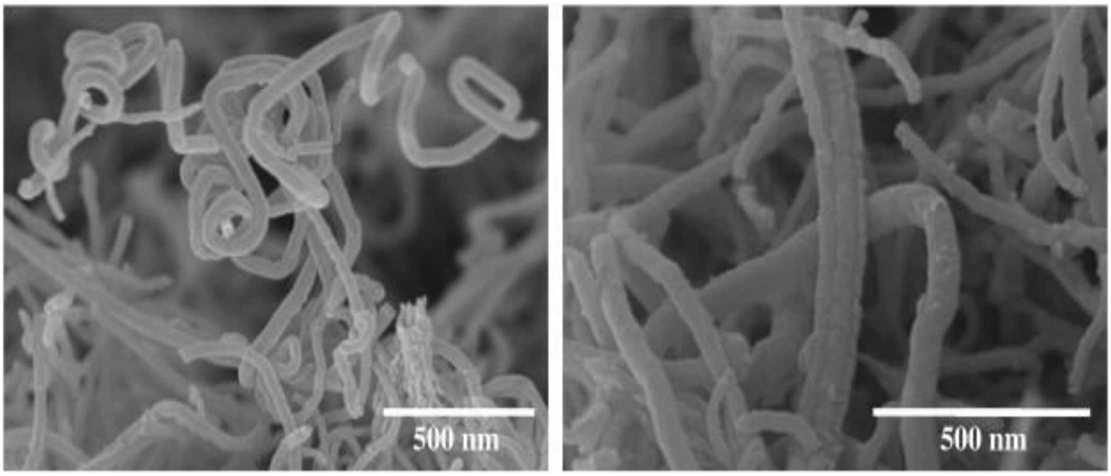

Figure 2.6. SEM images shows the poor dispersion of MWCNTs in cement paste (Konsta-Gdoutos et al., 2010).

2.3.3 Graphene

Graphene-based materials, including graphene (GO), graphene platelets (GP), graphene nanoplatelets (GNP), graphene nanofiber (GNF), and graphene oxide nanoplatelets (GONP), are known for their exceptional strength and remarkable electrical conductivity. It offers significant benefits in terms of developing highly conductive networks and mechanical properties in composites (Yao et al., 2022). For graphene-based SCCs, the piezoresistive properties have been investigated. A study examined the multi-layer graphene (MLG) for the mechanical properties, piezoresistive effect, and electrical properties of the cement-based composites, which were filled with different contents of up to 10% by volume (Sun et al., 2017). For the dispersion of the MLG, a mixture of the polycarboxylate superplasticizer with water was used, and ultrasonication was used for 1 hour. The compressive strength of cementitious composites filled with MLG increased by 54%, and the percolation thresholds achieved nearly 2 vol %. MLG-filled cementitious composites have demonstrated a sensitive piezoresistive response and reliable cyclic static and dynamic loading sensitivity.

(Belli et al., 2018) investigated the mechanical and piezoresistive properties of cement-based composites produced with graphene nanoplatelet filler and carbon fibres. Different concentrations of GNP and carbon fibres were added to the mortars to study their combined effects on the mechanical performance, electrical resistivity, and piezoresistive behaviour, and the polycarboxylate ether agent was used to disperse the GNP and fibres. The resulting mortars exhibited piezoresistive behaviour only after a drying treatment with dry specimens. Similar to CNTs, the difficulty associated with producing graphene is its high cost, which limits its potential use as a conductive filler in cement-based composites.

The materials mentioned above have shown good piezoresistive behaviour in general, and they may improve the mechanical properties of cementitious composites. However, the unit cost is very high, which hinders their large-scale applications in real construction projects. Another critical issue is the dispersion of the fillers in a cementitious matrix, as seen in **Figure 2.7**. It has been stated that most of the piezoresistive fillers have shown significant dispersion issues, which directly affect the piezoresistive behaviour. Piezoresistivity cannot be achieved without proper dispersion (techniques and treatment), and the mechanical properties are also compromised. It can be seen from **Table 2.1** that all the piezoresistive materials used in the previous studies need extensive dispersion materials and techniques to ensure the proper dispersion of the conductive fillers. It is challenging to achieve adequate dispersion, and it also increases the unit cost of the product.

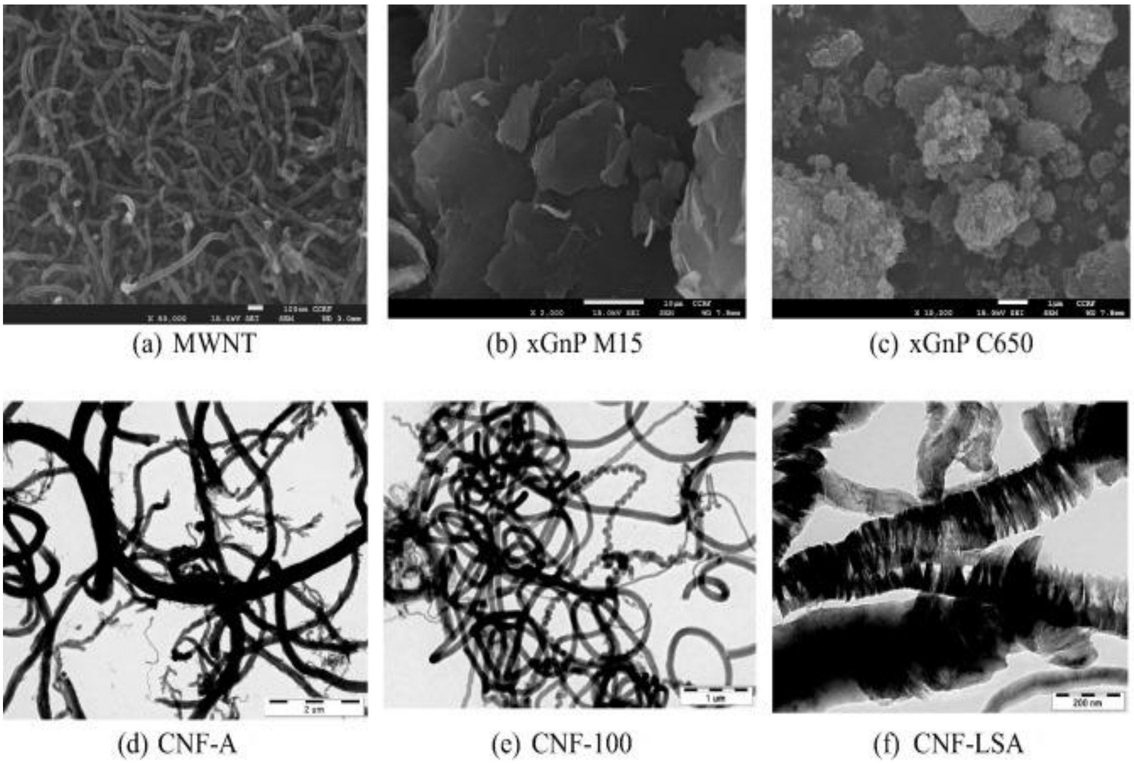

Figure 2.7. Microstructure of different carbon materials showing their dispersion. (a) MWCNT, (b) xGnP M15, (c) xGnP C650, (d) CNF-A, (e) CNF-100 and (f) CNF-LSA (Rhee et al., 2016).

Table 2.1. Summary of dispersion materials/methods used for different conductive fillers

Piezoresistive material	**Dispersion Material/Method**	**References**
CF, CNF	Methylcellulose, oxidation by H_2O_2, oxidation by ozone, superplasticizer, HNO_3, air and ozone, sonication, and mechanical mixing	(Azhari & Banthia, 2012; Baeza et al., 2013; Bontea et al., 2000; Catalá et al., 2011; Chen et al., 2012; Chen & Chung, 1995; Chen & Chung, 1993; Chu & Chen, 2016; Hoheneder et al., 2015; Meehan et al., 2010; Mosavinejad et al., 2018; Reza et al., 2003; Reza et al., 2004; Wang et al., 2018; Wen & Chung, 2003, 2007)

CNT, MWCNT	ultrasonication, Ammonium polyacrylate-based dispersant, PSS aqueous solutions superplasticizer, mechanical mixing, NaDDBS	(Adresi et al., 2017; D'Alessandro et al., 2016; D'Alessandro et al., 2016; D'Alessandro et al., 2015; Gupta et al., 2017; Han et al., 2009; Han et al., 2012; Han et al., 2012; Han et al., 2012; Islam et al., 2003; Mendoza et al., 2013; Parvaneh & Khiabani, 2019; Ruan et al., 2018; Sasmal et al., 2017; Ubertini et al., 2014; Yoo et al., 2017; Yoo et al., 2018; Yoo et al., 2019)
CB, nCB	Superplasticizer, water-reducing agent	(Ding et al., 2019; Li et al., 2006; Monteiro et al., 2017)
GO, GP, GNF, NGPs, GONPs	Superplasticizer, sonication, ultrasonication	(Kashif Ur Rehman et al., 2018; Li et al., 2018; Liu et al., 2016; Ozbulut et al., 2018; Rehman et al., 2017; Sun et al., 2017)

2.4 Nanocarbon Black (nCB)

Nanocarbon black (nCB) is a commonly used polymer addition that is employed as a filler to modify the mechanical, electrical, and optical properties of the polymer (Pantea et al., 2003). It is produced by the hydrocarbon fuel (oil or gas) reaction in a limited combustion air supply at temperatures of ~1400 °C (Taha, 2020). The use of electrically conductive carbon blacks in the production of conductive polymer composites has received special consideration. nCB is usually incorporated in polymer composites at a critical concentration that percolates the electrically insulating polymer to a conductive domain. The capability of the nCB transformation to electrical conductors depends upon the structure of the nCB that establishes and maintains the conductive pathway. The nCB is used in electromagnetic shielding and different electrochemical energy storage systems.

2.4.1 Morphology of nCB

The morphology of the nCB is specified at three different levels, including ‘particle,’ ‘aggregate,’ and ‘agglomerate’ (Youssry et al., 2013). The primary shape of the nCB is nearly spherical, which is adherently together in the form of the aggregate. The structure of the nCB refers to how well the primary particles combine and stick together. According to ASTM-D2414 (D2414-21, 2021), the oil absorption number (OAN), which is the dibutyl phthalate (DBP) paraffin or Epoxidized Fatty Acid Ester (EFA), is used to define the structure. High-structure carbon black is a class that shows a high void volume. The void volume can be characterized by the oil absorption capacity measured through DBP absorption, which reflects the porosity of the primary particles as well as the size and shape of the aggregates which reflects the porosity of the primary particles as well as the size and shape of the aggregates. These voids act as stress relievers and can prevent crack propagation, leading to improved toughness and resistance to mechanical deformation. It can enhance chemical reactions by providing more active sites for interacting with reactants. The DBP value is the factor that has a direct impact on the sensitivity and/or conductivity of nCB composites. The nCB grades with a DBP above 170 mL/100 g are specified as highly conductive carbon black (Spahr et al., 2017).

Agglomeration refers to the process by which multiple aggregates come together to form a larger mass. Generally, a number of interparticle forces lead to an agglomeration, including Van der Waals forces, magnetic forces, mechanical forces by irregular shapes of the particles and forces due to the presence of a pendular force of the moisture (Hartley et al., 1985). Carbon black is a nonmagnetic, nearly spherical particle shape and essentially hydrophobic surface. Therefore, it is sensible to presume that Van der Waals's force is the only interparticle force, which is the force responsible for the agglomeration of the carbon black particles (Hartley & Parfitt, 1985). TEM images of the Super P nCB can be observed in **Figure 2.8**.

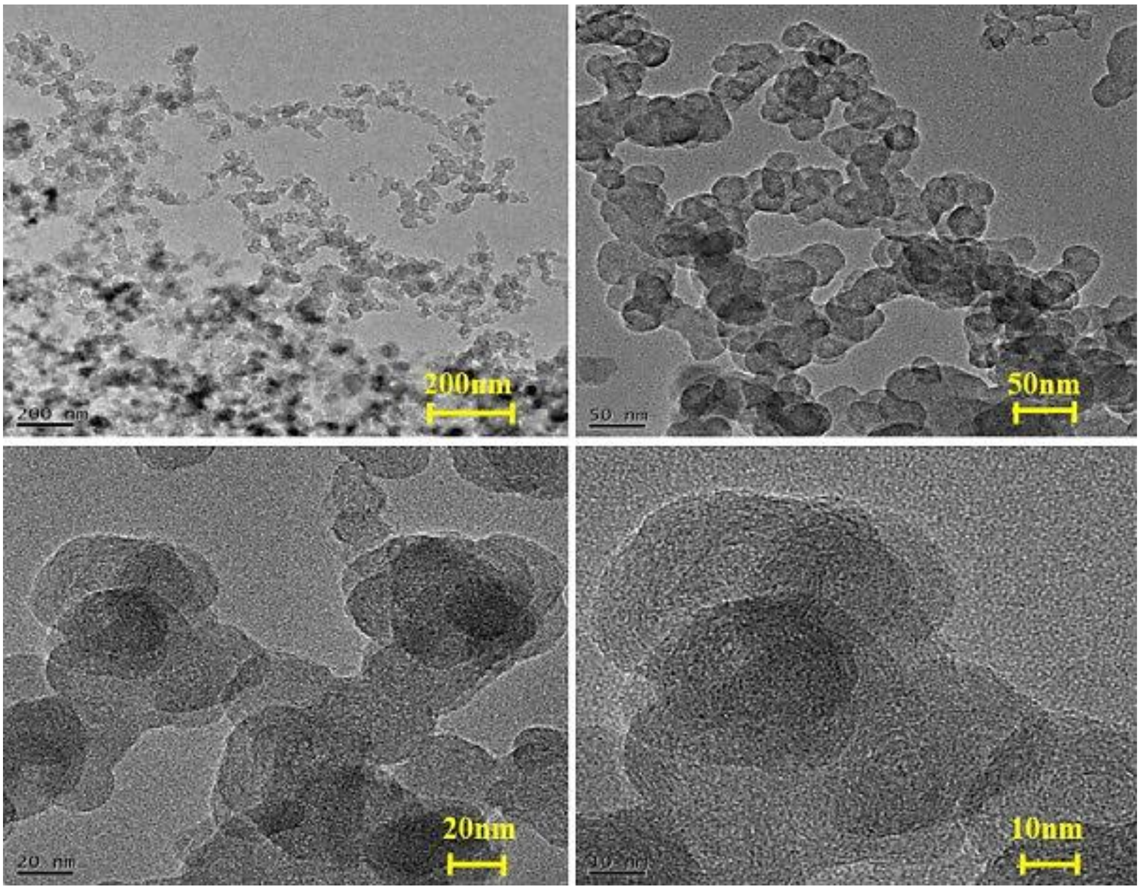

Figure 2.8. TEM images of nanocarbon black (Gnanamuthu & Lee, 2011).

The structure is the most critical parameter in choosing suitable candidates of nCB for the right job. The higher nCB structure grants electrical conductivity to polymers at lower critical volume fractions than the lower nCB structure, and it would be beneficial in many ways, lead to ease of the fabrication process and a decrease in the unit cost of the composite. A high-structure nCB has a higher surface area for electron conduction than a low-structure carbon black for the same amount of nCB aggregates (Rwei et al., 2002). The finer agglomerates enable more particles to adhere to one another for a given weight of nCB. Consequently, interparticle distances can be reduced, allowing the electrons to be transported between particles across the matrix. High-structure of nCB has a higher agglomeration. In fact, at some level, agglomeration is beneficial for the conductive phenomena of nCB due to the maintenance of the structure and volumetric wiring (Soliman et al., 2020).

Moreover, the thermogravimetric analysis (TGA) was performed to assess the thermal stability and carbon purity of the carbon black, which can be seen in **Figure 2.9**. The weight of the powder remained constant up to a temperature of 600 °C. Beyond this temperature, the carbon black began to evaporate and eventually completely dissolved at 765 °C (Milone et al., 2024).

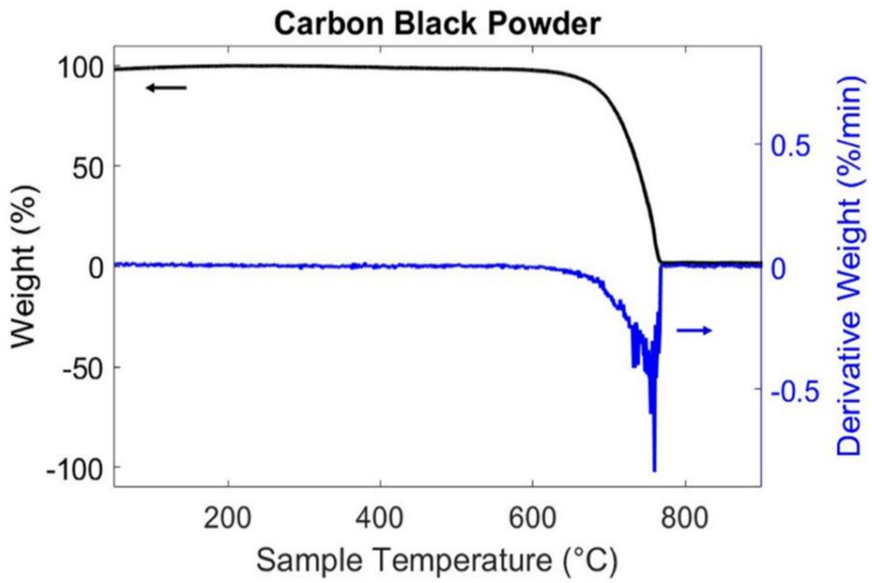

Figure 2.9. Weight and derivative weight for nCB powder (Milone et al., 2024).

2.4.2 Percolation Threshold of nCB

The percolation threshold is a critical parameter for designing and optimizing sensing properties. The percolation threshold is defined as a critical volume proportion of the conductive materials at which the resistivity of the matrix is abruptly decreased by several orders of magnitude (Han et al., 2015; Kovacs et al., 2007; Sun et al., 2017). Various methods explain percolation, with some considering the influence of filler size on the percolation threshold (Youngs, 2003), aspect ratio (Celzard et al., 1996), and shape (Saar & Manga, 2002) based on critical filler concentration (Chen et al., 2017). It can be observed in **Figure 2.10** that the conductivity is the function of the filler concentration. It can be described in three phases: the insulator, percolation, and conductive zone. As the concentration increased, the transformation from insulator to percolation zone started. A specific critical volume fraction (which depends upon the structure of the nCB and the matrix) of the conductive filler is the beginning point of the percolation zone.

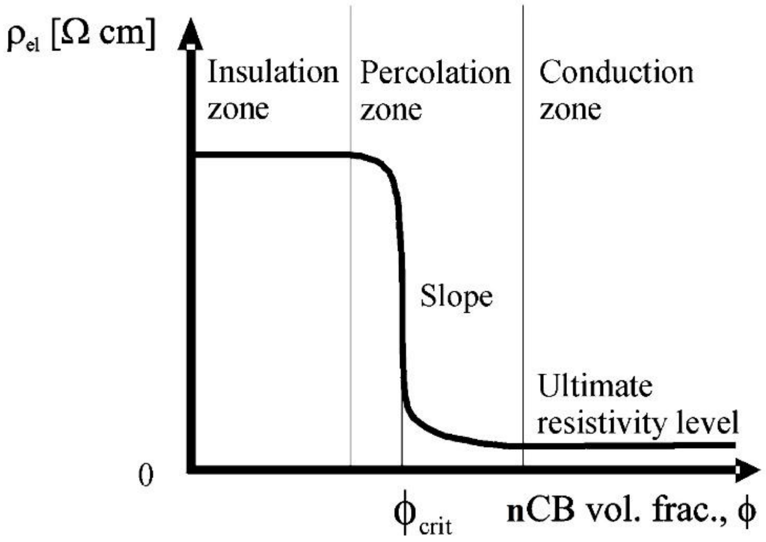

Figure 2.10. Schematic representation of the electrical resistivity as a function of the nCB (Spahr et al., 2017).

Further increase of the conductive fillers leads to a stable and permanent conductive network. It can be seen from **Figure 2.11** that the higher DBP value has the percolation threshold at the lower contention of the nCB. The higher structure of nCB has a greater ability to establish and maintain electrical conductivity at a lower concentration of the nCB. Therefore, a proper selection of the nCB is necessary to maintain the electrical conductivity, mechanical properties, and unit cost.

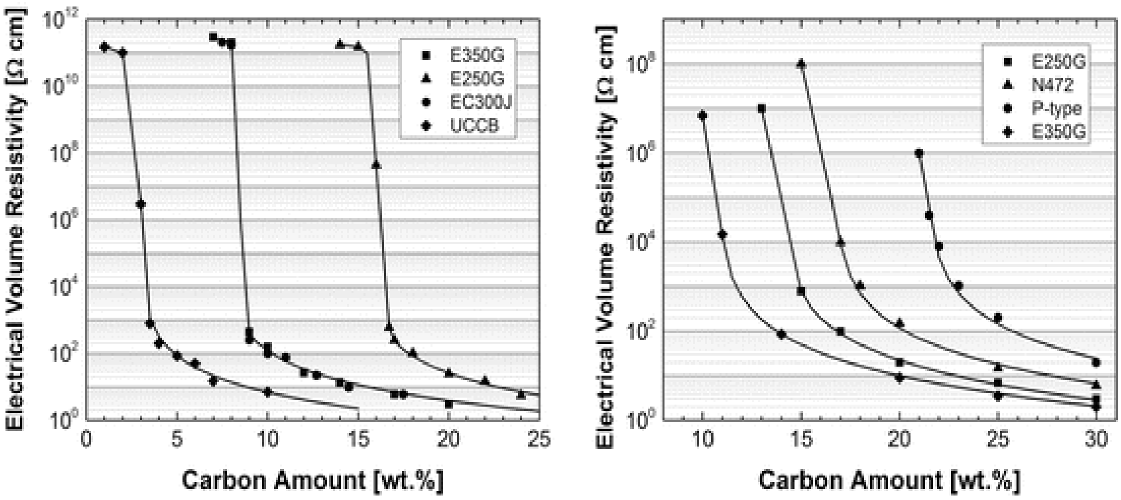

Figure 2.11. Electrical volumetric resistivity of different nanocarbon blacks including E350G, E250G, EC300J, UCCB, N472 and P-type with a DBP values of 320, 190, 330, 560, 175 and 100ml/100g, respectively (Spahr et al., 2017).

On the other hand, the conduction mechanism is also equally important for the percolation. The predominant conduction mechanism in carbon black particles is electron tunnelling (Spahr et al., 2017). The tunnel effect dominates the electrical conductivity of nCB (Li et al., 2006). According to tunnel effect theory (Simmons, 1963; Xiao et al., 2010), the current density in a tunnel resistor formed by two adjacent CB particles at a low voltage region can be described by the following equation:

$$J = \left[\frac{3(2m\varphi)^{1/2}}{2S_0}\right](\frac{e}{h})^2 U \exp\left[-\left(\frac{4\pi S_0}{h}\right)(2(2m\varphi)^{1/2}\right] \quad (2.4)$$

where ***J*** is current density, ***m***, ***e***, and ***h*** are the electron mass, a charge on an electron and Planck's constant, respectively, φ, S_0 and ***U*** are the height of tunnel potential barrier, tunnel width (i.e. the distance between conductive fillers) and voltage applied across tunnel resistor, respectively.

2.4.3 Cementitious Composites with nCB

Similar to polymer composites, the construction industry has also investigated the incorporation of nCB into cementitious composites. nCB can be used as a suitable admixture for conductive concrete due to its electric conductivity, lightweight, high thermal and chemical stability, permanent electrical conductivity, and fine filler effect (Ding et al., 2012; Feng & Chan, 2003; Han & Ou, 2007; Jahanbakhsh et al., 2018; Luo et al., 2010; Ou & Han, 2009; Shi et al., 2017; Wen & Chung, 2001, 2006; Wu et al., 2005; Yang et al., 2007). The nCB particles offer considerable benefits at a very low cost. It is a crucial parameter in structural health monitoring (SHM), leading to reduced inspection costs. Consequently, large-scale implementation is feasible, as the production and integration costs of the system are relatively low (Ding et al., 2012; Luheng et al., 2009). Many studies have employed the nCB in cementitious composites to investigate the piezoresistive behaviour. The results are very encouraging, showing that these cementitious composites can replace the traditional sensors with nCB-based cementitious sensors.

Additionally, different conductive materials have been employed with nCB to investigate the hybrid effect. The primary purpose of the hybrid use of nCB with different piezoresistive materials is to decrease the unit cost of the sensor while maintaining the electromechanical properties. It is observed that a hybrid use of CFs and nCB could improve the linearity and reproducibility of the sensing performance of cementitious materials (Ou & Han, 2009). A study described the combined use of fibrous and particle fillers, which led to the formation of a better conductive pathway for the movement of electrical charges, enhanced the contact and tunnelling conduction effect, and greatly decreased the cost and dispersion issue; it also showed better flexural and compressive strength, and the FCR of the beam was also increased (Ding et al., 2013). Another study investigates a triphasic conductive admixture (macro steel fibre nCB and CF) in order to improve the mechanical performance and conductivity of concrete (Ding et al., 2016). The results indicate a positive hybrid effect to improve the signal-to-noise ratio.

On the other hand, the replacement of the nCB with other expensive materials also appears to be a good strategy in order to improve piezoresistivity at a lower cost. CNTs were used to partially replace nCB to investigate the electromechanical properties (Han et al., 2015). The results state that the CNT-nCB composite filler could efficiently improve the flexural strength and lead to a highly stable and sensitive response of cementitious composites. It led to the formation of a grape bunch structure of CNT-nCB, which is highly beneficial for continuing the conductive path, as shown in **Figure 2.12**. In a grape bunch structure, the CNT is the stem, and nCB particles act as a grape attached to its stem. It is also explained that the percolation threshold zone of the CNT-nCB-based cement mortar composites ranged in the amount of 0.39-1.52 vol%.

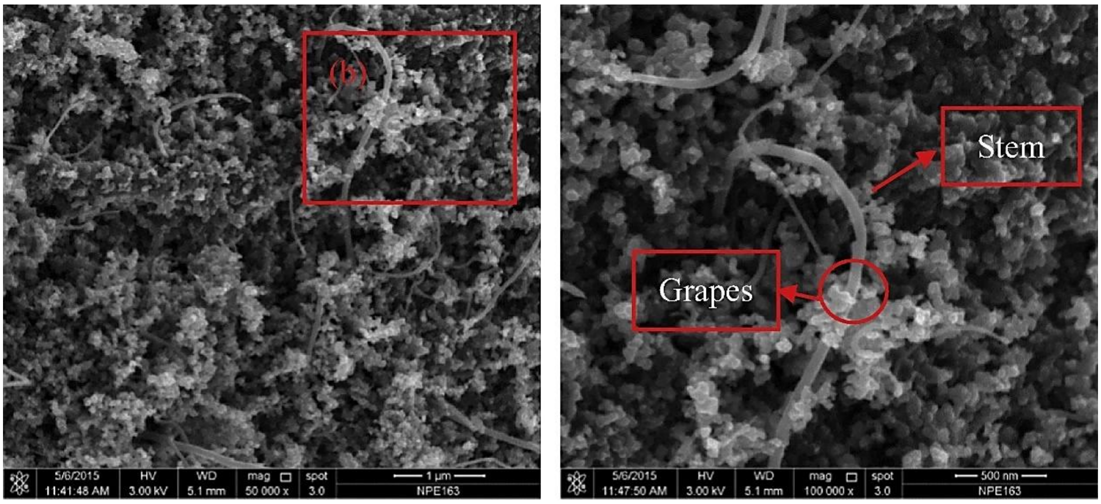

(a) (b)

Figure 2.12. SEM images of CNT-nCB-based cementitious composite at different scales (Han et al., 2015).

Another study has employed carbon black, graphite, and CFs to design and prepare electrically conductive asphalt mixtures with different dosages of materials (Wu et al., 2005). Experimental results indicated that the insulating-conductive percolation transition of resistivity occurred at approximately 5%, 10%, and 12%, by volume of the binder phase for carbon fibre, graphite, and carbon black, respectively. In fact, the specimens with CFs showed better results, but the expensive and inferior dispersion properties of CFs are unfavourable for large-scale practical solutions. So, a small amount of CF with a large amount of cheaper nCB can be a cost-effective and well-defined conductive system.

Furthermore, the piezoresistivity behaviour of the cementitious composites was investigated by using conductive rubber fibres filled with nCB (Dong et al., 2019). The nCB with a high structure (280 ml/100g, DBP) was added with a 0.1 to 4.0% concentration by a binder (cement and silica fume). The percolation threshold was 0.5 to 2.0%. The compressive strength steadily decreased with the increase of the nCB. At 2.0% nCB, which was the endpoint of the percolation zone, it showed better linearity and gauge factor. Another study added polypropylene (PP) fibres during the fabrication of a cement-based sensor with nCB to improve the sensing performance (Li et al., 2020). The hybrid system was shown to improve the electrical conductivity and piezoresistive behaviour of the nCB-based PP fibre cementitious composite. However, a minor reduction in compressive strength was observed. Microstructural analysis showed that nCB adhered to the surface of PP fibres considerably increased the formation of conductive paths and contact points in cement-based sensors.

Another study examined the utilization of nCB with different concentrations of impact forces and the energy released from cracks to evaluate the capacity of nCB-modified cementitious composites in sensing dynamic signals. The results demonstrated that 2.0% nCB had the highest sensing performance of these composites, which display exceptional piezoresistive behaviour and possess the capability to locally sense dynamic signals as sensors (Shi et al., 2024). It was also observed that the combined use of different conductive fillers, including carbon fibre, steel fibre, and carbon black, in the engineered cementitious composite

(ECC) led to improved self-sensing performance while maintaining its tensile strain-hardening behaviour (Hou & Lynch, 2005; Lin et al., 2011). In addition, it was observed that ECC with nCB shows a tensile strain capacity of up to 3.44% (Huang et al., 2018). The addition of nCB amazingly decreases the crack spacing with respect to the solo use of ECC. The self-sensing sensitivity to the first crack with nCB is the most sensitive response with regard to ECC, as shown in **Figure 2.13**. Furthermore, another study (Li et al., 2024), published in the final stage of this PhD study, developed the self-sensing UHPC by the incorporation of nCB and carbon nanofiber (CNF). A comparison was made between UHPCs filled with a single nCB and a hybrid nCB and CNF, focusing on strength, microstructures, percolation threshold, conductivity, and piezoresistive sensing performance.

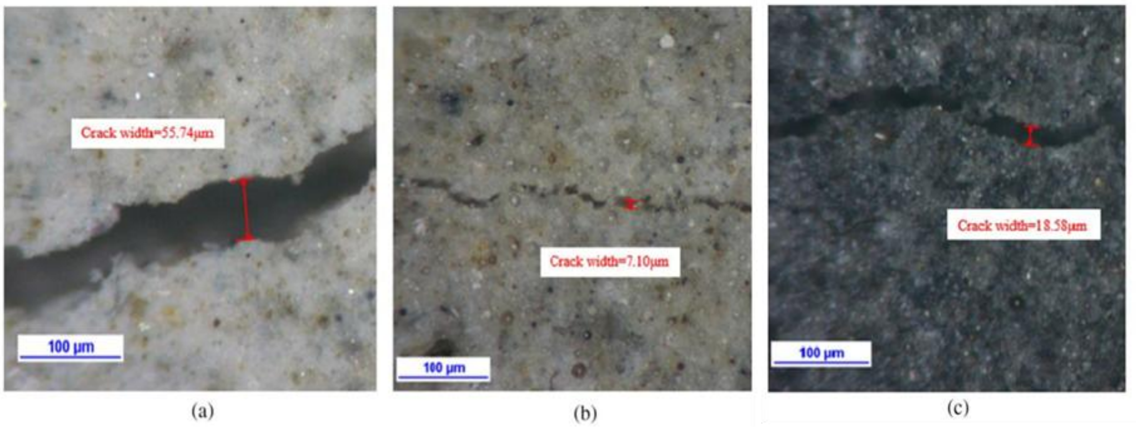

Figure 2.13. Typical crack width measurements with different ECC materials. (a) Plain ECC samples. (b) High-fly ash-ECC and (c) nCB-ECC (Huang et al., 2018).

2.4.4 Effects of nCB Structure on Electromechanical Properties

As mentioned above, the structure of nCB is the most important factor affecting the mechanical and piezoresistive properties of nCB-SSCs. The structure of nCB was not systematically explored previously, which is why many previous studies have not mentioned the structure of the nCB. A study explored the piezoresistive behaviour of nCB-based cement composites containing an amount of 5-25% nCB by weight of cement (Li et al., 2006). It can be seen in **Figure 2.14** that the percolation threshold zone was about 12-20%. The percolation zone is very high, which may affect both the mechanical properties and the cost of the sensor. This study (Li et al., 2006) provided no information regarding the structure of the nCB, and the compressive strength of the concrete was 40 MPa.

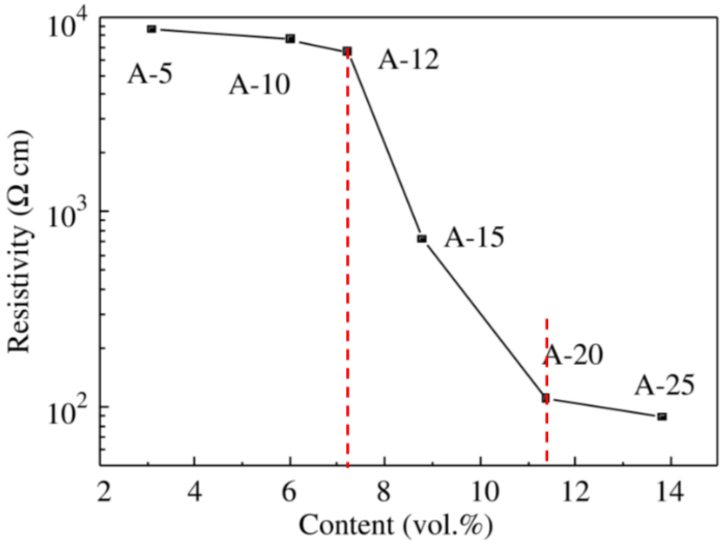

Figure 2.14. Resistivity of cementitious-based nCB at different volume content (Li et al., 2006).

In another study, carbon black was employed for up to 10% of the binder mass, and the resulting cementitious composites were tested under cyclic compression loading (Monteiro et al., 2017). The results indicate that more than the specimens with 7% of carbon black showed a reversible piezoresistive performance. A linear relation was established between compressive strain and the fractional change in resistivity, particularly for those with a relatively high dosage of nCB. The highest gauge factors, up to 30, were found at 7%, as it would be in the percolation zone. The compressive strength increased with the nCB content up to 4%, and then it decreased with the nCB content. This is due to the filling effect of the nCB which may have improved the compressive strength, but the tensile strength did not show any significant change. Another study explored the carbon black-filled cement composites as a piezoresistive sensor for traffic monitoring in different loading conditions and temperatures (Monteiro et al., 2017). The nCB concentration was about 6.5% by mass of the binder. The compressive strength was about 18.8 MPa, and nCB filler provided remarkably reproducible behaviour, with the average GF ranging from 40 to 60. On the other hand, the specimen's sensitivity decreased by 30% when the sensor temperature increased to 45℃.

The above two studies are comparable because they used the same nCB particle size of 120 nm. However, neither study included the DBP value to define the structure of the nCB used in these studies. Monteiro et al. (2017) claimed that the nCB quantity they used to achieve piezoresistive behaviour is lower than that by Li et al. (2006) because of the higher structure of the nCB.

On the other hand, Dai et al. (2010) investigated the high structure of carbon black with a DBP value of 380 ml/100g for the electromechanical properties of cement mortar with up to 6% nCB by weight of cement which shows the percolation threshold zone contained 0.7-2.85% nCB, which was around 7-20% in the previous studies. The lower percolation threshold is attributed to the nCB structure since the high structure nCB has a rich branch structure. The higher number of primary particles attached to each other leads to more branches and chains within an aggregate. The chain and branch structure are responsible for the lower percolation threshold. It was also observed by Dai et al. (2010) that the compressive strength decreased as the carbon content increased, and it was believed to be due to the strong van der Wall forces between the high-structure nCB particles, which makes it difficult to achieve uniform dispersion in a matrix, and leads to high agglomeration. Evidently, the structure of the nCB is a significant factor to study.

Moreover, a study investigated three different nCBs with the same concentration, which was 8% by weight of the cement, to investigate the sensing performance and compressive strength (Nalon et al., 2020). Dibutyl phthalate (DBP) absorption number (ml/100 g) was used to define the nCB type. The specimens were fabricated using cement, sand, and superplasticizer as dispersion agents. The results show that nCB aggregates with the lowest structure (DBP 125 ml/100 g) provided a high gauge factor (fractional change in resistivity per unit compressive strain (Wen & Chung, 2008)), stress sensitivity, and also compressive strength. In contrast, nCB with a very high structure (174 ml/100 g) provided high electrical conductivity, low internal capacitance, good linearity, and repeatability but the lowest sensitivity for stresses and strains. The high structure showed better repeatability and linearity, which shows the high structure nCB concentration in the above percolation zone. On the other hand, all these samples have reduced compressive strength compared to the reference samples without nCB. One thing that should be noted is that the different structures of nCB have different percolation zone and different effects on both the mechanical and piezoresistive properties of the cementitious composites. However, only a single concentration of nCB was investigated in this study, which could not give the complete information.

On the one hand, although conductivity can be improved by using high-structure nCB as their particles stick to each other because of interparticle forces, high-structure nCB leads to decreases in the mechanical properties because of the stress concentration points in a matrix and agglomeration. It can be seen from **Figure 2.15** that the high structure of carbon black and the agglomeration in a cement matrix.

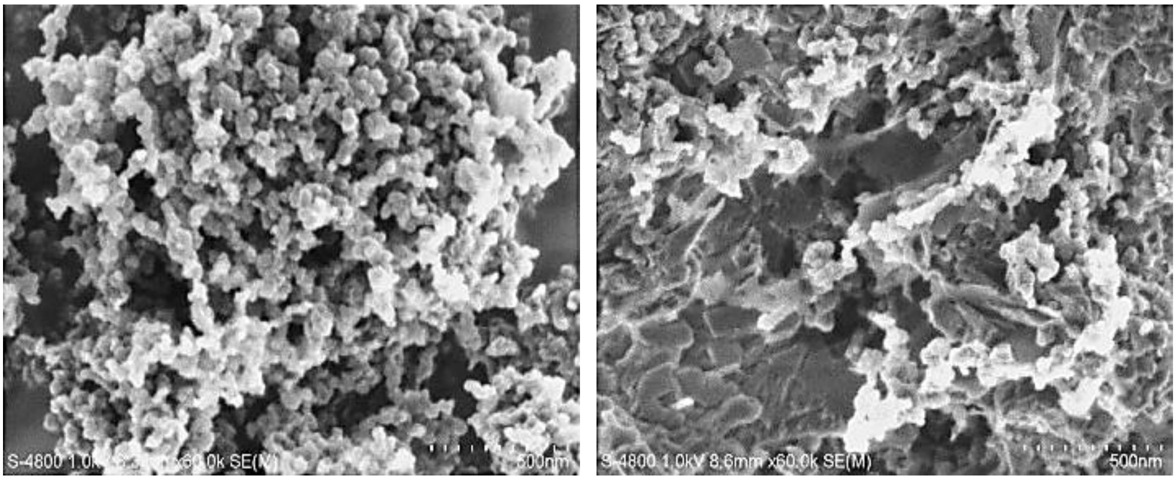

Figure 2.15. Micrograph of nCB observed by FE-SEM and nCB within the cement matrix (Dai et al., 2010).

The nCB fillers are regarded as a competitive candidate for achieving piezoresistive behaviour of SCCs (Han et al., 2020; Tian et al., 2019). Dispersion of the filler is an important factor in transforming the insulator into the conductor and maintaining or improving the mechanical properties. It is discussed above that compared to other nanofillers, nCB is regarded as one of the most promising candidates for SCC because of its stable conductivity and no critical dispersion issues (normal superplasticizer is used, which is also used for better workability of the concrete), high chemical and thermal stability, and fine filler behaviour (Dong et al., 2020; Leong & Chung, 2003, 2004; Monteiro et al., 2015; Wen & Chung, 2007; Youssry et al., 2013).

2.5 Durability of SCCs

Concrete durability is a matter of consideration all the time because of the high ions and fluid migration properties of cementitious composites. The durability of concrete structures largely depends on their capability to resist the penetration of moisture and aggressive ions through penetration, diffusion, and capillary sorption of the porous media of concrete (Wu et al., 2017). Similarly, its conductivity significantly depends on several factors simultaneously, including the hydration process, pore solution composition and concentration, tortuosity of the pore network, moisture content, and various environmental factors, including moisture level, humidity, temperature, and other conditions (Dong et al., 2019; Han et al., 2010; Rajabipour & Weiss, 2007; Spragg et al., 2013; Wen & Chung, 2008). Therefore, the study of durability is a primary concern of SCC.

2.5.1 Effects of Moisture Content

The moisture content increases the conductivity and reduces the overall resistance of the system because the moisture in concrete acts as an electrolyte that helps the movements of ions (Orellan et al., 2004). However, it is mentioned that it decreases the piezoresistive behaviour of the SCC (Dong et al., 2019). Dong et al. (Dong et al., 2019) investigate the piezoresistive behaviour of the carbon black-based cement sensor at different saturation states. The result indicates that the resistance increased as the saturation state of the sensor increased. The optimum water content of the sample with the highest sensitivity is 8%. After that, the FCR decreases, fluctuates, and becomes more volatile. The sensitivity variations were explained by a contact resistance formed by the moisture content at a high saturation state.

In contrast, another study investigated the effect of water content on the piezoresistive properties of nCB and CNTs (Zhang et al., 2019). After the 28-day curing, the samples were dried in air and oven dry for different durations. It reveals that the fully saturated sample (without any drying treatment) showed the highest strain sensitivity, which decreased as the drying time increased. However, the thoroughly dried (36-hour oven dry after 16 days of air drying) has improved strain sensitivity with respect to the 16d air-dry sample. Another study investigated the wet and dry state of the carbon fibre-reinforced cement paste (Wen & Chung, 2008). The content of fibre is below the percolation threshold. The results show that, while increasing electrical conductivity, moisture in cement paste diminishes piezoresistive behaviour, decreases the gauge factor by at least 12 %, and increases the scatter in the gauge factor. The water at the fibre-matrix interface restricts the electronic conductivity of the fibre, which reduces piezoresistivity. Furthermore, the saturated states have lower stability and repeatability when compared to dry samples because the increasing degree of saturation raises the polarization effect (Hong et al., 2018).

On the other hand, the chloride ion ingress has a different mechanism of piezoresistivity. The samples subjected to immersion in a sodium chloride solution perform better than those immersed in freshwater due to the high ion mobility of samples in a sodium chloride solution. It investigated the piezoresistivity of the samples after 90 days of immersion in fresh and sodium chloride solution (Dong et al., 2022). The results indicate that freshwater immersion has decreased the piezoresistivity by about 20 times, and the samples immersed in 3% NaCl solution improved the piezoresistivity up to 14 days, and then it started to decrease up to 25% at 90 days. The ionic conduction mainly comes from the dissolved ions (Na+, K^+, OH^-, Ca^{2+}, $SO^2{}_4$, and Cl^-) in a pore solution (Montanari et al., 2019; Snyder et al., 2003). The ionic activity increases as the concentration of the pore solution rises, which is why seawater is 1000 times more conductive than natural water because of the high number of ions (Dong et al., 2022; Gapparov & Isakova, 2023).

Owing to the fact that the different studies show different results, however, the common factor is that the moisture content and the other harmful ions have not only affected the durability of the cementitious composite but also directly impacted the sensitivity of the Therefore, the investigation of the sensitivity to different moisture content will give a better understanding of SSC. Furthermore, the durability aspects such as water absorption, different curing conditions and long-term exposure to aggressive environments are essential considerations to investigate for field applications (Ahlborn et al., 2011; Li et al., 2020).

2.5.2 Effects of Temperature

It is widely established that Ordinary Portland cement's hydration remains chemically stable up to 80°C. However, it loses absorbed water between 65 and 80 °C, interlayer water between 80 and 100 °C, and its stability decreases significantly between 100 and 200 °C (Ukpata et al., 2023). Further details are found in **Figure 2.16** (Khan et al., 2023). However, the use of different fibres can reduce explosive spalling and mass loss (Zhang et al., 2023; Zhu et al., 2021).

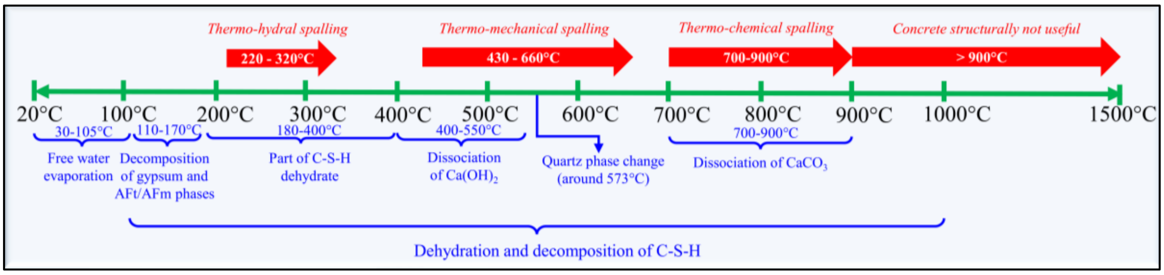

Figure 2.16. Types of spalling of concrete under elevated temperatures (Khan et al., 2023).

Due to the limited understanding and literature on the self-sensing behaviour of SSC and its durability considerations, the effect of temperature on the self-sensing properties of SSC is crucial for reliable and accurate monitoring. It impacts the electrical conductivity and resistivity of concrete, which are essential parameters for self-sensing. Differences in temperature change the ionic mobility within the concrete matrix, affecting the movement of charge carriers and, thus, the electrical properties (Chung & Xi, 2023; Ding et al., 2019). Moreover, temperature variations can induce thermal expansion or contraction of the concrete, leading to dimensional changes and altering the strain-sensing characteristics (Adresi & Pakhirehzan, 2023). As the temperature rises, the increased thermal energy in semiconductors allows more charge carriers (electrons or holes) to become mobile, decreasing overall resistivity (Adresi & Pakhirehzan, 2023; Chung & Xi, 2023; Xi & Chung, 2020; Xi et al., 2022). This behaviour is attributed to the temperature-dependent characteristics of the material's bandgap and the mobility of charge carriers. Similarly, self-sensing concrete is a composite material with conductive fillers such as carbon or graphite that exhibit semiconductive properties. These conductive fillers in the concrete matrix enable the material to conduct electricity. As the temperature of the sample increases, the increased thermal energy promotes more significant movement of charge carriers, resulting in a decrease in electrical resistivity (Chang et al., 2013; Ding et al., 2019; Han et al., 2017; Teomete, 2016).

Several studies have explored the effect of temperature on the self-sensing properties of concrete, providing valuable insights into this phenomenon. For instance, a study determined a linear relationship between temperature and electrical resistance of the material between 25°C and 50°C when using brass fibres (Demircilioğlu et al., 2019). The conductive materials directly affect electrical conductivity during temperature variation (Le et al., 2021). Another study investigated the impact of temperature on the piezoresistive behaviour of CNTs and nCB (CNT-nCB) based composite under variable temperatures ranging from −20°C to 60°C (Ding et al., 2021). It exhibits excellent temperature-sensitive repeatability. However, the temperature sensitivity property varies depending on the type of filler, which can be attributed to the different electrical conduction mechanisms that dominate based on the filler content. Wen et al. Wen et al. (1999) utilise CF in a cementitious composite, which can act as thermistors at a temperature up to 45°C, with electrical resistivity decreasing as temperature increases.

Furthermore, Dong et al. (Dong et al., 2019) have examined the impact of temperature on the durability of self-sensing concrete. Their findings indicate that, after removing the heat exchange interference, the piezoresistive sensitivity and repeatability remained relatively unchanged across a range of temperatures from -20°C to 100°C. However, significant fluctuations in piezoresistivity were observed due to water content variations, and freeze-thaw cycles reduced the piezoresistive sensitivity by 30.7%. This reduction could be attributed to microstructural damage caused by the expansion and shrinkage of pore solution, leading to volume changes. It has also been reported that during the freeze-thaw cycles (temperatures ranging from -0°C to -20°C), the rate of change in concrete electrical conductivity notably decreases around -10°C during the freezing process, which suggests that an enormous amount of pore solution in the concrete freezes below -10°C (Cai & Liu, 1998). According to Cao and Chung (Cao & Chung, 2002), the FCR exhibits limited repeatability when the temperature ranges from -20 to 52°C. However, the irreversibility is significantly reduced when the temperature cyclically varies from 0 to 52°C without freezing. Another study described that as the temperature decreased from 20°C to -30°C, the strain-sensing capability of CNF mortar deteriorated (Wang et al., 2020). When temperatures exceeded 20°C, the self-sensing property worsened with rising temperature. But the sensitivity of CNF mortars decreased first and then increased with higher water contents. The CNF mortar samples in a dried state exhibited the optimum self-sensing performance at 20°C.

Similarly, Hong et al. (Hong et al., 2018) investigated the effects of temperature and saturation level on the sensing properties of cement-based composites incorporating multiscale carbon materials such as carbon blacks, carbon fibres, and CNTs. Their study revealed that the FCR of the cement-based composites initially increased and then decreased with rising temperature, while it decreased with increasing humidity. Moreover, compared to the dry state, the stability and repeatability of the saturated samples were found to be lower. It is attributed to the enhanced polarization effect resulting from increased saturation levels.

2.6 Ultra-High-Performance Concrete (UHPC)

Ultra-high-performance concrete (UHPC) is the new high-class material in the field of concrete technology. It provides a long-term, feasible and sustainable construction due to ultra-high mechanical properties, lower porosity, and improved resistance against aggressive environments (Du et al., 2021; Soliman & Tagnit-Hamou, 2017). UHPC has good workability (slump flow ≥ 160 mm) and high mechanical properties (28-day compressive strength ≥ 120 MPa and tensile strength ≥ 5 MPa) due to its low water-to-binder ratio (w/b, 0.15–0.25), high particle packing density (0.825–0.855), and appropriate addition of chemical admixtures (Du et al., 2021). The UHPC was developed with the understanding that decreasing the water-to-cement ratio alone would not be sufficient to achieve the desired properties. However, it is all being considered that the size distribution, shape, and texture of fine and ultrafine particles must be carefully optimized to ensure the best possible packing. As illustrated in **Figure 2.17**, the density of the UHPC matrix increases with respect to normal concrete by using particle packing, which will help reduce the member geometry and overall cost of the structure apart from high durability. This necessarily involves the distribution of ultrafine particles at the microstructure level to fill the gaps between bigger particles (Wong & Kwan, 2008).

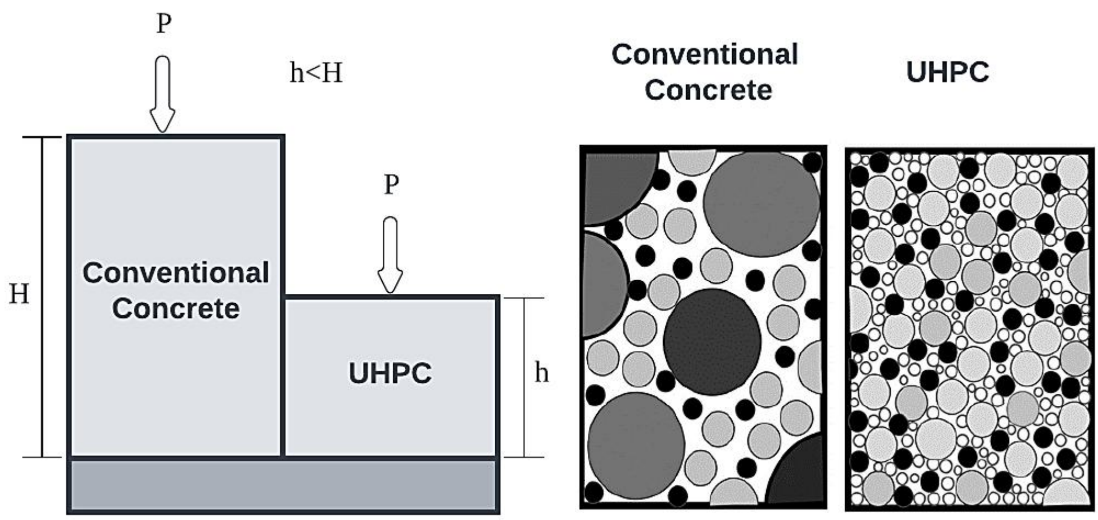

Figure 2.17. Comparison of normal concrete and UHPC (Bajaber & Hakeem, 2021).

UHPC is fabricated using constituent materials like cement, supplementary materials (silica fume, fly ash, quartz powder, etc.), fine-grained sand, water, and superplasticizer. The suggested ratios of the mixture proportions for designing UHPC are as follows (Wille & Boisvert-Cotulio, 2015)

- Cement: silica fume (SF): supplemental material (SM) = 1:0.25:0.25 by weight,
- Water to cement ratio = 0.2–0.3 by weight,
- Aggregate to cement = 1.0–2.0 by weight.

The strength enhances durability, and the overall performance of UHPC concrete will surely improve by the high packing system of the UHPC. There are many reasons behind the weakening of the concrete structure, with two main reasons for the poor conditions identified as corrosion of steel reinforcement and concrete weakening through invasive ions. UHPC could be one of the practical solutions for all these issues.

2.6.1 Particle Packing Theory

Concrete is a composite material consisting of a solid skeleton of granular particles bonded by a cementitious paste. The guiding concept of particle packing is to bond the grains with the lowest possible porous microstructure. Particle packing is the selection of suitable sizes and proportions of materials to obtain a compact mixture, which is influenced by density, particle characteristics, particle force, and particle structure. Optimized particle packing decreases the void ratio, which leads to decreased water requirement, restrains the amount of shrinkage and creep, reduces the amount of cement paste and has much more physical and strength properties. There are two types of models including, discrete and continuous. Given that concrete constituents are generally distributed continuously, it is reasonable to utilize continuous particle packing models in the design of concrete mixes.

Andreasen (Andreasen, 1930) proposed a model which assumes the minimum particle size to be infinitely small, presented in the following Equation

$$P(d) = \left(\frac{d}{d_{\max}} \right)^q \tag{2.5}$$

where ***P(d)*** is the cumulative size distribution function, ***d*** is the particle's diameter, $\boldsymbol{d_{max}}$ is the maximum diameter of the particle, and ***q*** is a parameter (0.33-0.5) which helps to adjust the curve for fineness or coarseness.

However, the Andreasen model was modified by Funk and Dinger (Funk & Dinger, 2013; Ragalwar et al., 2020), introducing finite particle size and proposing the modified Andreasen and Andersen model as described in the following Equation.

$$P_{tar}(D) = \frac{D^q - D_{\min}^q}{D_{\max}^q - D_{\min}^q} \tag{2.6}$$

where ***D*** is the particle size, $\boldsymbol{P_{tar}(D)}$ is the volume fraction of all the solids that are smaller than ***D*** (cumulative per cent passing a sieve of size D); $\boldsymbol{D_{min}}$ and $\boldsymbol{D_{max}}$ are the minimum and maximum size of particle, respectively, and the distribution modulus is represented by ***q***.

2.6.2 Durability of UHPC

UHPC is not only an ultra-high-strength material, but its durability is significantly improved. UHPC exhibits superior durability because of its dense microstructure matrix, which is highly resistant to carbon dioxide, chloride, sulphate, and other ion penetration. As shown in **Figure 2.18**, the durability of the UHPC is significantly improved with respect to high-strength concrete and normal concrete.

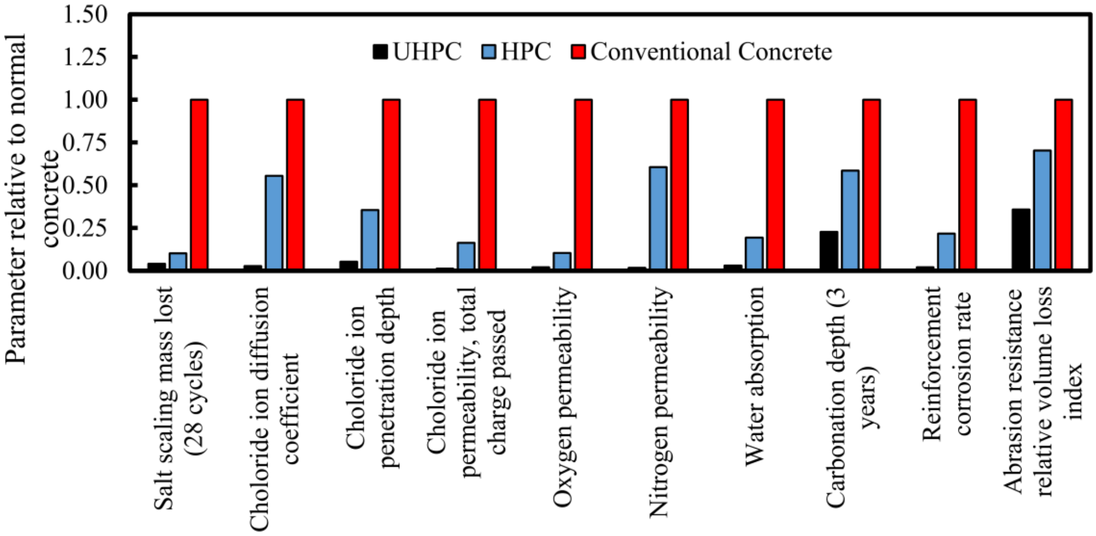

Figure 2.18. Assessment of durability for UHPC compared with high-performance and conventional concrete (Du et al., 2021).

Concrete structures are typically constructed where they are exposed to various unavoidable harsh environmental conditions, such as water saturation, chemical attacks, carbonation, steel corrosion and freeze-thaw cycles. The durability properties of all types of concrete, including UHPC, are inherently linked to their porosity. The incorporation of fine and ultrafine particles into the concrete mixture can contribute to a low and disconnected pore structure, which enhances durability. On the other hand, a high and interconnected pore of structure allows water and chemical ions to penetrate the concrete, thus reducing its durability. The permeability of the concrete matrix is primarily influenced by capillary pores, which play a crucial role in facilitating the movement of fluids into the structure. A lower permeability level in the concrete results in an extended lifespan.

The density, porosity and microstructure of the concrete matrix are the key parameters that affect permeability and, consequently, durability. The permeability coefficient of UHPC indicates the material's potential to absorb water and can be interpreted as a measure of its durability. A lower water absorption capacity of the UHPC means fewer pores associated with the matrix and, thus, higher durability (Bajaber & Hakeem, 2021). UHPC could be impervious when the size of the pores is less than one-tenth of those in normal concrete. Dobias et al. (2016) describe that the water absorption coefficient of the UHPC is five times lower than that of conventional concrete because the water-to-binder ratio of the UHPC concrete is much lower than that of traditional concrete.

Many studies have explored different environmental exposures, such as freeze-thaw cycles and different temperature effects. Freeze-thaw reactions occur when water molecules absorbed by the concrete matrix freeze and expand beyond the concrete pores (Li et al., 2020). Numerous researchers have observed minimal deterioration after hundreds of freeze-thaw cycles up to 800 cycles with negligible mass loss (Zhong & Wille, 2015). Ahmad et al. (2015) investigated wet-dry and heat-cool cycles. For the effect of long-term exposure (180 days), the sample goes through different wet, dry, and heat–cool cycles on the strength and modulus of elasticity. It demonstrated that UHPC maintains its mechanical strength under potentially severe exposure conditions, and the deterioration is negligible. In fact, the UHPC matrix will be resilient and durable enough to last for an extended period without having any additional coating or painting. It has also been mentioned that UHPC has a 55 times higher resistance to chloride ion diffusion than normal concrete. It is also worth noting that the water absorption capacity is 60 times lower than that of normal concrete (Du et al., 2021). The capillary porosity and total porosity are 5.5 and 2.5 times lower than the UHPC, which is directly related to the strength and durability of the concrete (Vande Voort et al., 2008).

2.6.3 UHPC with Seawater and Sea-sand

Global cement production in 2016 reached 4.1 billion metric tonnes and is predicted to rise to more than 5 billion metric tonnes (Imbabi et al., 2012; Mohamad et al., 2022; Naqi & Jang, 2019). In 2014, concrete consumption was anticipated to be over 25 billion tonnes, and aggregate production was estimated to be around 40 billion tonnes. (Li et al., 2020). In recent years, people have faced a shortage of river sand and tap water due to the increasing scale of engineering construction, especially in coastal and marine infrastructure (e.g., bridges, ports, and dry docks). According to the World Health Organization, water scarcity affects more than two billion people, and climate change and population expansion will likely worsen in some areas (Organization & Fund, 2022). The statistically predicted data for 2050 is presented in **Figure 2.19** (Armstrong, March, 2024). The construction industry consumes a substantial amount of freshwater, accounting for approximately 18% of global annual industrial water usage (Ebead et al., 2022). Therefore, they have turned their attention to abundant sea-sands and seawater resources, which will be a promising option for easing resource crises and construction costs, reducing energy consumption, and lowering carbon emissions, particularly in marine and coastal area.

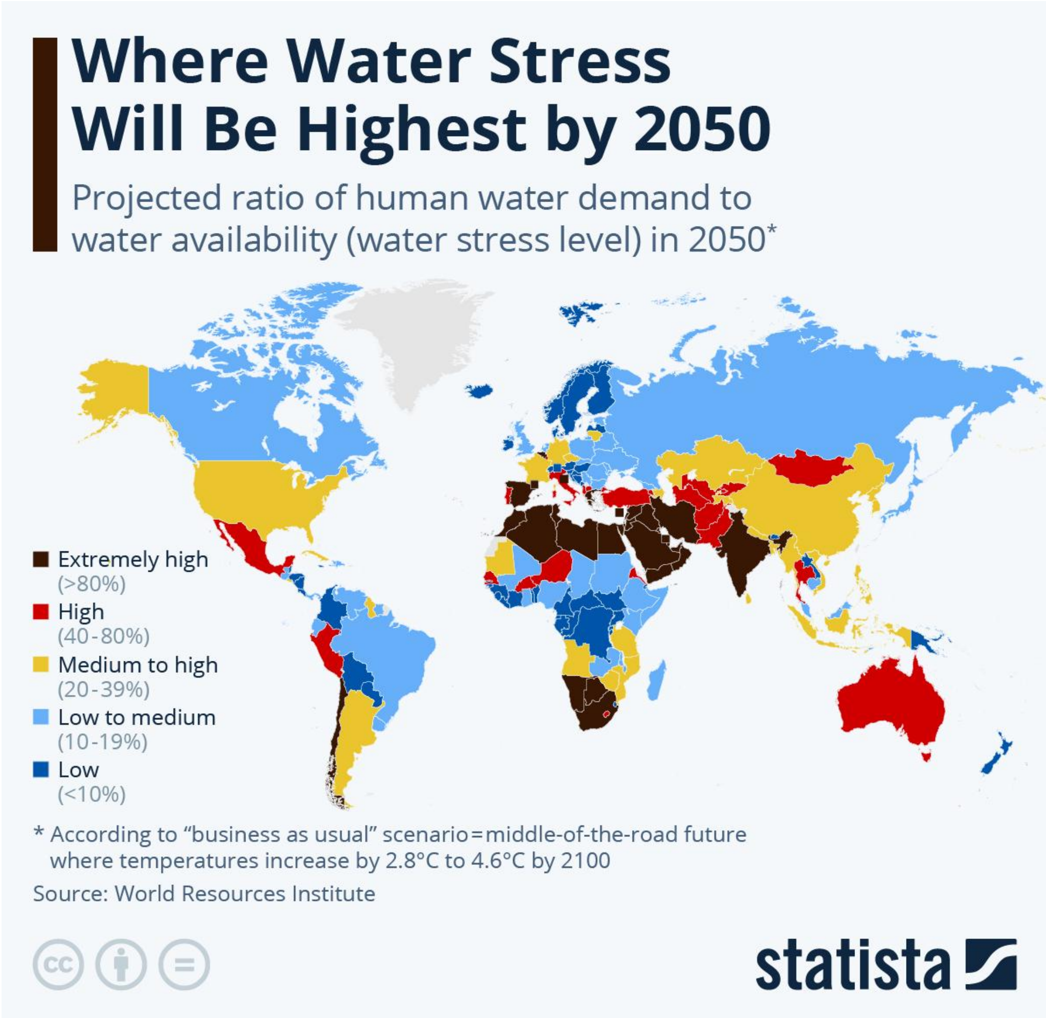

Figure 2.19. Water-stressed countries in 2050 (Armstrong, March, 2024).

Sea-sand and seawater are not allowed to be used directly without prior treatment due to their high chloride content, which adversely affects mechanical performance, rebar corrosion, and durability reduction. However, in 2011, Teng et al. (Teng, 2014; Teng et al., 2011) introduced a new type of concrete structure named seawater sea-sand concrete (SSC) structures reinforced with corrosion-free fibre-reinforced polymer (FRP) composites (i.e., FRP-SSC structures). This new structural concept allows for the direct use of seawater and sea-sand in the construction of coastal and marine infrastructure, creating highly corrosion-resistant structures without the need for any treatment.

Seawater has a high number of sodium, chlorides and sulphate ions, which can lead to loss of initial setting time of about 30%, slump flow of about 20%, increase the early age strengths, improved porosity and pore size, which leads to denser microstructure (Li et al., 2020; Zhao et al., 2021). Accelerated hydration of ordinary Portland cement, primarily due to chloride promoting calcium aluminate and ferrite precipitation, resulted in a 15% and 5% increase in compressive strength at 7 and 14 days, respectively, compared to a control mix with deionized water at a 0.4 water-to-binder ratio. (Li et al., 2020). However, the compressive strength of 28 days is reduced by about 7-13% compared to specimens with normal water (Kaushik & Islam, 1995; Pan et al., 2021; Younis et al., 2018). On the other hand, a higher amount of unhydrated C_3S in OPC leads to less mass of C-S-H than in deionised water (Li et al., 2020). Similarly, the changes in hydration products, dissolution of calcium hydroxide, and alterations in the C-S-H gel structure contribute to the decrease in the long-term compressive strength of Portland cement pastes prepared and cured with seawater (Zhang et al., 2022). Moreover, for ages beyond 28 days up to 90 days, there is an apparent decrease in compressive strength, possibly due to the formation of salt crystallisation, which negatively impacts strength gain (Orie & Ojaruega, 2015; Wegian, 2010). On the other hand, these high numbers of dissolved ions in seawater increase the ionic strength of the pore solution compared to deionised water. Its ionic strength is three to four times higher than the pastes made with deionised water (Montanari et al., 2019). This elevated ionic strength leads to a decrease in the electrical resistance of the pore solution by approximately 50% (Ebead et al., 2022). Furthermore, the inclusion of sea-sand in the mixture can further contribute to a reduction in the overall resistivity of the matrix.

Most researchers have found that adding seawater to concrete improves mechanical and physical properties such as elastic modulus, density and compressive strength without introducing substantial deficiencies (Li et al., 2020; Vafaei et al., 2021). However, the inconsistencies are essentially the strength developments in concrete with seawater at later curing ages. Furthermore, the corrosion of steel rebars remains a deep concern, and their durability is undetermined by chloride ions. It can also be observed from the available literature that contentious findings are reported about the influences of salt ions on the microstructure and durability of concrete without reinforcement. De Weeredt et al. (De Weerdt et al., 2014) have observed that plain concrete is susceptible to the attack of numerous salt ions found in seawater. Additionally, different hybrid fibres are used to investigate the durability of the SSC for different environmental conditions (Vafaei et al., 2021; Zeng et al., 2022). For instance, seawater sea-sand concrete is exposed to elevated temperatures with the addition of synthetic fibre. It is concluded that synthetic fibre improves fire resistance, where polyvinyl alcohol (PVA) is more efficient than polypropylene (PP) fibres. It would be a better replacement for normal concrete in oil and gas production and offshore construction (Elseady et al., 2024). On the other hand, it has been demonstrated that plain concrete structures built with seawater have good durability (Nishida et al., 2015). A summary of the effects of seawater on concrete properties can be seen in **Figure 2.20**. It should be noted that the number of studies on durability is limited.

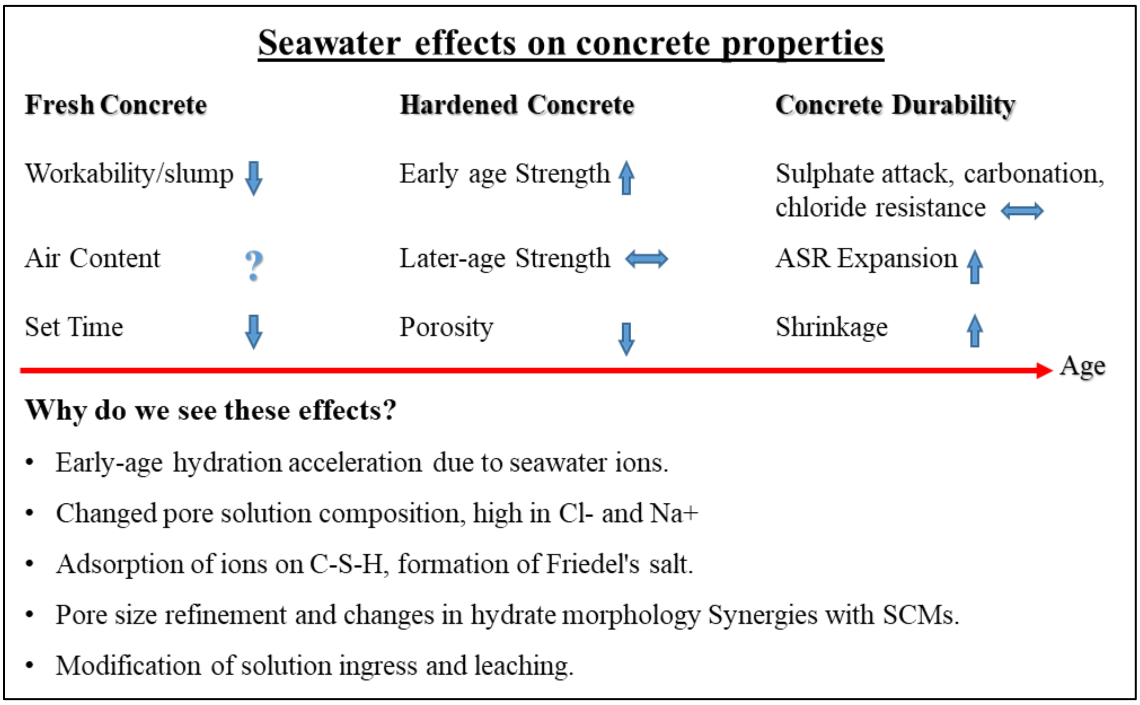

Figure 2.20. Macro and micro-scale influence of seawater on concrete properties at different ages (Ebead et al., 2022).

2.6.4 Development of New Functionalities in UHPC

The development of new functionalities in cementitious composites may bring a paradigm shift from strength-only performance to multifunctionality in the construction industry (Soliman et al., 2020). Ultra-high-performance concrete has demonstrated better mechanical and durability performance; however, the degradation of concrete structure monitoring is still under consideration for long-term serviceability.

UHPC is a novel type of concrete characterized by superior mechanical properties and durability (Du et al., 2021; Soliman & Tagnit-Hamou, 2017). The excellent durability of UHPC leads to a persistent service life of the constructed structures, which brings new challenges to their health monitoring in terms of durability and maintenance of the SHM systems. Addressing these challenges, the development of self-sensing UHPC presents a promising area. However, research into the piezoresistive behaviour of UHPC remains limited. Dong et al. (2016) investigated the mechanical properties and electrical conductivity of reactive powder concrete (RPC), a type of UHPC reinforced with 8 μm diameter short-cut super-fine stainless-steel wire (SSSW). Results demonstrated that the SSSW addition conferred strain-sensing capabilities to the RPC, yielding gauge factors (indicating strain sensitivity) of 22.5, 94.9, and 43.6 under cyclic and monotonic compression and flexure, respectively. The SSSW-reinforced RPC further demonstrated that the SSSW-reinforced RPC could monitor the crack opening and rupture induced by three- and four-point bending Dong et al. (2020). You et al. (2017) and Lee et al. (2018) explored the incorporation of steel fibres (SF) and CNTs into UHPC for self-sensing capability. Hybrid use of CNTs and steel fibres, their research showed that the resulting UHPC could detect damage and cracking—indicated by abrupt changes in electrical resistance due to disrupted conductive networks—but was ineffective at sensing variations in compressive strain. The lack of strain-sensing capability in their studies was attributed to the dense microstructure of UHPC, which limits the mobility of the CNTs and steel fibres. Moreover, Yoo et al. (2018) explored the hybrid use of CNTs and micro SF in a UHPC matrix and found that such UHPC can detect matrix cracking, which causes significant changes in electrical conductivity.

Furthermore, Lee et al. (2019) investigated replacing ordinary sand in steel fibre-reinforced UHPC with fine steel slag aggregate (SSA). They found that this substitution conferred strain-sensing capabilities, attributed to the fine dispersion of conductive steel slag forming conductive pathways via quantum tunnelling. However, the high free calcium oxide (CaO) and magnesium oxide (MgO) content in SSA raise concerns about potential volume expansion, premature cracking, and reduced long-term structural serviceability (Brand & Roesler, 2015; Feng et al., 2022; Wang et al., 2013). The addition of steel fibres, specifically stainless-steel fibres (SSFs) and copper-coated steel fibres (CCSFs), to UHPC results in substantial enhancements in both compressive strength and strain. The improvements in compressive strength range from 11.4% to 33.7%. Additionally, UHPC with steel fibres demonstrates excellent self-sensing capabilities, with a strain sensitivity of 26.6 under cyclic compressive loading of 37.5 MPa when SFs are used. Similarly, UHPC containing 1.2 vol% CCSFs achieves a strain sensitivity of 28.2 (Qiu et al., 2021).

Moreover, UHPC incorporating steel slag aggregates demonstrates remarkable tensile and compressive strengths, achieving about 207 MPa and 14 MPa, respectively. This enhanced performance is attributed to the high iron content of steel slag, which contributes to the self-sensing properties of UHPC. Notably, UHPC with steel slag exhibits superior self-sensing capabilities compared to UHPC with CF and is comparable to UHPC with MWCNT. The utilization of steel slag aggregates in UHPC offers multiple benefits, including environmental advantages, improved flowability, and impressive self-sensing capabilities (Kang et al., 2024). Additionally, the inclusion of short steel fibres and SSA in UHPC leads to improved stress-sensing capabilities. The highest stress-sensing characteristics are observed in UHPC with 5vol% short steel fibres, achieving stress levels of up to 200.6 MPa and a fractional change in resistance (FCR) of 33.7. Furthermore, the incorporation of steel slag aggregates in smart UHPC further enhances its stress-sensing abilities (Le et al., 2023).

Furthermore, the integration of MWCNTs into ultra-high-performance fibre-reinforced concrete (UHPFRC) is employed to enhance its self-sensing and repair capabilities while improving bond strength. The inclusion of MWCNTs enhances adhesion, cohesion, and mechanical interlocking in the interfacial zone, leading to improved bond strength and better repair properties. Additionally, MWCNTs exhibit notable sensing capabilities for crack initiation, crack localization, fibre pull-out, and debonding processes. Optimal composite layers are achieved with a content of 2 vol.% SF and 0.2 wt.% MWCNTs (Song et al., 2023).

In contrast, another research study focuses on the utilization of a nanoengineered UHPC that incorporates Carbon Nanofiber (CNF) and SF at volume ratios of 0.1% and 2%, respectively. The objective of this study is to detect cracks in concrete. The results demonstrate a strong correlation between the FCR curve and the progression of cracking, enabling the identification of crack initiation. Initially, there is a decrease in electrical resistance due to microcracking, followed by a sharp increase in resistance as the mechanical load-displacement curve exhibits a post-peak decline. This finding is significant as it indicates that the nanoengineered UHPC possesses the capability to self-sense even after crack localization occurs under tension (Ralli et al., 2023).

On the other hand, a hybrid nCB-CNF-filled UHPC consistently shows higher compressive strength compared to UHPC with a solo nCB, indicating the positive effect of combining carbon black and carbon nanofibers in the matrix. The percolation threshold for conductivity in UHPC starts at around 0.5% nCB content, regardless of CNF inclusion, showcasing the role of CNF in linking conductive pathways created by nCB nanoparticles. Increasing the content of conductive fillers enhances the stability and low noise of piezoresistive behaviour in response to dynamic cyclic loads, with hybrid nCB-CNF fillers reducing signal noise under monotonic compressive loading, thus improving the overall sensing stability of self-sensing UHPC (Li et al., 2024).

Steel fibres significantly enhance the properties of UHPC by improving its ductility, mechanical strength, and energy absorption capacity. Their addition increases the material's toughness and crack resistance, allowing UHPC to withstand greater loads and resist deformation under stress. Additionally, SF contribute to the electrical conductivity of UHPC, enhancing its piezoresistive behaviour for effective crack and damage sensing and structural health monitoring. Overall, the incorporation of steel fibres results in a more resilient and durable material, making it ideal for demanding construction applications. Although some studies have demonstrated crack and damage sensing in UHPC using steel fibres and CNTs, achieving effective strain sensing remains challenging due to the material's highly compact and dense microstructure, which restricts fibre mobility in matrix.

2.6.5 Summary

It can be observed from the literature that ultra-high-performance concrete has come to prominence in the construction industry due to its ultra-high compressive strength and durability performance. ACI 239R-18, has included the steel fibres in a UHPC mix. However, a concrete mix can be classified as UHPC even without the inclusion of fibres, provided it meets the necessary criteria for strength and durability. At the same time, fibres are commonly used to enhance certain properties like tensile and flexural strength and crack resistance. A non-fibre UHPC can still achieve high compressive strength and durability through the optimisation of mixed design and high-quality materials. However, it may not exhibit all the performance characteristics typically associated with fibre-reinforced UHPC. The codes ASTM C1856/C1856M – 17 and GBT31387-2015 (C1856/C1856M-17, 2017; Du et al., 2022; Wu et al., 2022) are described as if the compressive strength is higher than 120 MPa, generally considered as UHPC. Despite its exceptional performance, the concrete structures deteriorate over time due to the various loads and environmental conditions. Therefore, it has always been a matter of concern to develop a system that would improve serviceability and real-time monitoring of the civil infrastructure, significantly reduce unexpected accidents, save human life and resources, and lower maintenance costs in the later stages.

The introduction of novel capabilities in cement-based composites could lead to a significant change in the industry, shifting the focus from solely strength-based performance to multifunctionality. This development could enhance the overall life span of a concrete structure, as it can monitor its own structural health and provide early warnings of any damage, enabling timely repairs and maintenance. This shift towards multifunctionality could revolutionize the way of designing, building, and maintaining concrete structures, leading to improved safety and longevity. The introduction of self-sensing capability in UHPC has garnered considerable attention from researchers and engineers, as it enables the monitoring of internal stress and the deformation of structures. It is widely recognized that the conductivity of the matrix plays a crucial role in the sensing behaviour of UHPC. The transformation of the non-conductive system into a conductor has opened new possibilities for its sensing capabilities.

Although some studies have demonstrated crack and damage sensing in UHPC using steel fibers and CNTs, achieving effective strain sensing remains challenging due to the material's highly compact and dense microstructure, which restricts fiber mobility in matrix. Additionally, there are very limited studies that explore strain sensing capabilities by employing steel slag aggregates. However, these steel aggregates can lead to volumetric expansion and premature cracking in concrete structures due to corrosion. The existing literature presents conflicting results regarding the compressive strain-sensing behaviour of UHPC composites. Although some research has shown the potential for self-sensing capabilities in UHPC, the incorporation of complex and hybrid conductive materials often increases costs and complexity, making them impractical for field applications. Moreover, these materials typically have a high unit cost, which limits their scalability in real construction projects. Another significant challenge is the dispersion of fillers within the cementitious matrix. Many piezoresistive fillers exhibit substantial dispersion issues, which adversely impact both piezoresistive and mechanical performance. Achieving stable and effective piezoresistivity requires proper dispersion techniques and treatments, as well as attention to the mechanical properties of the composite.

Despite advancements in UHPC that incorporates various conductive materials for crack and damage sensing, effectively implementing strain sensing remains a significant challenge due to the material's dense microstructure. Additionally, some studies have claimed strain sensing capabilities using steel slag aggregates; however, these pose substantial risks of volumetric expansion and premature cracking due to corrosion. The solutions proposed in existing research are often hindered by the high costs and complexities associated with hybrid conductive mechanisms. Moreover, the dispersion of piezoresistive fillers within the cementitious matrix further complicates the situation, which adversely impacting both piezoresistive and mechanical performance. Therefore, there is an urgent need for effective strategies to improve the self-sensing capabilities of UHPC while addressing concerns related to material cost, complexity, and filler dispersion for practical field applications.

Chapter 3.

Structure of Nanocarbon Black and its Effects on Piezoresistive Performance

3.1 Abstract

The utilisation of nanocarbon black (nCB) in cementitious composites has shown potential in developing self-sensing concrete for strain monitoring and damage detection in concrete structures with a low cost and enhanced mechanical and electrical properties. It has been used with different structures, morphologies, and surface areas to produce cement-based materials, which significantly varies results. There is a considerable knowledge gap in understanding how the structure of carbon black influences the mechanical and electrical properties of these smart composites. Therefore, this study investigates the effect of different structures of nCB on the mechanical and piezoresistive properties of the cementitious composite.

The investigation concludes that the mechanical properties are nearly similar, and the compressive strength of all the nCBs has shown similar trends with a minor difference: initially, it increased, then it decreased. However, the nCB-290 showed a very low and distinct percolation zone compared to the other nCBs due to its branched structure. The lower percolation threshold is incredibly beneficial for achieving economical, stable, and durable piezoresistive behaviour for a field-deployable solution. The nCB-290 shows high repeatability and precisely synchronised behaviour to the corresponding stress/strain. It also shows the highest strain sensitivity among all, which is several times higher than conventional strain sensors.

3.2 Introduction

Various types of piezoresistive materials (e.g., CFs, CNTs) have been used in SCCs to achieve piezoresistive behaviour, as reviewed in Chapter 2. Among the nanofillers, nCB is regarded as one of the most suitable candidates for sensing concrete because of its low cost, permanent electric conductivity, no critical dispersion issues, high chemical and thermal stability, and fine filler effect (Dong et al., 2020; Hussain et al., 2019; Leong & Chung, 2003, 2004; Monteiro et al., 2015; Wen & Chung, 2007).

The influence of nCB on the piezoresistive and mechanical properties of cementitious composites has been explored in numerous studies. The structure (the number of particles making up the primary aggregate (Sánchez-González et al., 2005)) of nCB is considered to be the most critical parameter which influences its electromechanical properties. According to ASTM D2414-21 (D2414-21, 2021), the oil absorption number (OAN) defines the structure, indicating that a higher particle count per aggregate corresponds to a higher structure. A study demonstrates that the high-structure nCB composites decrease compressive strength and, at the same time, improve sensitivity at lower percolation ranges from 0.7% to 2.5% of the cement weight (Dai et al., 2010). The reduction in compressive strength was attributed to a higher number of aggregates, which leads to poor dispersion and ultimately reduces the strength. The high structure nCB has a high number of aggregates attached to each other to form a continuing structure, which is very difficult to disperse in a mix uniformly. Another study has achieved a low percolation zone of about 0.5-2.0% of nCB; however, the compressive strength decreased with the addition of nCB (Dong et al., 2019). Nevertheless, the lower carbon black structure maintains and improves the compressive strength of cementitious composites to some extent, but the sensitivity can only be achieved at a higher content of nCB. For instance, (Li et al., 2006) developed nCB-based cementitious composites with a 15.0% nCB concentration showing the piezoresistive behaviour. Similarly, 12.0% and 7.0% of binder mass have shown the percolation threshold in different studies, and the compressive strength is improved to a certain level with a particle size of 120 nm (Monteiro et al., 2017; Wu et al., 2005). While these studies did not specify the structure of the nCB, it is hypothesized that a low-structure nCB enhances mechanical properties up to a certain point, while the piezoresistive behaviour is achieved at a higher concentration of nCB. On the other hand, the high-structure nCB can reach the percolation threshold at a low nCB content but it may compromise the mechanical properties due to the high agglomeration. It can be summarized that nCB-based composites demonstrate a significant variation in the percolation zone, ranging from 0.50% to 20.0%.

Despite the extensive range of structures of nCB available in the market, it is challenging to make any decision about a suitable candidate for practical applications. The mechanical and piezoresistive behaviour of the cementitious composites is directly associated with the structure of the nCB. Moreover, the cost of the composites is directly related to the percolation threshold which defines the amount of nCB needed to establish the conductive network.

Against the above background, this chapter presents systematic investigations of different structures of nCBs for the mechanical and piezoresistive properties of cementitious composites.

3.3 Experimental Program

3.3.1 Raw Materials and Mix Design

This study used EN 197-1 CEM I 52.5N ordinary Portland cement (OPC) manufactured by Green Island Cement Limited, Hong Kong, and Silica fume (SF) as a supplementary material. A polycarboxylate-based superplasticiser (SP) was used with a solid content of

22.0% by mass and a specific gravity of 1.05. Three different nCB were used, including super P Li from Timcal with dibutyl phthalate oil (DBP) absorption number 290ml/100gm (nCB-290), nCB with DBP 245ml/100gm (nCB-245) from Henan Lebang Water Purification Technology Co., Ltd and VXC72 from CABOT with DBP 174ml/100gm (nCB-174). The physical and chemical properties of nCBs are given in **Table 3.1.**

Table 3.1. Physical properties of nanocarbon black from the manufacturer

Sample	DBP (ml /100gm)	Density (g/cm^3)	Resistivity (ohm-cm)	Particle size (nm)	Surface area (m^2/g)
nCB-290	290	0.160	0.18	~40	62
nCB-245	245	0.532	0.12	40-80	61
nCB-174	174	0.240	0.05	30-60	254

In this study, the base mix design plain concrete (PC) was obtained by adding cement, SF, and water. For nCB-based composites, a nCB of up to 5.0% of binder mass was used. The water-to-binder ratio was 0.33, and the SP was added according to nCB content to maintain the flowability. The mix design and the specimen IDs having a different dosage of nCB are detailed in **Table 3.2.**

Table 3.2. The ratio of the mixed proportion of all specimens.

Specimen No.	Cement	Silica fume	w/b ratio	SP (%)
PC	0.9	0.1	0.33	0
nCB0.5	0.9	0.1	0.33	0.25
nCB1.0	0.9	0.1	0.33	0.50

nCB1.5	0.9	0.1	0.33	0.75
nCB2.0	0.9	0.1	0.33	1.00
nCB2.5	0.9	0.1	0.33	1.50
nCB3.0	0.9	0.1	0.33	2.00
nCB3.5	0.9	0.1	0.33	2.50
nCB4.0	0.9	0.1	0.33	3.00
nCB5.0	0.9	0.1	0.33	3.50

Note: The water-to-binder ratio was 0.33, and the SP was added as a certain percentage of the weight of the binder.

3.3.2 Structure of nCB

The nanostructure of the nCB was revealed by transmission electron microscopy (TEM) (Talos F200S G2 TEM, Thermo Fisher Scientific Inc., USA), as shown in **Figure 3.1**(a-c). The morphology of the nCB was specified at three different levels, including particle, aggregate and agglomerate, as shown in **Figure 3.1**(d) (Youssry et al., 2013). It consisted of primary particles with sizes in the range of 20-80nm (Wang et al., 2020), which are covalently bonded to aggregates with sizes in the range of 100-300nm (Badot et al., 2009; Cadiou et al., 2019; Endo et al., 2008). The high-resolution TEM images of the nCB sample show a distinct core-shell structure exhibited by the primary particles. The central regions of the particle contained amorphous nuclei, which were surrounded by layers of graphitic carbon. Additionally, the imaging technique provided a clear and detailed visualisation of agglomerates formed by multiple particles, offering a comprehensive understanding of their morphology. The inner core of primary particles was similar for all three types of nCB, but their structure and agglomeration were different. The degree to which nCB particles aggregate is referred to as “structure” and is determined by the oil absorption capacity as measured by dibutyl phthalate (DBP) absorption (Pantea et al., 2003). Highly branched nCB refers to chain-like and highly branched aggregates, which consist of several primary particles, whereas aggregates with a lower number of primary particles demonstrate a less branched structure (Lin & Chung, 2007; Soboleva et al., 2010). Larger agglomerates are formed by the loose clustering of these nCB aggregates.

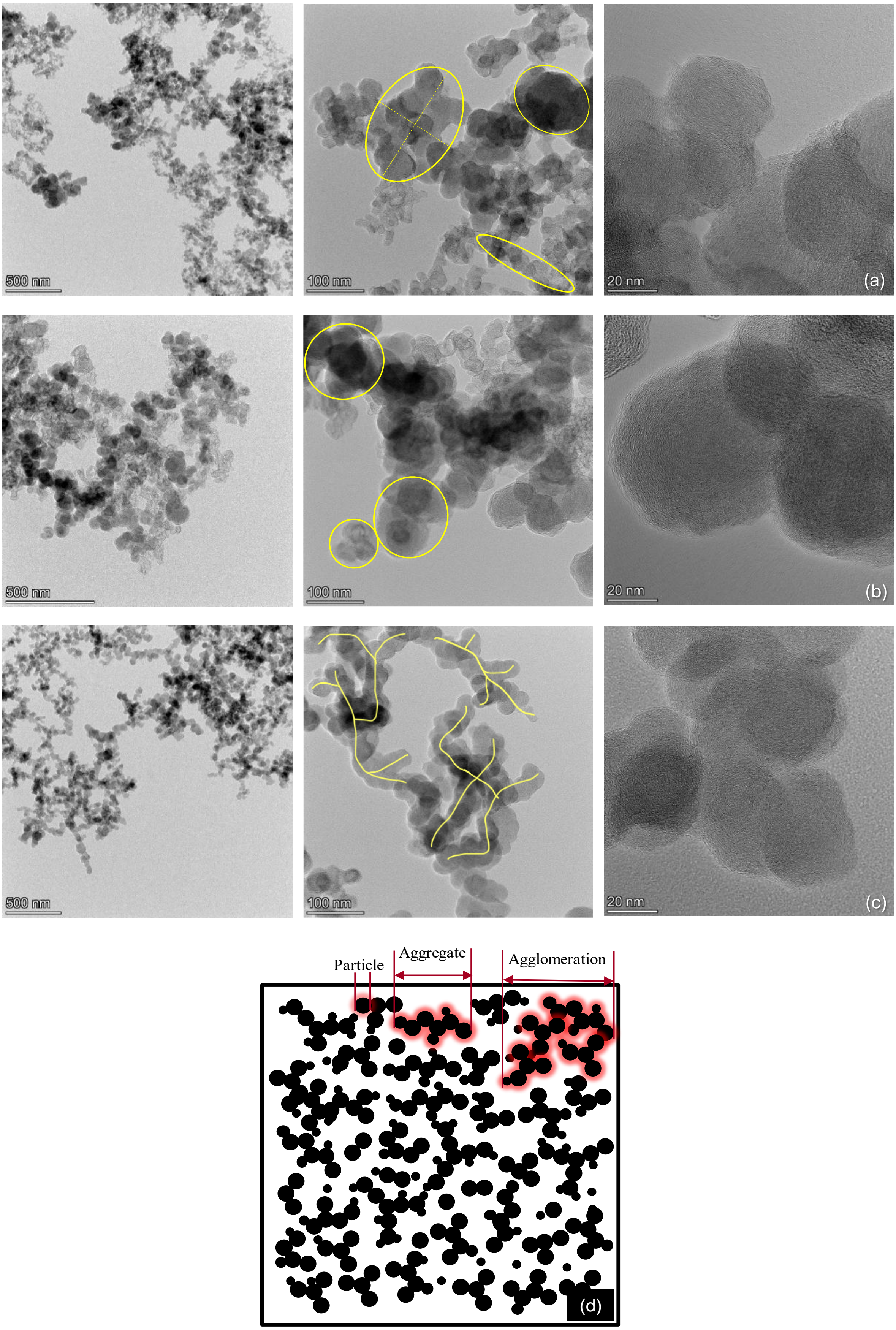
500 nm
100 nm
20 nm
(a)
500 nm
100 nm
20 nm
(b)
500 nm
100 nm
20 nm
(c)
Particle
Aggregate
Agglomeration
(d)

Figure 3.1. High magnification TEM images of nanocarbon black. (a) nCB-174 showing ellipsoidal and linear structure, (b) nCB-245 showing ellipsoidal and linear structure, (c) nCB-290 showing the branched structure, and (d) schematic diagram of nCB structures.

From **Figure 3.1,** it can be seen that the nCB-174 showed an ellipsoidal and linear structure. Similarly, the nCB-245 had a spherical or ellipsoidal structure. Notably, nCB-290 demonstrated a highly branched structure, which facilitates the formation of more conductive pathways. Some researchers called it a chain structure and a grape-like branch structure (Dou et al., 2022). As a result, it could exhibit a more distinct percolation at lower volume fractions compared to low-structure nCB. The structural characteristics are vital in selecting appropriate nCB for specific applications. The high structure of nCB offers several advantages, such as minimal impact on flowability due to the use of less amount of nCB, ease of fabrication, and reduced material unit cost. The high agglomeration would not be favourable for mechanical properties due to the creation of the stress concentration points. Interestingly, some level of aggregation is beneficial for the conductive behaviour of nCB. According to the literature (Soliman et al., 2020), achieving a high level of dispersion of nCB is not advantageous for conductive phenomena. It explains that excessive dispersion can disrupt the volumetric wiring structure responsible for conductivity.

It can be summarized that the branching and linear structure of nCB tend to form a more conductive network at a lower critical volume than the spheroidal and ellipsoidal shapes. Therefore, the selection of nCB with appropriate structure is very crucial to achieve the reasonable electrical and mechanical properties of the composite, making it suitable for various applications.

3.3.3 Specimen Preparation

Figure 3.2 explains the step-by-step preparation of the nCB-based smart cementitious composites. It started with a dry mixing of the cement, SF, and nCB, and then water and SP were added. The mixing continued until it reached an acceptable fluidity level. After that, it was poured into a mould for mechanical testing. Moreover, four copper meshes were embedded during the preparation of piezoresistive testing samples. After the casting, the samples were covered with a plastic sheet, left at room temperature for 24 hours, and then demoulded. After demoulding, the specimens were immersed in normal tap water for 28 days at 22°C ± 3°C.

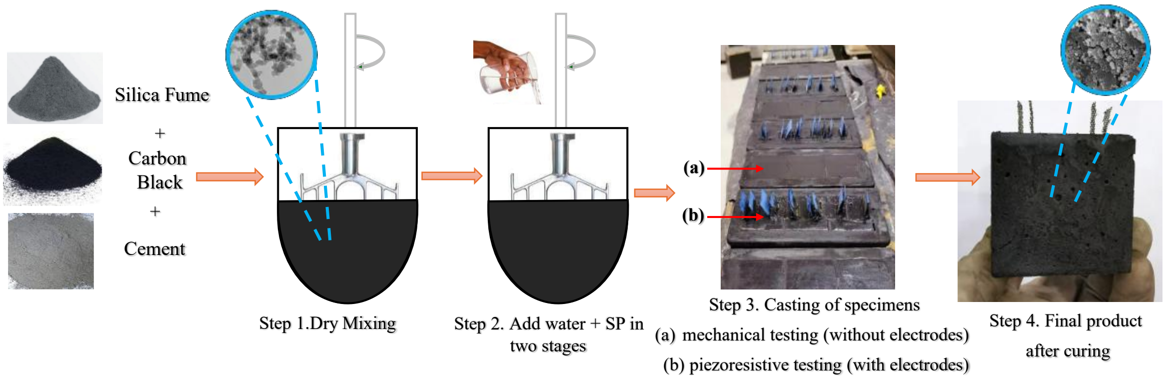

Figure 3.2. Fabrication procedures of nCB-filled smart cementitious composites.

3.3.4 Mechanical Tests

Compressive strength tests were conducted using 50 mm cubic samples according to ASTM C109 (C109/C109M-21, 2021). For each mix, three specimens were tested to obtain an average value. The loading rate of 0.5 MPa/s was applied for the compression tests.

3.3.5 Piezoresistive Tests

A four-probe testing method was employed to avoid contact resistance for the resistivity measurement due to added contact resistance to the actual specimen resistance while applying the two-probe method (Chung, 2020). After 28 days of curing, the samples were dried at 50°C for three days to minimise the moisture content. Before undergoing the monotonic and cyclic compressive test, the samples were kept in an ambient environment to cool down because the temperature influences the electrical properties of the specimen (Dong et al., 2019; Dong et al., 2019; Lipscomb et al., 2009). The resistance of the samples was measured by the LCR meter U1733C (Keysight Technologies, Inc., USA). The measurement of piezoresistive behaviour during the compressive cyclic and monotonic loading was performed using the experimental setup, which can be seen in **Figure 3.3,** in which V_r is the voltage of the resistor, V_s is the voltage measured between the two inner electrodes, and R_f is the electrical resistivity of the resistor. The specimens were first subjected to cyclic compressive loading using a universal testing machine (Instron 5982, Instron Inc., USA) with a loading rate of 0.40 mm/min (Ding et al., 2019; Han et al., 2015). Four compressive cycles were applied to examine the repeatability of the sensor with a stress amplitude of 15 MPa. The monotonic loading was continued to be applied to the samples up to failure to measure the maximum change in fractional change in resistivity (FCR) at failure. The axial strain was measured by the strain gauges attached to two opposite sides of the sample. The data logger recorded the stress and strain data.

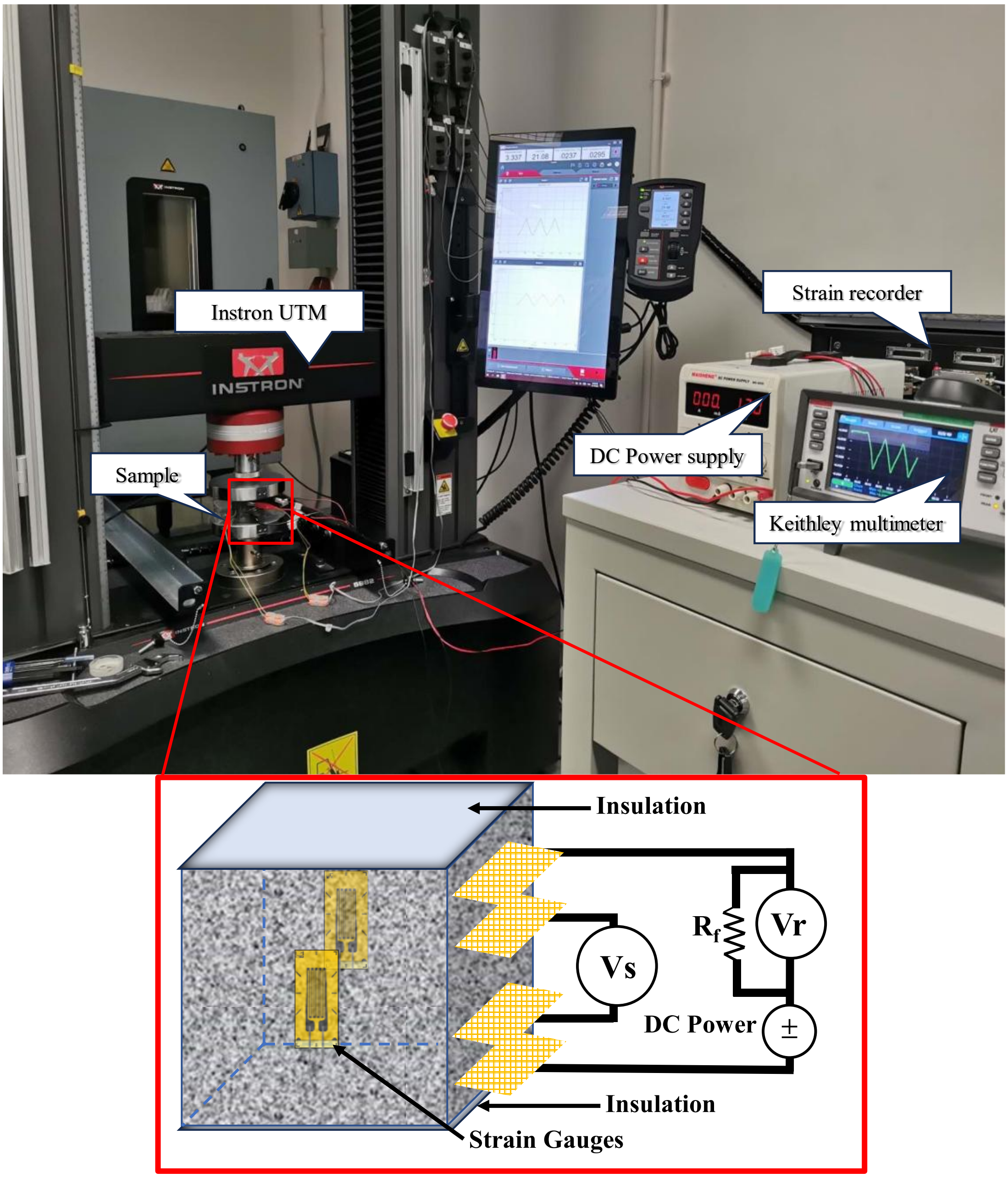

Figure 3.3. Piezoresistive behaviour testing setup and circuit diagram of nCB-based SCC.

Monotonic compression tests were conducted to evaluate the strain sensitivity for all the mixes. The strain sensitivity is generally indicated by the so-called gauge factor (GF) (Amjadi et al., 2016), which is defined by:

$$GF = \frac{FCR}{\varepsilon} \tag{3.1}$$

where ε is the compressive strain while FCR is the fractional change in resistivity defined by the following equation:

$$FCR = \frac{\rho - \rho_0}{\rho_0} \times 100\% \tag{3.2}$$

where ρ_0 is the initial resistivity of the material before being loaded, while ρ is the resistivity of the material subjected to loading.

3.4 Results and Discussions

3.4.1 Compressive Strength

The compressive strength results of three different nCB composites with different dosages are illustrated in **Figure 3.4**. It can be observed that the compressive strength of nCB composites follows a similar trend, initially increasing with the nCB content up to a specific level and then decreasing. However, the turning point of reduction and its ratio is different for different nCB structures. For instance, the samples of nCB-290 and nCB-245 show an increasing trend of compressive strength up to 1.0% nCB, and the nCB-174 samples show an increasing trend up to 1.50% nCB with respect to PC. Generally, the compressive strength improvement is attributed to the pores-filling phenomena of the nCB. Nanoparticles of nCB can fill the nano-level pore to improve porosity and strength (Ding et al., 2019; Leong et al., 2006; Li et al., 2008; Wen & Chung, 2007). It seems that the nCB-174 has a higher range of particle size than the other two types. Apparently, the high range of the particles has a higher capability to fill a high number of pores of different sizes. The increased compressive strength of nCB-174 demonstrated more filling effects than the other two nCB composites. The reduction in strength beyond a certain level is typically linked to the lower flowability and improper compaction of the matrix, caused by the absorption of the higher amount of water and SP and the higher agglomeration due to the high nCB content. This generally leads to a more porous microstructure and decreases the compressive strength (Hussain et al., 2022). Moreover, the hydration process is essential for strength development. The absorption of a significant amount of water can slow down hydration, and the presence of nCB particles can hinder water molecules from effectively reacting with the cement particles (Hussain et al., 2022; Lu et al., 2021). Furthermore, the agglomeration due to strong Van der Waal forces between the nCB particles creates weak stress concentration points that show less resistance to applied forces as compared to the C-H-S product (Dong et al., 2019; Han et al., 2017).

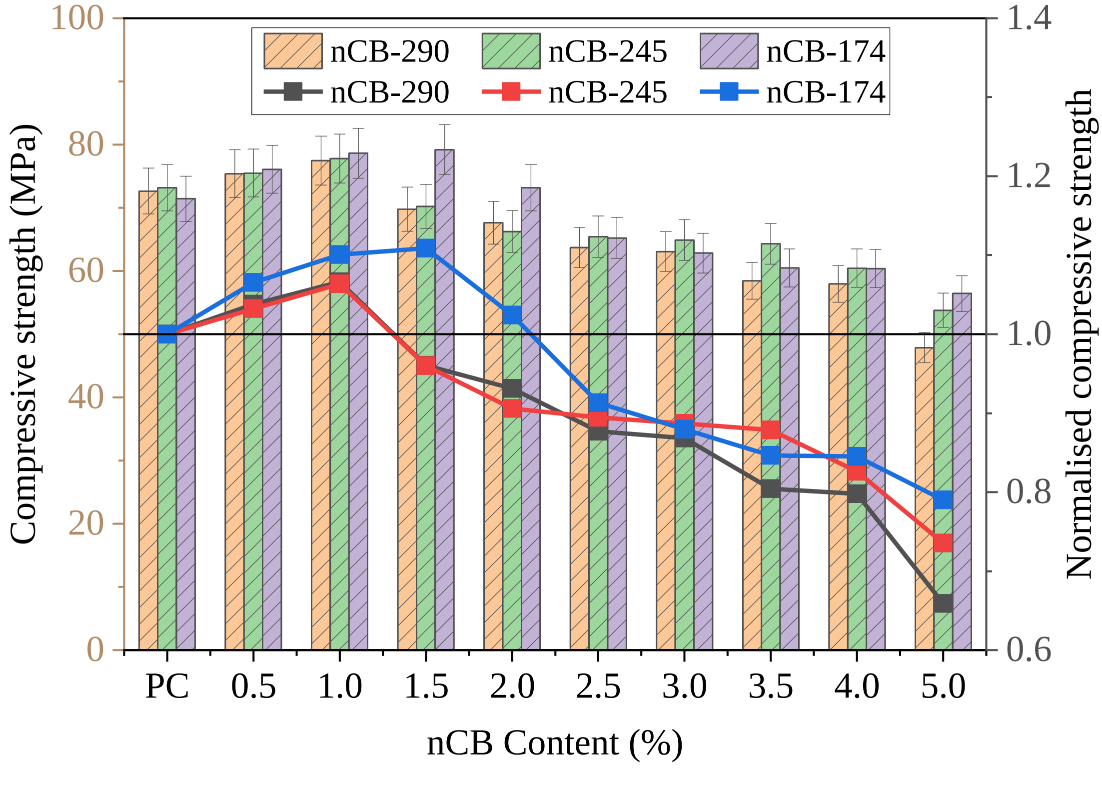

Figure 3.4. Compressive strength of three different structures of nCB with respect to the different concentrations.

3.4.2 Piezoresistive Behaviour

3.4.2.1 Percolation Threshold

The percolation threshold is a crucial parameter for designing and optimising self-sensing properties. The percolation threshold is featured by a significant drop in resistance when the filler content reaches a certain level (Han et al., 2015; Sun et al., 2017). In cementitious composites, the basic phenomena of the conduction of the electrical charges are in two ways: ionic and electronic (tunnelling, field emission and direct contact) conduction (Han et al., 2014). SCCs may be categorized into three zones, including an insulation zone, where the system behaves like an insulator. The composites are partially conductive in a percolation zone, where both ionic and electronic conduction are influenced. When the concentration of the conductive filler is low, ionic conduction takes part in the conduction mechanism through the pore solution of the cementitious matrix (acts as an electrolyte (Demircilioğlu et al., 2019; Han et al., 2020)), which is connected by capillary pores to form a conductive path. Lastly, when the composites are in the above percolation zone, they are fully conductive, and direct contact between the fillers is dominant and influences the conduction mechanism. **Figure 3.5** demonstrates the percolation threshold of the three different nCB composites. Each data point is an average of three specimen readings. It has been mentioned in the literature that the different fillers and matrix have a direct effect on percolation (Chiarello & Zinno, 2005; Dai et al., 2010; Li et al., 2006; Monteiro et al., 2017; Parvaneh & Khiabani, 2019; Sun et al., 2017). However, the same matrix and nCB filler were used in this study but the nCB had different structures. It can be observed from **Figure 3.5** that each nCB has a very different and distinct percolation threshold.

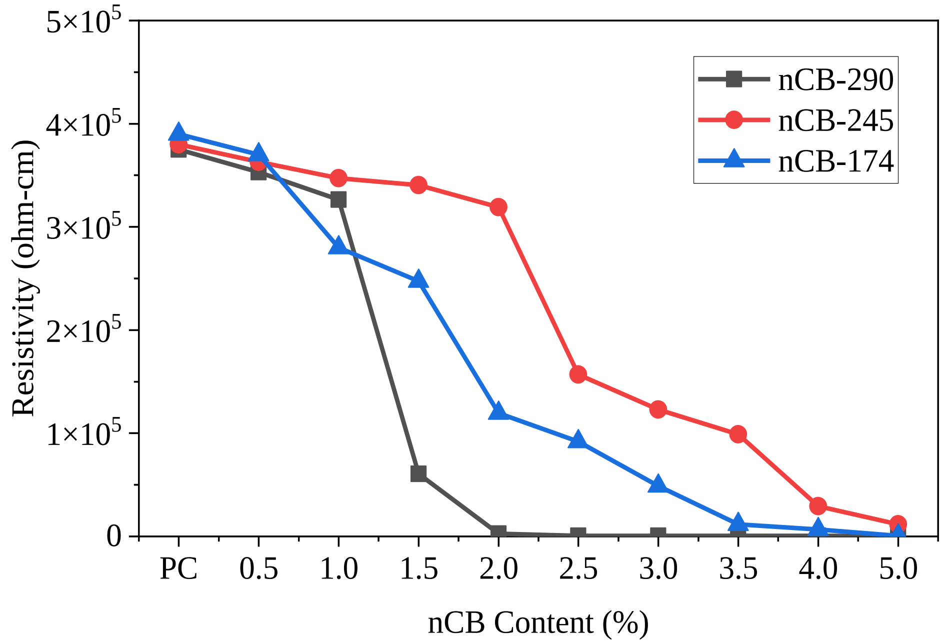

Figure 3.5. Resistance change of three different structures of nCB with respect to the different concentrations.

For instance, nCB-174 has a percolation zone of 0.5% - 3.5% nCB. Whereas the nCB-245 and the nCB-290, the percolation zones are located from 2.0% - 4.0% nCB and 1.0% - 2.0% nCB, respectively. It seems that the nCB-290 has a very distinct and the narrowest percolation zone among all: the zone starts at 1.0%, and the resistance decreases steeply and reaches to a minimal value at 2.0%. When the nCB is above 2.0%, the cementitious composite is in the percolation zone, where the resistance change is minimal due to the stable conductive network formed by the particles of nCB. The reason behind the lowest and most distinct percolation zone of nCB-290 is its chain structure and the widespread volumetric wiring structure which are responsible for conductivity.

Table 3.3 summarises the percolation threshold of the previous studies utilising the nCB as a conductive material, noting that a lower percolation zone is beneficial for developing the cementitious sensors in terms of cost, mechanical properties, and ease of handling.

Table 3.3. Comparison of the percolation threshold of the carbon black incorporated studies.

Matrix	Percolation (%)	Particle size (nm)	Compressive strength (MPa)	Reference
Paste	12.0-20.0	120	40	(Li et al., 2006)
Mortar	0.7-2.5	33	50-60	(Dai et al., 2010)
Mortar	7.0-10.0	120	14-15	(Monteiro et al., 2017)
Mortar	6.50	120	18	(Monteiro et al., 2017)
Mortar	8.0	20-30	9.87	(Nalon et al., 2020)
UHPC	0.5-1.5	40	158-144	(Hussain et al., 2022)
Paste	0.5-3.5	30-60	76-60	This study
Paste	2.0-4.0		66-60	This study
Paste	1.0-2.0	40	77-67	This study

3.4.2.2 Cyclic Compressive Loading

To better understand the repeatability of the nanocomposite within a matrix, it can be assessed through cyclic loading (Georgousis et al., 2017). The literature has mentioned that the endpoint of the percolation zone shows the highest strain sensitivity (Han et al., 2019; Han et al., 2015; Han et al., 2015; Hussain et al., 2022; Hussain et al., 2023; Sun et al., 2017; Zhang et al., 2018). The piezoresistive behaviour of nCB samples at the percolation threshold point was tested for repeatability and strain sensitivity.

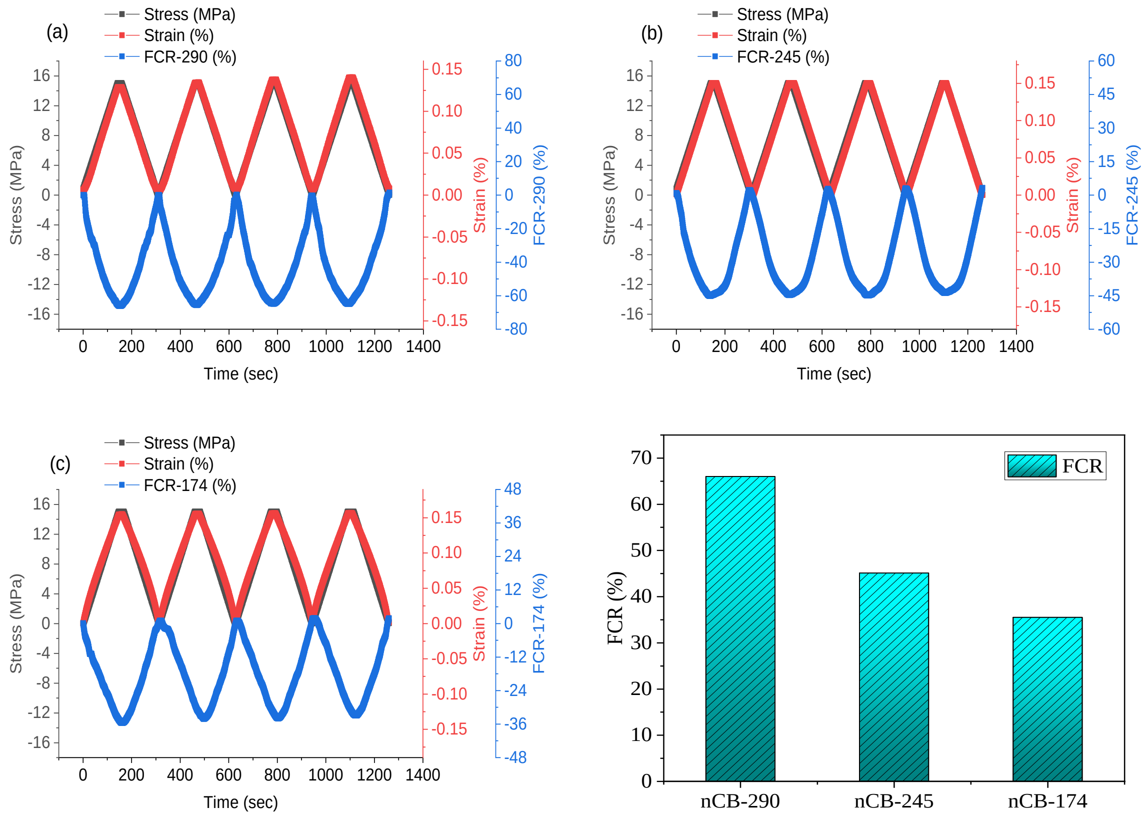

Figure 3.6. FCR response to corresponding stress-strain of different structures of nCB during cyclic compressive loading at the percolation threshold. (a) nCB-290 at 2.0%. (b) nCB-245 at 4.0%. (c) nCB-174 at 3.5% nCB.

It can be said that the results demonstrated in **Figure 3.6** show a precise synchronisation of the FCR with uniaxial cyclic compressive stress and strain. When the load was applied, the resistance decreased, and it increased as it was unloaded. It is attributed to the fact that the distance between the nanoparticles of carbon black was reduced during the compressive loading, which facilitated reconstruction of new conductive pathways by quantum tunnelling mechanism. Likewise, the distance between nanoparticles increased and the interruption of the conductive paths occurred during the unloading, so the resistance increased again. The significantly enhanced piezoresistive response at the percolation threshold can be attributed to tunnelling conduction. This observation aligns with the understanding that changes in the tunnelling distance between conductive fillers play a crucial role in the piezoresistive response of cement-based sensors within the percolation zone (Ding et al., 2019; Li et al., 2024). The predominant conduction mechanism in carbon black particles is electron tunnelling (Spahr et al., 2017; Xiao et al., 2010). According to the tunnel effect theory, the current density in a tunnel resistor formed by two adjacent CB particles at a low voltage region can be described by Equation 2.4.

It can be concluded that the nCB-290 has the highest FCR at the percolation threshold, followed by the nCB-245 and nCB-174, with precise synchronised responses to the applied corresponding stresses and strains. The highest strain sensitivity of the nCB-290 is attributed to its chain-like structure, which has a high number of connected aggregates. As a result, the change in electrical resistivity in the nCB-290 samples was higher than the samples with other nCBs at the same strain.

3.4.2.3 Strain Sensitivity or Gauge Factor

The strain sensitivity or gauge factor (GF) of the samples was evaluated by using a linear fitting curve. The slope of the fractional change of electrical resistivity regarding the applied strain is considered the gauge factor of strain sensors (Amjadi et al., 2016). The strain sensitivity, the so-called GF of the three different nCB-composites, was obtained by applying monotonic loading to the cracking point. **Figure 3.7** illustrates the GF of all three nCB structures at the percolation threshold point. Similar to cyclic response, it can be observed that the nCB-290 samples had the highest GF among all, following the nCB-245 and nCB-174 samples. Moreover, the coefficient of determination (R^2) value shows a high level of linearity for all three nCB samples. The high linearity indicates that the relationship between changes in resistance and strain is strong, suggesting that resistance variations can be reliably predicted by corresponding changes in strain. This reflects a robust and consistent connection between the two variables.

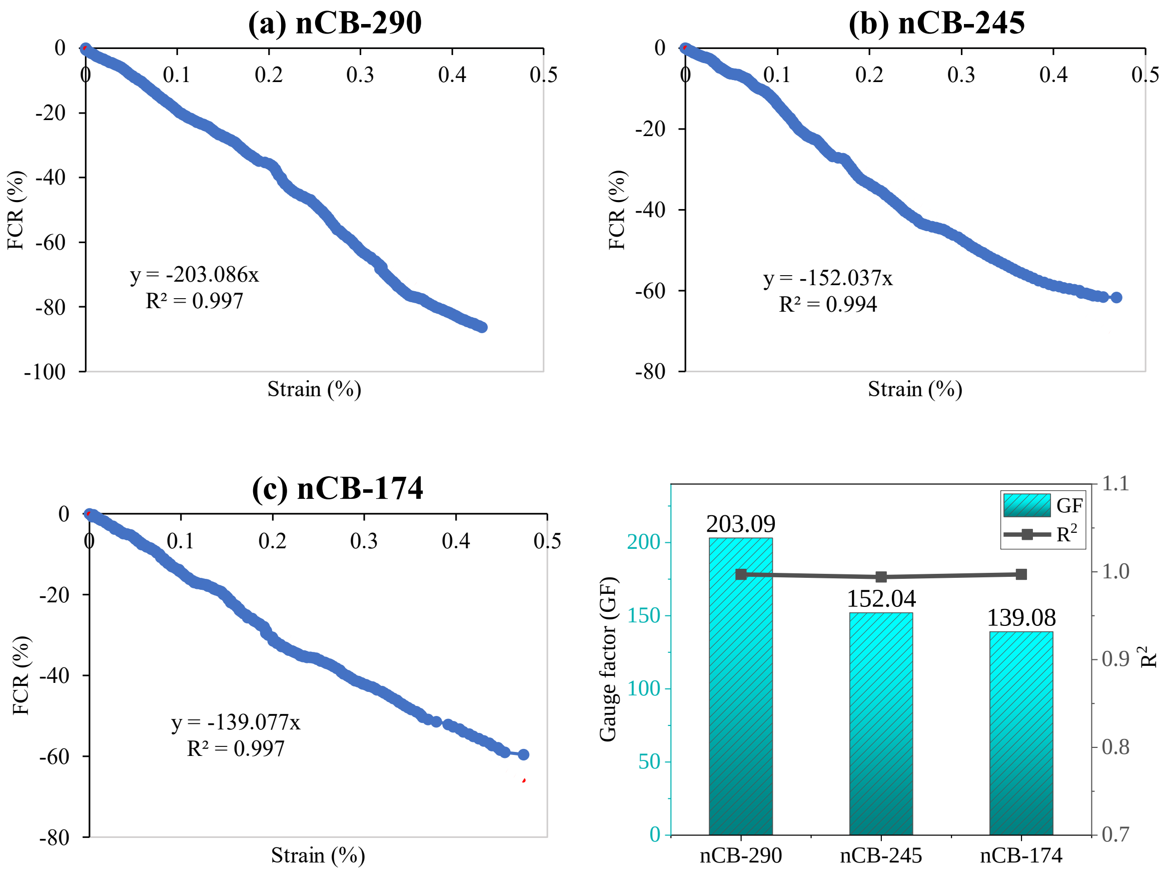

Figure 3.7. Experimental and fitting curves (FCR vs. strain) and the gauge factor of different structures of nCB during monotonic compressive loading at percolation threshold. (a) nCB-290 at 2.0%. (b) nCB-245 at 4.0%. (c) nCB-174 at 3.5%.

3.5 Summary and Conclusions

This study aims to investigate the effects of nCB structure on the mechanical and piezoresistive behaviour of the cementitious composite. The use of nCB in cementitious composites has shown great potential in developing self-sensing concrete for monitoring and damage detection in concrete structures. However, the structure of nCB is a critical parameter in the development of economic and enhanced durability and electrical conductivity. This study has explored the potential of nCB with different structures and concentrations to optimise the performance and application of these innovative materials. After systematic investigations of three different nCBs, the following conclusions can be drawn from this study:

The compressive strength of the cementitious composites incorporating the three different nCBs showed similar trends: initially, the strength increased with the nCB content, it then decreased with additional nCB due to high agglomeration and porosity. The nCB-174 led to better mechanical properties than the other two.

The percolation zone of nCB-290 showed a very low and distinct behaviour compared to the other two nCB samples due to the branched structure of nCB-290. The lower percolation threshold is incredibly beneficial for achieving economical, stable, and durable piezoresistive behaviour for a field-deployable solution.

The strain sensitivity and repeatable piezoresistive behaviour of all the samples at the percolation threshold showed a linear and precisely synchronised behaviour. The maximum strain sensitivity (GF) of 203.08 was achieved by the nCB-290, followed by 152.07 and 139.03 with nCB-245 and nCB-174, respectively, all being several times higher than conventional strain sensors.

These highly strain-sensitive smart cementitious composites can be employed as a field-deployable solution to monitor the health of the concrete infrastructure in the field. After the analysis of the testing results, nCB-290 was determined to be the most suitable nCB structure, which will be incorporated into a UHPC matrix in the next chapter to investigate the strain-sensing capability of UHPC.

Chapter 4.

Development of Nanocarbon Black-Based Ultra-High-Performance Concrete with Strain-sensing Capability

4.1 Abstract

Ultra-high-performance concrete (UHPC) exhibits exceptional mechanical properties and durability. While the dense microstructure contributes significantly to the superior performance of UHPC, it limits the mobility of potential piezoresistive additives. Therefore, it is generally considered challenging to achieve the compressive strain-sensing capability of UHPC. This paper presents the development of a new type of UHPC with strain-sensing capability by incorporating chain-structured nanocarbon black (nCB-UHPC). Nanocarbon black is a highly conductive and low-cost material; when used as a filler material in a concrete mix, it makes the cementitious matrix conductive through a quantum tunnelling mechanism due to its chain structure.

The present study involves comprehensive experimental investigations into various properties of the nCB-UHPC, including its mechanical and piezoresistive properties as well as its microstructure. The nCB content was taken as the key variable in the tests. The test results show that by incorporating nCB of a proper content (e.g., 1.0-1.5%), the resulting nCB-UHPC can have an ultra-high 28-day compressive strength (>140 MPa), sufficiently good workability (slump spread ≥170 mm) and excellent strain-sensing capability (gauge factor >130) at the same time.

4.2 Introduction

Ultra-high-performance concrete is the new high-class achievement in the field of concrete technology which provides a long-term, feasible and sustainable construction due to ultra-high mechanical properties, lower porosity and improved resistance against aggressive environments (Du et al., 2021; Soliman & Tagnit-Hamou, 2017). Although it exhibits exceptional performance, the durability and long-term performance evaluation techniques may bring a paradigm shift from strength-only performance to multifunctionality in the construction industry (Soliman et al., 2020). The intrinsic ability of UHPC to sense stress and strain offers a pathway towards more sustainable and cost-effective construction practices. However, the piezoresistive behaviour of the UHPC is not studied widely. It is mentioned that the compact and dense microstructure of the UHPC is unfavourable for compressive strain sensing, while using steel fibre and CNT (Lee et al., 2018; You et al., 2017). The immobility of the piezoresistive materials during elastic loading and unloading will lead to no piezoresistive synchronization.

By contrast, (Lee et al., 2019) explored the use of fine steel slag aggregate to replace the normal sand in UHPC with steel fibres and reported that by doing so, the UHPC possesses the strain sensing capability despite its dense microstructure due to conductive matrix approach. However, the steel slag aggregates have high contents of free calcium oxides and magnesium oxide which tend to cause volume expansion of concrete, leading to premature cracking and diminishing the mechanical properties and long-term serviceability of concrete structures (Brand & Roesler, 2015; Feng et al., 2022; Wang et al., 2013). Therefore, this study aims to investigate the piezoresistive behaviour of the UHPC composite by incorporation of nCB (nCB-290, which was identified as most suitable among three nCB structures). nCB is regarded as one of the most promising candidates for cementitious composites because of its permanent electric conductivity, very low cost (130 times lower than CNTs), no critical dispersion issues, high chemical and thermal stability, no corrosive and expansive behaviour and fine filler effect (Dong et al., 2020; Hussain et al., 2019; Leong & Chung, 2003, 2004; Monteiro et al., 2015; Wen & Chung, 2007; Youssry et al., 2013). The branched structure of nCB-290 is a critical factor that enables the formation of a conductive network within the UHPC matrix through a quantum tunnelling mechanism. It is ascribed that due to the strong Van der Waal forces, the nCB particles are firmly adhered to one another and form a chain structure (Hartley & Parfitt, 1985), which improves the overall conductivity of the matrix.

In light of the above context, this chapter provides a comprehensive investigation into the development of nCB-based UHPC and examines its mechanical and piezoresistive properties.

4.3 Experimental Program

4.3.1 Raw Materials

This study used EN 197-1 CEM I 52.5N ordinary Portland cement produced by Green Island Cement Limited, Hong Kong. The supplementary materials were silica fume (SF) and quartz powder (QP). The cement and supplementary materials were tested for their chemical composition by X-ray fluorescence (XRF), as detailed in **Table 4.1**. The chemical composition of the SF shows that it had a silica content of over 96%, and the quartz powder with a mean particle diameter of 7.47 µm. River sand was rinsed with tap water to remove clay, preventing negative impacts on UHPC workability and strength, and then oven-dried at 105°C for 48 hours (Fernandes et al., 2007). Following Wille and Boisvert-Cotulio's recommendation, particles of dried river sand larger than 1.18 mm were removed (Wille & Boisvert-Cotulio, 2015). A polycarboxylate-based superplasticizer (SP) was used with a solid content of 22.0% by mass and a specific gravity of 1.05. Nanocarbon black (Super P Li) was used, which has a high dibutyl phthalate (DBP) oil absorption (i.e., 290 ml/100gm) and thus a high probability of establishing a conductive network (Pantea et al., 2003). The transmission electron microscopy (TEM) images in **Figure 4.1** explain the branched structure of nCB particles. The physical and chemical properties of nCB are given in **Table 4.2**.

Table 4.1. Chemical components of cement and supplementary materials.

Oxides (%)	SF	Cement	QP
SiO_2	96.950	14.900	97.700
CaO	0.073	70.500	0.028
K_2O	0.143	0.886	0.606
Al_2O_3	0.141	3.530	1.340
P_2O_5	0.412	0.093	0.000
SO_3	0.004	3.000	0.000
Fe_2O_3	0.643	0.000	0.204
ZrO_2	1.605	0.000	0.000
NiO	0.037	0.049	0.000
MgO	0.015	0.957	0.000
Na_2O	0.000	0.167	0.000
TiO_2	0.000	0.375	0.000

Table 4.2. Physical properties of nanocarbon black.

DBP (ml /100gm)	**Pour density** (g/cm^3)	**Resistivity** (ohm-cm)	**Particle size** (nm)	**Surface area** (m^2/g)
290	0.16	0.18	~40	62

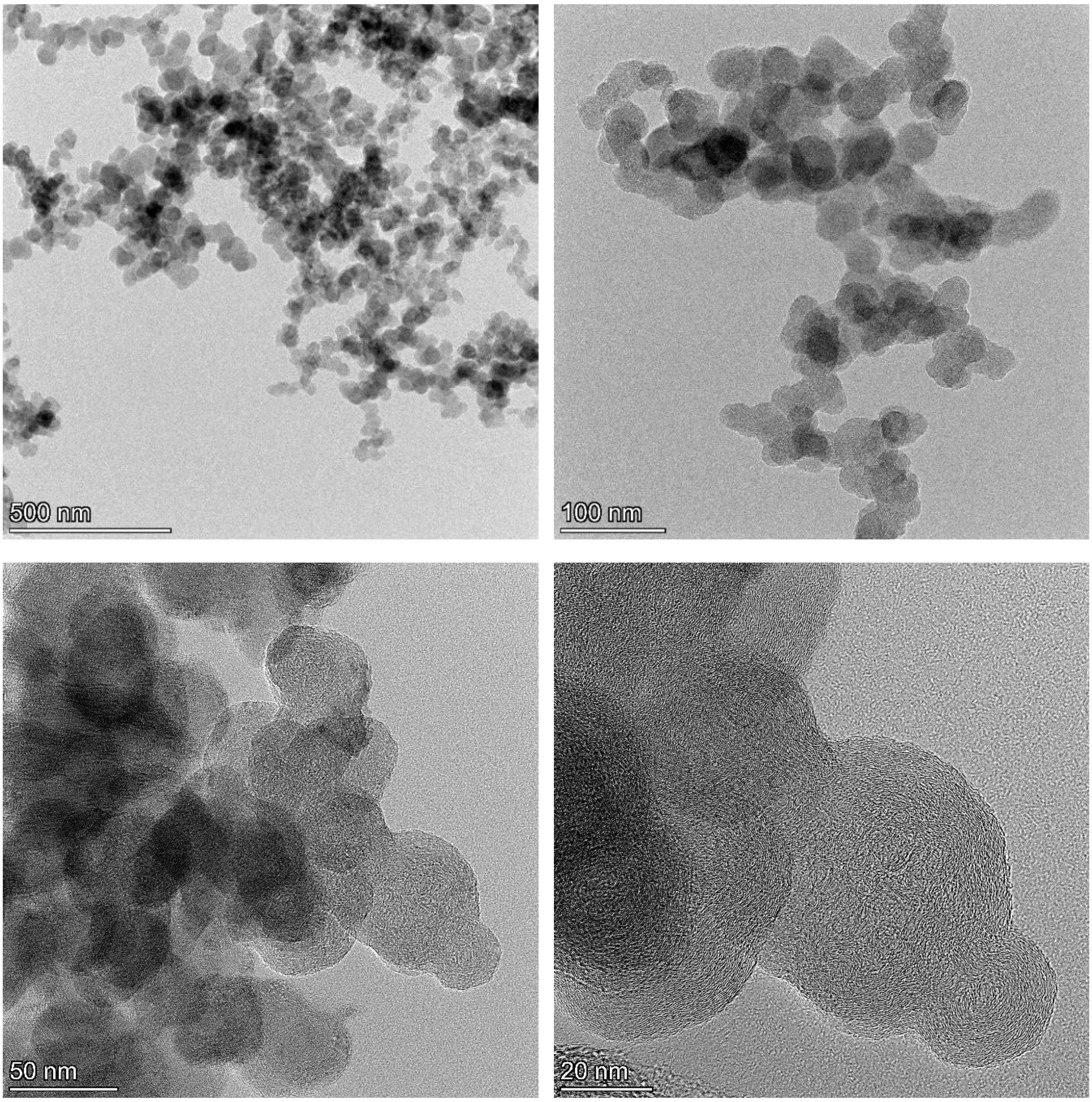

Figure 4.1. Morphology of nanocarbon black particles by TEM at different scales.

The Zetasizer Nano ZS90 particle size and zeta potential analyser measured the particle size of all the raw materials, and the cumulative particle size distribution of various UHPC mix proportions is shown in **Figure 4.2**.

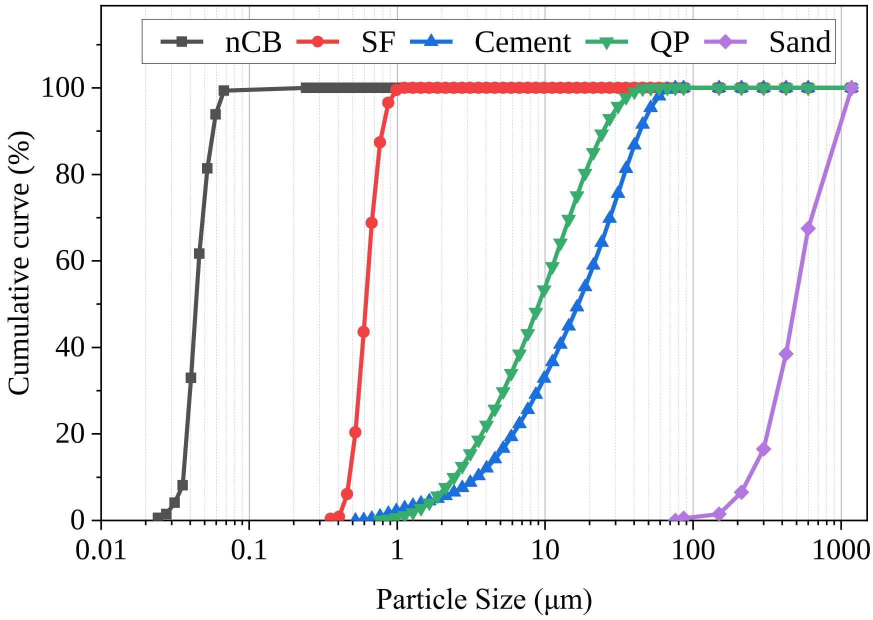

Figure 4.2. Cumulative particle size distribution of UHPC mixes.

4.3.2 Mix Design

The present study prepared and tested nine mixes, including one control mix without nCB and eight with different nCB contents. The control mix was developed based on the UHPC mix reported in (Teng et al., 2019), with slight adjustments to address the differences in the raw materials. The constituents of the control mix included cement, SF, QP, sand, water, and SP. On the other side, eight mixes use nCB as a filler material. The mass of nCB ranged from 0.25 to 2.00% of the binders (i.e., cement and silica fume). The nCB replaced an equal volume of non-conductive fillers (quartz powder and sand), while the proportions of cement, silica fume, water, and superplasticizer (SP) remained constant across all mixes. The quantities of the constituents in the nine mixes are detailed in **Table 4.3**.

Table 4.3. Base mix design of nCB-UHPC (kg/m^3).

Notation	Cement	SF	QP	Sand	Water*	SP	nCB#
UHPC	842.0	210.5	210.5	926.2	169.4	42.1	0.00
0.25nCB-UHPC	842.0	210.5	190.5	902.2	169.4	42.1	2.63
0.50nCB-UHPC	842.0	210.5	170.5	878.2	169.4	42.1	5.26
0.75nCB-UHPC	842.0	210.5	150.5	854.2	169.4	42.1	7.89
1.00nCB-UHPC	842.0	210.5	130.5	830.2	169.4	42.1	10.53
1.25nCB-UHPC	842.0	210.5	110.5	806.2	169.4	42.1	13.16
1.50nCB-UHPC	842.0	210.5	90.5	782.2	169.4	42.1	15.79
1.75nCB-UHPC	842.0	210.5	70.5	758.2	169.4	42.1	18.42
2.00nCB-UHPC	842.0	210.5	50.5	734.2	169.4	42.1	21.05

0.25nCB-UHPC means that 0.25% by binder mass nCB added into UHPC

**The total amount of water includes the SP (i.e., 78% of SP), leading to a water-to-binder ratio of 0.19.*

#This column represents the mass ratio of nCB to the binders (i.e., cement and silica fume)

4.3.3 Preparation of Specimens

The nano size and large specific surface area of nCB particles absorb a significant amount of free water in concrete mixes, which leads to reduced workability and nCB dispersion (Wu et al., 2016). The high water absorption of nCB brings significant challenges to the UHPC, which has a relatively low water-to-binder ratio (e.g., 0.19 in the present study). On the other hand, the preparation process greatly affected the workability and electrical properties of self-sensing concrete (Al-Dahawi et al., 2016). In this study, a series of preliminary tests were first performed to identify a proper preparation process for good dispersion of nCB and an acceptable level of the workability of the nCB-UHPC.

The preliminary tests led to the following preparation process for nCB-UHPC specimens, as can be seen in **Figure 4.3**. Step (1) is mixing of cement, silica fume and quartz powder for five minutes; (2) mixing water with SP and adding 75-85% of the mixture to the dry constituents in two phases, and then continuing mixing until a slurry of UHPC was ready; (3) mixing the nCB and sand with the remaining water and SP, adding them into the slurry, and continuing mixing until an acceptable fluidity level was reached; (4) casting the UHPC into cube moulds with a side length of 50 mm and embedding four copper meshes into each specimen for measurement of electrical resistivity (the embedment depth of the meshes was 20 mm while their positions are shown in **Figure 4.3**, and (5) covering the specimens with a plastic sheet and leaving them at room temperature for 24 hours before demoulding. After demoulding, two different types of curing conditions were employed. One-day heat curing at 90℃ ± 1℃ in a heat-curing chamber for 24 hours following similar existing studies (Meng & Khayat, 2016; Teng et al., 2019). The second curing is the 28-day water immersion curing in ordinary tap water at 22℃ ± 3℃.

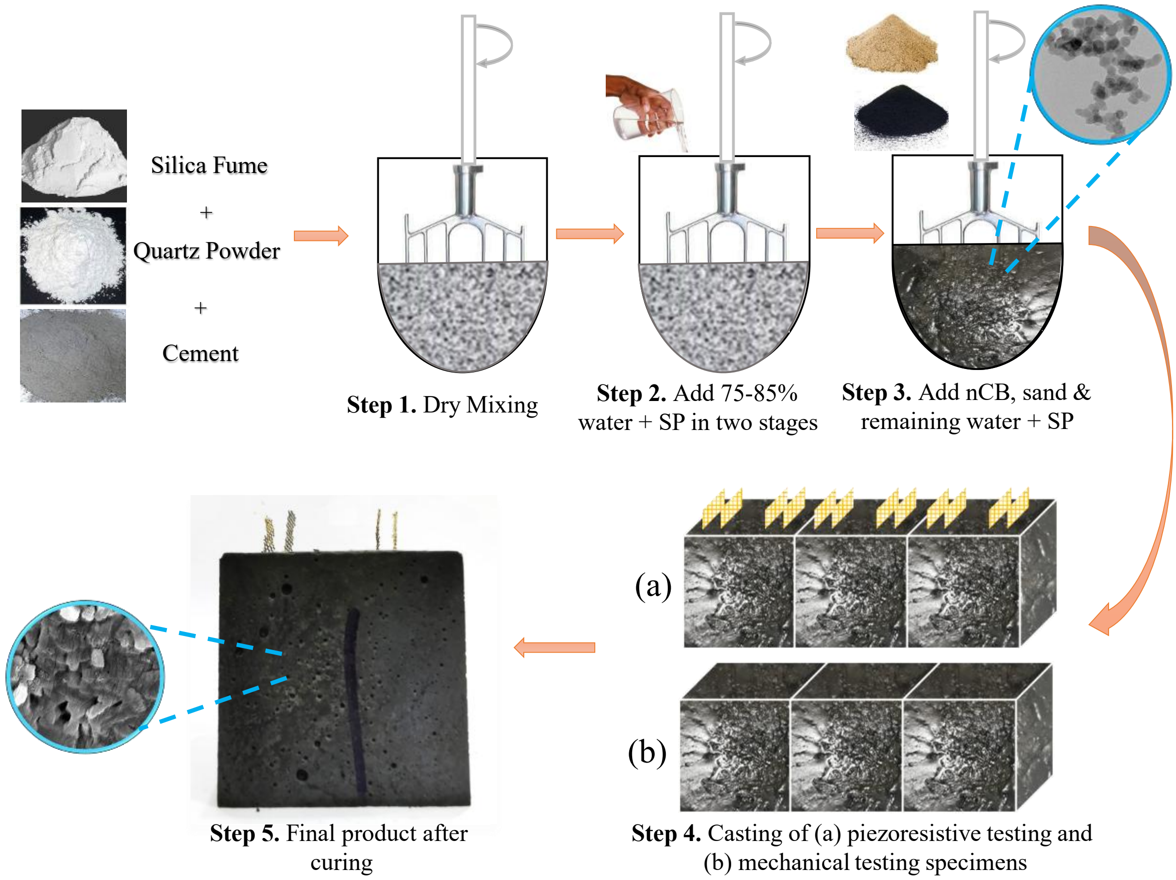

Figure 4.3. Fabrication procedures of nCB-filled UHPC sample.

4.3.4 Workability

Workability is an essential property of fresh concrete, which directly affects the hardened properties of concrete (e.g., compressive strength). The mini-slump measured the workability of the nCB-UHPC spread in accordance with ASTM C1437/C1437M–20 (C1437-20, 2020) using a flow table specified in ASTM C230/C230M-21 (C230/C230M-21, 2021).

4.3.5 Compressive Strength

The UHPC samples are fabricated and tested by following (C1856/C1856M-17, 2017). Two different curing conditions were applied including one-day heat curing at 90°C and samples are labelled as UHPC-1d, while the normal water immersion curing samples at the age of 28 days are labelled as UHPC-28d. The loading rate of testing samples was 1 MPa/s.

The remaining details are given in section 3.2.4.

4.3.6 Piezoresistive Properties

The resistance of the samples before loading is measured at the different curing ages up to 28d. The samples were removed from the curing tank, wiped off the water with a paper towel, and let the surface dry in the air for at least one hour. The samples for the drying treatment were placed in an oven at 80℃ following 28 days of water curing for 72 hours. Their resistance was measured after three days. The samples were cooled down for one hour after being removed from the oven and allowed to measure the resistance (Dong et al., 2019; Lipscomb et al., 2009). The monotonic compression tests loaded the specimens with a 0.4 mm/min displacement control rate until failure using the MTS 815 rock mechanics test system (Ding et al., 2019; Han et al., 2015). In the cyclic compression tests, the same testing machine was adopted with the same loading rate; four loading/unloading cycles were applied to examine the repeatability of the resistivity results with a stress amplitude of 40 MPa, which is in the elastic range of the specimens. The testing method and circuit diagram are detailed in **Figure 3.3.**

The remaining details are given in section 3.2.5.

4.3.7 Microstructure Analysis

A high-resolution FE-SEM (Tescan MAIA3) was used to investigate the micromorphology of the nCB samples and plain UHPC samples. The nCB-UPHC samples were obtained from the inner core of the cubic specimens, dried out treatment was applied, and then gold-coated was used before being investigated to ensure the quality of the images.

4.4 Results and Discussions

4.4.1 Workability

The workability of all nine mixes can be seen in **Table 4.4**, where they are measured by measuring their respective slump spreads using the flow table apparatus. The slump spread was taken as the average value of the measurements in two perpendicular directions (Wille et al., 2011), as seen in **Figure 4.4**(a-b). The slump spread values and the reduction ratio of the nine mixes are depicted in **Figure 4.5**. It is not a surprise to see that the workability decreases with the content of nCB, with the maximum value being 331 mm for the plain concrete (PC) mix while the minimum value being 143 mm for the mix with a nCB content of 2.0% (2.00nCB-UHPC). Besides the high water absorption of nCB, the increase of nCB content also led to increasingly high viscosity due to the strong interparticle van der Waals forces of nCB (Hartley & Parfitt, 1985; Wu et al., 2016).

On the other hand, the rate of decrease in the workability appears to reduce as nCB content increases, which can be seen in **Figure 4.5**: the difference between the slump spreads of mixes PC and 0.25nCB-UHPC is about 15.0%, which is about three times that between mixes 1.75nCB-UHPC and 2.00nCB-UHPC. Nevertheless, the workability of all the mixes, including mix 2.00nCB-UHPC, was found to be satisfactory in terms of the ease of casting and the uniformity of concrete quality, as demonstrated by their various properties presented in the subsequent sections. Indeed, the slump spreads of all the mixes are higher than or close to the value representing good workability reported by the existing studies [e.g., 160 mm (Du et al., 2021)].

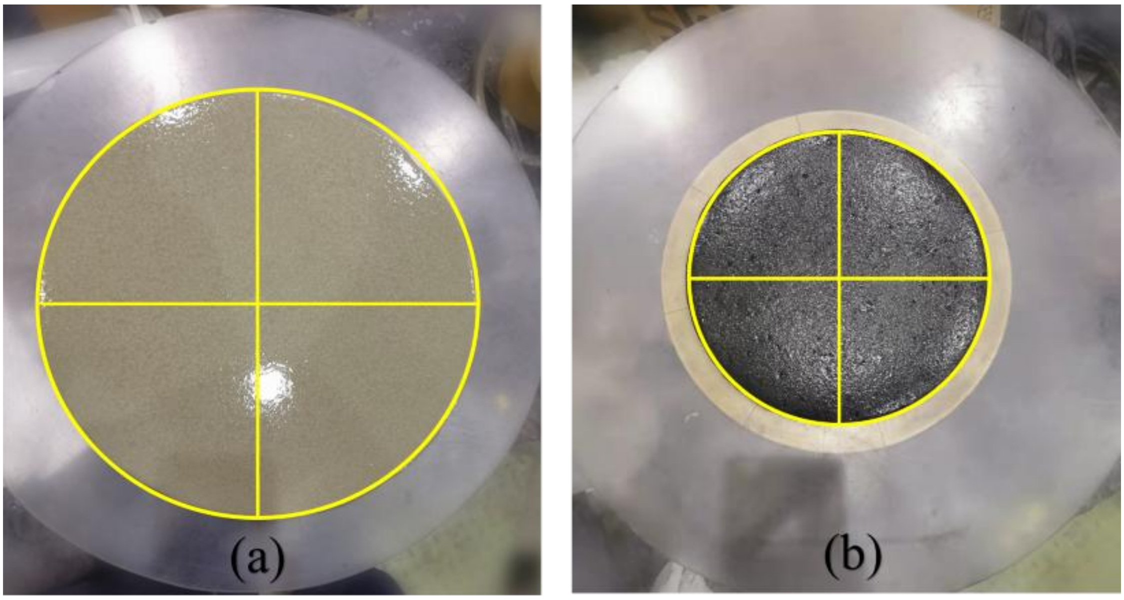

Figure 4.4. Slump spread of UHPC and nCB-UHPC. (a) Plain UHPC and (b) 1.00nCB-UHPC.

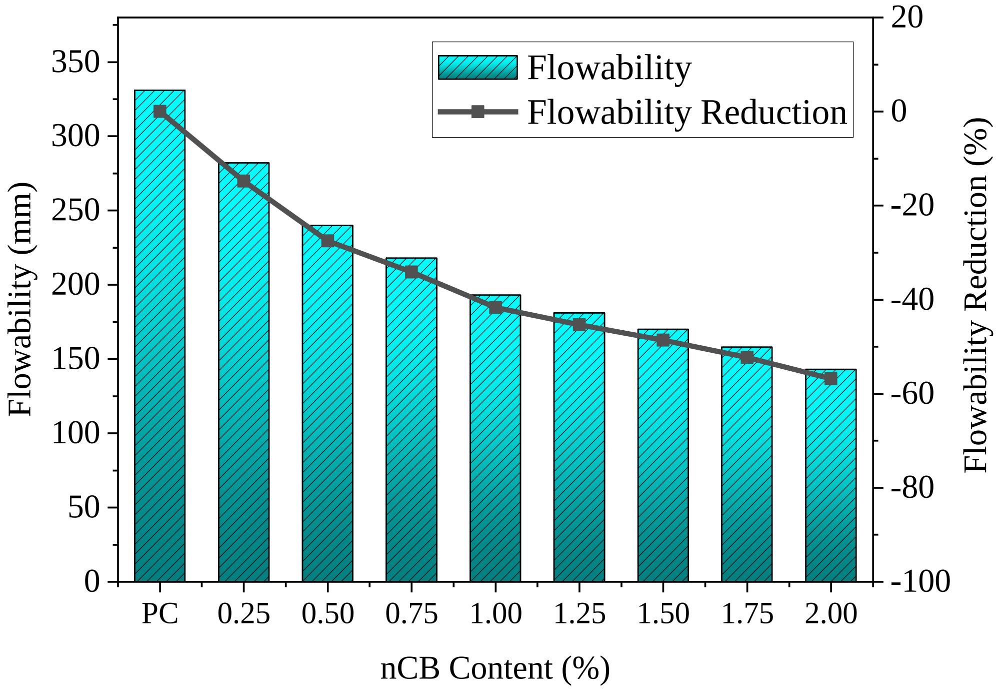

Figure 4.5. Flowability and reduction ratio with respect to nCB content.

4.4.2 Compressive Strength

The compressive strength and the standard deviation of UHPC-1d and UHPC-28d are detailed in **Table 4.4**.

Table 4.4. Compressive strengths, workability, and density of nCB-UHPC.

Notation	$f_{cu, UHPC-1d}$ (MPa)		$f_{cu, UHPC-28d}$ (MPa)		Slump Spread (mm)	Density
	Mean	SD	Mean	SD		Kg/m^3
UHPC	181.70	6.95	183.90	6.83	331.00	2380.7
0.25nCB-UHPC	163.70	3.57	168.50	3.95	282.00	2339.8
0.50nCB-UHPC	153.50	1.75	158.70	1.57	240.00	2301.3
0.75nCB-UHPC	145.50	1.24	151.70	2.37	218.00	2262.6
1.00nCB-UHPC	143.10	1.29	150.40	0.91	193.00	2221.6
1.25nCB-UHPC	137.90	4.42	147.50	3.73	181.00	2182.8
1.50nCB-UHPC	133.40	2.41	144.80	3.72	170.00	2144.0
1.75nCB-UHPC	131.40	1.94	142.50	3.07	158.00	2102.9
2.00nCB-UHPC	130.10	2.21	141.60	3.51	143.00	2045.6

The test results and the improvement are shown in **Figure 4.6**, which explains that the strength of both curing conditions decreases as the nCB content increases (i.e., UHPC-1d and UHPC-28d). The maximum values of compressive strength are 181.7 MPa (UHPC-1d) and 183.9 MPa (UHPC-28d) for mixed PC, while the minimum values are 130.1 MPa (UHPC-1d) and 141.6 MPa (UHPC-28d) for mix 2.00nCB-UHPC. It is not difficult to understand that this observation is consistent with that of the workability of the mixes, as both the strength and workability are highly related to the particle packing density (Cai, 2017; Fennis & Walraven, 2012; Karadumpa & Pancharathi, 2021). With the increase of nCB content, the nanoparticles absorbed an increasing amount of free water and SP, which was detrimental to the hydration process and thus negatively affected the compressive strength. The decrease in compressive strength with respect to nCB content may also be explained by the differences in the microstructure of the UHPCs, as illustrated by the FE-SEM images. **Figure 4.7**(a-b) shows the microstructure of a 0.50nCB-UHPC and 2.00nCB-UHPC specimen, while **Figure 4.7**(c-f) shows a 2.00nCB-UHPC specimen. By observing the images, the following reasons contributing to the decrease in strength might be identified: (1) the porosity and nonuniformity of UHPC increased with the nCB content due to the decrease in workability. The 0.50nCB-UHPC, which has lower porosity as compared to the 2.00nCB-UHPC, which can be seen in **Figure 4.7**(a-b), (2) the agglomeration of nCB particles due to strong van der Waal forces led to relatively large aggregates, and thus stress concentration points with relatively small resistance to the applied forces (**Figure 4.7**(c-d)) (Dong et al., 2019). Nevertheless, the strengths of all the mixes are considerably higher than 120 MPa and can be classified as UHPC according to the definition of ASTM C1856/C1856M-17 (C1856/C1856M-17, 2017).

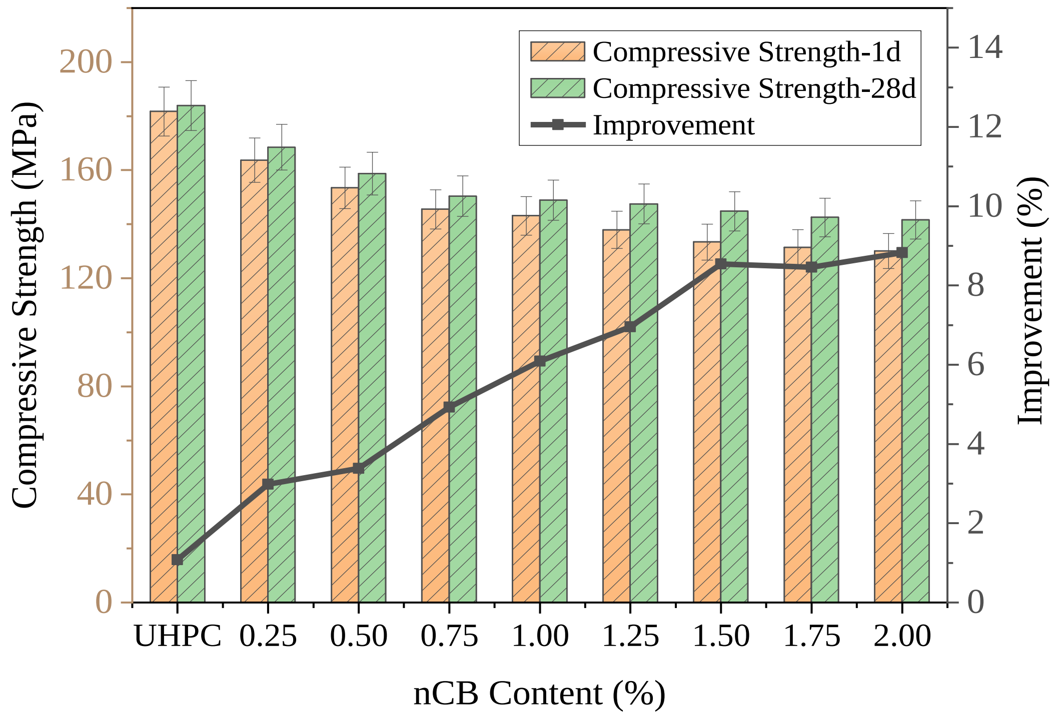

Figure 4.6. Compressive strengths of different curing systems and strengths improvement of UHPC specimens at different concentrations of nCB.

On the other hand, it can be easily observed that the UHPC-28d strength is consistently higher than the UHPC-1d strength for all the mixes, as can be seen from **Figure 4.6**, where these findings reported are consistent with the existing studies (Teng et al., 2019). It is also interesting to note that the difference between the UHPC-28 and UHPC-1d strength increases with the nCB content. The difference for mix PC is 1.0%, while that for mix 2.00nCB-UHPC is 8.8%. The higher strength of UHPC-28 compared to that of UHPC-1d is believed to be due to the improved hydration process of the former by the continuous provision of water over a relatively long period (Monteiro et al., 2017); this improvement appears to be more pronounced for the mixes with a higher nCB content whose hydration process was more significantly affected by the nCB particles. As mentioned by other researchers (Dong et al., 2019; Taha, 2020), nCB particles may enclose some cementitious particles and may thus delay the hydration process by hindering the latter from interacting with water molecules. Moreover. the higher nCB content leads to greater water absorption during the fabrication process due to its high surface area. As a result, the 28 days of water immersion curing contributes additional water content to the sample, further promoting the hydration process.

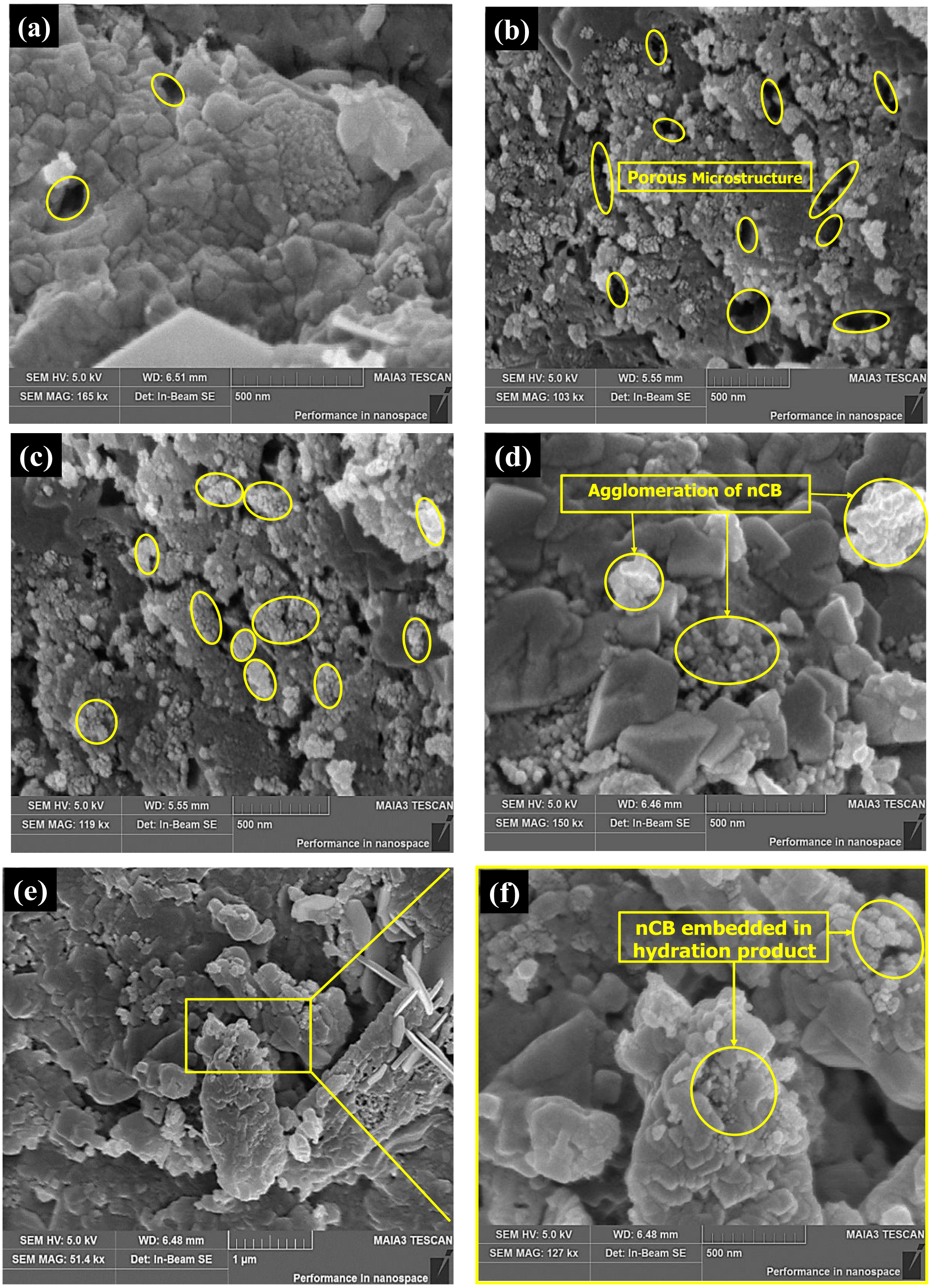
(a)
SEM HV: 5.0 kV
WD: 6.51 mm
MAIA3 TESCAN
SEM MAG: 165 kx
Det: In-Beam SE
500 nm
Performance in nanospace
(b)
Porous Microstructure
SEM HV: 5.0 kV
WD: 5.55 mm
MAIA3 TESCAN
SEM MAG: 103 kx
Det: In-Beam SE
500 nm
Performance in nanospace
(c)
SEM HV: 5.0 kV
WD: 5.55 mm
MAIA3 TESCAN
SEM MAG: 119 kx
Det: In-Beam SE
500 nm
Performance in nanospace
(d)
Agglomeration of nCB
SEM HV: 5.0 kV
WD: 6.46 mm
MAIA3 TESCAN
SEM MAG: 150 kx
Det: In-Beam SE
500 nm
Performance in nanospace
(e)
SEM HV: 5.0 kV
WD: 6.48 mm
MAIA3 TESCAN
SEM MAG: 51.4 kx
Det: In-Beam SE
1 μm
Performance in nanospace
(f)
nCB embedded in hydration product
SEM HV: 5.0 kV
WD: 6.48 mm
MAIA3 TESCAN
SEM MAG: 127 kx
Det: In-Beam SE
500 nm
Performance in nanospace

Figure 4.7. Microstructure analysis shows the porosity and agglomeration of nCB-UHPC. (a) 0.50nCB-UHPC and (b) 2.00nCB-UHPC. (c-d) Agglomeration and larger aggregate size of nCB. (e-f) nCB particles embedded in hydration products.

On the other hand, the fresh density of the samples decreased to 2045.6 kg/m3, which can be seen from **Table 4.4**. Lightweight concrete is a versatile construction material that provides numerous technical, economic, and environmental advantages. These benefits include reduced dead loads, leading to savings in foundation and reinforcement costs, enhanced thermal properties and fire resistance, and more efficient transportation and handling of precast units on construction sites (Ismail et al., 2004; Wang et al., 2022). Researchers have used a number of natural and artificial expensive and special materials to reduce the LWC, which has compromised many properties of the concrete (Elango et al., 2021; Haque et al., 2004; Lu, 2023; Wang et al., 2022). The nCB-UHPC has an intrinsic lower density, which could be one of the biggest advantages along with sensing capability. The combination of lightweight properties and the built-in sensing capabilities of nCB-UHPC makes it an ideal choice for construction projects demanding both reduced structural loads and real-time monitoring of the concrete's condition and surrounding environment.

4.4.3 Piezoresistive Behaviour

4.4.3.1 Percolation Zone

The percolation zone is a key parameter for designing and optimizing self-sensing concrete. It refers to a range of conductive filler (e.g., nCB) contents, within which resistivity decreases dramatically with conductive filler content (Han et al., 2015; Sun et al., 2017). Self-sensing concrete relies on a percolation zone enabled by two primary electrical conduction mechanisms: ionic conduction and electronic conduction (via tunnelling, field emission, and direct contact) (Han et al., 2014). Ionic conduction is generally dominant for concrete with relatively low conductive filler content, in which conductive routes between fillers cannot be established, and electrical charges are passed through the free water in the voids connected by capillary pores within the concrete matrix. On the other hand, electronic conduction can be achieved when conductive filler content is sufficiently high to breed conductive networks established by the quantum tunnelling effect and/or direct contact between conductive fillers. The percolation theory of the nCB incorporated in UHPC is described in **Figure 4.8**.

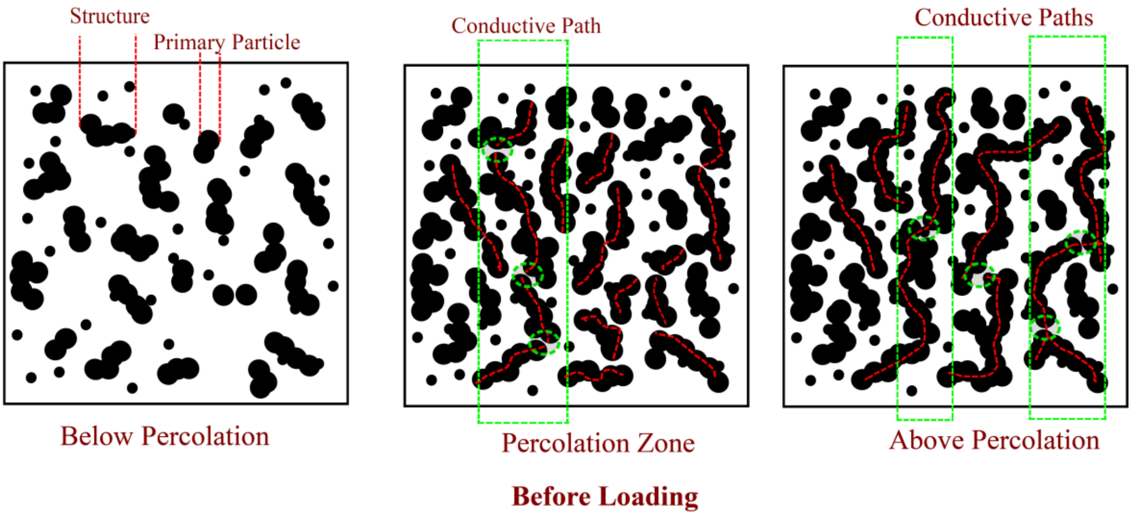

Figure 4.8. Schematic diagram illustrating the mechanism of the percolation threshold of nCB before application of external load.

As stated in the above section, the resistivity of normal water-immersed specimens was measured at various ages up to 28 days. The results are shown in **Figure 4.9**, where each data point represents the average result of three identical specimens. It is evident that the resistivity generally increases with the curing time for all the mixes, mainly due to the reduction of free water in the hydration process, which consumes water and forms new products (Qureshi & Panesar, 2020). It is also evident that the change of resistivity with time is much more pronounced for the mixes with a relatively low (or zero) nCB content than for those with a relatively high nCB content, suggesting that the ionic conduction, which depends mainly on the amount of free water (Demircilioğlu et al., 2019), plays a more critical role in the former.

As an example, the plain concrete specimens (PC) showed a lower resistivity than those of mix 2.00nCB-UHPC at early ages (i.e., Days 1 and 2), but the 28-day resistivity of the former became much higher than the latter in which electronic conduction routes by nCB played a dominant role. Further examination of the FE-SEM images (**Figure 4.7**(f)) of the specimens suggests that the increase of resistivity of nCB-UHPC might also be due to the change in the microstructure of the material. It can be seen that the hydration products may have encircled and trapped some nCB particles and thus broken some conductive paths between them.

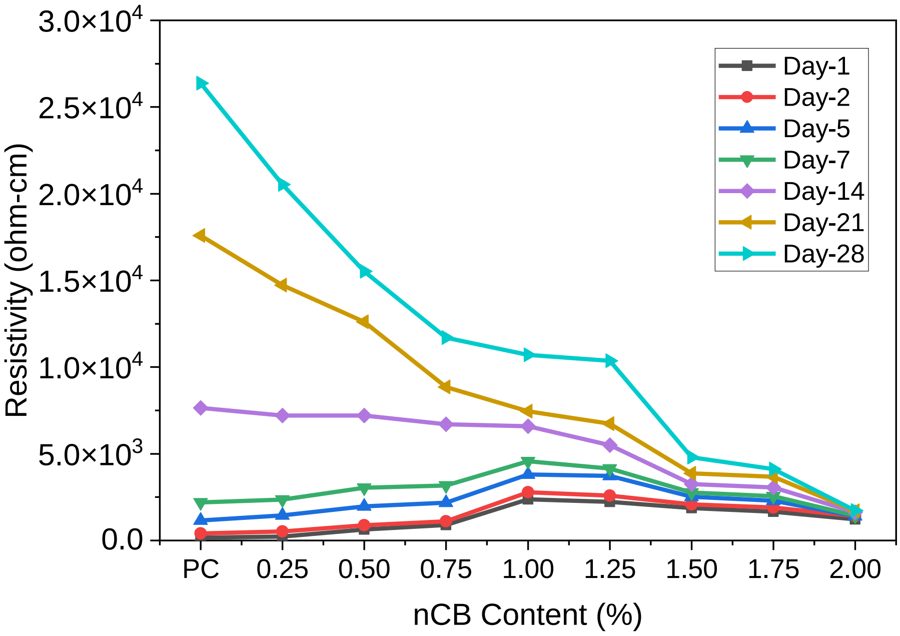

Figure 4.9. Variation of the electrical resistivities of nCB-UHPC specimens at different curing ages.

To identify the percolation zone, the 28-day resistivities of all the mixes are further plotted in **Figure 4.10**(a-b). However, **Figure 4.10**(a). shows that the rate of resistivity decrease remains almost the same for the tested range of nCB contents, so the percolation zone cannot be clearly established. This may be due to the moisture content in the specimens, which facilitated the ionic conduction and made the resistivity change caused by the electronic conduction via nCB particles not clearly identified. The specimens were put in an oven at 80

°C for three days to minimize the effect of moisture content. Their resistivities were then measured again, and the results are shown in **Figure 4.10**(b). It is evident by comparing that the resistivity of the specimens increased significantly due to the significant loss of ionic conductivity. The percolation zone can now be identified from **Figure 4.10**(b). to be from 0.50% to 1.50% of the nCB content, within which the resistivity is seen to decrease dramatically. By contrast, the rate of decrease in resistivity is significantly lower for the nCB contents outside the percolation zone, especially for the higher nCB contents (i.e., 1.50% to 2.00%) where the nCB particles have established a stable conductive path.

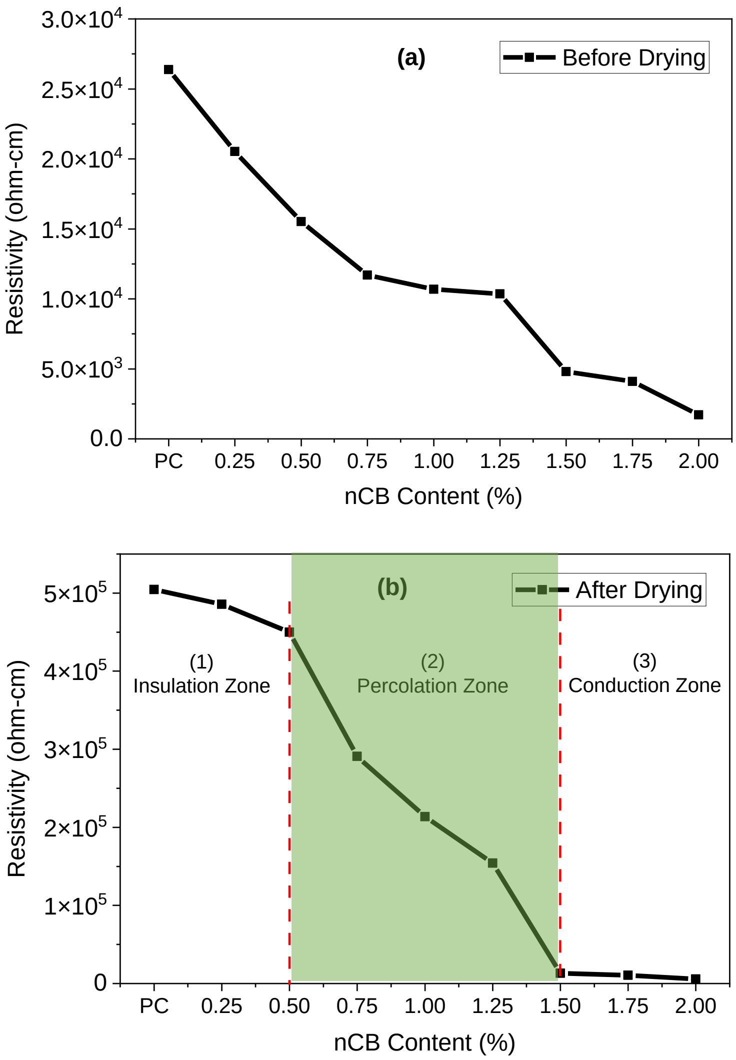

Figure 4.10. Change in the electrical resistivity of nCB-UHPC specimens before and after oven-drying.

Compared to previous studies, the percolation zone obtained in the present study is relatively low compared with other studies. This may be due to the difference in the structure of nCB: the branched structure nCB used in this study has a relatively larger surface area for electron conduction than a low-structure nCB (Rwei et al., 2002). Furthermore, the concrete mixing procedure has been reported to significantly impact its electrical conductivity (Al-Dahawi et al., 2016). The relatively low percolation zone is beneficial for practical applications of the self-sensing UHPC in terms of cost, ease of handling and mechanical properties.

4.4.3.2 Cyclic Compressive Tests

Cyclic compression tests were conducted to examine the repeatability and reproducibility of the piezoresistive behaviour of the nCB-UHPC developed in the present study, following the approach of similar previous studies (Georgousis et al., 2017). As stated in Section 4.2.6, four loading/unloading cycles were applied with a stress amplitude of 40 MPa, which is sufficiently large for examining the piezoresistive behaviour while still in the elastic range of the UHPC. This stress amplitude (40 MPa) is also significantly higher than those reported in similar previous studies, which are generally concerned with normal strength concrete/mortar/cement paste with nCB. The test results are presented in **Figure 4.11**, in which the following parameters are plotted against the time: (1) stress, (2) strain, and (3) FCR. The stresses were calculated using the applied load recorded by the machine; the strain gauges measured the strains, and the FCR was calculated using the equation. 3.2 based on the measured resistivities.

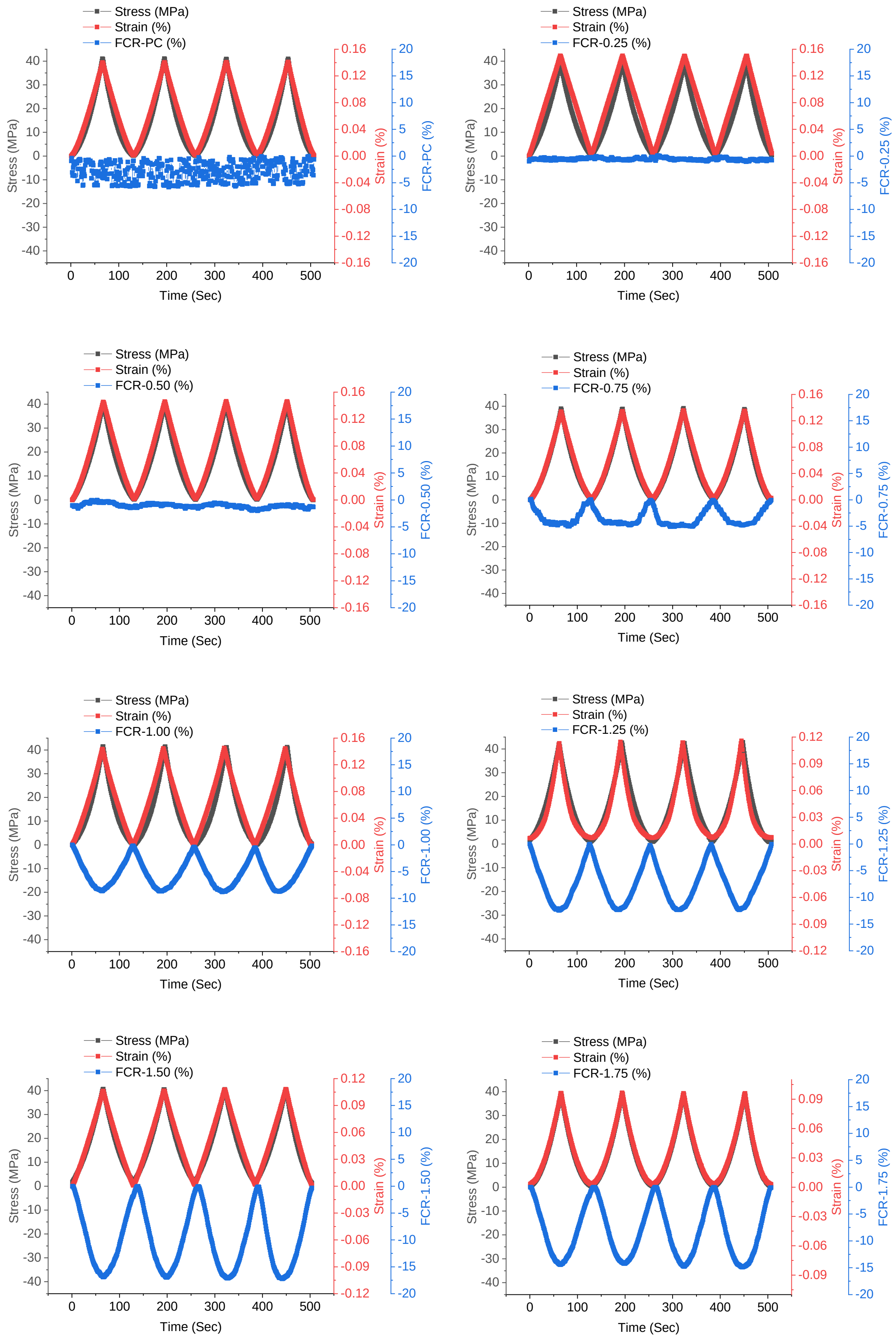
Stress (MPa)
Strain (%)
FCR-PC (%)
Time (Sec)
Stress (MPa)
Strain (%)
FCR-0.25 (%)
Time (Sec)
Stress (MPa)
Strain (%)
FCR-0.50 (%)
Time (Sec)
Stress (MPa)
Strain (%)
FCR-0.75 (%)
Time (Sec)
Stress (MPa)
Strain (%)
FCR-1.00 (%)
Time (Sec)
Stress (MPa)
Strain (%)
FCR-1.25 (%)
Time (Sec)
Stress (MPa)
Strain (%)
FCR-1.50 (%)
Time (Sec)
Stress (MPa)
Strain (%)
FCR-1.75 (%)
Time (Sec)

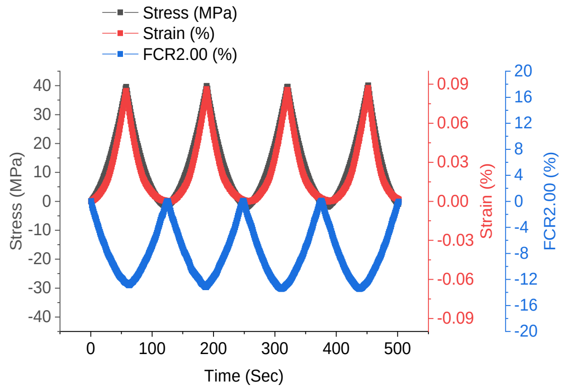

Figure 4.11. FCR response to corresponding stress-strain of nCB-UHPC specimens at different concentrations of nCB during cyclic compressive loading.

It is evident that for the mixes with an nCB content of no less than 1.0%, there is a precise synchronization of the FCR with the compressive stress and strain during the loading/unloading cycles. The FCR of the nCB-UHPC specimens decreased proportionally with the compressive stress-strain in the loading stages while corresponding in the unloading stages. This is due to the change of conductive paths in this process, as illustrated in **Figure 4.12**. The distance between the nCB particles was generally reduced with the compressive load, which led to the reconstruction of new conductive paths by the quantum tunnelling mechanism and decreased the resistivity; similarly, the distance between the nCB particles increased in the unloading stages, which led to an interruption to some of the conductive paths and thus increases in the resistivity.

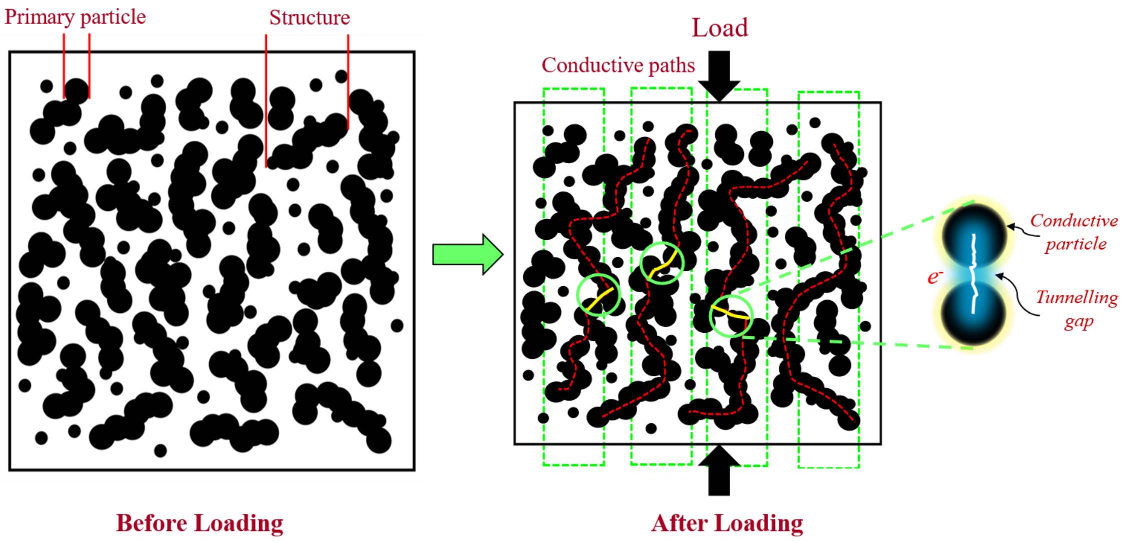

Figure 4.12. Schematic diagram of the conductive mechanism of nCB before and after application of external load.

According to tunnelling theory (Liu et al., 2022; Xiao et al., 2010), the tunnelling resistance exponentially correlates with the distance between adjacent conductive fillers (barrier width). The local tunnelling resistance (R) as a function of the distance between adjacent conductive fillers (d) can be expressed by equation 3.3 (Ding et al., 2019; Simmons, 1963):

In these figures, the peak values of FCR may be used to indicate the sensitivity of resistivity to stress-strain, so they are compared in **Figure 4.13** for all the mixes. It can be seen that the peak FCR value increases with the nCB content until it reaches 1.50% and then decreases afterwards. This is consistent with the observation of the gauge factor and demonstrates again that mix 1.50nCB-UHPC has the highest stress-strain sensitivity. This observation is also consistent with the relevant existing studies, which repeatedly show that the highest FCR generally occurs in the mixes within the percolation zone and that the FCR may then decrease with the content of conductive materials when stable and pre-established conductive networks already exist before loading (Han et al., 2015; Han et al., 2015; Sun et al., 2017; Zhang et al., 2018).

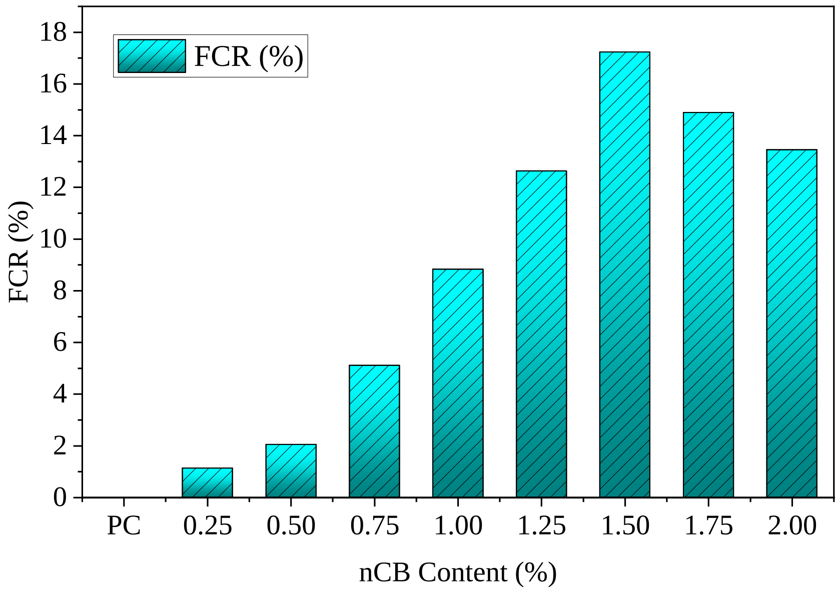

Figure 4.13. Peak FCR values of UHPC and nCB-UHPC specimens.

It can also be seen that the plain UHPC specimen did not exhibit any piezoresistive behaviour (**Figure 4.11**). For the specimens with a relatively low nCB content of 0.25-nCB and 0.50-nCB, the FCR varied with the stress-strain in the loading/unloading cycles. However, the synchronization of FCR with the stress-strain is not sufficiently clear. The FCR response is also noisy due to the lack of a stable conductive network by the nCB particles. It is not difficult to understand as the distance between nCB particles was relatively far from one another due to the relatively low content, making it relatively difficult to develop conductive paths during loading (Han et al., 2015).

4.4.3.3 Strain Sensitivity or Gauge Factor

Monotonic compression tests were conducted to evaluate the strain sensitivity of the system by resistivity to compressive strain (i.e., strain sensitivity) for all the mixes. The strain sensitivity is generally indicated by the so-called gauge factor (GF) (Amjadi et al., 2016), defined by equation 3.1. Fractional change in resistivity (FCR) is divided by compressive strain (ε).

Figure 4.14(a-i) shows the variation of FCR with compression strain for typical specimens in the nine mixes, respectively. It is evident that the plain concrete mix shows no strain sensitivity at all, with the FCR varying randomly with the strain **Figure 4.14**(a). By contrast, the FCR value appears to change almost linearly with the strain for all the mixes with nCB **Figure 4.14**(b-i). To evaluate the gauge factor of the mixes, a straight-line linear passing through the origin, which was obtained by a regression analysis of the test data, is plotted on each subfigure. By doing so, the slope of the straight line represents the average gauge factor of the specimen. The gauge factors of all the mixes that were obtained are summarized in **Figure 4.15**. It can be seen that the gauge factor increases with the nCB content until it reaches 1.5%, which is the upper limit of the percolation zone. The gauge factor of mix 1.50nCB-UHPC (i.e., 130.93) is over 12 times that of mix 0.25nCB-UHPC (i.e., 10.67). After that, a further increase of nCB content leads to a decrease in gauge factor, as evident from those of 1.75nCB-UHPC (i.e., 110.25) and 2.00nCB-UHPC (i.e., 96.15). This is expected as the conductive network by nCB is believed to have been well-established and relatively stable in these mixes before being loaded (Li et al., 2006). It is also worth noting that the gauge factor of 1.50nCB-UHPC (i.e., 130.93) is significantly higher strain sensitivity of UHPC self-sensing studies.

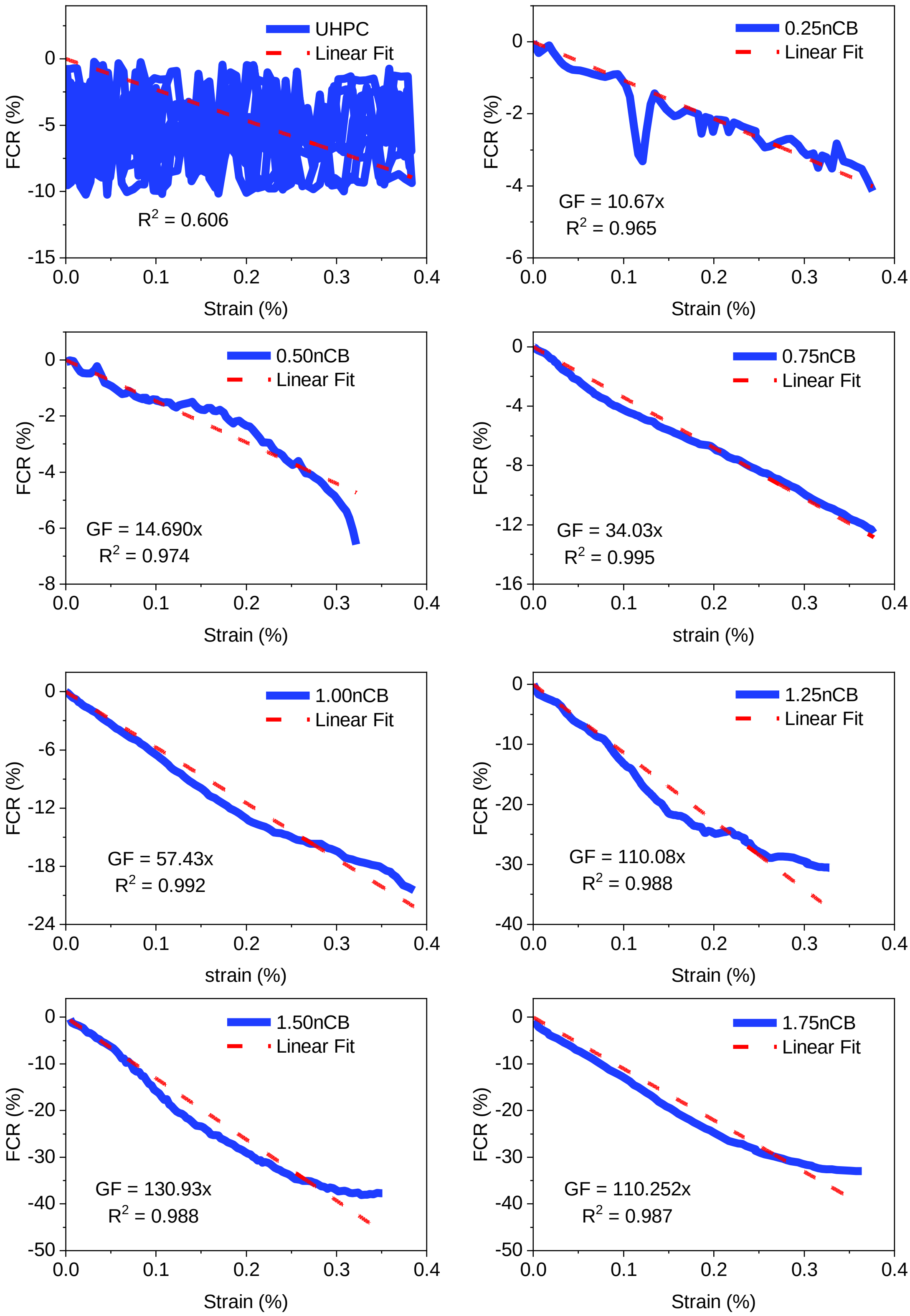
UHPC
Linear Fit
R2 = 0.606
FCR (%)
Strain (%)
0.25nCB
Linear Fit
GF = 10.67x
R2 = 0.965
0.50nCB
Linear Fit
GF = 14.690x
R2 = 0.974
0.75nCB
Linear Fit
GF = 34.03x
R2 = 0.995
strain (%)
1.00nCB
Linear Fit
GF = 57.43x
R2 = 0.992
1.25nCB
Linear Fit
GF = 110.08x
R2 = 0.988
1.50nCB
Linear Fit
GF = 130.93x
R2 = 0.988
1.75nCB
Linear Fit
GF = 110.252x
R2 = 0.987

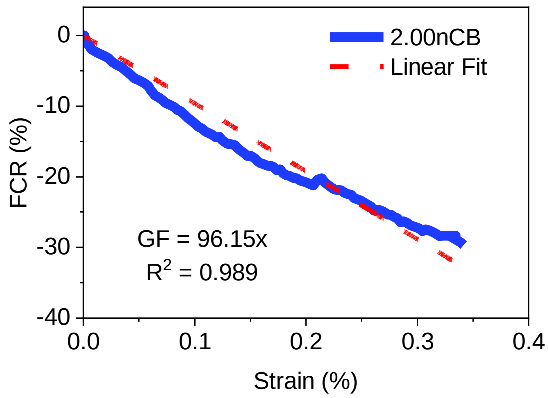

Figure 4.14. Experimental and fitting curves (FCR vs. strain) along with the gauge factor of nCB-UHPC specimens at different concentrations of nCB during monotonic compressive loading.

To further evaluate the correlation between the strain and FCR, the coefficient of determination of the fitting line in each subfigure was calculated; the R^2 value was shown to be not smaller than 0.97 for all the mixes with nCB, demonstrating an excellent linear relationship between the strain and FCR.

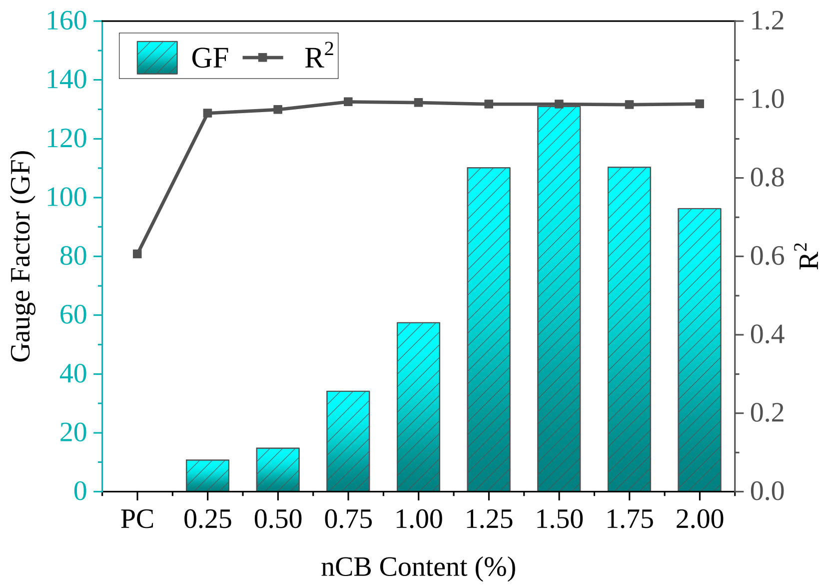

Figure 4.15. Gauge factors and R^2 values of nCB-UHPC specimens at different concentrations of nCB.

4.5 Summary and Conclusions

This chapter has presented a comprehensive experimental study on the development of UHPC with the strain-sensing capability by incorporating cost-effective chain-structured nCB (i.e., nCB-UHPC). The experimental program, including the formulation of new mix proportions, the preparation process, and the test methods, have been presented in detail, followed by the test results and discussions. The test results have shown that by incorporating nCB of a proper content (e.g., 1.0-1.5%), the resulting nCB-UHPC can have an ultra-high compressive strength (28-day compressive strength > 140 MPa), sufficiently good workability (slump spread ≥ 170 mm) and excellent strain-sensing capability (gauge factor >130) at the same time. The effects of the nCB content on various properties of nCB-UHPC have also been examined. The results and discussions presented in the chapter allow the following conclusions to be drawn:

1. The compressive strength of UHPC generally decreases with the nCB content. The strength of nCB-UHPC specimens subjected to 28-day normal water immersion curing is higher than their counterparts subjected to one-day heat curing at 90℃ ± 1℃, and the difference between the two increases with the nCB content.
2. The percolation zone of nCB in a UHPC matrix was found to be between 0.50-1.50%, which is significantly lower than those from the previous studies on normal-strength cement paste/mortar/concrete incorporating nCB.
3. The strain sensitivity of nCB-UHPC, as demonstrated by both monotonic and cyclic compression tests, increases with the nCB content until it reaches the upper limit of the percolation zone (i.e., 1.50%), after which it starts to decrease. The highest gauge factor of the nCB-UHPC, which indicates its strain sensitivity, is >130. This value is several times higher than those of conventional strain gauges.

4. For the nCB-UHPC with a proper nCB content (i.e., ≥1.0%), the resistivity is precisely synchronised with the compressive stress-strain during the loading/unloading cycles with a stress amplitude of 40 MPa.
5. The density of the nCB-UHPC samples decreased up to 2045.6 kg/m3, which could be one of the biggest advantages along with sensing capability. The combination of lightweight properties and the built-in sensing capabilities of nCB-UHPC makes it an ideal choice for construction projects demanding both reduced structural loads and real-time monitoring of the concrete's condition and surrounding environment.

With their excellent properties summarized above, it is evident that the nCB-UHPC developed in this study has great potential for practical applications serving as both a structural material and a health monitoring measure. The low percolation zone of nCB in the developed UHPC leads to reduced material costs. It is incredibly beneficial for ease of implementation, while its high strain sensitivity is an essential advantage for strain-sensing purposes. With the dense microstructure of UHPC, the newly developed smart material can be expected to have excellent durability.

Nevertheless, for the field applications and long-term serviceability of this work, the effects of moisture content, harmful ions ingression, and other environmental factors on the piezoresistive behaviour of nCB-UHPC needs to be investigated. In particular, the development of a relationship between the moisture content and the resistivity and gauge factor of nCB-UHPC would contribute to this study for field applications, where moisture sensors can monitor the moisture content. The effects of moisture content and sea-salt solution exposure were studied by a comprehensive experimental programme which is presented in the next chapter.

Chapter 5.

Effects of Moisture Content and Sea-Salt Solution Exposure on Nanocarbon Black-Based Ultrahigh-Performance Concrete

5.1 Abstract

Self strain-sensing capability of UHPC is introduced by the authors by employing cost-effective nanocarbon black (nCB-UHPC). Since it is known that the strain sensing performance of smart cementitious composites may be affected by various environmental factors and that the mechanical properties of UHPC depend significantly on curing condition and may deteriorate under environmental exposure, this paper presents a recent study aiming to investigate the properties of the new nCB-UHPC under different curing and working conditions.

The test results indicate that the mechanical properties of the nCB-UHPC can be improved by prolonged curing duration, and also by dry curing at 105 ℃ due to the accelerated hydration activity at an elevated temperature. However, exposure to sea-salt solution is shown to decrease the mechanical properties due to the formation of cracks by secondary hydration products. On the other hand, the fractional change in resistivity of the nCB-UHPC exhibits a distinct synchronization to the applied compressive stress. Nonetheless, the strain sensitivity decreases with an increase of moisture content due to increasing contact resistance between nCB particles. Furthermore, exposure to the sea-salt solution increases the strain sensitivity of fully saturated nCB-UHPC specimens, thanks to

the high mobility of the dissolved ions from the saline solution – an important finding in the context of marine construction. This study lays a foundation for the large-scale implementation of the nCB-UHPC as a field-deployable solution for monitoring the condition of concrete structures.

5.2 Introduction

Introducing an intrinsic self-sensing capability to UHPC could revolutionize the construction industry by providing a cost-effective real-time structural health monitoring solution. Interestingly, our previous study has successfully developed a UHPC possessing strain-sensing functionality through the integration of low-cost nCB (Hussain et al., 2022). It shows a very low percolation threshold that helped to decrease the overall cost, reasonable mechanical properties and stable piezoresistive behaviour. Despite the advanced characteristics of UHPC, various working environments affect the self-sensing performance of cementitious smart materials during their service life, which may limit their large-scale application in concrete structures (Demircilioğlu et al., 2019; Dong et al., 2019; Han et al., 2010; Le et al., 2021; Wen & Chung, 2008). Many studies have explored various environmental conditions, demonstrating that moisture content and harmful ions not only impact the durability of cementitious composites but also directly influence their sensitivity. Thus, investigating the strain sensitivity of SCC with different moisture contents would give a better understanding of the material. Furthermore, different aspects such as water absorption, different curing conditions and long-term exposure to aggressive environments are essential factors to consider for the field applications of SCC (Ahlborn et al., 2011; Li et al., 2020). Therefore, this study aims to investigate the properties of nCB-based self-sensing UHPC (referred to as nCB-UHPC hereafter) under different curing and working conditions. This study focuses on the UHPC with 1.50% of nCB content, which demonstrated the highest sensitivity in the previous work (Chapter 4). The mechanical and microstructural properties of the nCB-UHPC under different curing conditions and long-term exposure to high-salinity sea-salt solution for up to 180 days were investigated.

5.3 Experimental Program

5.3.1 Mix Design and Raw Materials

This study uses similar raw materials used in section 4.2.1. Detailed information regarding the mixture design and the quantities of each material can be found in **Table 5.1**. The mixes have a water-to-binder ratio of 0.19, a superplasticizer content of 5% cement, and a nCB content of 1.5% binder. **Figure 5.1** (a) describes the TEM image of the nCB and (b) describes the X-ray diffraction (XRD) patterns of the nCB and SF, illustrating the amorphous nature of the two materials.

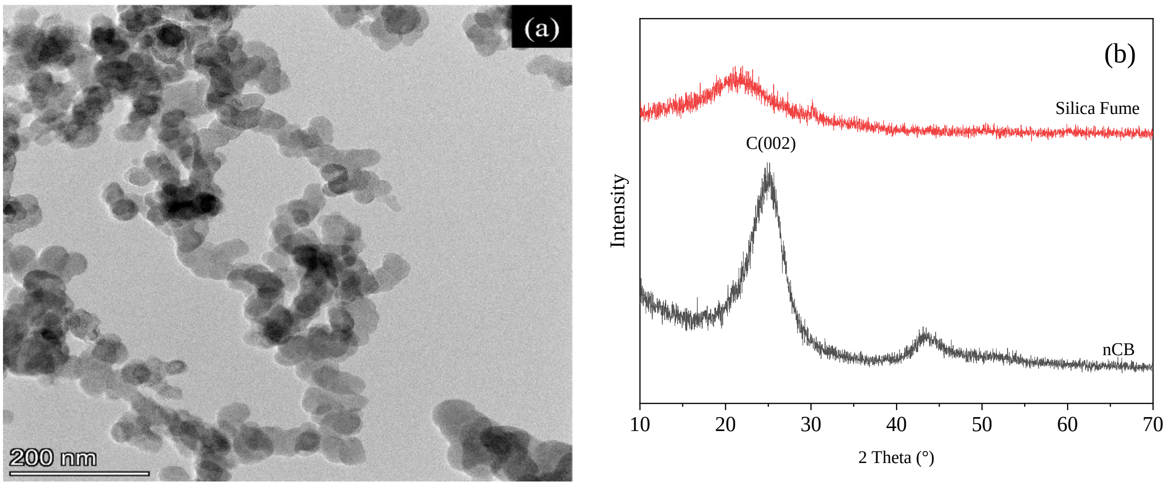

Figure 5.1. TEM micrographs of nCB particles and XRD patterns of SF and nCB.

Table 5.1. Mix design of nCB-UHPC (kg/m^3).

Notation	Cement	SF	QP	Sand	Water*	SP	nCB
UHPC	840.0	210.0	210.0	924.0	169.0	42.0	0.0

1.50nCB-UHPC	840.0	210.0	90.0	781.5	169.0	42.0	15.75

The water-to-binder ratio is 0.19, including 0.78% water of superplasticizer.

5.3.2 Sorptivity Test

The water sorptivity of UHPC and 1.50nCB-UHPC was assessed to evaluate their resistance to water infiltration. Cylindrical specimens (Φ100 mm × 50 mm) were used to perform the measurements in accordance with ASTM C1585-20 (ASTM, 2020). The specimens were oven-dried for 72 hours at 80 ± 2 °C (Han et al., 2013; Hussain et al., 2022; Hussain et al., 2023) and then placed in an environmental chamber at of 50 ± 2 °C and 80 ± 3% relative humidity for 3 days. Afterwards, the specimens were placed into a sealable container at 23 ± 2 °C for 15 days before tested. Epoxy resin was used to seal the side surface of each specimen. The samples were put on a supporting device in a testing setup as seen in **Figure 5.2**. The water uptake was measured as a function of time. The measurements were taken for up to 49 days because the specimens had a dense microstructure and a slow water absorption rate (Lu et al., 2021). The average test results were obtained from at least three specimens. The amount of water absorbed by a specimen per unit area (*I*) is measured by

$$I = \frac{m_t}{a/d} \tag{5.1}$$

I = the absorption,

m_t = the change in specimen mass in grams at the time t,

a = the exposed area of the specimen, in mm2, and

d = the density of the water in g/mm3.

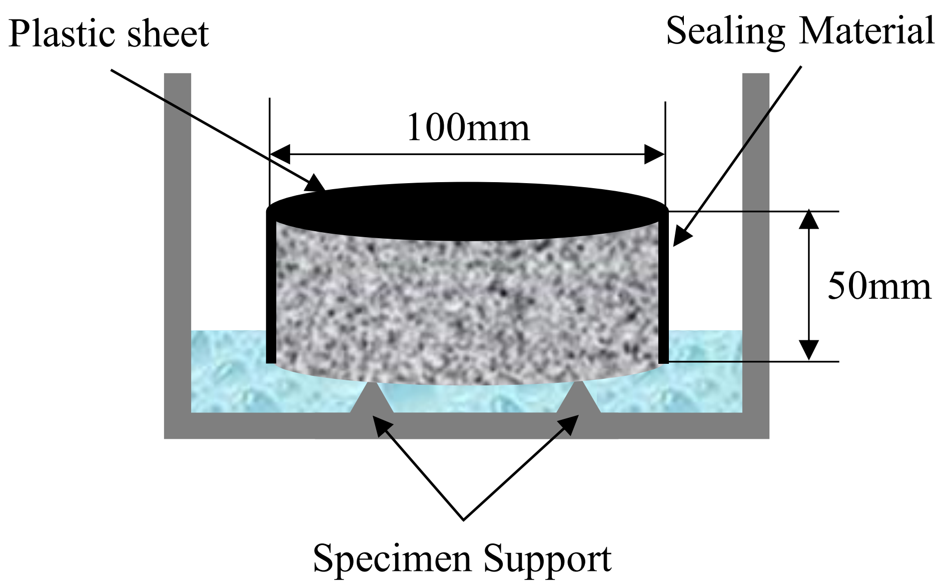

Figure 5.2. Sorptivity testing setup of UHPC and nCB-UHPC specimens.

5.3.3 Moisture Content Test

Moisture content (*w*) was calculated as the mass of water contained in the sample (*m*) per mass of its 105 °C oven-dried states (m_d) (Wu et al., 2017), expressed as a percentage:

$$w = \frac{m - m_d}{m_d} \times 100\% \tag{5.2}$$

w = moisture content,

m = mass of water

m_d *= mass of its 105 °C oven-dried state*

5.3.4 Curing Conditions

After demoulding the specimens, different curing conditions and durations were studied for compressive strength. The curing conditions are 28 days of water immersion curing, 90 days of air curing at 22°C ± 3°C and dry cured at 105°C ± 5°C for one day (after 90 days of air curing).

The remaining testing details for compressive strength are given in section 4.2.5.

5.3.5 Sea-salt Solution Exposure

Two sets of samples were put in a sea-salt solution with a 16.5% salinity (165 *g/l*, normal seawater 35 *g/l*) for 90 days and 180 days to investigate the mechanical and microstructure of the plain UHPC and 1.50nCB-UHPC samples.

5.3.6 Microstructure Analysis

5.3.6.1 X-ray Diffraction

An X-ray diffractometer (Rigaku SmartLab, Japan) equipped with a 9-kW rotating anode X-ray source (λ: ~1.54 Å) under Bragg-Brentano mode was used for analysis. Powder samples obtained by grinding dried concrete were scanned using a semiconductor detector (Rigaku HyPix-3000, Japan) at a 5°/min speed and a 0.01° step size over a 5° to 70° range.

5.3.6.2 Scanning Electron Microscopy and Energy-dispersive X-ray Spectroscopy

The micro-morphology of nCB-UHPSSC was examined using a high-resolution scanning electron microscope (TESCAN VEGA3, Czech Republic) equipped with energy-dispersive x-ray spectroscopy. Samples were taken from the inner cores of specimens, dried out, and then coated with gold before testing. For backscattered electron observation, epoxy-filled samples were polished using sandpapers with various degrees of fineness (180 grit, 9.0 μm, 3.0 μm and 0.05 μm). Subsequently, the samples were cleaned with ethanol in an ultrasonic bath for 5 minutes to eliminate any residual suspensions. Afterwards, the samples were dried out, and then coated with gold before testing (Lu et al., 2021).

5.3.6.3 Mercury Intrusion Porosimeter

A mercury intrusion porosimeter (MicroActive AutoPore V 9600, USA) was adopted to analyze the porosity and pore size distribution. The samples were smaller than 5 mm in particle size and were collected from crushed specimens following compression tests. The smallest pore size that can be detected is 3 nm.

5.3.6.4 X-ray Microtomography

The microporosity and 3D structures of plain UHPC and 1.50nCB-UHPC were characterized using a micro-CT scanner (Bruker SKYSCAN 1276, USA). 10 mm cubic shape samples were employed. During initial observation, the current and voltage of the X-ray tube were kept at 200A and 100 kV, respectively. Micro-CT scanning was performed at 8 μm resolution to examine the distribution of pores. The size of the reconstructed images was chosen to be 2.5 mm × 2.5 mm × 2.5 mm (Ahmad et al., 2023).

5.3.7 Effect of Moisture Content on Piezoresistivity

The piezoresistive behaviour of the 1.50nCB-UHPC was examined with different moisture levels, ranging from fully dried to fully saturated, including 10%, 20%, 50%, 80%, and 100% moisture content. Initially, the mass of the dried samples was recorded, after which each sample was immersed in water, and the wet mass was measured for each saturation level. It is further explored to establish a relationship between the moisture content and the piezoresistive behaviour. The samples were loaded by displacement control with a loading rate of 0.6 mm/min, and four cycles of repeated compressive loading were applied with a stress amplitude of 38 MPa. The compressive strain was measured by the strain gauges attached to two opposite sides of the sample. The specimens were subjected to cyclic compressive loading using a universal testing machine (Instron 5982, Instron Inc., USA). The resistivities were measured with a digital multimeter (DMM6500 Keithley Instruments Inc., USA). The detailed circuit diagram is plotted in **Figure 3.3**.

5.3.8 Effect of Sea-salt Solution Exposure on Piezoresistivity

The 1.50nCB-UHPC samples are further explored for piezoresistive behaviour after exposure to a high salinity sea-salt solution for the duration of 90 and 180 days. The samples are tested for repeatability (cyclic loading response) and sensitivity (monotonic loading response) at saturated and dry states.

The remaining details are given in section 4.2.6.

5.4 Results and Discussions

5.4.1 Sorptivity Test

The sorptivity of both plain UHPC and 1.50nCB-UHPC was determined following ASTM C 1585-20 (C1585-20, 2020) (see Supplementary Information for the test method). Three cylindrical specimens (Φ100 mm × 50 mm) were employed to obtain the average value. The absorption process involved two phases: initial absorption and secondary absorption. For normal-strength concrete, the initial absorption typically occurs from 0 to 6 hours, while the secondary absorption typically runs from 1 to 8 days. However, Ref. (Lu et al., 2021) extended the secondary absorption phase to 49 days due to the highly dense microstructure and low absorption rate of UHPC. The water absorption rate of a specimen is defined as the slope of the amount of water absorbed per unit area plotted against the square root of time. The water absorption rate of unsaturated concrete indicates its capacity to absorb and transport water, which directly affects its durability. A low sorptivity is a strong indication of excellent durability. The amounts of water absorbed per unit area by plain UHPC and 1.50nCB-UHPC, as well as the total amounts of water absorbed, are presented in **Figure 5.3**. The water absorption rates in the initial and secondary phases are obtained by the least-square linear regression method, with R^2>0.98 (C1585-20, 2020).

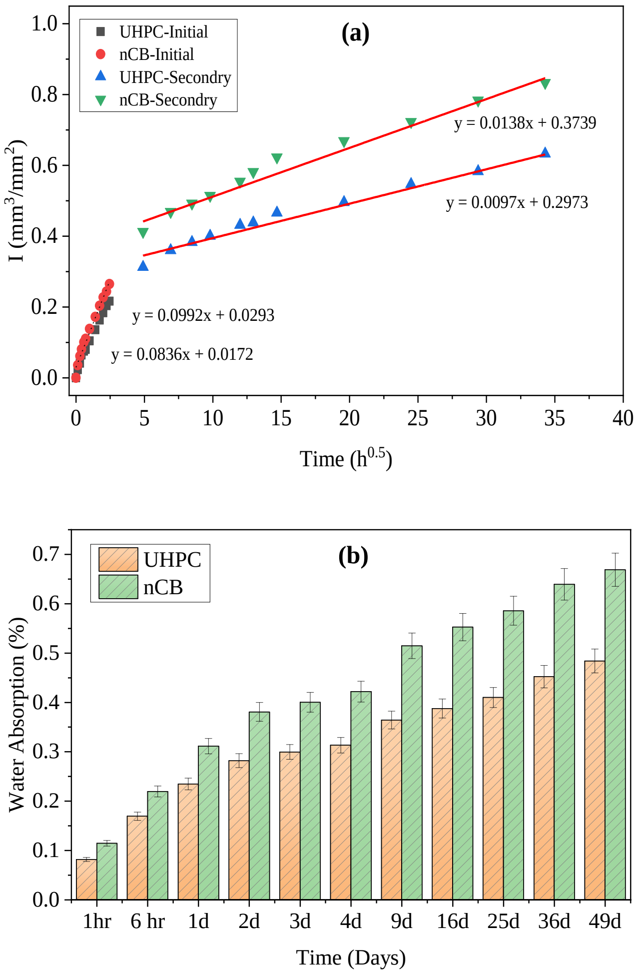

Figure 5.3. Sorptivity of plain UHPC and 1.50nCB-UHPC. (a) The amounts of water absorbed per unit area in the initial and secondary phases. (b) The total amount of water absorbed.

In the initial phase, the water uptake of plain UHPC and 1.50nCB-UHPC was fast, with the maximum water absorption rates being 0.0836 mm/$h^{0.5}$ and 0.0992 mm/$h^{0.5}$ after 6 hours, respectively; 1.50nCB-UHPC exhibits 15.73% higher sorptivity than plain UHPC. After 49 days of testing, the water absorption rates of plain UHPC and 1.50nCB-UHPC became 0.0097 mm/$h^{0.5}$ and 0.0138 mm/$h^{0.5}$, respectively; the water absorption rate of plain UHPC is 29.71% lower than that of 1.50nCB-UHPC during the secondary absorption phase. The results indicate that 1.50nCB-UHPC has higher sorptivity than plain UHPC in both the initial and secondary absorption phases, while the sorptivity of either UHPC mix is much lower than that of normal-strength concrete. According to the RILEM Technical Committee for Performance-Based Specifications and Control of Concrete Durability (RILEM TC 230-PSC), concrete with sorptivity lower than 6 mm/$h^{0.5}$ after 28 days is considered to be of excellent quality (Beushausen & Luco, 2016). The amounts of water absorbed by plain UHPC and 1.50nCB-UHPC after 49 days were 0.484% and 0.669%, respectively, merely 8-12% of what is observed in normal-strength concrete after 9 days (Lu et al., 2022).

It is well known that water transport is largely controlled by capillary suction, and low sorptivity corresponds to dense microstructure and low capillary porosity. Although the total amount of water absorbed by 1.50nCB-UHPC is 27.67% higher than that by plain UHPC, it is still much lower than that by normal-strength concrete. Nonetheless, the reasons behind the higher sorptivity of 1.50nCB-UHPC are: (1) the increased porosity due the agglomeration of nCB particles, as observed in the authors' previous study (Hussain et al., 2022; Hussain et al., 2023); (2) nCB particles absorbing a significant amount of water due to their high surface area, which reduces the flowability of the matrix, in turn negatively affecting the compaction of the matrix and leading to a more porous microstructure.

5.4.2 Effect of Curing Conditions on Mechanical Properties

Following ASTM C109/C109M-21 (C109/C109M-21, 2021), 50 mm cubic specimens were prepared for compressive strength test. After demoulding, the specimens were subjected to various curing systems, which include: 28 days of water immersion curing, 90 days of air curing at 22 ℃ ± 3 ℃ after 28 days of water immersion curing, and one day of oven-dry curing at 105 ℃ ± 5 ℃ after 90 days of air curing. For each curing system, three specimens were tested to obtain an average value. The compressive loading rate is 1 MPa/s.

Figure 5.4(a) shows that after 28 days of water immersion curing, plain UHPC and 1.50nCB-UHPC had compressive strengths of 160.5 MPa and 138.5 MPa, respectively. After another 90 days of air curing, the compressive strengths of plain UHPC and 1.50nCB-UHPC increased by 0.91% and 5.86%, respectively. Further oven-dry curing at 105 °C for 24 hours had increased the strength of plain UHPC and 1.50nCB-UHPC by 8.35% and 14.70%, respectively. The improvement of the compressive strengths of the dried specimens is attributed to the pozzolanic reaction, which produced additional calcium silicate hydrate (CSH) by utilizing calcium hydroxide ($Ca(OH)_2$.

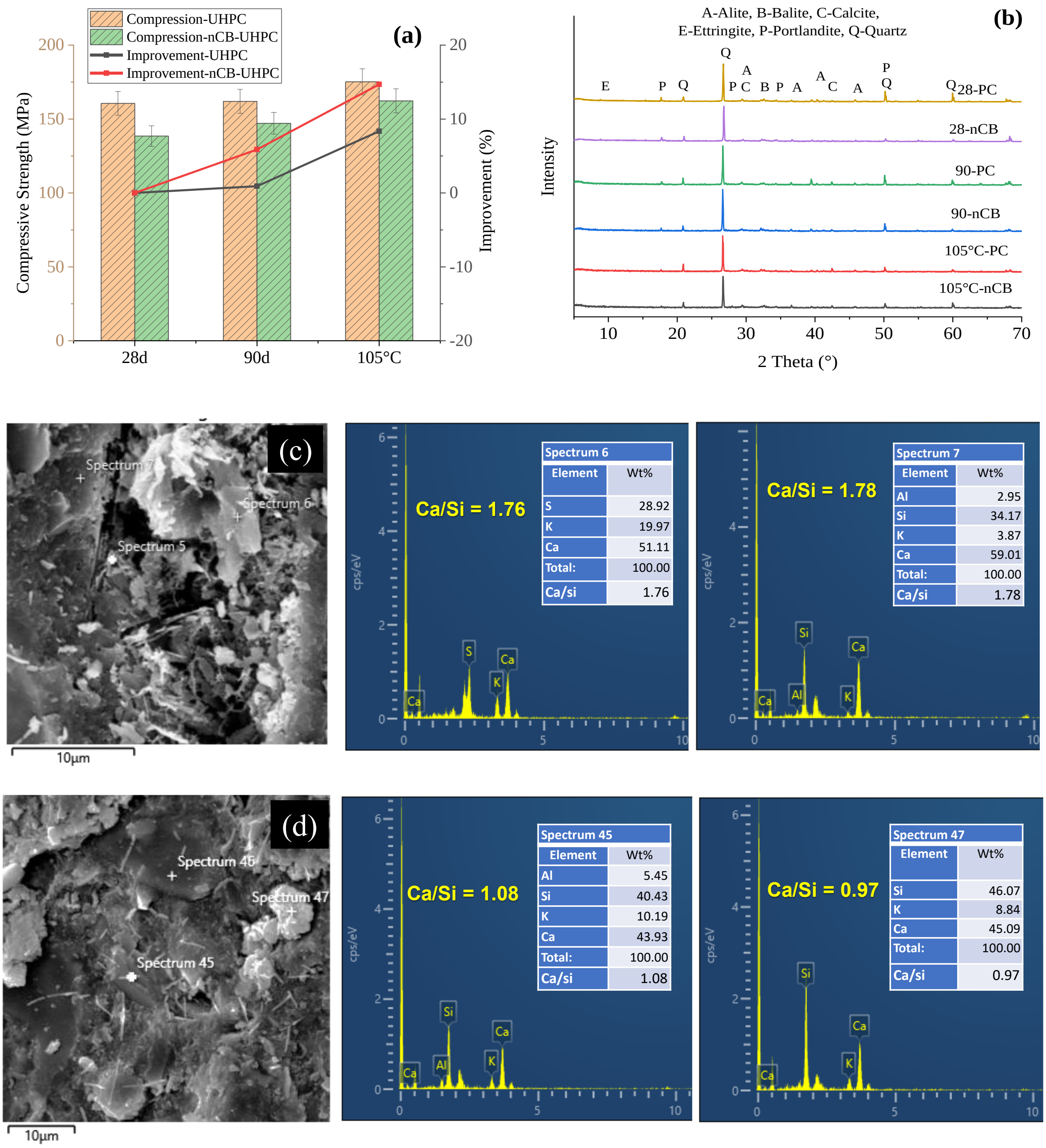
(a)
Compression-UHPC
Compression-nCB-UHPC
Improvement-UHPC
Improvement-nCB-UHPC
Compressive Strength (MPa)
Improvement (%)
0
50
100
150
200
-20
-10
0
10
20
28d
90d
105°C
(b)
A-Alite, B-Balite, C-Calcite,
E-Ettringite, P-Portlandite, Q-Quartz
Intensity
28-PC
28-nCB
90-PC
90-nCB
105°C-PC
105°C-nCB
10
20
30
40
50
60
70
2 Theta (°)
(c)
Spectrum 7
Spectrum 6
Spectrum 5
10µm
Ca/Si = 1.76
Spectrum 6
Element Wt%
S 28.92
K 19.97
Ca 51.11
Total: 100.00
Ca/si 1.76
Ca/Si = 1.78
Spectrum 7
Element Wt%
Al 2.95
Si 34.17
K 3.87
Ca 59.01
Total: 100.00
Ca/si 1.78
cps/eV
(d)
Spectrum 46
Spectrum 47
Spectrum 45
10µm
Ca/Si = 1.08
Spectrum 45
Element Wt%
Al 5.45
Si 40.43
K 10.19
Ca 43.93
Total: 100.00
Ca/si 1.08
Ca/Si = 0.97
Spectrum 47
Element Wt%
Si 46.07
K 8.84
Ca 45.09
Total: 100.00
Ca/si 0.97

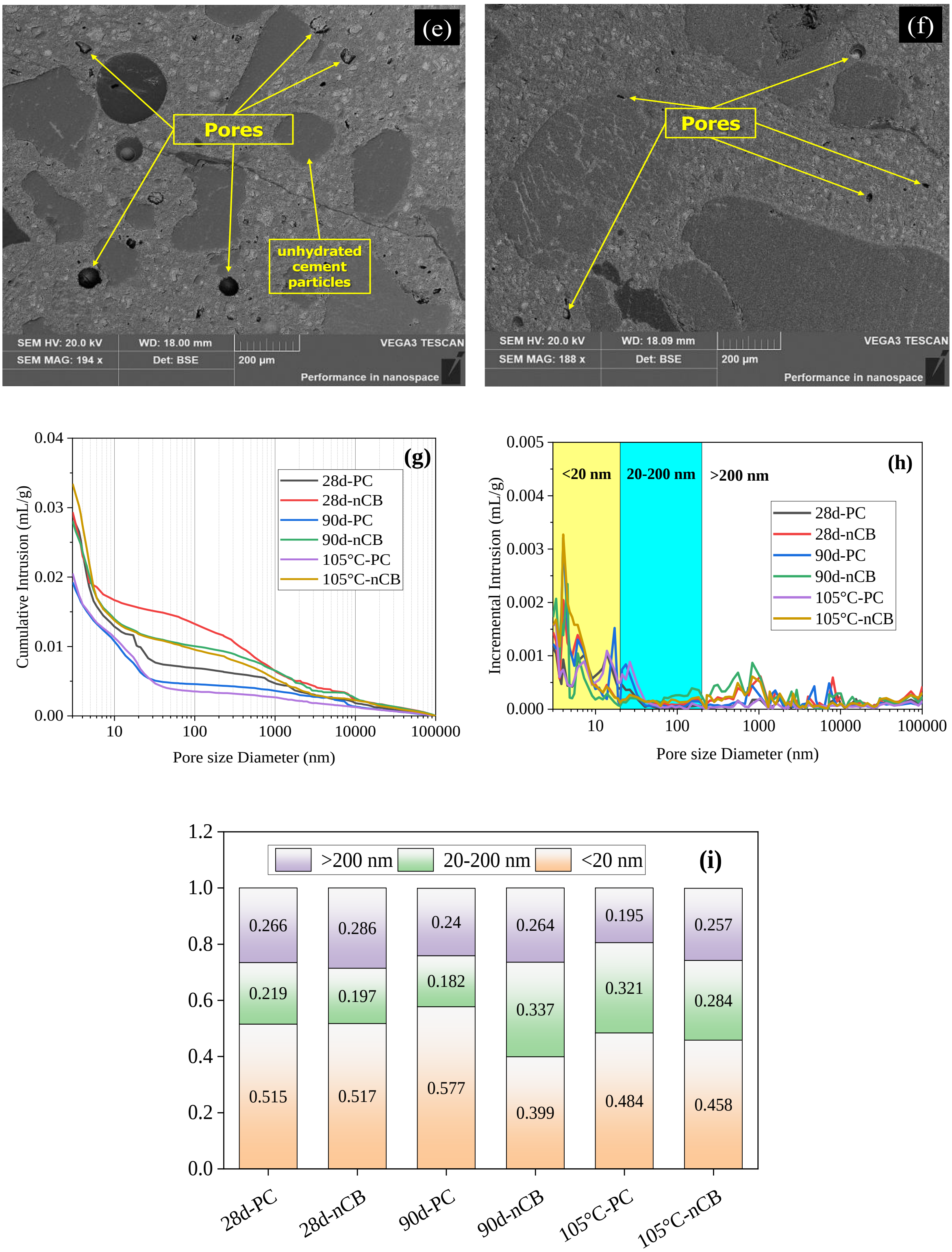
(e)
Pores
unhydrated cement particles
SEM HV: 20.0 kV
WD: 18.00 mm
VEGA3 TESCAN
SEM MAG: 194 x
Det: BSE
200 μm
Performance in nanospace
(f)
Pores
SEM HV: 20.0 kV
WD: 18.09 mm
VEGA3 TESCAN
SEM MAG: 188 x
Det: BSE
200 μm
Performance in nanospace
(g)
Cumulative Intrusion (mL/g)
Pore size Diameter (nm)
28d-PC
28d-nCB
90d-PC
90d-nCB
105°C-PC
105°C-nCB
(h)
Incremental Intrusion (mL/g)
Pore size Diameter (nm)
<20 nm
20-200 nm
>200 nm
28d-PC
28d-nCB
90d-PC
90d-nCB
105°C-PC
105°C-nCB
(i)
>200 nm
20-200 nm
<20 nm
28d-PC: 0.266, 0.219, 0.515
28d-nCB: 0.286, 0.197, 0.517
90d-PC: 0.24, 0.182, 0.577
90d-nCB: 0.264, 0.337, 0.399
105°C-PC: 0.195, 0.321, 0.484
105°C-nCB: 0.257, 0.284, 0.458

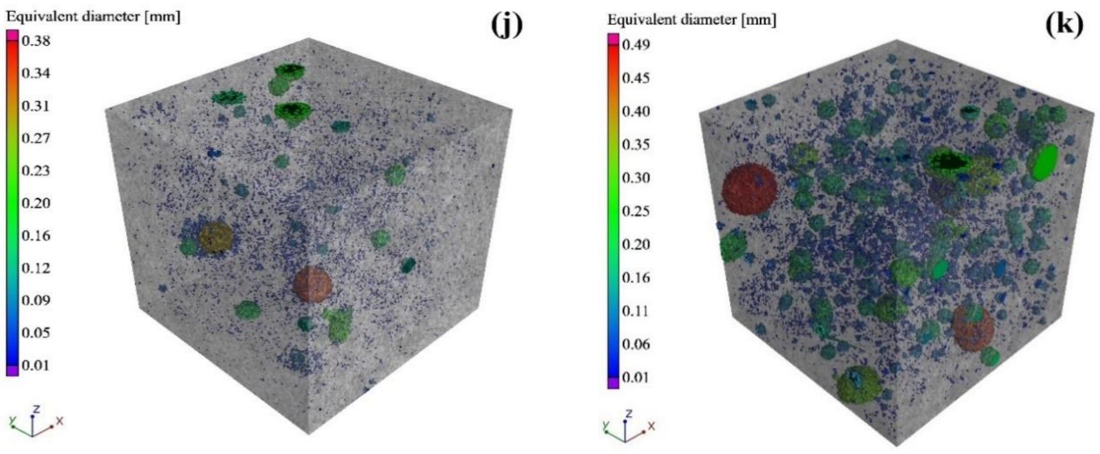

Figure 5.4. Mechanical properties and microstructures of plain UHPC and 1.50nCB-UHPC cured under different systems. (a) Compressive strengths. (b) XRD patterns. (c-d) SEM images of plain UHPC cured for 90 days in air (c) and oven-dry cured for 24 hours at 105 °C (d). (e-f) BSE images showing unhydrated cement clinkers and porosity in plain UHPC cured for 90 days in air (e) and oven-dry cured for 24 hours at 105 °C (f). (g-i) Cumulative pore structures, incremental pore structure and pore size distribution ratios. (j-k) X-ray microtomography results of plain UHPC (j) and nCB-UHPC (k) cured for 90 days in air.

The improved compressive strength can be explained through **Figure 5.4**(b), which shows the XRD patterns obtained under different curing systems (see Supplementary Information of the test method). The addition of nCB in a mix did not result in the formation of any new chemical phases, as observed from the peaks of specimens with and without nCB. It is known that nCB is an inert nanomaterial and does not undergo any chemical reactions with cementitious materials (Li et al., 2024; Zhang et al., 2022). The specimens cured under 28 days of water immersion possessed portlandite and ettringite, but no considerable secondary reaction was observed. The peaks of unhydrated cement clinkers, such as alite and belite, can be detected, which may be due to the extremely low water-to-cement ratio of the UHPC matrix (Lu et al., 2021). The presence of calcite, a carbonate phase, is likely attributed to carbonation during specimen preparation (Fehervari et al., 2020; Zhang et al., 2022). With another 90 days of air curing, the intensities of the ettringite and portlandite peaks weakened due to the acceleration of the pozzolanic reaction. Additional oven-dry curing at 105°C for 24 hours further lowered the ettringite and portlandite peaks, since $Ca(OH)_2$ was consumed to form more CSH (Shen et al., 2019).

QP with finely ground particles may have pozzolanic reactivity depending on the particle size. Otherwise, it would only offer filler effect. There is no agreement on the critical size required for quartz to have pozzolanic reactivity (Khan et al., 2021; Qing et al., 2006; Seo et al., 2022; Tavares et al., 2020). However, Benezet and Benhassaine (Benezet & Benhassaine, 1999) determined using the Chapelle test that quartz particles with a diameter smaller than 5 μm have pozzolanic reactivity, providing fine silicate surfaces to react with portlandite to form additional CSH. It can further be explained through **Figure 5.4**(c-d), which shows the SEM-EDX micrographs of plain UPHC cured under different systems (see Supplementary Information of the test method), that the calcium to silicon (Ca/Si) ratio of hydrates decreased with increasing curing duration and temperature, as reported in Ref. (Yazıcı et al., 2013). The Ca/Si ratio of the specimen cured in air for 90 days was 1.78. After being exposed to an elevated temperature, the ratio decreased to 0.97. This observation suggests that some silicates from QP had taken part in secondary hydration during oven-dry curing. Furthermore, it explains why the oven-dry cured specimen had a high compressive strength without further adding a source of silica.

The backscattered electron (BSE) images in **Figure 5.4**(e-f) (see Supplementary Information of the test method) show that the quantities of unhydrated cement particles in plain UHPC decreased as curing extended from 90 days of air curing to an additional 24 hours of oven-dry curing at 105°C. These images also indicate that the fineness of pores increased during this process, meaning that the equivalent diameter of pores decreased. Previous research has reported that, after 36 years, normal concrete can still contain up to 25%

unhydrated cement clinker (He et al., 2022). This unhydrated cement content could be even higher in UHPC due to its low water-to-cement ratio (Du et al., 2021). The elevated temperature helps to accelerate the cement hydration in UHPC and also promotes the secondary hydration reactions between portlandite ($Ca(OH)_2$) and SF, as well as fine silicates from QP, leading to the formation of additional CSH (Abdulkareem et al., 2021; Benezet & Benhassaine, 1999; Khan et al., 2021; Yazıcı et al., 2013). QP would typically be non-reactive during standard curing at lower temperatures. The elevated temperature, therefore, helps to facilitate and speed up these beneficial hydration processes in UHPC.

It can be observed that 1.50nCB-UHPC generally had a lower compressive strength than plain UHPC. Previous investigations have shown that nCB particles absorb free water, which decreases the flowability and compaction of the UHPC matrix, resulting in higher porosity and reduced compressive strength (Hussain et al., 2022). Additionally, the strong van der Waal force between nCB particles leads to the formation of large aggregate size and agglomeration of nCB particles, which create stress concentration points in concrete and make it less resistant to applied forces, as compared to CSH products (Dong et al., 2019). Moreover, nCB particles, which have high surface energy, surround cement particles, in turn delaying the hydration process is delayed by obstructing the water molecule from reacting with unhydrated cement (Hussain et al., 2022). However, despite the initial reduction in compressive strength as compared to plain UHPC, 1.50nCB-UHPC showed greater improvement in compressive strength than plain UHPC with continuing air curing and further heat curing, during which the hydration process of unhydrated cement particles occurred.

The porosity and pore size distribution of the matrix are investigated by MIP (see Supplementary Information of the test method). The cumulative pores, incremental pores, and pore size distribution ratios of plain UHPC and 1.50nCB-UHPC are presented in **Figure**

5.4(g-i). **Figure 5.4**(g) shows that the maximum porosity of plain UHPC and 1.50nCB-UHPC after 28 days of water immersion curing was 6.28% and 7.09%, respectively. Moreover, the 90-day air curing and 24-hour oven-dry curing at 105 °C reduced the porosity by up to 44% as compared to the situation after 28 days. Dry curing at high temperatures is beneficial for microstructure densification as it amplifies the pozzolanic reactivity, which helps to produce more CSH (Lu et al., 2022). Furthermore, the pore size distributions are illustrated in **Figure 5.4**(h), where the pores are divided into harmful (>200 nm), less harmful pores (20-200 nm) and harmless (<20 nm) (Ali et al., 2023; Li, 2021; Wang et al., 2018). The harmful pores are primarily responsible for the reduction in the strength and durability of materials. It can be observed from **Figure 5.4**(i) that the harmful pores of 1.50nCB-UHPC had a 12.89% higher concentration than plain UHPC at 28 days of water immersion curing, which was subsequently reduced by the prolonged air curing and elevated curing temperature.

X-ray microtomography was used as an additional technique to investigate the porosity and obtain the complete 3D microstructures of the cementitious materials (see Supplementary Information of the test method). In this study, the plain UHPC specimen and 1.50nCB-UHPC specimen selected for the test were cured in air for 90 days. The results are presented in **Figure 5.4**(j-k). It is important to note that X-ray microtomography is primarily used to detect macropores and mesopores in specimens, while nanopores are challenging to observe using this technique (Zhang et al., 2022). The analysis shows that the plain UHPC specimen had a cumulative porosity of 0.68%, with the pore size ranging between 10 and 380 microns, as indicated by the scale showing the equivalent pore diameters. In contrast, the 1.50nCB-UHPC specimen had a higher porosity of 3.10%, and the pore size ranged from 10 to 490 microns. This indicates that the 1.50nCB-UHPC had a higher percentage of pores, and its pores were also larger in diameter than the plain UHPC specimen. This is likely due to nCB particles increasing the overall porosity and pore size in the 1.50nCB-UHPC specimen. The X-ray microtomography results cover the range of 10 to 500 microns, while the MIP results cover up to 100 microns. Therefore, the combined use of the two sets of results could provide the total porosity of the material.

5.4.3 Effect of Sea-salt Solution Exposure on Mechanical Properties

Plain UHPC and 1.50nCB-UHPC specimens cured for 28 days in water were immersed in sea-salt solution with a 16.5% salinity (salinity of normal seawater: 3.5%) for 90 days and 180 days of accelerated exposure. The mechanical and durability properties of the specimens were investigated. The results show that the compressive strengths of both plain UHPC and 1.50nCB-UHPC decreased after the sea-salt solution exposure, as seen in **Figure 5.5**(a). Compared to the 28-day strengths, the compressive strength reductions for plain UHPC and 1.50nCB-UHPC, after 90 days of exposure, were about 13.31% and 10.24%, respectively; the compressive strength reductions after 180 days of exposure were 18.64% for plain UHPC and 14.79% for 1.50nCB-UHPC. The reasons for these compressive strength reductions were explored further through the analysis of the XRD patterns shown in **Figure 5.5**(b). The reductions are attributed to secondary ettringite formation, also known as delayed ettringite formation (DEF) (Taylor et al., 2001), as it has been shown by the XRD peaks and the SEM micrographs in **Figure 5.5**(c-d). The formation of DEF can induce volumetric expansion and create microcracks within the cementitious matrix, leading to a decrease in the overall mechanical strength of the materials. Comparing the specimens with and without nCB, no secondary hydration products were detected in either case due to the inert nature of the carbon nanoparticles (Han et al., 2017; Li et al., 2024; Zhang et al., 2022).

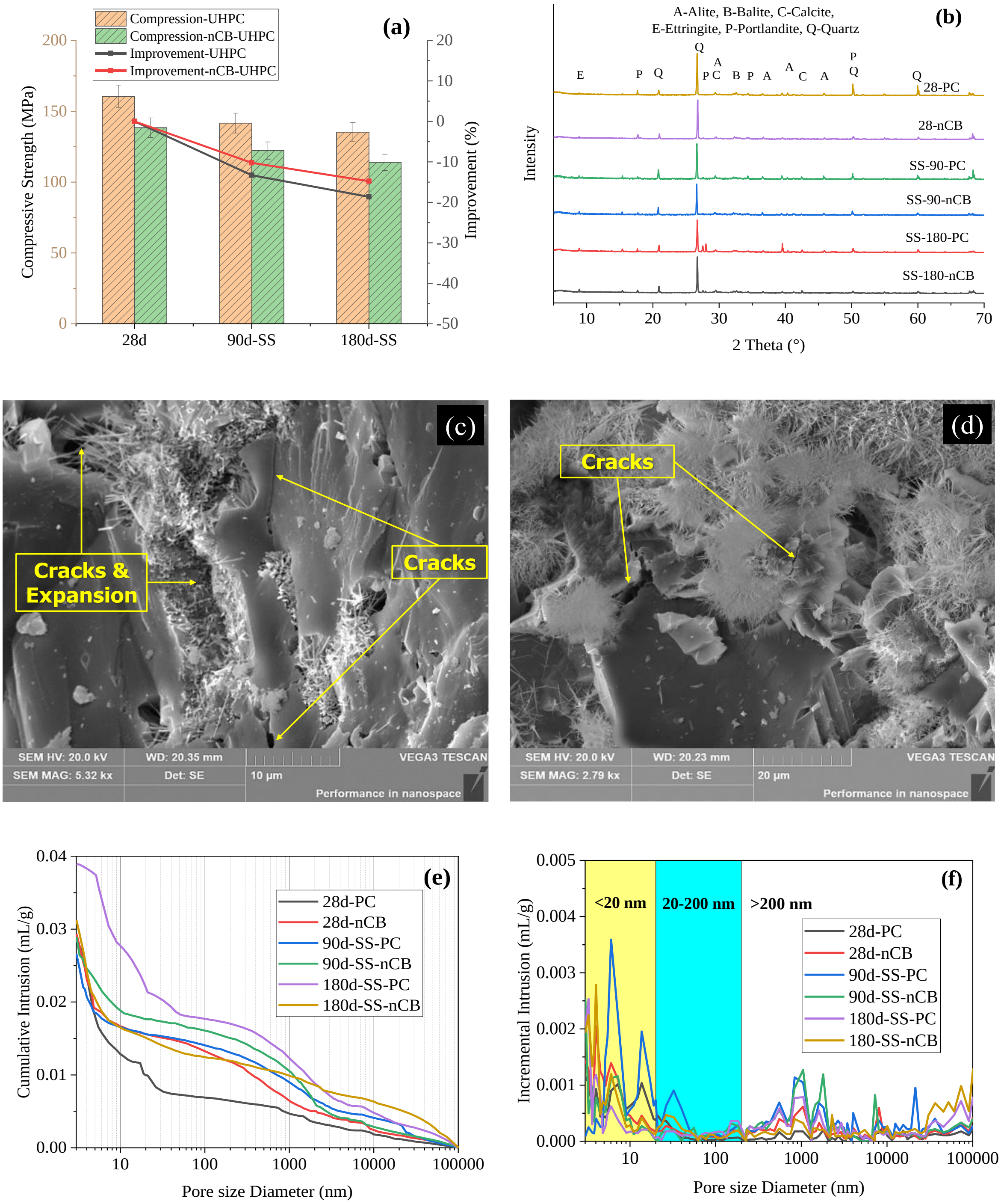

(a)
Compression-UHPC
Compression-nCB-UHPC
Improvement-UHPC
Improvement-nCB-UHPC
Compressive Strength (MPa)
Improvement (%)
28d
90d-SS
180d-SS
(b)
A-Alite, B-Balite, C-Calcite,
E-Ettringite, P-Portlandite, Q-Quartz
28-PC
28-nCB
SS-90-PC
SS-90-nCB
SS-180-PC
SS-180-nCB
Intensity
2 Theta (°)
(c)
Cracks & Expansion
Cracks
(d)
Cracks
(e)
28d-PC
28d-nCB
90d-SS-PC
90d-SS-nCB
180d-SS-PC
180d-SS-nCB
Cumulative Intrusion (mL/g)
Pore size Diameter (nm)
(f)
<20 nm
20-200 nm
>200 nm
28d-PC
28d-nCB
90d-SS-PC
90d-SS-nCB
180d-SS-PC
180-SS-nCB
Incremental Intrusion (mL/g)
Pore size Diameter (nm)

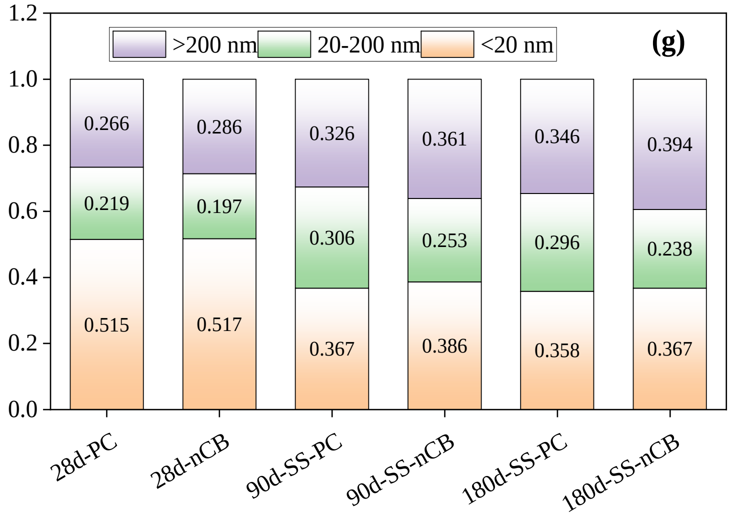

Figure 5.5. Mechanical properties and microstructures of plain UHPC and 1.50nCB-UHPC under different exposure durations. (a) Compressive strengths. (b) XRD patterns. (c-d) SEM images showing expansion and cracks after 90 days and 180 days of sea-salt solution exposure. (e-g) Cumulative pore structures, incremental pore structure and pore size distribution ratios.

It has been established that high salt contents in pore solution can lead to the formation of secondary compounds and the crystallization of salts within the pore structure. The growth of salt crystals can exert pressure on the surrounding concrete matrix, leading to internal damage, cracking, and reduced strength (Ting et al., 2021; Yang et al., 2022). As the exposure time increases, the sulphates in the high-salinity sea-salt solution can react with tricalcium aluminate (C_3A) to form secondary ettringites and gypsum (Zhao et al., 2021). Another reason contributing to the compressive strength reductions after sea-salt solution exposure is that the ions between the interlayers of CSH may reduce the bonding capacity and the cohesiveness of CSH, so that the mechanical attributes of CSH decrease remarkably and become more easily damaged, as evidenced by a molecular dynamics study (Sun et al., 2021) and also mentioned in Ref. (Zhang et al., 2022).

Moreover, as shown in **Figure 5.5**(e-g), the pore population of the specimens increased after exposure. The specimens exposed in sea-salt solution for 90 days and 180 days exhibited higher porosity compared to those cured for 28 days. Specifically, the porosity of plain UHPC and 1.50nCB-UHPC increased by about 12.02% and 10.56%, respectively, after 90 days; after 180 days of exposure, the porosity increased by 19.33% and 18.38%, respectively. This increase in porosity is believed to be due to the high salt contents in seawater, which can trigger chemical reactions that dissolve CSH, form secondary minerals, and cause expansion and cracking, resulting in a more porous microstructure. The degradation of strength can also be linked to the alteration of CSH, leading to the dissolution of calcium hydroxide (CH) and an increase in the overall pore volume. It has been reported that in concrete exposed to seawater, the pore volume increase is approximately 22% (Zhang et al., 2022). Furthermore, **Figure 5.5**(g) shows that the population of harmful pores increased with exposure time. It has been mentioned that secondary compound formation leads to volume expansion and formation of microcracks, and eventually, the population of harmful pores increases. 1.5nCB-UHPC had a higher porosity than plain UHPC, and the population of harmful pores in 1.50nCB-UHPC increased more significantly than that in plain UHPC. These observations are again due to the relatively low workability, poor compaction, and the agglomeration of nCB in 1.50nCB-UHPC.

5.4.4 Effect of Moisture Content on Piezoresistive Behaviour

The piezoresistive behaviour of the smart cementitious composite is calculated by the repeatable cyclic response of FCR to the corresponding stress-strain. The strain sensitivities are evaluated using a linear fitting curve. The strain sensitivity is also called the gauge factor (GF). The slope of the fractional change in electrical resistivity regarding the applied compressive strain is considered a gauge factor of strain sensors (Amjadi et al., 2016), which is evaluated by Equation 3.1. The fractional change in resistivity (FCR) is calculated by Equation 3.2. The piezoresistive behaviour of 1.50nCB-UHPC specimens was examined under different moisture contents, ranging from fully dried to fully saturated, including 10%, 20%, 50%, 80%, and 100% moisture contents (see Supplementary Information for the test method). The moisture content of a specimen (*w*) is calculated by Equation 5.2.

Figure 5.6(a-f) shows that the dried specimen had the highest strain sensitivity compared to the specimens with moisture. The GF of the dried specimen was 105.4, and the coefficient of determination (R^2) was 0.999. When load was applied, the resistance of the specimen decreased, and it increased during unloading. This behaviour can be explained by the reduction of distance between nCB particles under loading, which leads to the formation of new conductive pathways through quantum tunnelling. Conversely, the distance between nCB particles increases during unloading, interrupting the conductive pathways and causing the resistance to rise again. Additionally, it is observed that the sensitivity of the specimens decreased as the moisture content increased. Specifically, the GFs were reduced by 7.50%, 20.8%, 25.9%, 33.7%, and 39.9%, respectively, under 10%, 20%, 50%, 80%, and 100% moisture contents, as compared to the dried specimen. However, the coefficients of determination (R^2) for specimens with varying moisture contents remained above 0.99, indicating a strong correlation between the compressive strain and FCR. As depicted in **Figure 5.6**(g-l), the cyclic FCR responses of specimens with various moisture levels, ranging from fully saturated to fully dried, demonstrate precise synchronization between FCR and applied compressive stress. As with the trend of the GFs, the dried specimen exhibited the highest FCR compared to those with different moisture contents. The FCR for the dried specimen was 13.97, whereas that for the fully saturated (100% moisture) was 8.76. A summary of the GFs and FCRs under different moisture contents is presented in **Figure**

5.6(m-n). The results indicate that the piezoresistive response decreased with increasing moisture content, with the fully saturated specimen showing a reduction in FCR of up to 37.3% compared to the dried specimen.

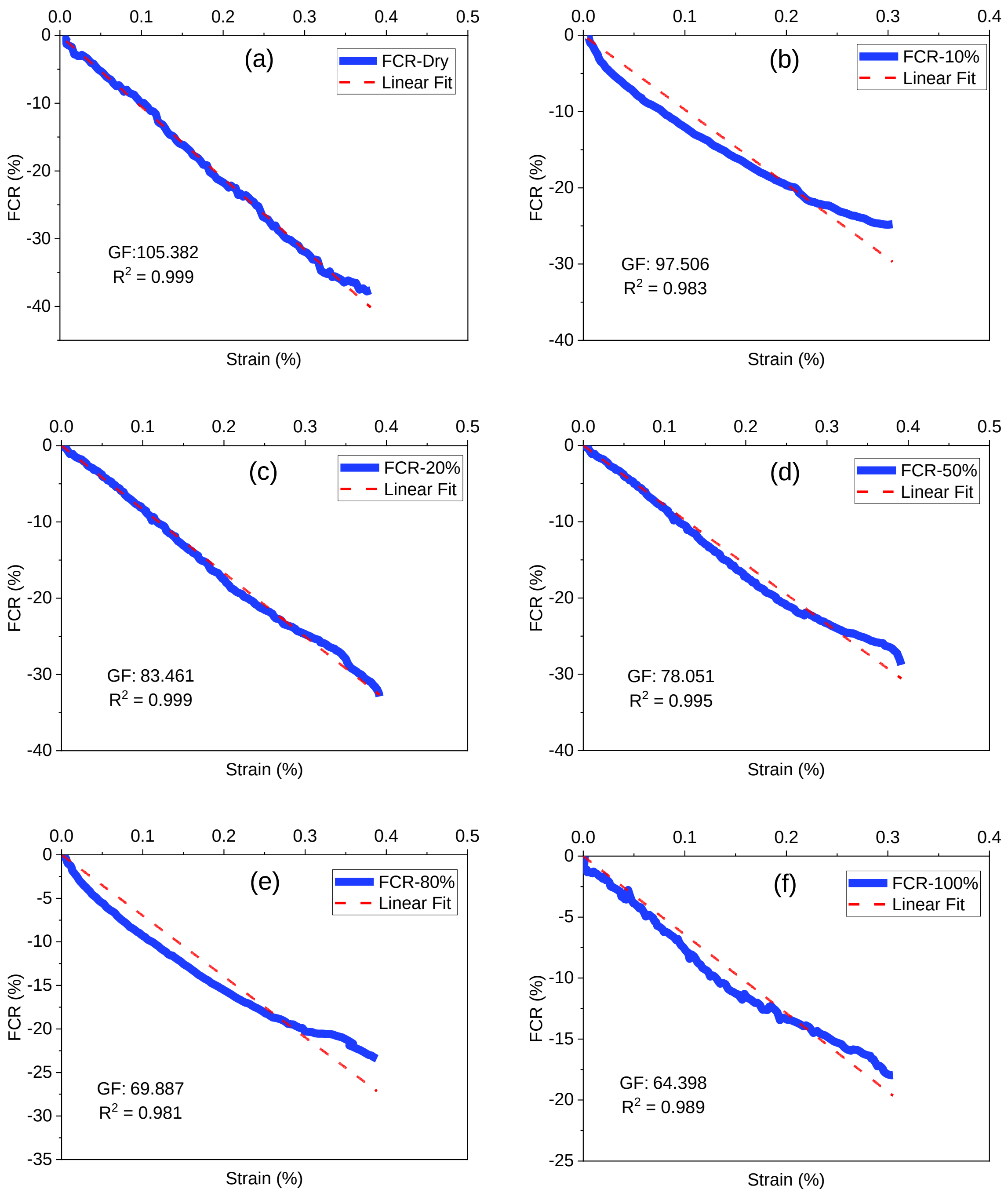
(a)
FCR-Dry
Linear Fit
GF:105.382
R2 = 0.999
FCR (%)
Strain (%)
(b)
FCR-10%
Linear Fit
GF: 97.506
R2 = 0.983
FCR (%)
Strain (%)
(c)
FCR-20%
Linear Fit
GF: 83.461
R2 = 0.999
FCR (%)
Strain (%)
(d)
FCR-50%
Linear Fit
GF: 78.051
R2 = 0.995
FCR (%)
Strain (%)
(e)
FCR-80%
Linear Fit
GF: 69.887
R2 = 0.981
FCR (%)
Strain (%)
(f)
FCR-100%
Linear Fit
GF: 64.398
R2 = 0.989
FCR (%)
Strain (%)

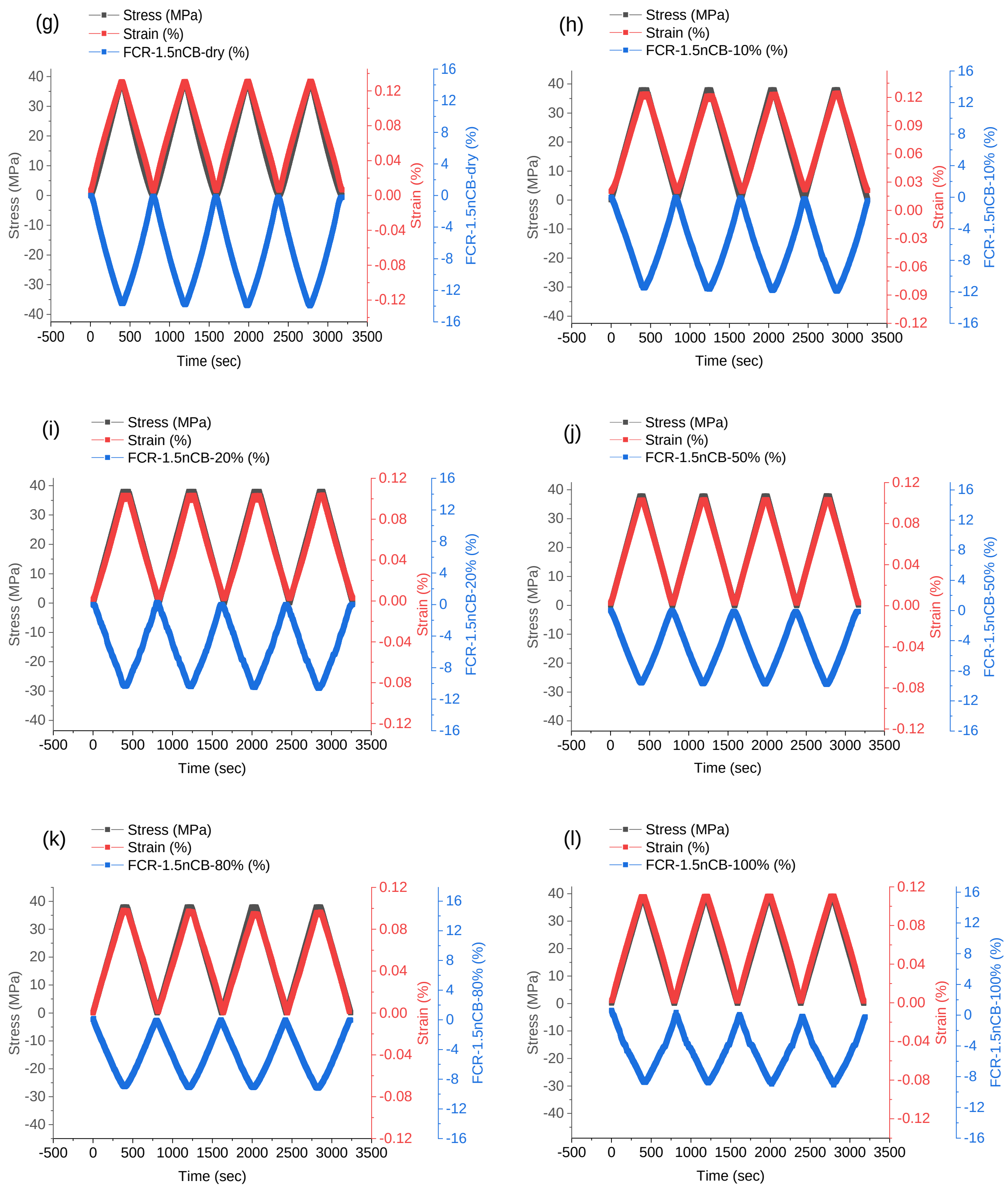
(g)
Stress (MPa)
Strain (%)
FCR-1.5nCB-dry (%)
(h)
Stress (MPa)
Strain (%)
FCR-1.5nCB-10% (%)
(i)
Stress (MPa)
Strain (%)
FCR-1.5nCB-20% (%)
(j)
Stress (MPa)
Strain (%)
FCR-1.5nCB-50% (%)
(k)
Stress (MPa)
Strain (%)
FCR-1.5nCB-80% (%)
(l)
Stress (MPa)
Strain (%)
FCR-1.5nCB-100% (%)
Time (sec)

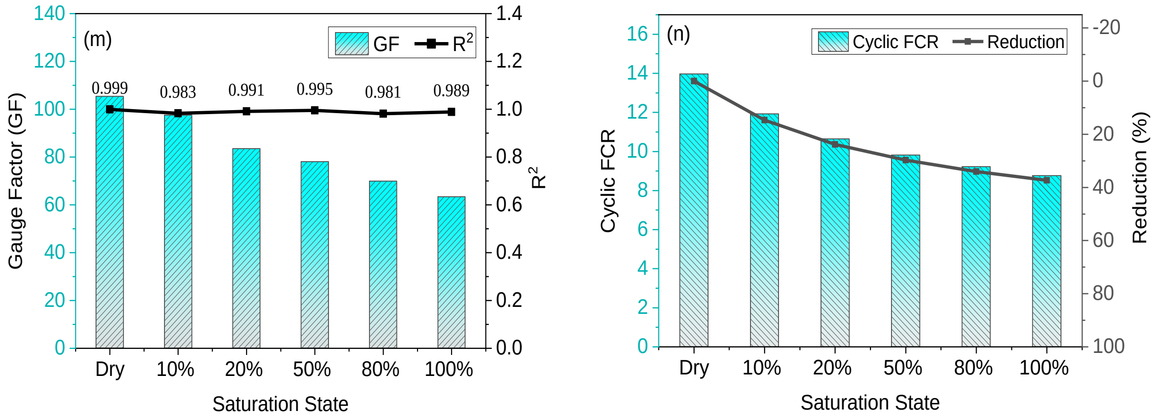

Figure 5.6. Piezoresistive behaviours of 1.50nCB-UHPC specimens at dry state, and 10%, 20%, 50%, 80% and 100% saturation state. (a-f) Monotonic compressive loading. (g-l) Cyclic compressive loading. (m) GFs under monotonic loading. (n) FCRs under cyclic loading.

Apparently, the dominant conduction mechanism of 1.50nCB-UHPC is electronic conduction, which relies on nCB particles to improve the overall conductivity of the matrix. However, introducing moisture content into the cementitious material decreased its piezoresistive behaviour. The reason behind the reduction is believed to be the contact resistance between nCB particles: a layer of water molecules was formed around each nCB particle, which increased the resistance to the movement of electrons between nCB particles. **Figure 5.7** illustrates the water molecules around nCB particles, which introduce a resistive layer between two neighbouring particles and work as an insulating barrier. As moisture content increases, the lamination degree increases, meaning that the hindrance of the movement of electrons between nCB particles is also increased. In other words, the number of conductive paths may be reduced as moisture content increases. It has also been mentioned in Ref. (Dong et al., 2022) that while the numerous water channels in the microstructure amplify the overall electrical conductivity, they reduce piezoresistivity due to contact resistance. The moisture content decreases the connectivity of nCB particles by layering up around nCB particles. It can be concluded from the test results of this study that the sensitivity of a specimen is directly related to the moisture content: when moisture content increased to 100%, sensitivity decreased by 39%.

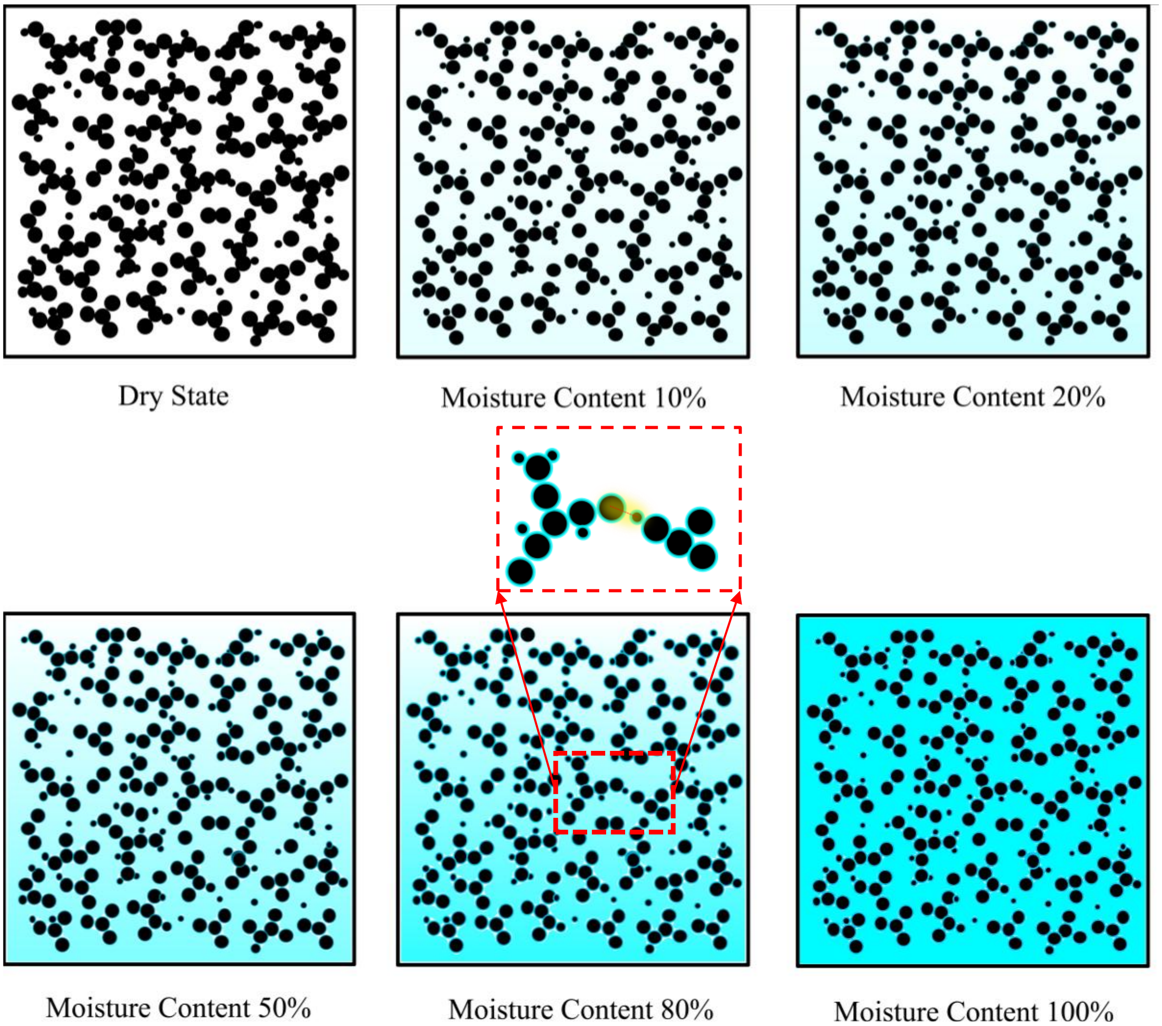

Figure 5.7. Schematic diagram of the relationship between moisture content and the contact resistance between nCB particles.

5.4.5 Effect of Sea-salt Solution Exposure on Piezoresistivity

1.50nCB-UHPC specimens were subjected to sea-salt solution exposure for 90 days and 180 days. Some were then subjected to drying treatment for 72 hours at 80°C ± 2°C (Hussain et al., 2022), but others were not (100% saturation state). The monotonic and cyclic sensing responses of these specimens can be seen in **Figure 5.8**(a-h). It is evident that the dried specimens after sea-salt solution exposure still exhibited excellent piezoresistive behaviour, although their GFs appeared to be slightly smaller than that of the specimen without exposure (**Figure 5.6**(a)). The smaller GFs could be caused by the microcracks produced by the secondary hydration products induced by the exposure, which discontinue some of the conductive pathways. It can also be observed from the results that the GFs of the specimens without drying treatment were higher than that of the dried specimen. The GF of the saturated specimen after 90-day exposure was 110.84 (R^2 = 0.99), while the GF of the dried specimen after 90-day exposure was 99.10, which was about 10.60% lower. Similarly, the GFs of the saturated and dried specimens after 180-day exposure were 94.48 and 85.87, respectively, with a difference of 9.10%. The above observation is opposite to that presented in Section 3.4 on the effect of moisture content and is believed to be due to the high salinity of the sea-salt solution with high ionic mobility.

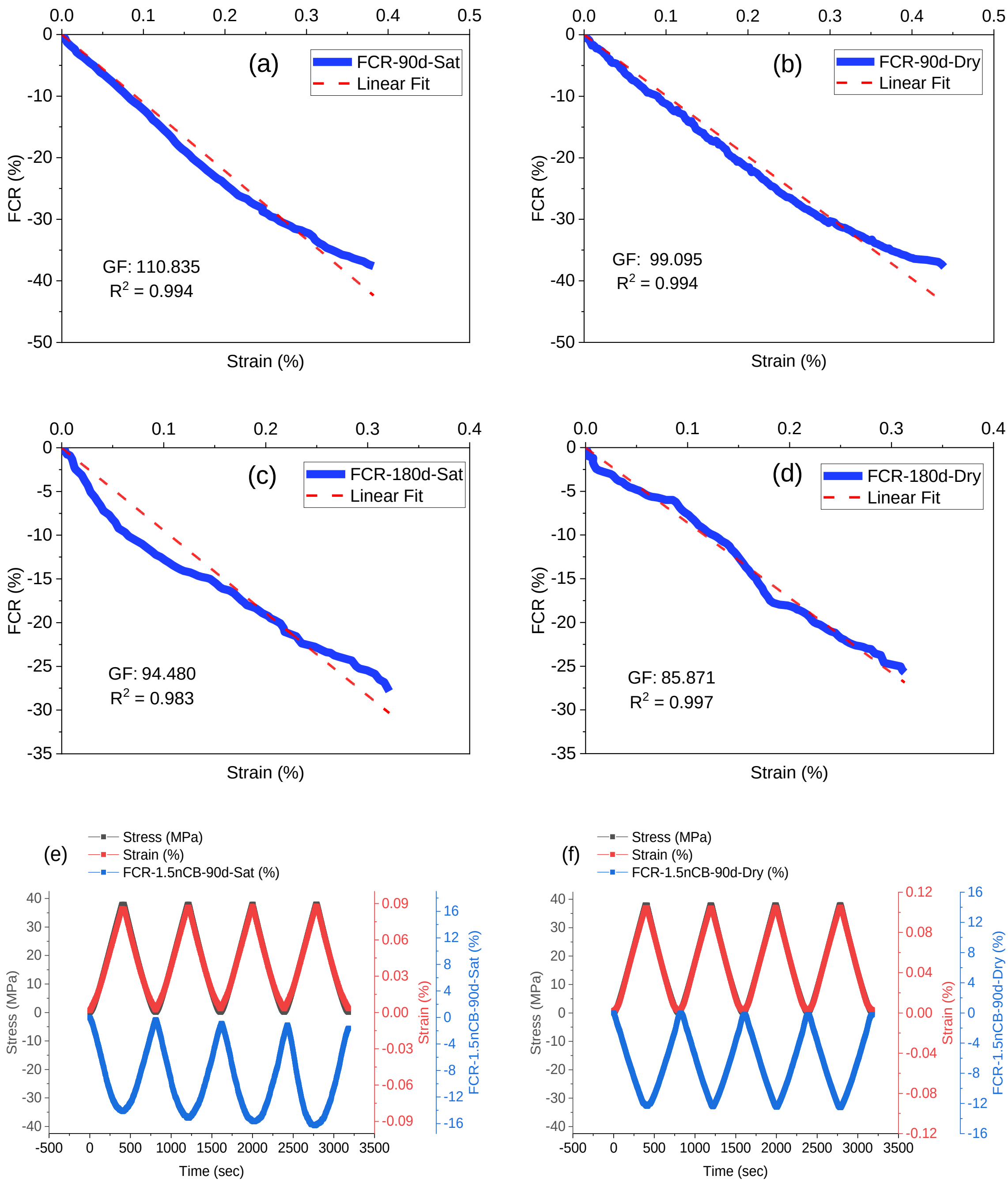
(a)
FCR-90d-Sat
Linear Fit
GF: 110.835
R^2 = 0.994
Strain (%)
FCR (%)
(b)
FCR-90d-Dry
Linear Fit
GF: 99.095
R^2 = 0.994
Strain (%)
FCR (%)
(c)
FCR-180d-Sat
Linear Fit
GF: 94.480
R^2 = 0.983
Strain (%)
FCR (%)
(d)
FCR-180d-Dry
Linear Fit
GF: 85.871
R^2 = 0.997
Strain (%)
FCR (%)
(e)
Stress (MPa)
Strain (%)
FCR-1.5nCB-90d-Sat (%)
Time (sec)
(f)
Stress (MPa)
Strain (%)
FCR-1.5nCB-90d-Dry (%)
Time (sec)

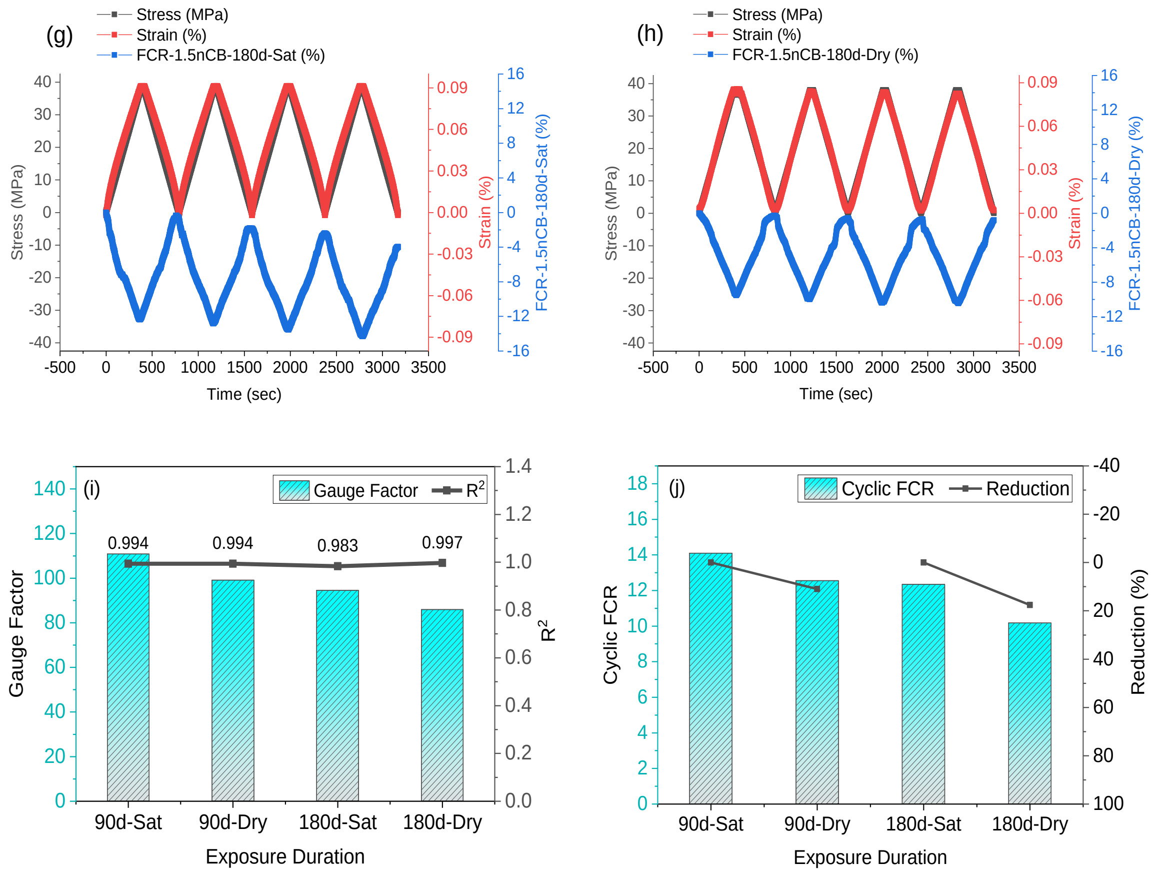

Figure 5.8. Piezoresistive behaviours of 1.50nCB-UHPC specimens after 90 days and 180 days of exposure, with and without post-exposure drying treatment. (a-d) Monotonic compressive loading. (e-h) Cyclic compressive loading. (i) GFs under monotonic loading. (j) FCRs under cyclic loading.

Furthermore, **Figure 5.8**(e-h) shows that the saturated specimens after sea-salt solution exposure had a higher FCR than their corresponding dried specimens. After 90-day exposure, the cyclic FCR of the saturated specimen was 14.10%, and the FCR of the dried specimens was 12.55%, which was about 11.0% lower, as seen in **Figure 5.8**(j), suggesting that about 11.0% of the piezoresistivity of the saturated specimen was contributed by the moisture content and ingress of ions during the exposure. It should be noted that the salinity of the solution used in this study is five times that of normal seawater. The higher FCR of the saturated specimen owes to the higher ionic activity due to the ions from the high-salinity sea-salt solution. The free ions, such as Na^+, Mg^{2+}, and Cl^-, increased the ionic activity and concentration of the pore solution (Dong et al., 2022). Similarly, the saturated specimens after 180-day exposure had a higher FCR (i.e., 12.34%) than the corresponding dried specimen (i.e., 10.17%). It is also noted that the specimens after 180-day exposure had lowers FCR than those after 90-day exposure, although their FCRs still had perfect synchronization to the applied stress. Moreover, it is observed the cyclic FCR responses of the specimens after 180-day exposure showed slight fluctuation. This might be due to the polarization effect (for saturated specimens) as well as damage to the bond between conductive materials during the exposure (Fu & Chung, 1997). Nevertheless, the overall piezoresistive behaviours of these specimens are still considered to be excellent.

Furthermore, the FCR response after 180 days of exposure has shown slight fluctuation after drying. It has been mentioned in the literature that apart from the polarization, damage to the bond between the conductive materials and cementitious matrix may cause fluctuation (Fu & Chung, 1997). It means the formation of the microcracks in a matrix in case of more prolonged exposure to an aggressive environment. As observed from the microstructure analysis in **Figure 5.5 (b-d),** the sea salt solution exposure has formed secondary ettringites, which produce microcracks, which would be the critical factor of this fluctuated response of the FCR during loading and unloading.

5.5 Summary and Conclusions

This chapter has presented a comprehensive study on the effects of curing and working conditions on the properties of a new breed of self-strain sensing UHPC, namely, nCB-UHPC, which was presented in previous chapter. By incorporating nCB as the conductive filler, nCB-UHPC possesses excellent sensing capability while being cost-effective. In this study, the test variables include curing condition, moisture content and period of exposure to high-salinity sea-salt solution, while the properties of concern include microstructure, compressive strength, and piezoresistive behaviour. The following conclusions can be drawn from this study:

1. The compressive strength of nCB-UHPC improves with extended curing duration and oven-dry curing at 105℃, as compared to standard 28-day water immersion curing. However, exposure to high-salinity sea salt solution for up to 180 days reduces the compressive strength in both plain UHPC and 1.50nCB-UHPC due to the formation of secondary hydration products. Additionally, 1.50nCB-UHPC exhibits a lower compressive strength than UHPC because of the high water absorption capacity of nCB.
2. The fractional change in electrical resistivity (FCR) responses of 1.50nCB-UHPC specimens with different moisture contents all perfectly synchronized with the applied compressive stress, though their strain sensitivities decreased as moisture content increased, thanks to increasing contact resistance between nCB particles.
3. 1.50nCB-UHPC specimens dried after sea-salt solution exposure still exhibited excellent piezoresistive behaviour, although their GFs appear to be slightly smaller than those of the specimens without exposure. The reduction in GF could be caused by the microcracks produced by the secondary hydration products.

4. After exposure to high-salinity sea-salt solution, the saturated 1.50nCB-UHPC specimens exhibited higher sensitivity than the dry specimens due to the high concentration of dissolved ions in the pore solution. This is contrary to the effect of normal water saturation, which decreases piezoresistivity.

The results presented in this paper demonstrate that this new multifunctional nCB-UHPC exhibits excellent durability and well-synchronized responses in various working conditions. This study laid a foundation for the large-scale implementation of nCB-UHPC as a field-deployable solution for monitoring the condition of concrete structures.

Chapter 6.

Development of Nanocarbon Black-based Seawater Sea-sand Ultra-High-Performance Concrete with Strain-Sensing Capability

6.1 Abstract

Using seawater sea sand concrete (SSC) in marine infrastructure offers significant sustainability benefits that minimize energy consumption and carbon emissions associated with transportation activities. Furthermore, it helps mitigate the environmental impact caused by excessive sand mining in riverbeds and using fresh water. This study aims to contribute to this growing area of research by introducing self-strain sensing capabilities to ultra-high-performance seawater sea sand concrete (UHPSSC) by incorporating nCB as a functional filler. Mix designs with different concentrations of nCB are formulated and tested for impact on the material's properties, including mechanical strength, microstructure and piezoresistive behaviour under different curing conditions.

The study concludes that adding nCB generally decreases the compressive strength of UHPSSC, and dry curing at high temperatures improves the strength compared to normal water curing. The percolation threshold determined for the nCB-UHPSSC in both saturated and after-drying treatment samples is 1.40% of nCB, which corresponds to a compressive strength of 131 MPa. The highest strain sensitivity of the nCB-UHPSSC composite is achieved at 1.40% of nCB, both in saturated and dry conditions. Notably, the saturated samples demonstrate 18% higher sensitivity than the dry samples, indicating that moisture

content and high dissolved ions from seawater contribute to the additional sensitivity. Moreover, the repeatable cyclic response demonstrates a well-synchronized fractional change in resistivity (FCR) corresponding to the stress-strain relationship.

In summary, the newly developed nCB-UHPSSC exhibits excellent mechanical and piezoresistive properties, making it a promising material for monitoring concrete infrastructure conditions in the field.

6.2 Introduction

Concrete is a widely used construction material in the world (Miller et al., 2018), known for its durability, strength, and versatility. Its production relies on natural resources like freshwater, aggregates, and river sand, which are increasingly becoming scarce in many areas today. According to the World Health Organization (WHO), water scarcity affects more than two billion people, and climate change and population expansion will likely worsen it in some areas (WHO, 2022). The construction industry is a major consumer of freshwater, accounting for approximately 18% of global annual industrial water use (Ebead et al., 2022; Miller et al., 2018). Likewise, the river sand crisis has also emerged exponentially, and its usage has reached up to 50 billion tons annually (UNEP, 2022). The heavy extraction of the river sand damages the river ecosystem and affects navigation, leading to flood disasters in many regions (Zhao et al., 2021). Furthermore, the extraction and transportation of these materials contribute to environmental degradation and carbon emissions. Therefore, alternate abandoned resources like seawater and sea-sand would be a reasonable choice for sustainable and economical construction, especially offshore construction. It can also save billions of dollars in energy in terms of transportation and contribute to lower carbon emissions. However, seawater with 3.5% average salinity, which typically around 78% is sodium chloride (NaCl), is generally considered to be unsuitable for steel-reinforced concrete structures because of the steel corrosion problem (Antonov et al., 2010; El-Reedy, 2007). The damage and crack formation due to corrosion of reinforcement will lead to structure failure and, as a result, loss of human life, infrastructure and billions of dollars to economies (an estimated investment of $3.6 trillion was required by 2020 to address the infrastructure issues (Wille & Boisvert-Cotulio, 2015)).

SCCs have emerged as a new real-time monitoring technology that has a low cost, is compatible with concrete structures, and has a long service life. Different piezoresistive fillers have been extensively explored, while their use still faces many challenges including dispersion issues and the relatively high costs (Azhari & Banthia, 2012; Kashif Ur Rehman et al., 2018; Konsta-Gdoutos et al., 2010; Sun et al., 2017). Furthermore, recent studies have explored steel fibres, carbon nanotubes (CNTs), and steel slag aggregates to develop self-strain sensing capability of UHPC, and they have achieved success to different extents (Dong et al., 2020; Dong et al., 2016; Dong et al., 2024; Lee et al., 2018; Yoo et al., 2018). However, steel fibres and slag are generally not suitable for use with seawater concrete due to potential corrosion issues, while CNTs are known to be costly.

Built upon the successful development of the nCB-UHPC, this study aims to develop ultra-high-performance seawater sea-sand concrete (UHPSSC) with sensing capability by incorporating nCB as conductive fillers, which is a very suitable piezoresistive material by considering cost and potential corrosion issues. Therefore, this chapter sets out to explore the feasibility of introducing the self-sensing capability to seawater sea-sand ultra-high-performance concrete (UHPSSC) by incorporating the nCB.

6.3 Experimental Program

6.3.1 Raw Materials

This study used raw materials similar to those detailed in section 4.2.1. Washed sea-sand was soaked in a commercial sea salt solution with a dosage of 35 g/L for 48 hours following Ref. (Teng et al., 2019) and was then dried for 48 hours in an oven at 105 °C. Furthermore, dried sand particles with a size smaller than 0.75 µm (i.e., clay) or larger than 1.18 mm were removed as they may adversely affect the properties of UHPC (Fernandes et al., 2007). A polycarboxylic polyether-type superplasticiser (SP) with a specific gravity of 1.07 and a solid content of 44.0% was used.

The artificial seawater used was made by dissolving commercial sea salt in tap water. The chemical compositions and ion concentrations of the artificial seawater and the lixivium of sea-sand were calculated by ion chromatography, as presented in **Table 6.1**.

Table 6.1. Comparison of chemical compositions of average, natural and artificial seawater, tap water and sea-sand lixivium (in g/L).

Ions	Avg. Seawater (Dickson & Goyet, 1994)	Artificial Seawater	Tap water	Sea-sand Lixivium
Na^{+}	10.783	10.8024	0.1014	0.8707
$NH4^{+}$	-	0.3134	0.0149	0.0496
K^{+}	0.3991	0.6783	0.0101	0.0055
Mg^{2+}	1.2837	1.0717	0.0137	0.1161
Ca^{2+}	0.4121	0.4838	0.0187	0.1898
F^{-}	0.0013	0.0854	0.0276	0.1748
Cl^{-}	10.3524	15.7835	0.0951	1.6264
NO^{2-}	-	0.3932	0.0000	0.0126

Br^-	0.0673	3.5667	0.0000	0.3118
NO^{3-}	-	0.0281	0.0089	0.2860
SO^{2-}_4	2.7123	0.2450	0.0092	0.2590
Salinity	35.0119	33.4515	0.2996	3.9023

6.3.2 Mix Design and Specimen Preparation

nCB was used as a conductive filler in this study to improve the piezoresistive properties of UHPSSC details in **Table 4.2** and **Figure 4.1**. Typically, UHPC utilises a low water-to-binder ratio of around 0.20 (Shi et al., 2015). While producing UHPC is already challenging with such a low water-to-binder ratio, the addition of nCB makes it more difficult due to the high surface area and water-absorbing nature of nCB. Therefore, preliminary experiments were performed to finalise the mix design with desirable fresh and hardened properties. The mix proportions of the nCB-UHPSSC design are detailed in **Table 6.2**. In all the mixes, the contents of cement and SF were the same, and the water-to-binder ratio, which included the water from SP (i.e., 66% of the mass of SP), was consistently 0.19. The nCB content varied in different mixes and was up to 1.80% of the mass of the binder.

Table 6.2. Mix proportion of nCB-filled cementitious composites (kg/m^3).

Notation	Cement	SF	QP	Sand	Water	SP	nCB
UHPSSC	842.0	210.5	210.5	926.2	172.6	42.1	0.00
0.20nCB	842.0	210.5	194.5	907.2	172.6	42.1	2.11
0.40nCB	842.0	210.5	178.5	888.2	172.6	42.1	4.21
0.60nCB	842.0	210.5	162.5	869.2	172.6	42.1	6.32

0.80nCB	842.0	210.5	146.5	850.2	172.6	42.1	8.42
1.00nCB	842.0	210.5	130.5	831.2	172.6	42.1	10.53
1.20nCB	842.0	210.5	114.5	812.2	172.6	42.1	12.63
1.40nCB	842.0	210.5	98.5	793.2	172.6	42.1	14.74
1.60nCB	842.0	210.5	82.5	774.2	172.6	42.1	16.84
1.80nCB	842.0	210.5	66.5	755.2	172.6	42.1	18.95

0.20nCB means that 0.20% nCB by binder mass added into UHPSSC

6.3.3 Mechanical Properties

The detailed specimen preparation procedure, workability, and compressive strength testing methods are detailed in sections 4.2.3, 4.2.4 and 4.2.5, respectively. The compressive strength of additional curing conditions is dry curing, where samples are set out at 105℃ for 24 hours in an oven after 28 days of water immersion are tested.

6.3.4 Microstructure Analysis

The details of the microstructure analysis are listed in section 5.2.6, including SEM-EDX, XRD and MIP, respectively.

6.3.5 Piezoresistive Properties

For piezoresistive testing, 40 mm cubic samples with four copper meshes inserted are prepared. After demoulding, the specimens were put in a normal water immersion curing for 28 days at 22℃ ± 3. The piezoresistive behaviour test of the samples is done under two different conditions, including before and after drying treatment. For drying treatment, the samples were dried out at 70 ℃ for six days to eliminate the moisture content before undergoing the cyclic compressive test. During all piezoresistive tests, plastic sheets were used as electrical insulation between the specimen and the contact points of the load cell to remove electrical interference. The specimen was loaded by displacement control at a rate of 0.6 mm/min. At first, four cycles of compressive loading were applied to a stress amplitude of 30 MPa, and then, monotonic loading was applied all the way to the cracking point.

The remaining details are listed in section 4.2.6.

6.4 Results and Discussions

6.4.1 Flowability of nCB-UHPSSC

A series of preliminary experiments and investigations were conducted to enhance the flowability of nCB-UHPSSC to an acceptable level. Due to the very small size and high specific surface area of nCB particles, they absorb more free water and SP than other fillers (Wu et al., 2016), leading to a decrease in flowability. It was also found in previous studies that the incorporation of nanomaterials in cementitious composites dramatically affected their workability (Al-Dahawi et al., 2016). In this study, the mixing technique, water-to-cement ratio, and SP content were finalised after preliminary investigations to achieve desirable properties in nCB-UHPSSC. Plain UHPSSC and nine groups of UHPSSC with different nCB contents were cast. The flowability of the mixes was measured using a flow table apparatus and based on the mean value of the horizontal and vertical sides, as exemplified in **Figure 6.1**

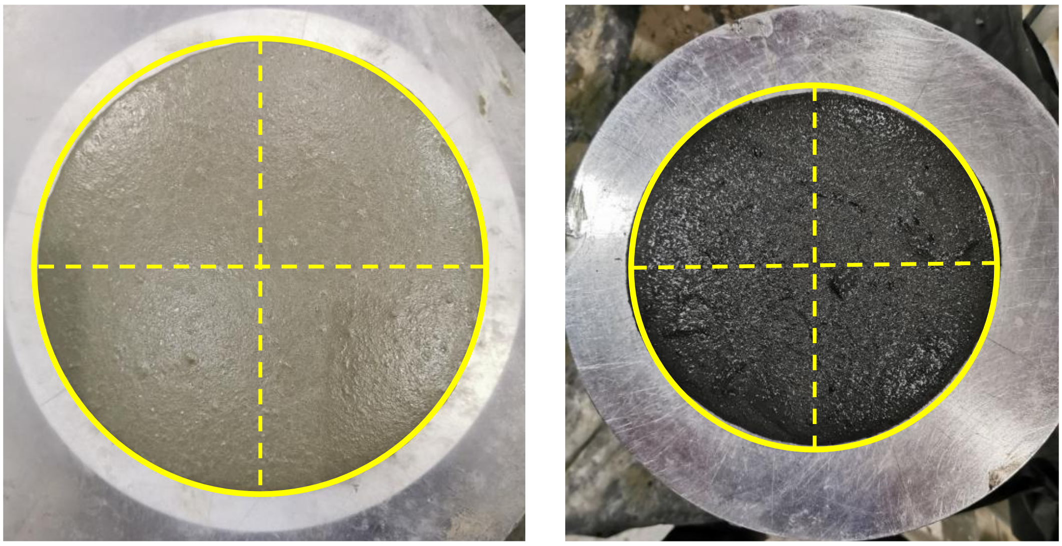

Figure 6.1. Slump spread of UHPSSC and nCB-UHPSSC. (a) Plain UHPSSC and (b) 1.00nCB mix.

The flowability of the UHPSSC samples is plotted in **Figure 6.2**. The flow spread of the UHPSSC mix without nCB was 295 mm (**Figure 6.1**(a)**),** while the flowability significantly decreases with an increase in nCB content due to the excessive water absorption capability, high surface area, and agglomeration of nCB (Hartley & Parfitt, 1985). As a result, the flowability of the 1.00nCB mix was found to be 203 mm (**Figure 6.1**(b)), while the number was reduced to 141 mm for the 1.80nCB mix, which is about 52% lower than plain UHPSSC. This observation is consistent with the findings of previous studies (Hussain et al., 2022; Hussain et al., 2023). It is generally agreed that a flow spread of over 160 mm may be considered good for UHPC (Du et al., 2021). All the mixes tested in this study have a flow spread higher than 160 mm, except for the 1.80nCB mix.

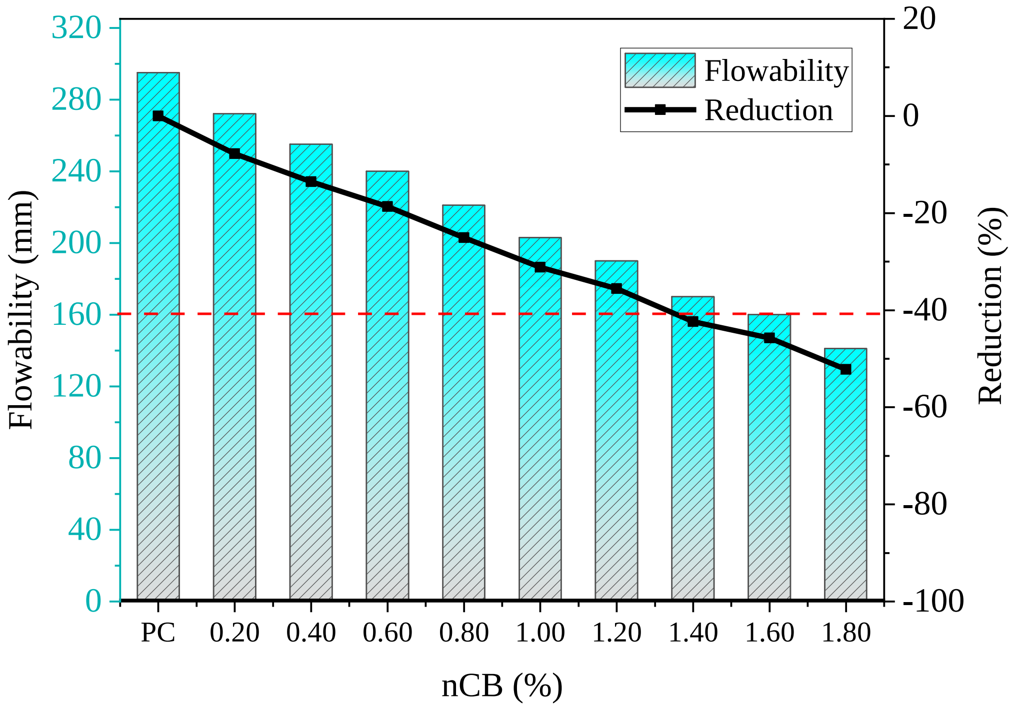

Figure 6.2. Flowability of UHPSSC mixes with different nCB contents.

6.4.2 Compressive Strength

Figure 6.3 illustrates the results of the compression tests, showing that a plain UHPSSC specimen achieves a compressive strength of approximately 145 MPa after undergoing heat curing for one day (hereinafter referred to as 1d-heating strength). The 1d-heating strength gradually reduces with increasing nCB content, reaching 119.6 MPa for the 1.80nCB specimen, with the cumulative reduction being about 17.50%.

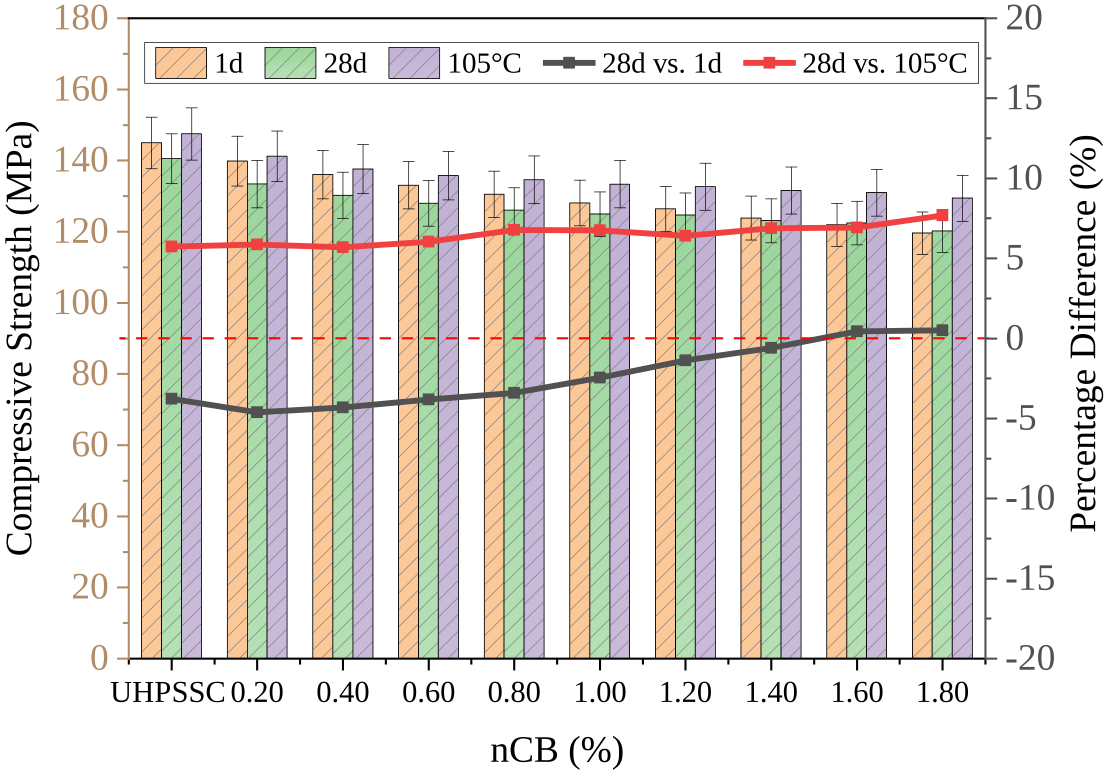

Figure 6.3. Compressive strength achieved under different curing conditions for all UHPSSC specimens with different nCB content.

The decrease in compressive strength with nCB content can be attributed to a number of reasons. First, when nCB particles are added to a mix, they decrease flowability, causing improper compaction of the matrix, a relatively high number of voids, and thus a reduction in the compressive strength. Another possible reason is the agglomeration of the nCB particles, which creates stress concentration points in the matrix. It can be seen from **Figure 6.4**(a) that the 1.80nCB specimen has a porous microstructure.

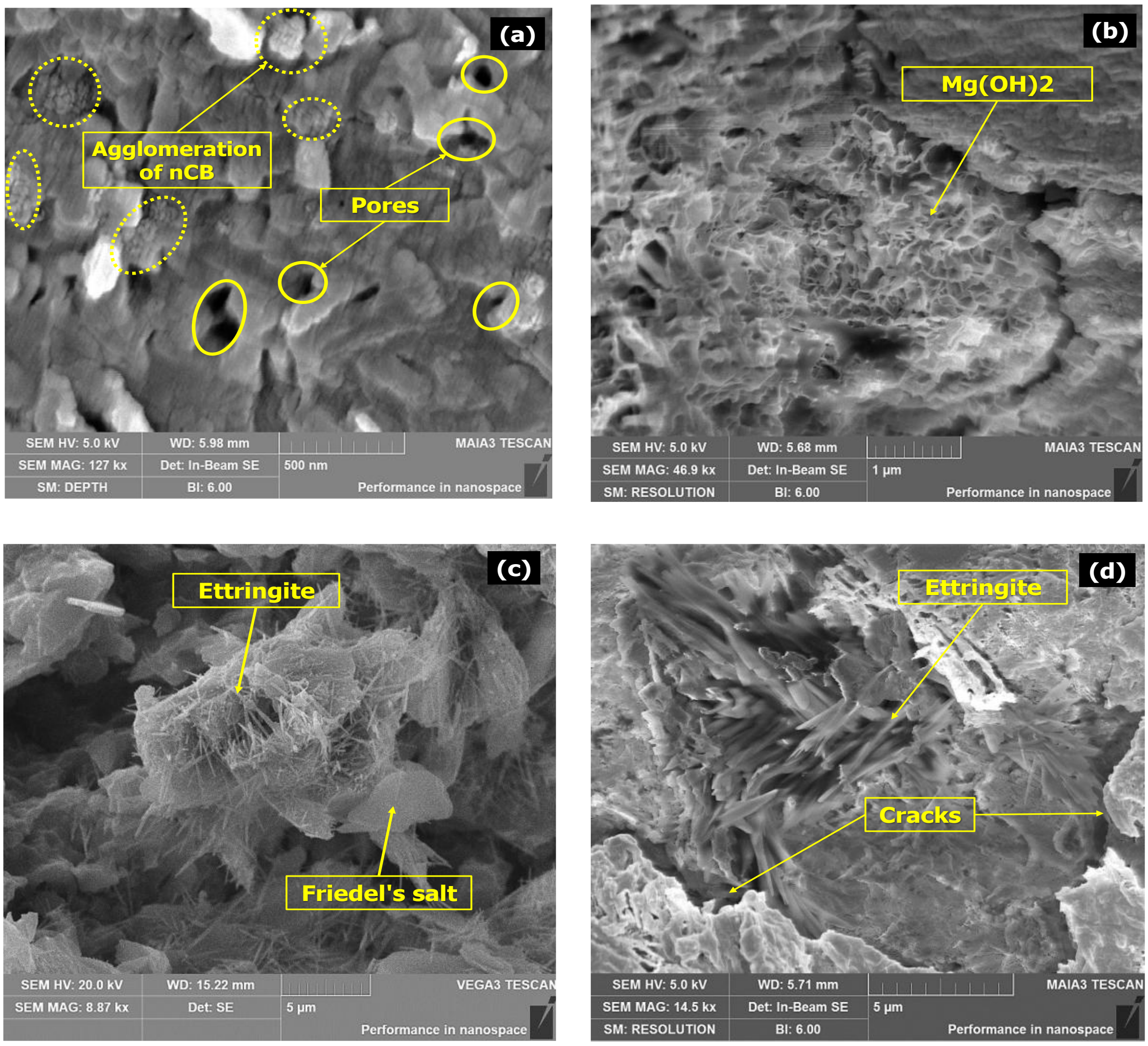

Figure 6.4. Microstructure showing the porosity and formation of the secondary products. (a) Pores and nCB agglomeration in the 1.80nCB specimen. (b) Formation of $Mg(OH)_2$. (c-d) Formation of Friedel's salt, secondary products and cracks.

On the other hand, the plain UHPSSC specimen under 28-day water immersion curing has a compressive strength of 140.49 MPa (hereinafter to as 28d-strength). Similar to the trend of the 1d-heating strength, an increase in nCB content also leads to a decrease in 28d-strength by up to 13.84% for the 1.80nCB specimen. By comparing the two groups of specimens under different curing conditions (i.e., one-day heat curing and 28-day water immersion curing), it is noted that: (1) for the same nCB content, the 28d-strength is lower than the 1d-heating strength; (2) the strength difference between the two groups of specimens decreases with an increase in nCB content until the nCB content reaches 1.40%; and (3) at relatively high nCB contents (i.e., 1.60% and 1.80%), the 28d-strength is higher than the 1d-heating strength. The strength difference between the two groups of specimens is further illustrated in **Figure 6.3** by the black line, which shows the percentage difference between the strengths at the same nCB content under two different curing conditions.

An interesting thing to note from the above observation is that the 28-day water immersion curing appears to be more beneficial for nCB-UHPSSC than for plain UHPSSC. This could be due to the fact that the 28-day water immersion provides an additional source of water to boost hydration reactions, which is particularly important for nCB-UHPSSC due to the excessive water absorption capability of nCB. This might also be due to the more porous microstructure of nCB-UHPSSC, which allows more room to accommodate the expansive hydration products of seawater-mixed concrete (e.g., magnesium hydroxide $Mg(OH)_2$, ettringites and Friedel's salt, as shown in **Figure 6.4**(b-d) and **Figure 6.5**); these hydration products may otherwise cause formation of cracks and thus the reduction of compressive strength.

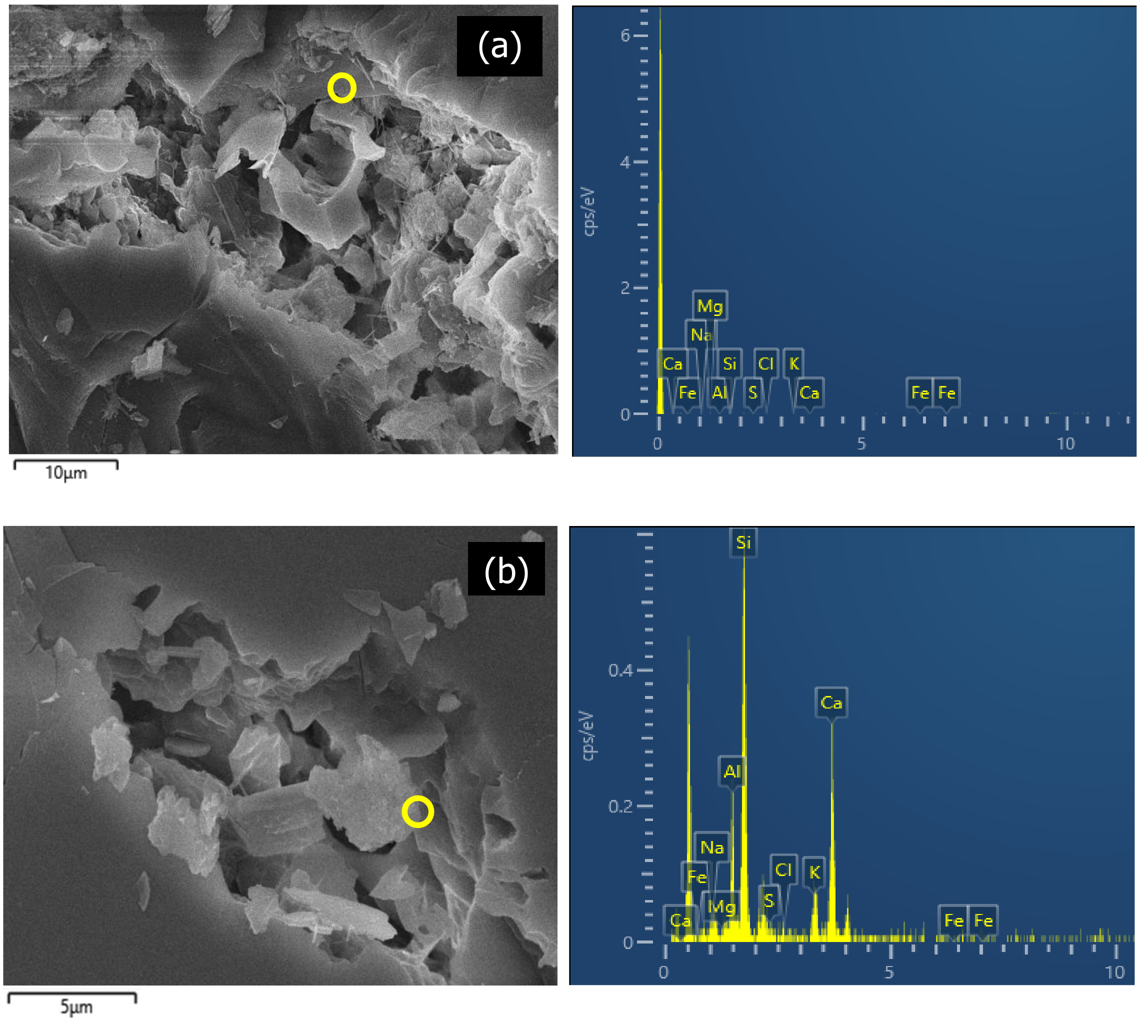

Figure 6.5. SEM images and EDX spectrum points (highlighted with yellow circle) showing $Mg(OH)_2$ and Friedel's salt.

Furthermore, some specimens went through dry curing at 105℃ for 24 hours after 28 days of water immersion curing. It is not a surprise to see that the compressive strength improved due to the additional dry curing process, as illustrated by the red line in **Figure 6.3**, which shows the percentage increase. It appears that the percentage increase grows with nCB content, possibly attributed to the fact that more unhydrated cement particles exist in a specimen with a higher nCB content due to the high water absorption capability of nCB. When being subjected to heat treatment, these unhydrated cement particles undergo further hydration. It has also been established that in UHPC, an elevated temperature not only helps to speed up the hydration process but also promotes the secondary hydration between cementitious materials and portlandite (Abdulkareem et al., 2021; Hamada et al., 2022; Hiremath & Yaragal, 2017). The heat treatment facilitates the pozzolanic activity between the portlandite and SiO_2 of SF and fine silicates from QP, which are typically non-reactive with water during standard curing (Yazıcı et al., 2013) and may only react with $Ca(OH)_2$ in the alkaline environment of cement hydration products to produce C-S-H gel (Khan et al., 2021).

On the other hand, MIP was employed to investigate the pore structure of the plain UHPSSC specimens and the 1.40nCB specimens obtained under different curing conditions. **Figure 6.6** illustrates the pore structures of the UHPSSC mix and 1.40nCB mix with the curing condition being 28-day water immersion with or without one-day 105°C dry curing. **Figure 6.6**(a) describes the cumulative pore concentration of each sample, represented by the area under the curve, while the distributions of pores with different sizes are detailed in **Figure 6.6**(b). According to Ref. (Ali et al., 2023; Li, 2021; Wang et al., 2018), pores in cement-based materials can be divided into three categories, including harmless pores (< 20 nm), less harmful pores (20-200 nm) and harmful pores (> 200 nm). The harmful pores include the capillary and meso pores, which are mainly responsible for the reduction in strength and durability.

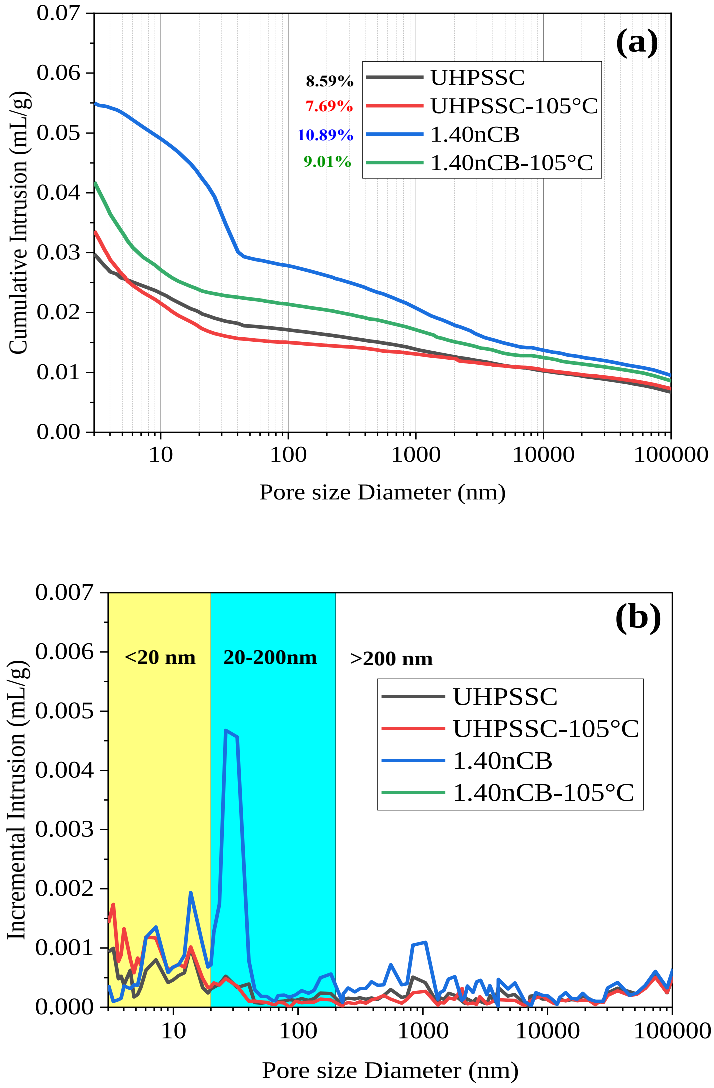

Figure 6.6. Cumulative and intrusion pore structures of the plain UHPSSC mixes and 1.40nCB mixes obtained under different curing conditions.

The total porosities of the plain UHPSSC specimen and 1.40nCB specimen after 28-day water immersion curing were 8.59% and 10.89%, respectively, slightly higher than those reported in the literature for typical UHPC obtained under heat curing (Matos et al., 2021; Vande Voort et al., 2008). The 1.40nCB specimen is 26.72% more porous than the plain UHPSSC specimen. On the other hand, the porosities of the plain UHPSSC specimen and 1.40nCB specimen after an additional one-day 105 ℃ dry curing reduced to 7.69% and 9.01%, respectively, with a 17.16% difference between the two. The results presented above suggest that the effect of additional heat curing on reducing porosity is more pronounced for nCB-UHPSSC than for plain UHPSSC, consistent with the compressive strength results (**Figure 6.3**). It should be noted that previous literature also discussed that dry curing benefits microstructure densification by amplifying pozzolanic reactivity and the polymerization of C-H-S gel (Lu et al., 2022).

The quantitative analysis of pores presented in **Figure 6.7** shows the impact of different curing regimes on pore size distribution. The data indicate that both the plain UHPSSC specimen and 1.40nCB specimen after 28-day water immersion curing have more pores in the harmful and less harmful categories compared to those undergoing additional 105 °C dry curing. The 1.40nCB specimen has more harmful pores than the plain UHPSSC specimen, but this difference became smaller after they were subjected to an additional 105 °C dry curing. It is evident that dry heat curing is beneficial for the densification of microstructures, and this effect is more pronounced for nCB-UHPSSC than for plain UHPSSC.

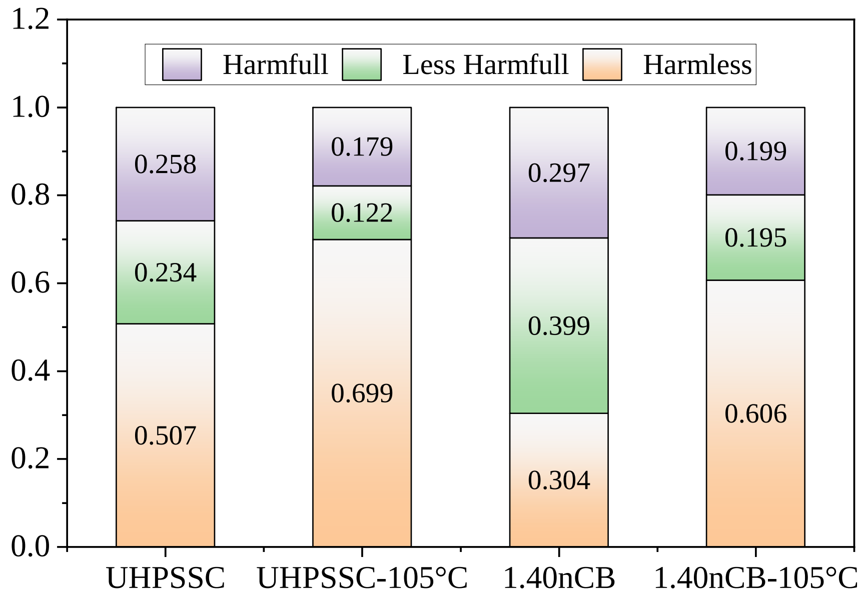

Figure 6.7. Pore size distributions of the plain UHPSSC mixes and 1.40nCB mixes obtained under different curing conditions.

Additionally, **Figure 6.8** depicts the X-ray diffraction (XRD) patterns of different specimens under different curing conditions. The prominent quartz peaks are associated with the QP used in UHPSSC. As observed from the patterns of the 1.40nCB specimen and 1.80nCB specimen, the incorporation of nCB in a mix does not result in any new chemical phases. The peaks of the unhydrated cement clinkers, including alite and belite, which are at least partially due to the extremely low w/b ratio of the UHPC matrix (Lu et al., 2021), can be identified from **Figure 6.8**; for nCB-UHPSSC, the inclusion of inert nCB may also retard cement hydration (Li et al., 2024; Zhang et al., 2022). Moreover, the formation of Friedel's salt and $Mg(OH)_2$, as a result of using seawater as the mixing water, is evident in **Figure 6.8**. Furthermore, compared to 28 days of curing, the additional dry curing at 105 °C facilitated hydration, as evidenced by the reduced intensities of the ettringite, portlandite and quartz peaks. The reduction of the quartz peaks was due to the consumption of QP in the pozzolanic reaction at the elevated temperature, as mentioned by Ref. (Shen et al., 2019; Tavares et al., 2020).

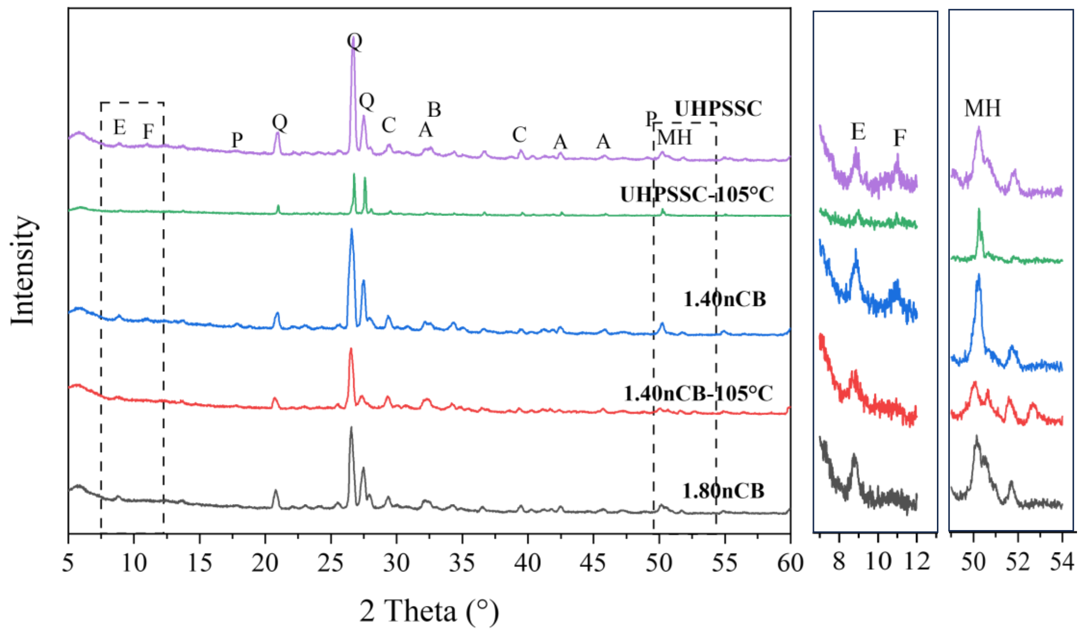

Figure 6.8. XRD patterns of A-Alite, B-Belite, C-Calcite, E-Ettringite, F-Friede's Salt, MH- magnesium hydroxide, P-Portlandite and Q-Quartz.

6.4.3 Piezoresistive Behaviour

In this study, the piezoresistive behaviour of nCB-UHPSSC was investigated under two different conditions: (1) testing directly after 28-day curing (i.e., saturated state); and (2) testing after 6 days of drying treatment at 70℃ in an oven (i.e., dried state).

6.4.3.1 Piezoresistive Behaviour at Saturated State

The electrical resistances of saturated nCB-UHPSSC specimens are shown in **Figure 6.9**, from which it can be inferred that the percolation threshold was achieved at 1.4% nCB content, while 1.6% and 1.8% nCB contents are in the above-percolation zone.

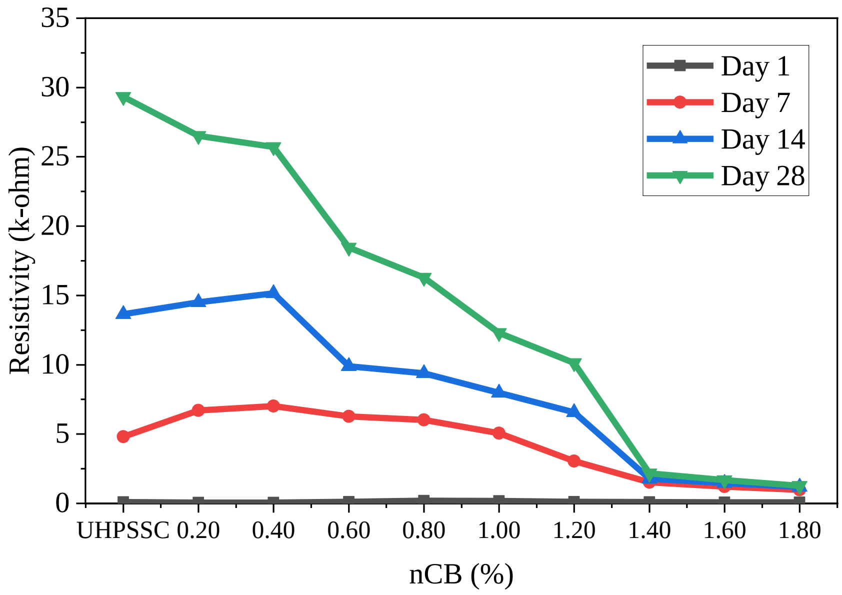

Figure 6.9. Electrical resistances of UHPSSC specimens with different nCB contents at different curing ages.

The piezoresistive responses of the saturated nCB-UHPSSC specimens during cyclic loading are presented in **Figure 6.10**. It is evident that the plain UHPSSC specimen already possesses piezoresistivity, although the FCR response is not well synchronized with the applied stress/strain. The piezoresistivity of plain UHPSSC purely comes from ionic conductivity in which the free ions in the pore solution act as an electrolyte for the electrical conductivity (Fulham-Lebrasseur et al., 2020; Hussain et al., 2022; Xie et al., 1996). Ionic movement is more pronounced in UHPSSC than in freshwater UHPC due to the high number of dissolved ions, which can be visualized in **Figure 6.11**. Notably, the dissolved ions (Na+, K^+, OH^-, Ca^{2+}, SO^{2}_{4} , and Cl^-) in the pore solution of seawater concrete can increase ionic strength by three to four times compared to their deionised water counterpart and reduce resistivity by 50% (Ebead et al., 2022; Montanari et al., 2019; Snyder et al., 2003). However, it is worth noting that the noise level in the piezoresistive response of the plain UHPSSC specimen is high, attributed to the polarization effect (Hong et al., 2018).

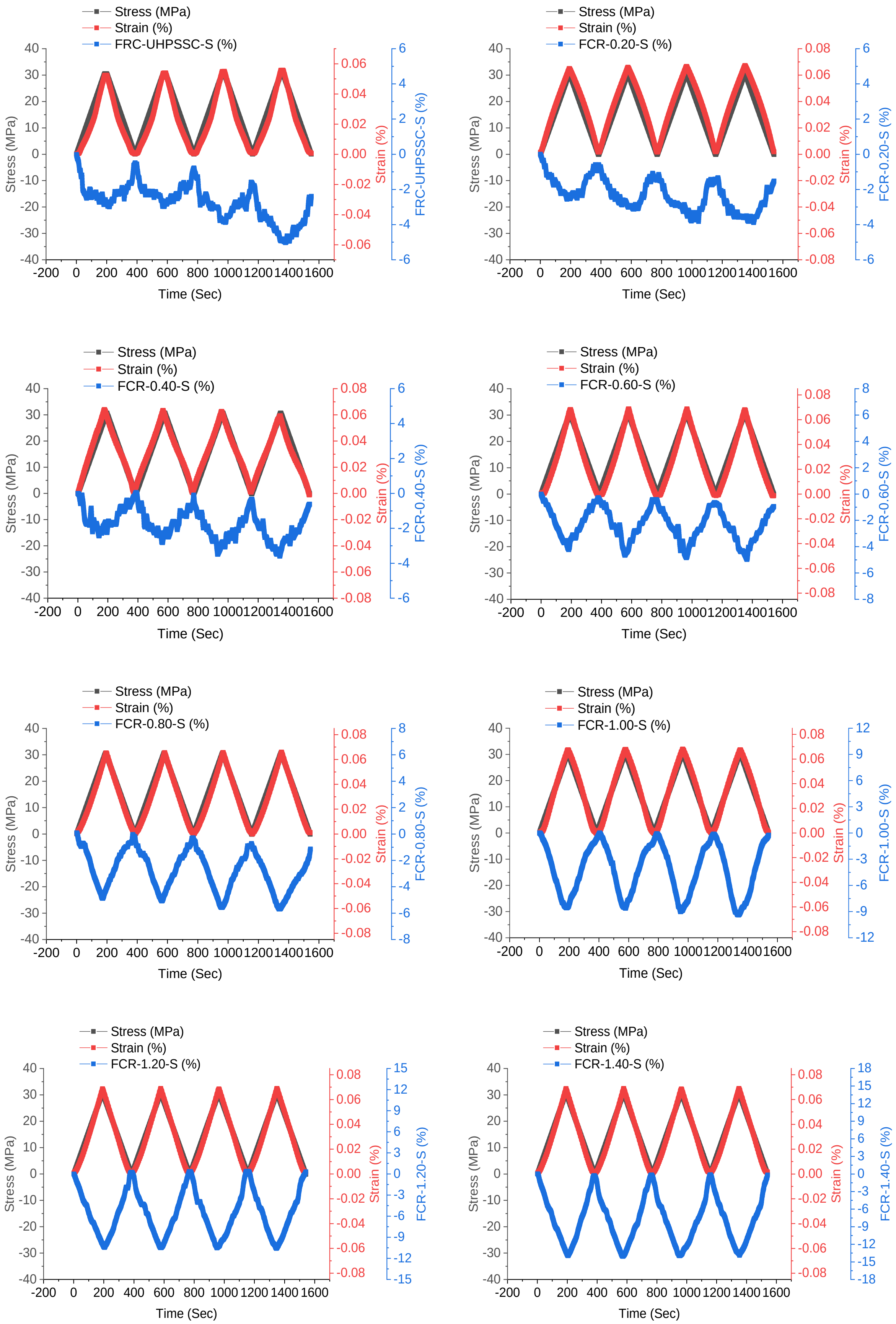
Stress (MPa)
Strain (%)
FRC-UHPSSC-S (%)
Time (Sec)
Stress (MPa)
Strain (%)
FCR-0.20-S (%)
Time (Sec)
Stress (MPa)
Strain (%)
FCR-0.40-S (%)
Time (Sec)
Stress (MPa)
Strain (%)
FCR-0.60-S (%)
Time (Sec)
Stress (MPa)
Strain (%)
FCR-0.80-S (%)
Time (Sec)
Stress (MPa)
Strain (%)
FCR-1.00-S (%)
Time (Sec)
Stress (MPa)
Strain (%)
FCR-1.20-S (%)
Time (Sec)
Stress (MPa)
Strain (%)
FCR-1.40-S (%)
Time (Sec)

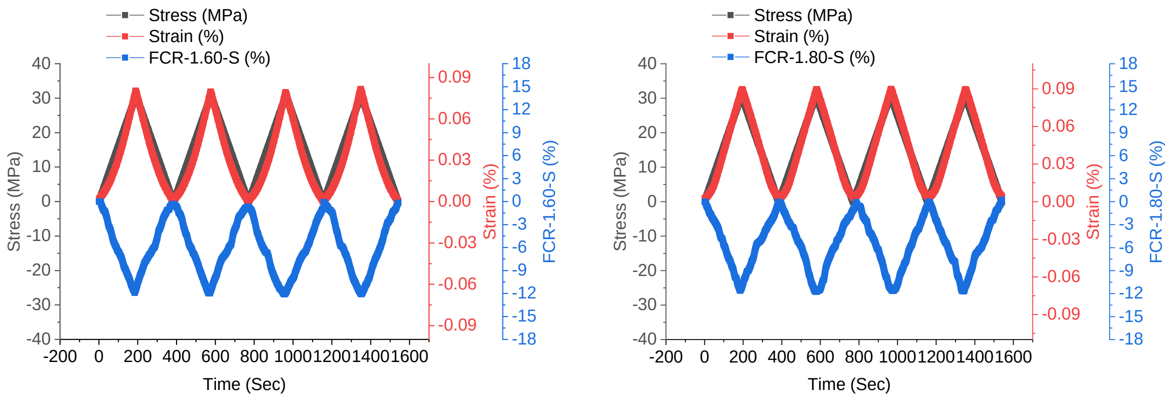

Figure 6.10. Piezoresistive responses of saturated UHPSSC specimens with different nCB contents during cyclic loading.

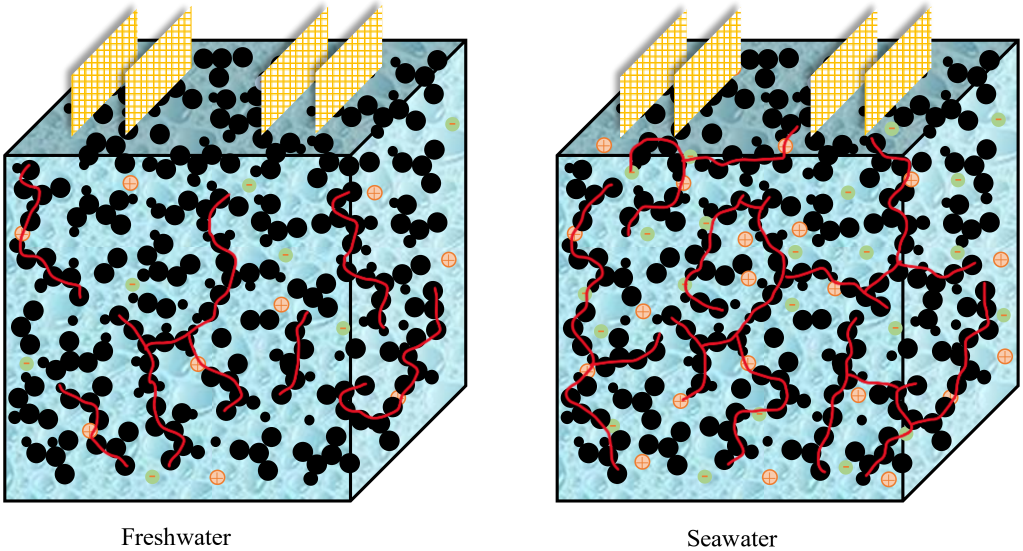

Figure 6.11. Schematic diagram of ionic conductivity in nCB-filled UHPC mixed with freshwater and seawater.

With an increase in nCB content, both the value and the repeatability of FCR response improve significantly. In nCB-UHPSSC, the distance between nCB particles is reduced when load is applied, and new conductive pathways are therefore constructed due to quantum tunnelling and direct contact between nCB particles. On the other hand, during unloading, the distance between nanoparticles increases, causing conductive pathways to break down and, hence, the resistance to increase again. The maximum FCR values of the 1.40nCB specimen, 1.60nCB specimen and 1.80nCB specimen are 13.96%, 12.07% and 11.74%, respectively. It is observed that FCR values reach the highest at 1.4% nCB content and then gradually decrease with a further increase in nCB content. It can be explained by the fact that at the above-percolation zone, the conduction network of nCB is well-established: even without loading, the neighbouring particles are already very close to, or in direct contact with, each other, so the conductive network is relatively stable. Therefore, the change in resistivity may not be as pronounced as those of specimens with less nCB.

Nevertheless, it is evident that perfect synchronization between FCR response and applied stress/strain can be achieved by all nCB-UHPSSC specimens with a nCB content of 1.40% and greater. From **Figure 6.12**, it can be observed that the FCR responses of all saturated UHPSSC specimens show an approximately linear correlation with the applied strain. The 1.40nCB specimen has the highest GF of 161.98 with a high coefficient of determination (R^2) of 0.99. The result aligns with the understanding that the highest sensitivity is usually achieved at the endpoint of the percolation zone (Han et al., 2019; Han et al., 2015; Hussain et al., 2022; Sun et al., 2017; Zhang et al., 2018).

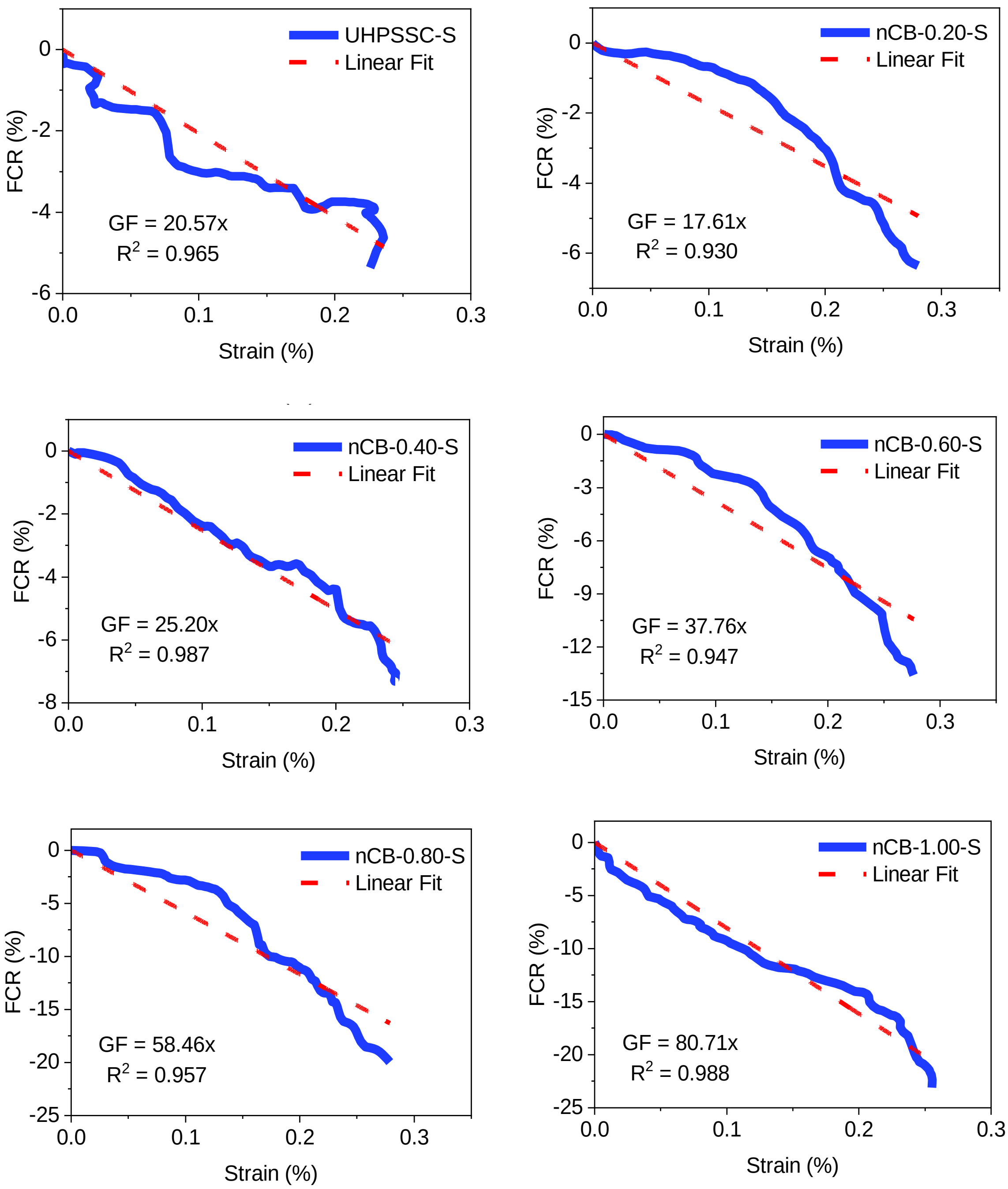
UHPSSC-S
Linear Fit
GF = 20.57x
R^2 = 0.965
FCR (%)
Strain (%)
nCB-0.20-S
Linear Fit
GF = 17.61x
R^2 = 0.930
FCR (%)
Strain (%)
nCB-0.40-S
Linear Fit
GF = 25.20x
R^2 = 0.987
FCR (%)
Strain (%)
nCB-0.60-S
Linear Fit
GF = 37.76x
R^2 = 0.947
FCR (%)
Strain (%)
nCB-0.80-S
Linear Fit
GF = 58.46x
R^2 = 0.957
FCR (%)
Strain (%)
nCB-1.00-S
Linear Fit
GF = 80.71x
R^2 = 0.988
FCR (%)
Strain (%)

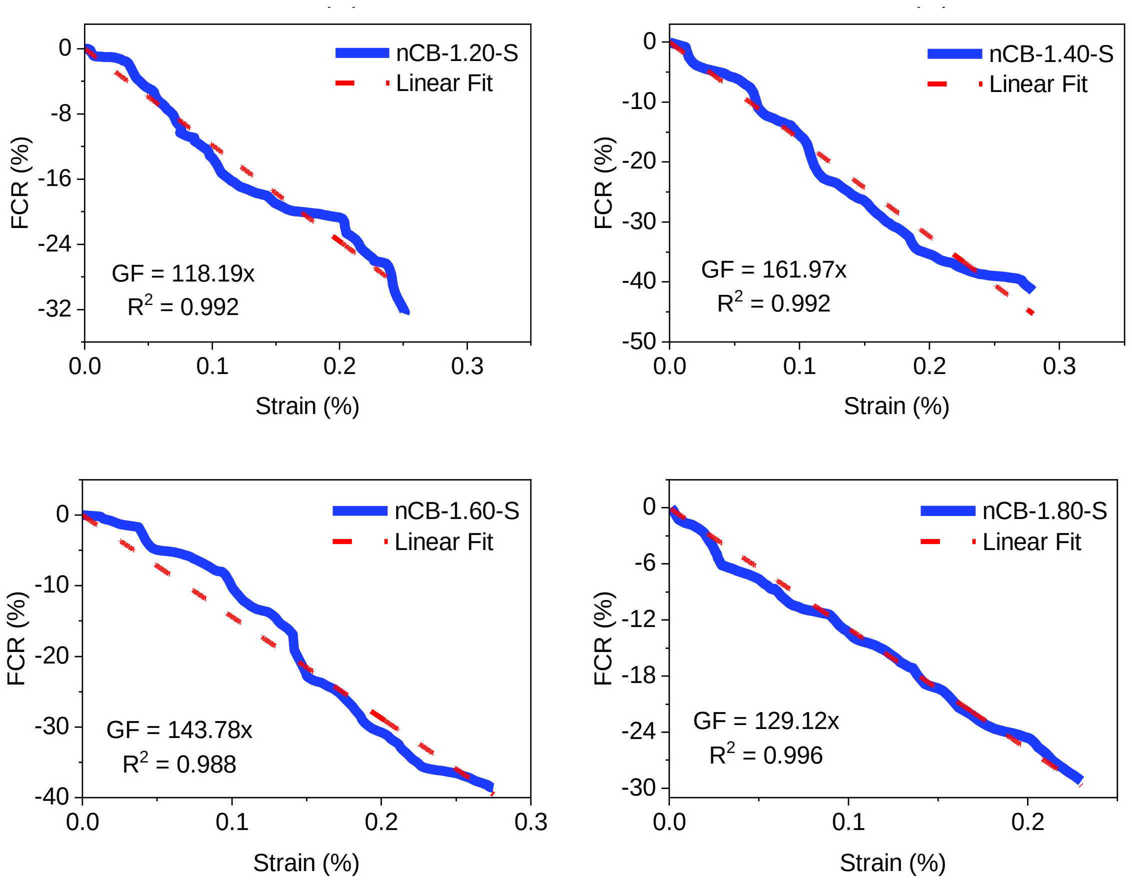

Figure 6.12. Piezoresistive responses of saturated UHPSSC specimens with different nCB contents during monotonic loading.

6.4.3.2 Effect of Drying Treatment

The piezoresistive behaviours of the dried specimens that underwent drying for six days at 70°C after completing the 28-day curing period were examined with a view to understand the impact of moisture content. The changes in electrical resistance during the drying process are depicted in **Figure 6.13**(a). After drying, a significant increase in resistance is observed for plain UHPSSC and nCB-UHPSSC with relatively low nCB contents. The change in resistance is not as pronounced for nCB-UHPSSC with relatively high nCB content, as its resistance has a relatively weak dependence on ionic conductivity.

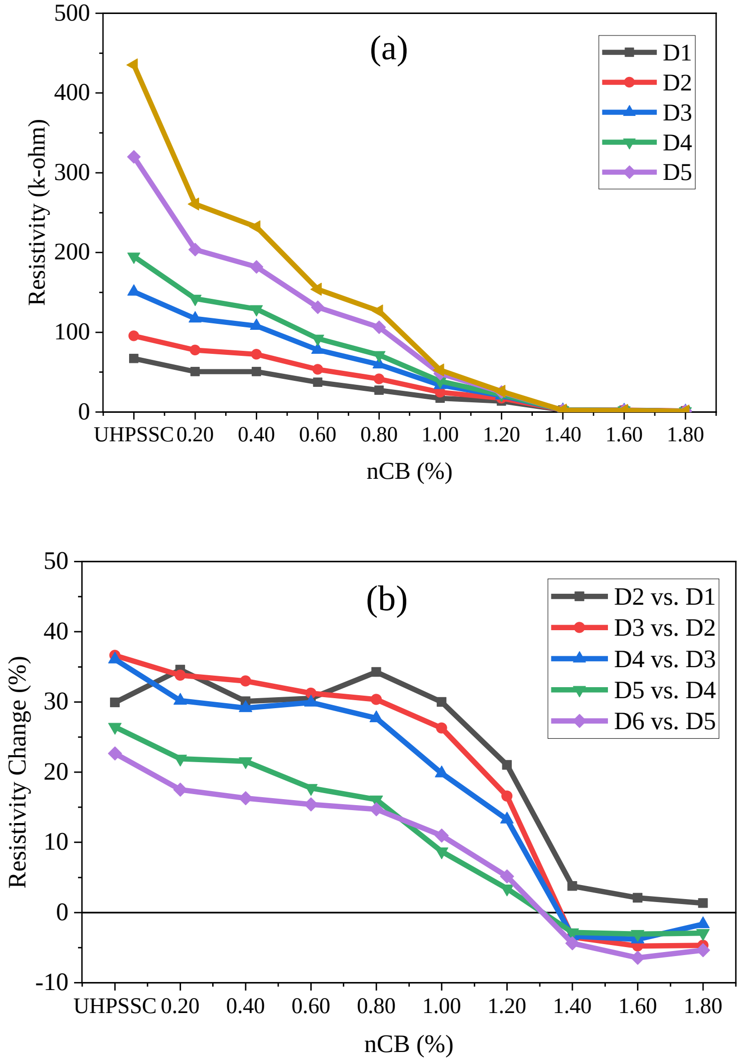

Figure 6.13. Changes in the electrical resistance of UHPSSC specimens with different nCB contents at different drying stages.

Furthermore, **Figure 6.13**(b) illustrates the variation in resistance change during the drying process. It is observed that from Day 1 to Day 2, resistance increases for all the specimens, but in later days, resistance actually decreases for the specimens at the above-percolation zone. This decrease in resistance can be attributed to the dominance of electronic conduction in these specimens, where conductivity comes from movement of electrons rather than movement of ions. In fact, drying treatment enhances conductivity by reducing the contact resistance between nCB particles induced by the moisture around the nCB particles

(Dong et al., 2019; Hussain et al., 2022). Furthermore, the dispersion of nCB in the 1.40nCB specimen (percolation threshold) was explored by using EDS mapping image of carbon element, which describes the distribution of nCB particles within the hardened 1.40% nCB-UHPSSC matrix, as illustrated in **Figure 6.14**. The red dots seen in the SEM-EDX image represent carbon, which enhances the piezoresistive sensitivity of the matrix by facilitating the formation of a highly stable and well-connected conductive network.

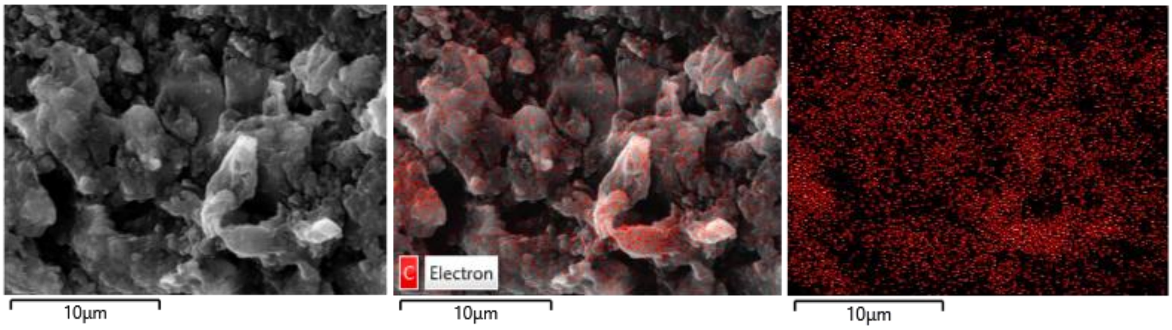

Figure 6.14. SEM-EDX mapping of carbon element (red dots) showing the dispersion of carbon in 1.40nCB-UHPSSC.

6.4.3.3 Piezoresistive Behaviour after Drying Treatment

The cyclic piezoresistive responses of the dried samples are displayed in **Figure 6.15**. It can be observed that the plain UHPSSC specimen shows no piezoresistivity. In **Figure 6.16**, FCR responses are plotted against the applied strain, again showing that the plain UHPSSC specimen has no strain sensitivity. This is consistent with the observation of the authors' previous study on freshwater nCB-UHPC (Hussain et al., 2022). Although UHPSSC has a higher ionic strength in its pore solution compared to normal UHPC, the drying treatment eliminates the ionic conductivity, which was the primary source of the conductivity of saturated plain UHPSSC.

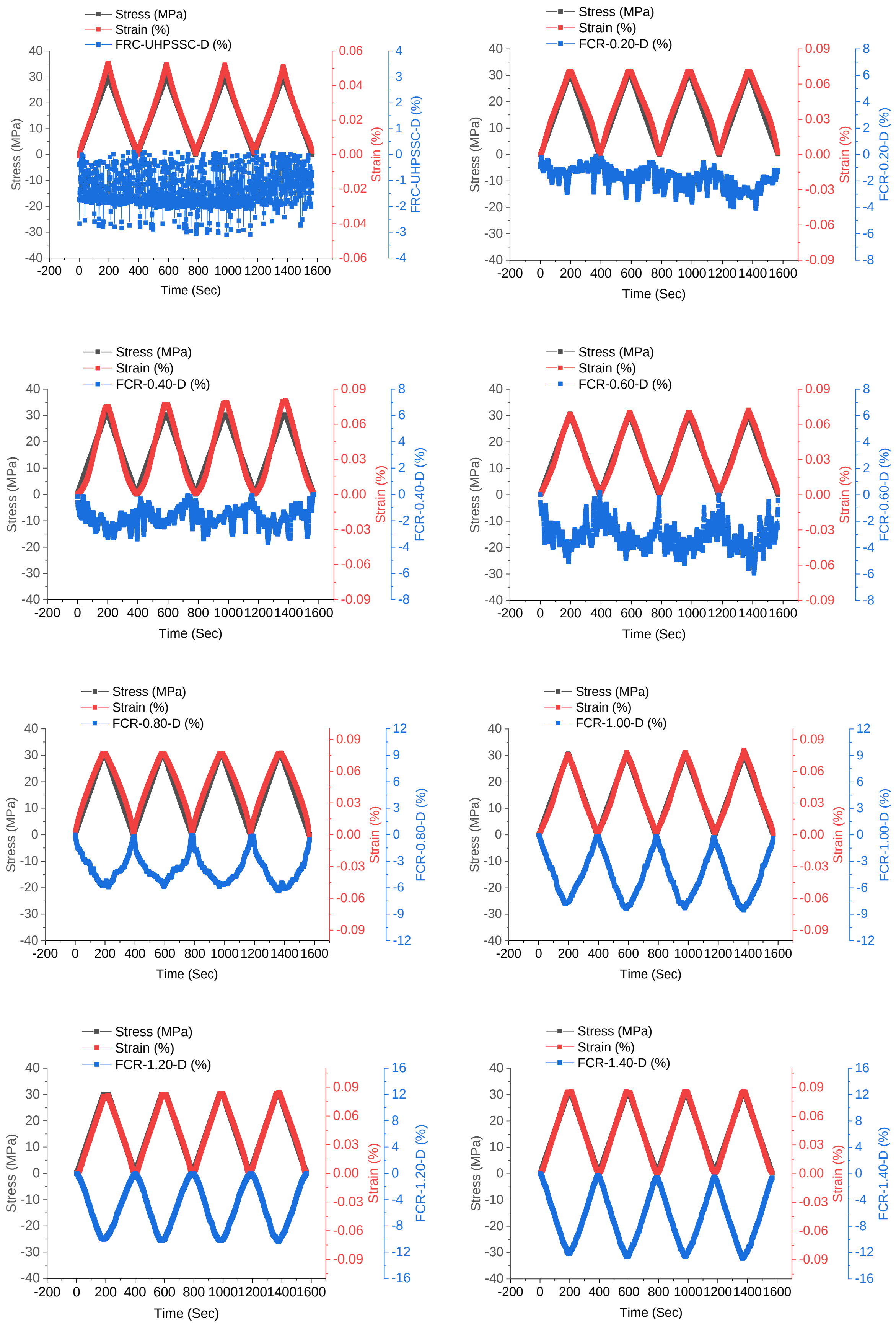
Stress (MPa)
Strain (%)
FRC-UHPSSC-D (%)
FCR-0.20-D (%)
FCR-0.40-D (%)
FCR-0.60-D (%)
FCR-0.80-D (%)
FCR-1.00-D (%)
FCR-1.20-D (%)
FCR-1.40-D (%)
Time (Sec)

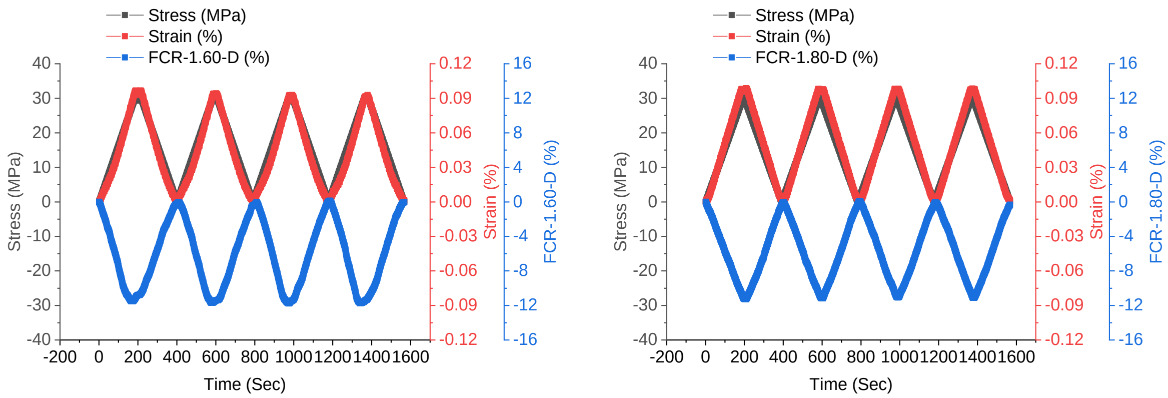

Figure 6.15. Piezoresistive responses of dried UHPSSC specimens with different nCB contents during cyclic loading.

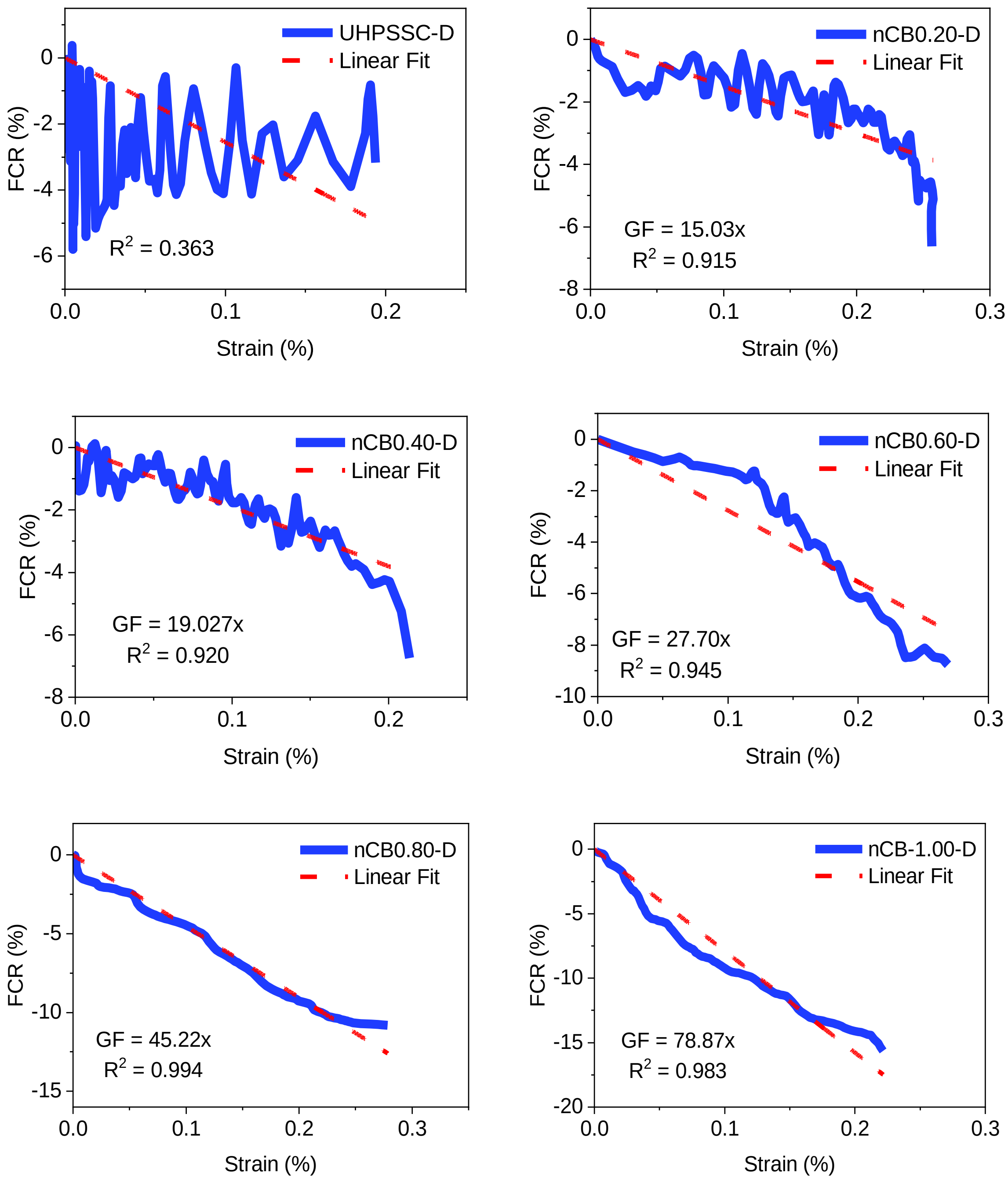
UHPSSC-D
Linear Fit
R^2 = 0.363
nCB0.20-D
Linear Fit
GF = 15.03x
R^2 = 0.915
nCB0.40-D
Linear Fit
GF = 19.027x
R^2 = 0.920
nCB0.60-D
Linear Fit
GF = 27.70x
R^2 = 0.945
nCB0.80-D
Linear Fit
GF = 45.22x
R^2 = 0.994
nCB-1.00-D
Linear Fit
GF = 78.87x
R^2 = 0.983
FCR (%)
Strain (%)

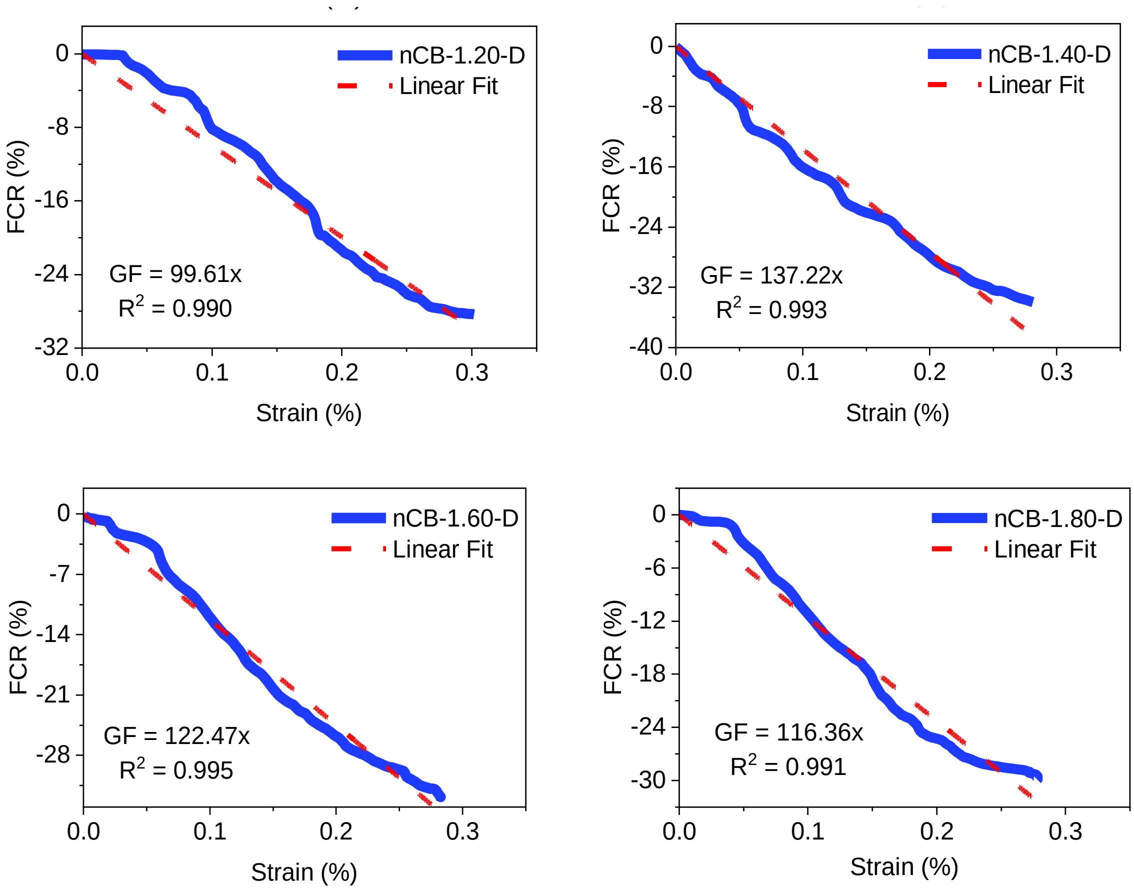

Figure 6.16. Piezoresistive responses of dried UHPSSC specimens with different nCB contents during monotonic loading.

With 0.6% nCB content, the FCR response of the specimen exhibits some synchronization with the applied stress/strain, but the noise is still high. By contrast, the FCR response of the 0.80nCB specimen shows a good synchronisation with the applied stress/strain. With 1% nCB content and higher, the FCR responses of the specimens may be considered precisely synchronized with the applied stress/strain. Among all, the 1.40nCB specimen possesses the highest GF of 137.22 with a high R^2 value of 0.99. Furthermore, **Figure 6.17** compares the GFs of all the saturated and dried samples, showing that the GF of the saturated 1.40nCB specimen is around 18.0% higher than that of its dried counterpart. This is due to the existence of large quantities of dissolved ions in seawater, as explained above. However, at the above-percolation zone, GF decreases with nCB content for both saturated and dry specimens.

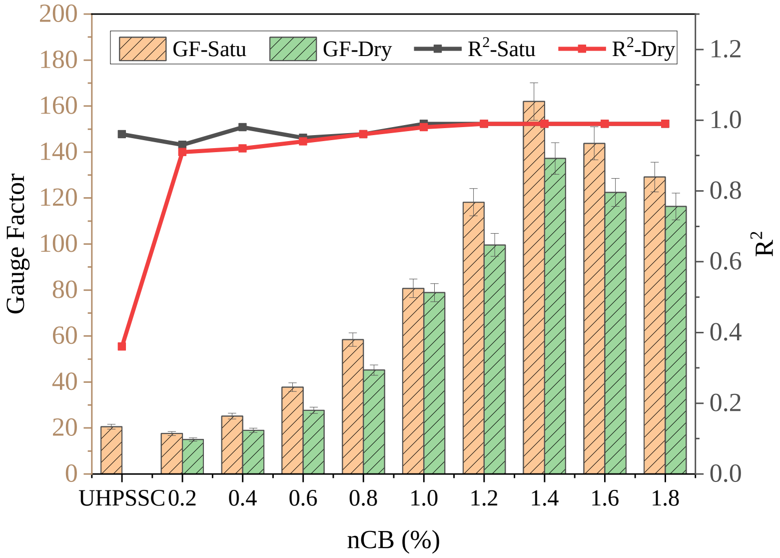

Figure 6.17. Strain sensitivities of saturated and dried UHPSSC specimens with different nCB contents.

6.5 Summary and Conclusions

This chapter has presented a study aiming to develop a novel type of intrinsic self-strain sensing concrete by utilising UHPSSC with the addition of cost-effective nCB as a functional filler (i.e., nCB-UHPSSC). A comprehensive experimental program and extensive test results have been presented, including the formulation of new mix designs, mechanical properties, microstructure analysis, as well as the piezoresistive behaviour and conduction mechanism of the developed nCB-UHPSSC with different nCB contents (up to 1.80%). The following conclusions can be drawn from this study:

1. Although the addition of nCB generally decreases the workability and compressive strength of UHPSSC, nCB-UHPSSC with reasonably good properties (i.e., slump spread > 160 mm, compressive strength > 140 MPa) was successfully achieved. The compressive strength of nCB-UHPSSC can be considerably increased by one-day dry curing at 105℃ ± 1℃ after 28-day water immersion.
2. Both the saturated and dried nCB-UHPSSC specimens showed very well-synchronized FCR responses with the applied stress/strain when the nCB content is equal to or higher than 1.0%. Although the dried plain UHPSSC specimen does not show any piezoresistive behaviour, the saturated specimen possesses piezoresistivity due to the large quantities of dissolved ions in seawater.
3. The strain sensitivity of the nCB-UHPSSC increases with nCB content up to 1.40%. The highest GFs of the nCB-UHPSSC with 1.40% nCB content are 161.98 and 137.22 for saturated and dried samples, respectively.

In summary, the newly developed nCB-UHPSSC exhibits outstanding mechanical and piezoresistive properties, making it a promising candidate for the practical monitoring of civil infrastructure in the field. Its low percolation threshold (i.e., 1.4%) and stable piezoresistive behaviour are particularly advantageous for field applications, while the use of low-cost nCB as conductive fillers makes the new concrete highly cost-effective. Additionally, the use of sustainable materials such as seawater and sea-sand contributes to achieving the development of sustainable infrastructure with reduced energy consumption and carbon emissions. Therefore, nCB-UHPSSC is an economically viable and environmentally friendly option for marine and coastal infrastructure applications.

Chapter 7.

Effects of Temperature and Accelerated Exposure on Seawater and Sea-sand-based Nanocarbon Black-reinforced Ultra-High-Performance Concrete

7.1 Abstract

Our previous study developed UHPSSC by incorporating nCB, demonstrating reasonable mechanical and piezoresistive performance at 1.40% nCB content (1.40nCB). Therefore, this study aims to explore its durability parameters by investigating the compressive strength and microstructural characteristics of UHPSSC with 1.40nCB under different curing conditions and exposure durations. Additionally, it explores the influence of in-situ temperature variations on the piezoresistive properties to gain insights into the sensitivity and reliability of the self-sensing capabilities.

The results demonstrate that the compressive strength of samples subjected to normal water curing (NWC) is higher than that of samples with seawater curing (SWC) for both UHPSSC and 1.40nCB. However, exposure to sea salt solution for up to 90 days decreased compressive strength. Furthermore, the study reveals that the fractional change in electrical resistivity (FCR) increases with rising temperature. The piezoresistive response at cyclic loading exhibited a well-synchronized relationship with stress-strain under all tested conditions. However, the strain sensitivity at elevated temperatures initially decreases and then increases compared to ambient temperature, thanks to the increasing strain response with

temperature. Additionally, the sensitivity at freezing temperatures and exposure to sea salt solution decreases relative to ambient temperature.

7.2 Introduction

Chapter 6 has presented the development of nCB-based ultra-high-performance seawater sea-sand concrete (nCB-UHPSSC) with self-sensing capabilities (Hussain et al., 2024). This chapter presents further investigations on the mechanical and piezoresistive properties of nCB-UHPSSC under various working conditions. The experimental programme focused on nCB-UHPSSC with 1.40% nCB, which is the optimum content found in Chapter 6. The compressive strength and microstructural characteristics under different curing conditions and exposure durations were examined. Additionally, the influence of in-situ temperature variations on the piezoresistive properties was examined to gain insights into the sensitivity and reliability of the self-sensing capabilities of nCB-UHPSSC.

7.3 Experimental Program

7.3.1 Raw Materials and Mix Design

This study utilised the raw materials described in section 6.2.1. The mix design and quantities of materials are detailed in **Table 7.1**.

Table 7.1. Base mix design of UHPSSC and 1.40nCB-UHPSSC (kg/m^3).

Notation	Cement	SF	QP	Sand	Water	SP	nCB
PC	842.0	210.5	210.5	926.2	172.6	42.1	0.00
1.40nCB	842.0	210.5	98.5	793.2	172.6	42.1	14.74

7.3.2 Curing Conditions

After demoulding the specimens, different types of curing conditions and duration were studied, including 28 days of normal water immersion curing (NWC), 28 days of seawater immersion curing (SWC) and 90 days of exposure in seawater after the 28 days of NWC for durability consideration.

The remaining testing details are given in section 4.2.5.

7.3.3 Sea-salt Solution Exposure

After 28 days of curing, the samples were put in a sea-salt solution with a salinity of 3.5% for 90 days to investigate the mechanical properties of the plain UHPSSC and 1.40nCB samples.–The 1.40nCB samples were further explored for piezoresistive behaviour after exposure to a sea-salt solution for the duration of 90 days. The samples were tested for repeatability (cyclic loading response) and sensitivity (monotonic loading response). Before testing, the samples were air-dried for one day after taking out from the exposure unit.

7.3.4 Microstructure Analysis

The details of the microstructure analysis are the same as those listed in section 5.2.6, including SEM-EDX, XRD and MIP, respectively.

7.3.5 Piezoresistive Properties

For the piezoresistive testing, all the 40 mm cubic samples were dried after 28 days of normal water curing in an oven at a temperature of 70°C for a period of five days before conducting the test to minimize the impact of water content on the piezoresistive properties. After the drying process, different temperature ranges were selected to test what the material may encounter during its service life. This is because extreme temperatures can significantly impact the structural integrity and performance of the concrete. The samples were tested to investigate the piezoresistive behaviour under different temperatures including, -25℃, 0℃, ambient temperature (25℃ (23℃±2℃)), 50℃ and 75℃. The specimen was placed in an environmental chamber for one hour at each temperature before testing to ensure thermal equilibrium between the external and internal temperatures. The load was then applied while the sample remained in the environmental chamber to maintain equilibrium at the respective temperature. The experimental setup can be seen from **Figure 7.1**. The specimens were subjected to using a universal testing machine (Instron 5982, Instron Inc., USA). The cyclic compressive loading test was performed by using a universal testing machine (Instron 5982, Instron Inc., USA) with an environmental chamber to achieve a minimum temperature of -150 °C using a liquid nitrogen cooling module. This setup allowed for the evaluation of the concrete's performance under controlled temperature conditions. A temperature was recorded separately by a thermocouple. Before loading, 15V DC power was applied to the samples to minimize the influence of the polarization for about 20 minutes (Hussain et al., 2019).

The remaining testing details are the same as those listed in section 4.2.6.

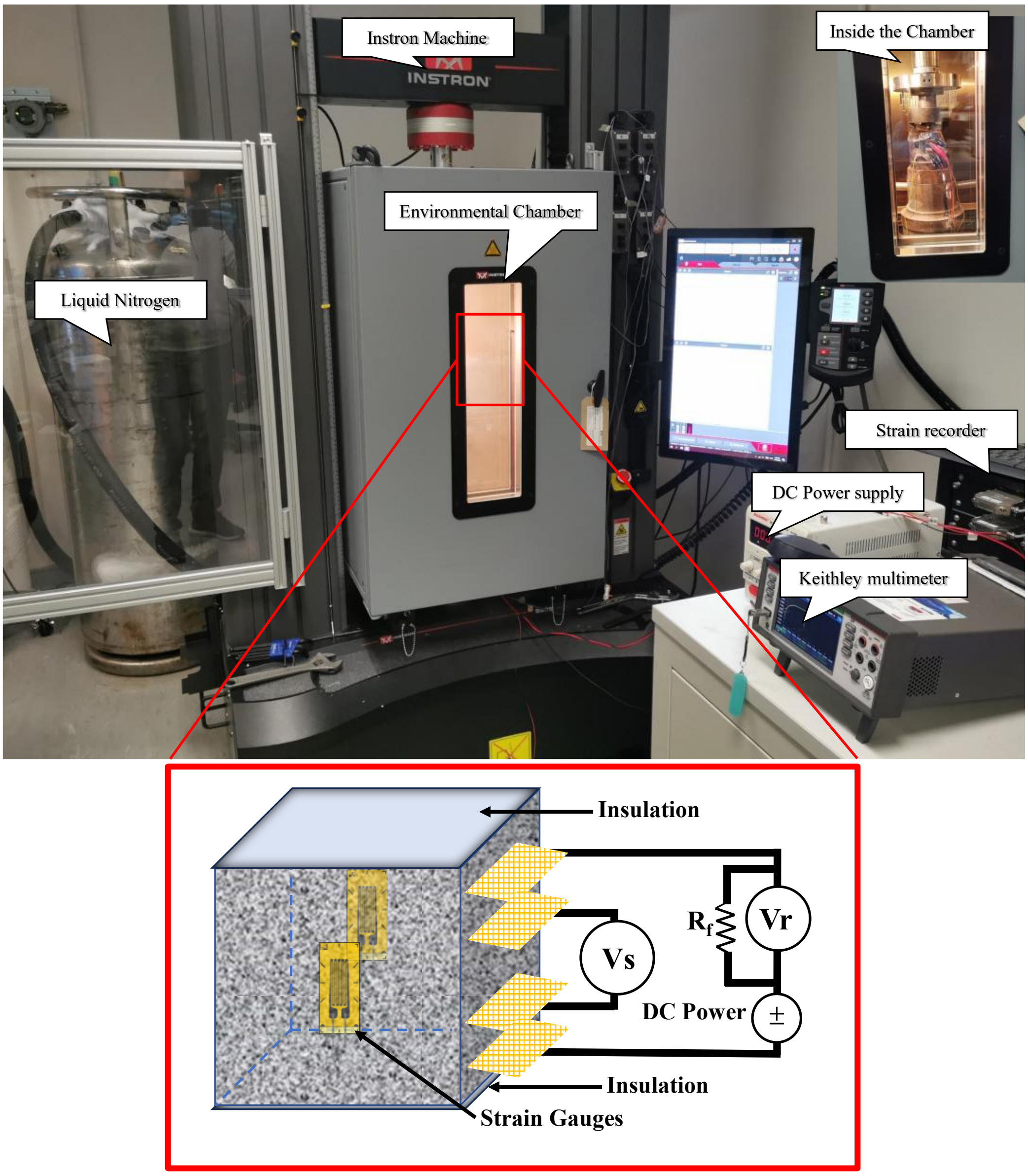

Figure 7.1. Experimental setup and circuit diagram to measure the piezoresistive behaviour of nCB-UHPSSC samples under different temperatures.

7.4 Results and Discussions

7.4.1 Sorptivity Test

The sorptivity test of both plain UHPSSC and 1.40nCB was conducted according to ASTM C 1585-20 (C1585-20, 2020). The testing setup and details are the same as those detailed in section 5.2.2. The absorption rate of the sample is described as the slope of the line that best fits water uptake (*I*) plotted against the square root of the time ($h^{1/2}$). There are two phases, called initial absorption and secondary absorption, described in the code. For normal concrete, the initial absorption is from 0 to 6 hours, and the secondary absorption is from 1 day to 9 days. According to (Lu et al., 2021), this study adopted a 49-day cycle of secondary absorption because of the highly dense microstructure and low absorption rate of the UHPSSC. The water absorption rate of unsaturated concrete quantifies its ability to absorb and transport water, which directly influences its durability. A lower sorptivity is a strong indication of durability improvement. The sorptivity measurement of the 1.40nCB and plain UHPSSC is presented in **Figure 7.2**.

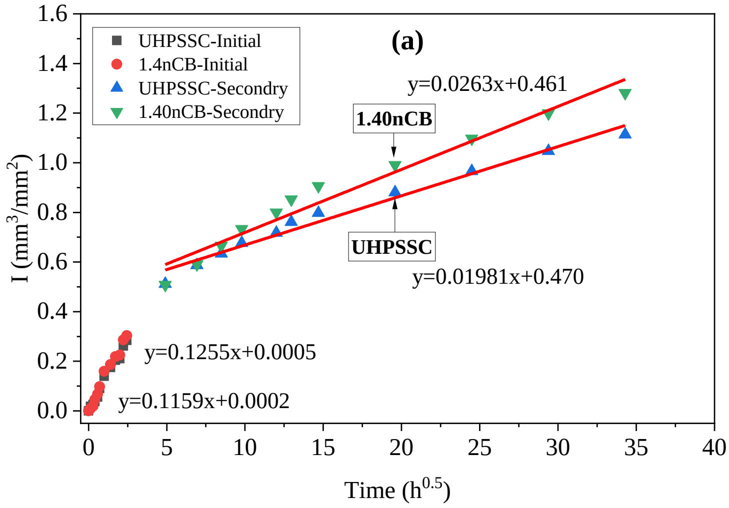

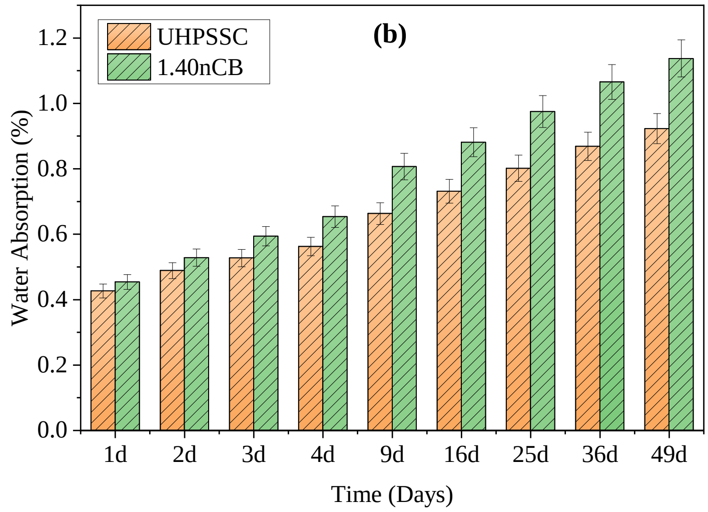

Figure 7.2. Sorptivity of plain UHPC and 1.40nCB. (a) The amounts of water absorbed per unit area in the initial and secondary phases. (b) The total amount of water absorbed.

In the initial absorption, the water uptake of the plain UHPSSC and 1.40nCB samples was steadily fast, with a maximum value of 0.115 mm/$h^{0.5}$ and 0.125 mm/$h^{0.5}$ after 6 hours. The 1.40nCB had 7.65% higher absorption rate than UHPSSC. Similarly, in the secondary absorption stage, a maximum value of 0.0198 mm/$h^{0.5}$ and 0.0263 mm/$h^{0.5}$ after 49 days, respectively. The 1.40nCB had 24.11% higher absorption rate than plain UHPSSC, which means that 1.40nCB has a higher sorptivity than UHPSSC in both the initial and secondary absorption stages. On the other hand, the cumulative water absorption of the plain UHPSSC and 1.40nCB after 49 days is 0.923% and 1.138%, respectively, about 8-12% for normal strength concrete after nine days (Lu et al., 2022). The water absorption of the 1.40nCB is about 18.87% higher than the UHPSSC, and the reason behind this is believed to be its higher porosity by lower flowability, improper compaction and the agglomeration of the nCB particles (Hussain et al., 2022).

7.4.2 Effect of Curing Conditions on Mechanical Properties

After demoulding the specimens, different types of curing conditions were studied for the compressive strength of the UHPSSC and 1.40nCB samples: 28 days of normal water immersion curing and 28 days of seawater immersion curing. According to ASTM C109 (C109/C109M-21, 2021), 50 mm cubic samples were prepared for the compressive strength tests. Three specimens were tested for each curing system to obtain an average value. The loading rate was 1 MPa/s applied for the compression test. **Figure 7.3** illustrates that the samples subjected to normal water curing (NWC) exhibit higher compressive strength than the seawater curing (SWC).

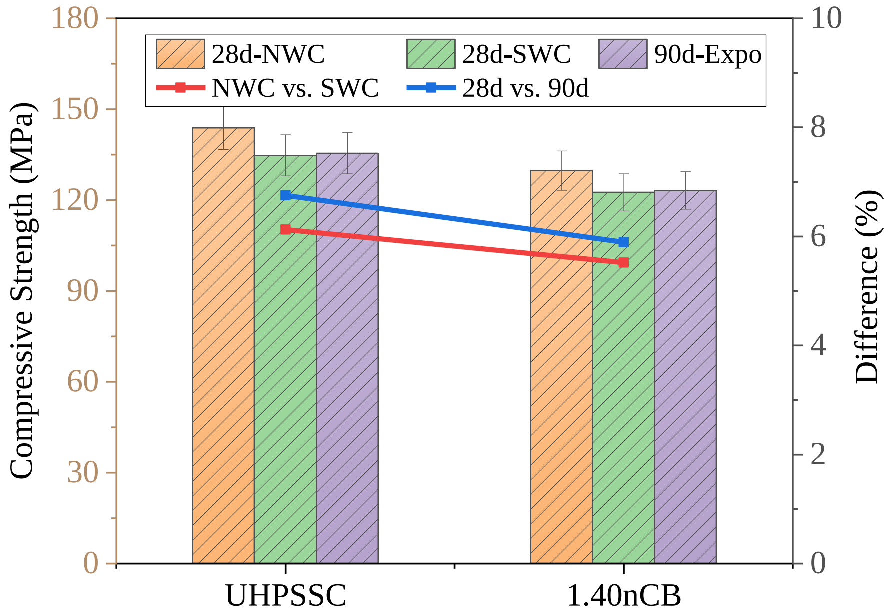

Figure 7.3. Compressive strengths of the UHPSSC and 1.40nCB at different curing conditions and exposure durations.

The lower compressive strength of SWC over NWC is attributed to higher concentrations of salts in seawater that can react with the cementitious components of concrete, leading to the formation of secondary compounds and altering the hydration process. Notably, the amount of ettringite formed in seawater systems is 67% greater than that produced in freshwater after 28 days of curing. The increased levels of portlandite, ettringite, and Friedel's salt may reduce the volume fraction of C-S-H gel relative to the total hydration products over time (Zhao et al., 2021). A molecular dynamic study also found that the ions of NaCl ingress in C-S-H nanochannels change the interfacial bonding and also cause the leaching of Ca, which leads to reduced strength (Hayat et al., 2024). These mechanisms can affect the development of the microstructure of the concrete and result in the reduction of strength. Moreover, sulphate ions can react with the hydration products of cement, forming expansive compounds like secondary ettringite or gypsum. These expansive compounds can generate internal stresses within the concrete, resulting in cracking and reduced compressive strength.

In addition, it can be seen in **Figure 7.4**(a-b) that the formation of magnesium hydroxide $Mg(OH)_2$ and cracks formation by expansion of the volume of the system.

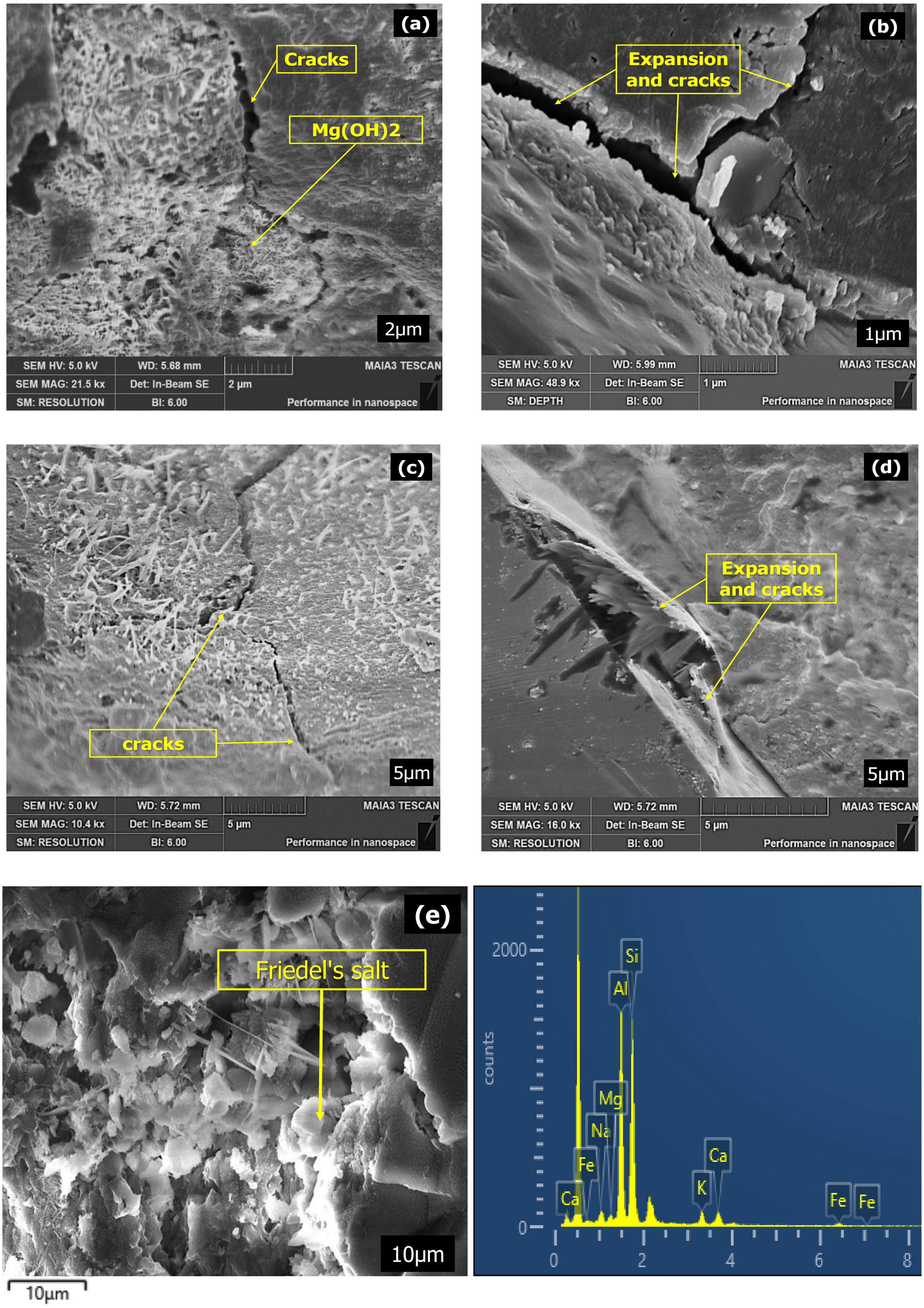
(a)
Cracks
Mg(OH)2
2µm
SEM HV: 5.0 kV
WD: 5.68 mm
MAIA3 TESCAN
SEM MAG: 21.5 kx
Det: In-Beam SE
2 µm
SM: RESOLUTION
BI: 6.00
Performance in nanospace
(b)
Expansion and cracks
1µm
SEM HV: 5.0 kV
WD: 5.99 mm
MAIA3 TESCAN
SEM MAG: 48.9 kx
Det: In-Beam SE
1 µm
SM: DEPTH
BI: 6.00
Performance in nanospace
(c)
cracks
5µm
SEM HV: 5.0 kV
WD: 5.72 mm
MAIA3 TESCAN
SEM MAG: 10.4 kx
Det: In-Beam SE
5 µm
SM: RESOLUTION
BI: 6.00
Performance in nanospace
(d)
Expansion and cracks
5µm
SEM HV: 5.0 kV
WD: 5.72 mm
MAIA3 TESCAN
SEM MAG: 16.0 kx
Det: In-Beam SE
5 µm
SM: RESOLUTION
BI: 6.00
Performance in nanospace
(e)
Friedel's salt
10µm
10µm
2000
counts
0
Si
Al
Mg
Na
Fe
Ca
Ca
K
Fe
Fe
0
2
4
6
8

Figure 7.4. Microstructure showing the formation of the secondary products, expansion and cracks. (a-d) the formation of $Mg(OH)_2$, and cracks (e) SEM-EDX formation of Friedel's salt at sea-salt solution exposure.

On the other hand, the 1.40nCB had a lower compressive strength than the UHPSSC. The difference between UHPSSC and 1.40nCB at NWC and SWC is 10.90% and 10.26%, respectively. It could be articulated that the nCB particles absorbed a high amount of water content at the initial stage, and also, the low w/b ratio of the UHPSSC matrix resulted in slowing down the hydration process and left many anhydrous cement clinker phases (Lu et al., 2021; Zhang et al., 2022). Similarly, with the high surface energy of nanofillers, the cement particles were surrounded by these nCB which delayed the hydration process by obstructing the water molecule from reacting with unhydrated cement (Hussain et al., 2022). Moreover, the lower flowability, improper compaction, and a high number of agglomerations of nCB created a more porous microstructure (Hussain et al., 2023). Additionally, it can be observed that the reduction ratio between the NWC to SWC of the 1.40nCB is lower than that of the UHPSSC. This can be attributed to the greater pore volume of 1.40nCB, which effectively dissipated the pressure generated by the volumetric expansion of the microstructure, suggesting that the larger pore volume could contribute to its ability to withstand expansion-induced pressure.

7.4.3 Effect of Sea-salt Solution Exposure on Mechanical Properties

The samples cured with normal water were exposed to the 3.5% sea salt solution for 90 days. The compressive strength of 1.40nCB and UHPSSC after 90-day exposure is lower than the 28-day NWC samples, as seen in **Figure 7.3**. Similar to other curing systems, the 1.40nCB-90d had a lower reduction ratio than the UHPSSC-90d. The reduction in strength is attributed to the formation of secondary hydration products, which can induce the expansion of volume and microcrack formation, leading to reduced mechanical strength. It is evident from the SEM micrographs shown in **Figure 7.4**(c-d) that the formation of ettringites has led to the formation of the crack due to the expansion of the matrix (Taylor et al., 2001). It can also be found in the literature that the high salt content in the solution can lead to the formation of secondary compounds and the crystallization of salts within the pore structure, and the growth of salt crystals can exert pressure on the surrounding, leading to internal damage and cracking (Ting et al., 2021; Yang et al., 2022). When concrete is exposed to sea salt solution, chloride ion reacts with calcium aluminate (C_3A) and monosulphoaluminate (AFm) to form Friedel's salt ($3CaO\ Al_2O_3\ CaC_{l2}\cdot 10H_2O$) (Baroghel-Bouny et al., 2012; Birnin-Yauri & Glasser, 1998; Lubelli et al., 2006; Rocha et al., 2015).

On the other hand, a Mercury Intrusion Porosimeter (MIP) was employed to investigate the pore structure of the UHPSSC and 1.40nCB with different curing conditions and exposure durations. The cumulative and incremental pores of the UHPSSC and 1.40nCB are presented in **Figure 7.5**(a-b) under various conditions. **Figure 7.5**(a) describes the cumulative pore concentration of the different samples, representing the area under the curve. The pore distribution with different diameters is detailed in **Figure 7.5**(b). According to the literature (Ali et al., 2023; Li, 2021; Wang et al., 2018), the pores in cement-based materials are divided into three distinct categories, including harmless pores (<20 nm), less harmful pores (20-200 nm) and harmful pores (>200 nm). The harmful pores include the capillary and meso pores, which are mainly responsible for reducing strength and durability.

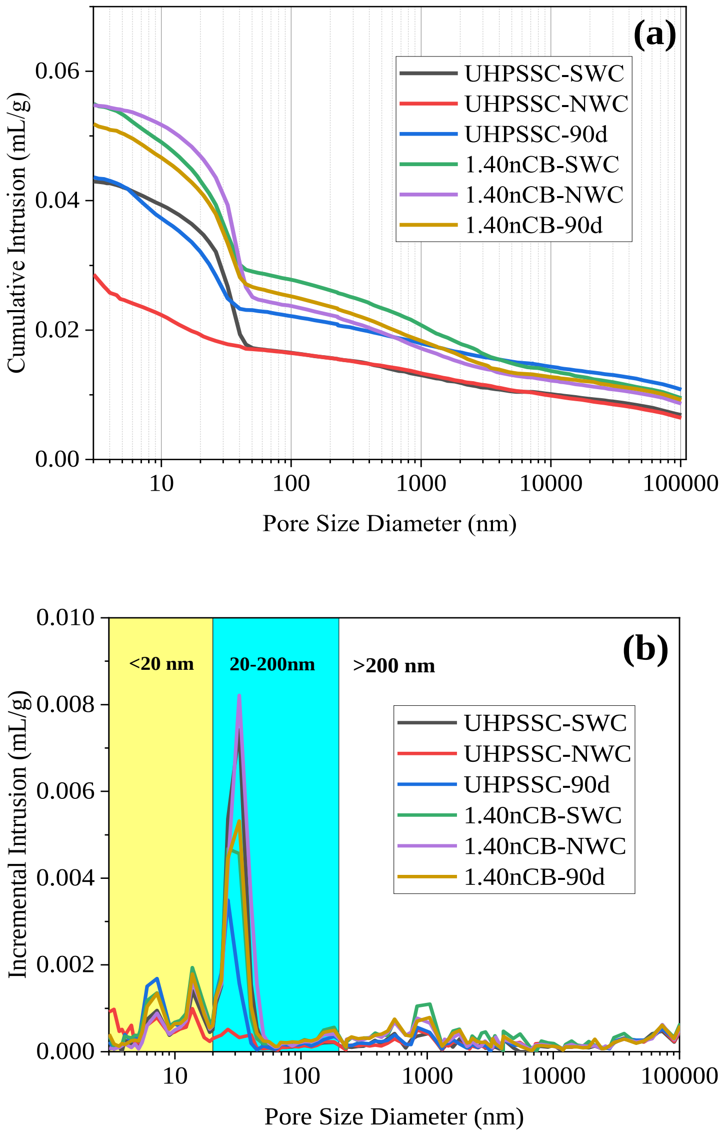

Figure 7.5. Cumulative and intrusion pore structures of the plain UHPSSC mixes and 1.40nCB mixes obtained under different curing environments and exposure duration.

The total porosity of UHPSSC cured with seawater and normal water at 28 days was 9.47% and 8.59%, respectively, which are slightly higher than normal UHPC with heat curing (Matos et al., 2021; Vande Voort et al., 2008). The difference in porosity between UHPSSC-NWC and UHPSSC-SWC indicates that the samples cured with normal water had a less porous microstructure compared to those cured with seawater. On the other hand, the porosity of the 1.40nCB-SWC and 1.40nCB-NWC was 10.986% and 10.890%, which is about a 0.87%

difference in the porous microstructure. The higher porosity of 1.40nCB would help to dissipate the pressure generated by volumetric expansion. Moreover, the 1.40nCB exhibited a more porous microstructure than UHPSSC due to its lower flowability and compaction and higher water absorption capacity of nCB nanoparticles. Furthermore, the reduction ratio of UHPSSC to 1.40nCB with SWC was more significant than that with NWC. Interestingly, after 90 days of exposure, UHPSSC and 1.40nCB exhibited a less porous microstructure compared to 28 days of SWC, indicating that the curing conditions have a greater impact than the exposure (cured in normal water and exposure to seawater).

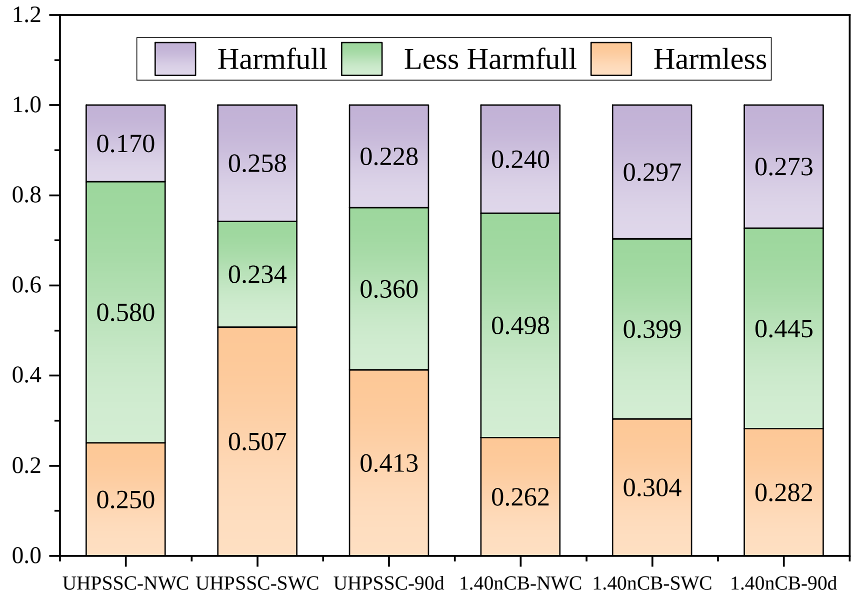

Figure 7.6 Pore size distribution ratios of UHPSSC and 1.40nCB at different curing environments and exposure duration.

Moreover, further analysis of the pore size distribution data in **Figure 7.6** shows that UHPSSC-SWC had a higher number of harmful pores than UHPSSC-NWC. Similarly, the 1.40nCB sample had a similar trend with UHPSSC in that the 1.40nCB-SWC had a higher ratio of harmful pores than 1.40nCB-NWC. However, the effect of SWC appears to be less pronounced for 1.40nCB, which could be attributed to a larger room for expansion in 1.40nCB than the UHPSSC. On the other hand, when comparing the specimens after 90d exposure of

UHPSSC and 1.40nCB, it is observed that both exhibited a higher proportion of harmful pores compared to the specimens after 28d curing.

Additionally, **Figure 7.7** provides the X-ray Diffractometer (XRD) patterns of various chemical compositions found in different samples under different curing conditions. The patterns indicate the presence of distinct peaks associated with quartz, a component of the quartz powder utilized in UHPSSC. Notably, no new chemical phases are visible due to the inclusion of nCB, as nCB is an inert nanomaterial (Li et al., 2024; Zhang et al., 2022). Inert nanofillers, such as nCB, do not actively participate in the cement hydration process but can serve as nucleation sites and potentially slow the cement hydration process (Han et al., 2017). The absence of new chemical phases in the XRD patterns suggests that incorporating nCB does not introduce significant changes in the chemical composition of the UHPSSC.

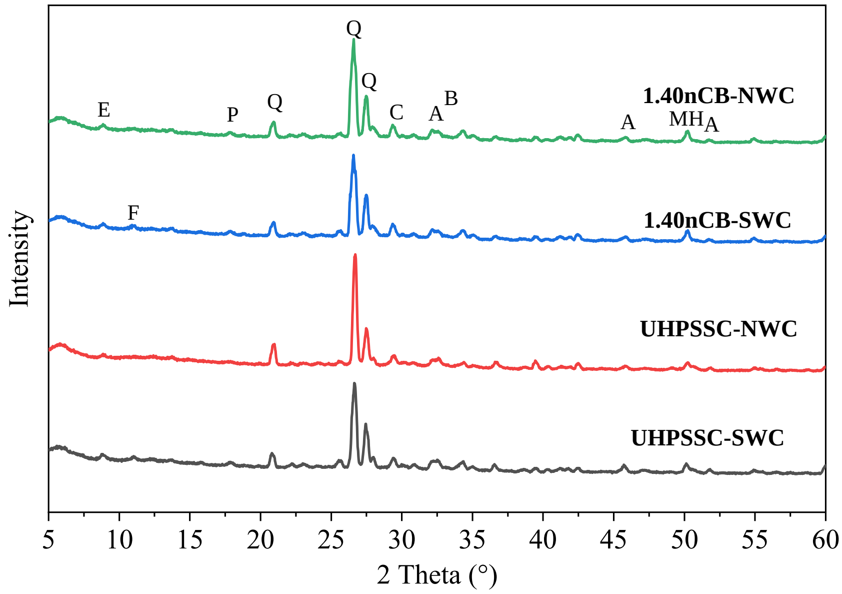

Figure 7.7. XRD patterns of the A-Alite, B-Belite, C-Calcite, E-Ettringite, F-Friedel's Salt, G-Gypsum, MH-$Mg(OH)_2$, P-Portlandite, Q-Quartz.

The detectable peaks are associated with unhydrated cement clinkers, alite and belite. These peaks can be attributed to the low water-to-binder (w/b) ratio employed in the UHPSSC matrix and the presence of the 1.40nCB with a high surface area. Moreover, the XRD pattern of the UHPSSC sample indicates the formation of Friedel's salt and magnesium hydroxide ($Mg(OH)_2$). Magnesium hydroxide is a relatively weak compound compared to cementitious phases, which can potentially reduce the overall strength of the concrete. It has an expansive behaviour and contributes to increased porosity, which leads to the formation of less dense regions by changing the pore structure and microstructure of the UHPSSC (Cao et al., 2018). The $Mg(OH)_2$ content in UHPSSC-SWC samples was 16% higher than in UHPSSC-NWC samples. This can affect the durability of the material, including its resistance to chemical attack, carbonation, and freeze-thaw cycles, which can compromise the long-term durability of the concrete (Zhang et al., 2022).

Furthermore, Friedel's salt can accelerate the early strength development of concrete by acting as a source of calcium ions, which can promote the formation of calcium silicate hydrates (C-S-H). However, the formation of excessive amounts of Friedel's salt through dissolution and precipitation can potentially cause damage through two distinct mechanisms. The first mechanism involves hydraulic pressure, wherein stress occurs due to volume expansion during the phase transition. The second mechanism involves internal crystallization pressure, which leads to damage and potential cracking, irrespective of volume changes associated with the crystallization, which can compromise the long-term durability and strength of the concrete (Qiao et al., 2018; Saxena & Baghban, 2023). Identifying unhydrated cement clinkers and observing Friedel's salt and magnesium hydroxide in the XRD analysis provide valuable insights into the mineralogical composition and the hydration behaviour of the UHPSSC sample.

7.4.4 Electrical Properties

All the 40 mm cubic samples were dried after 28 days of normal water curing in an oven at a temperature of 70°C for a period of five days before conducting the test. The electrical properties of 1.40nCB samples with different temperatures are presented in **Figure 7.8.** The fractional change in electrical resistivity (FCR) was calculated using Equation 3.2.

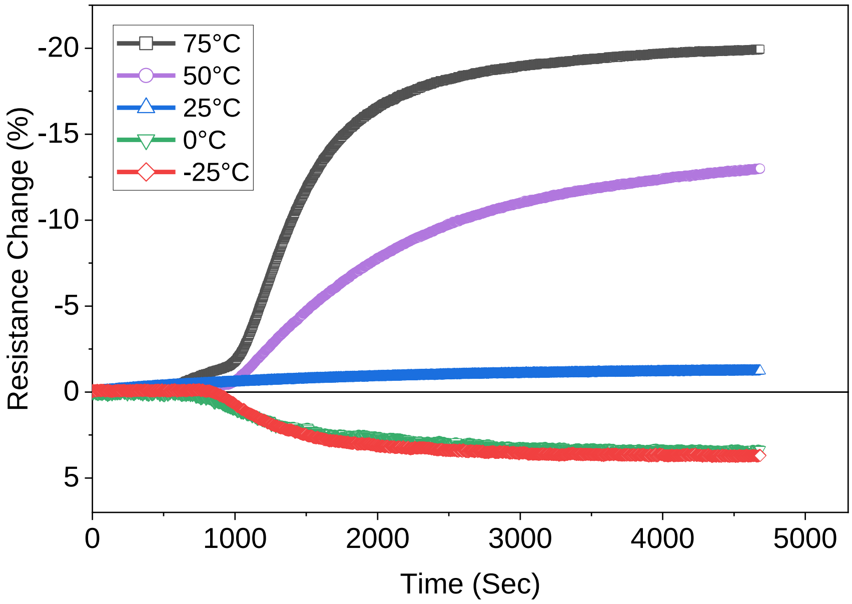

Figure 7.8. Change in resistance with respect to different temperatures (-25°C to 75°C).

It can be observed from the figure that as the temperature rose, the resistance of the sample decreased due to enhanced ion mobility at higher temperatures (Chang et al., 2013; Dehghanpour & Yilmaz, 2020; Lee et al., 2019; Vlachakis et al., 2020). Compared to room temperature (≈25°C), the FCR of samples at 50°C and 75°C increased while those at the freezing temperatures of -25°C and 0°C exhibited a reduction. The results indicate that the increase ratio of FCR at elevated temperatures was several times higher than the reduction ratio of FCR at freezing temperatures, compared to room temperature. As temperature increases, the thermal energy in the material rises, resulting in enhanced charge mobility and greater conductivity. This allows electric current to flow more easily, leading to a decrease in overall resistance. At elevated temperatures, charges gain sufficient energy to overcome barriers, further facilitating the movement of charges and improving current flow. This thermally activated motion of charges could be an effective mechanism in the case of cementitious composites as their conduction mechanism is the combined movement of the electron and ions in the matrix (electron from the nCB and ions from the pore water solution in a cement matrix) (Ding et al., 2021).

On the other hand, a quick door open test was performed at 75℃. The samples with a temperature of 75℃ were subjected to FCR testing to assess the impact of a rapid temperature drop. This was achieved by opening the door of the environmental chamber for a brief period. The variation in FCR in response to the corresponding temperature drop is illustrated in **Figure 7.9.** While the drop ratio is not substantial, the FCR demonstrated a strong correlation and synchronization with the temperature changes. Based on the results, it can be inferred that the 1.40nCB sample exhibited favourable characteristics as a temperature-sensitive cementitious composite. The synchronization of FCR to temperature suggests that the material is highly sensitive to temperature changes, which could be one of the important parameters to include when designing the nCB-based cementitious composites for practical applications.

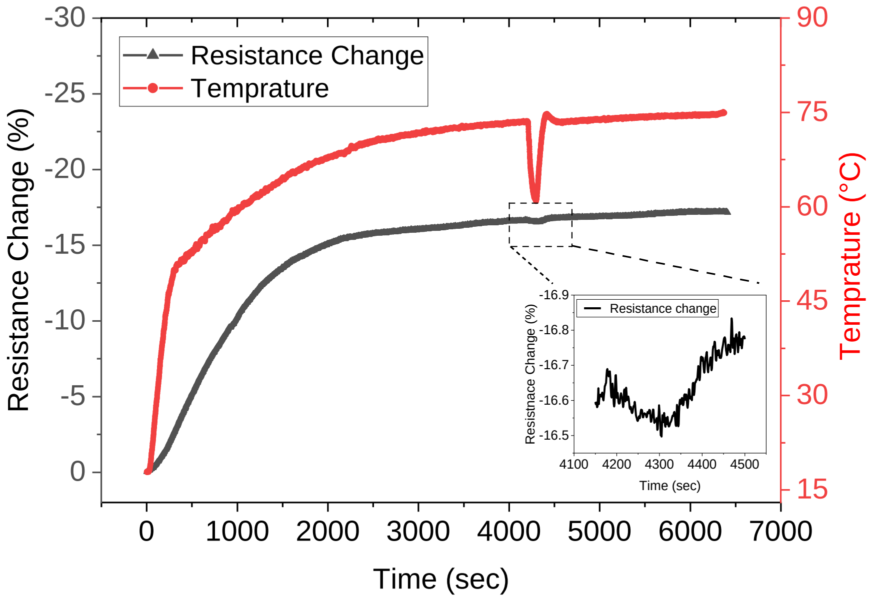

Figure 7.9. Change in FCR response with respect to temperature during a rapid open-door test.

7.4.5 Piezoresistive Behaviour

All the 40 mm cubic samples were dried after 28 days of normal water curing in an oven at a temperature of 70°C for a period of five days before conducting the test to minimize the impact of water content on the piezoresistive properties. After the drying process, the samples were tested under different temperatures including, -25°C, 0°C, ambient temperature (25°C (23°C±2°C)), 50°C and 75°C, to investigate the piezoresistive behaviour, so as to simulate what the material may encounter during its service life. This is because extreme temperatures can significantly impact the structural integrity and performance of the concrete. The piezoresistive behaviour of the cementitious smart composite is evaluated by the repeatable cyclic response of FCR to the corresponding stress-strain and gauge factor (GF). The GF of the samples was calculated by the slope of the fractional change in electrical resistivity to the applied compressive strain (Amjadi et al., 2016) by Equation 3.1.

7.4.5.1 Cyclic Compressive Loading

The piezoresistive behaviour during repeated cyclic loading can be seen in **Figure 7.10.** It can be said that the results clearly show the synchronisation of the FCR with uniaxial cyclic compressive loading. When the load was applied, the resistance of the sensor decreased, and it increased as it was unloaded. It can be explained that the distance between the nCB particles decreased when a load was applied, which reduced the particle-to-particle distance and facilitated the reconstruction of new conductive networks through quantum tunnelling mechanism and direct connections between the particles. Likewise, the distance between nanoparticles increased and the interruption of the conductive paths occurred during the unloading, so the resistance increased again.

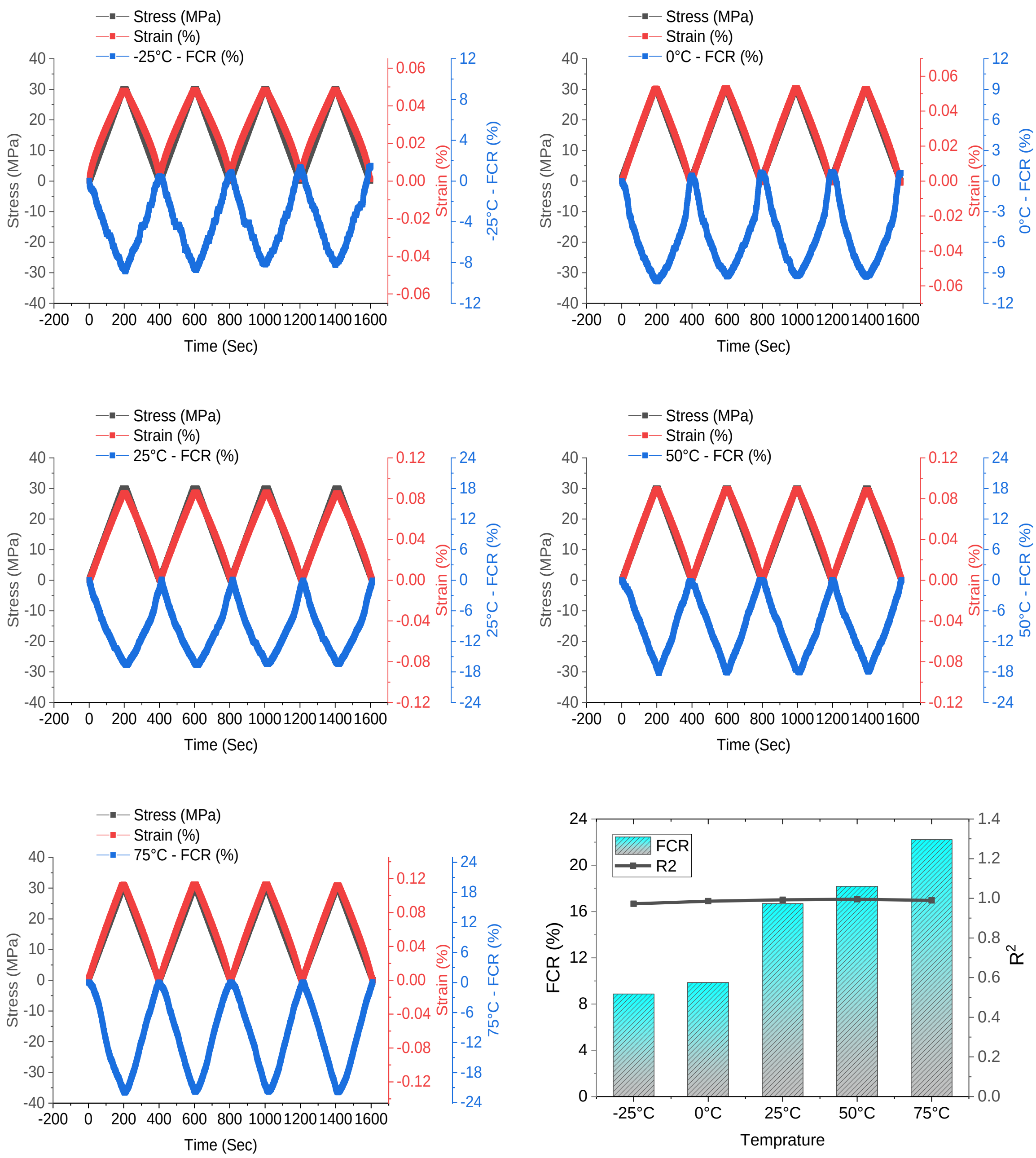

Figure 7.10. FCR response to corresponding stress-strain of 1.40nCB-UHPC specimens during cyclic compressive loading at different temperature ranges from -25℃ to 75℃.

The FCR, in response to temperature, exhibits a highly synchronized behaviour with the applied stresses and strains across all the samples. The sample subjected to -25℃ demonstrated precise synchronization with the applied stress-strain. However, it is noticeable that on each cycle, the FCR decrease incrementally, corresponding to the stresses and strains, accompanied by some level of noise in the signal. It can be attributed to thermal contraction, which induced volumetric changes and led to microcracks and damage. Although the freezing process contributed to the damage, it was reported that the primary cause of damage at -20°C was thermal contraction during cooling rather than the freezing process itself (Cao & Chung, 2002). It has also been reported that the electrical resistivity increases after one cycle of temperature change, especially after experiencing the freezing procedure (Azhari, 2008). This indicates that the freezing temperature plays a crucial role in causing permanent changes in cracks, pores, and the associated irreversible resistivity (Dong et al., 2019).

On the other hand, the sample at 0°C shows a high degree of synchronization and an increasing trend in FCR in response to the applied stresses and strains. However, the signal at 0°C appears smoother, with minimized noise levels compared to the -25°C sample. It is evident that by comparing these results to the room temperature (25°C), the freezing temperatures of -25°C and 0°C led to a substantial reduction in FCR by 46.9.2% and 40.9%, respectively. On the other hand, the FCR response improves with heating temperatures of 50°C and 75°C, showing an increase of 8.9% and 33.2%, respectively. Elevated temperatures may activate additional conductive pathways within the material, facilitating the movement of charge carriers and reducing resistivity. This phenomenon can increase FCR as the material becomes more conductive under elevated temperature conditions.

7.4.5.2 Strain Sensitivity or Gauge Factor

The strain sensitivity of the samples subjected to different temperatures is presented in **Figure 7.11**. The GF of the 1.40nCB samples tested at freezing temperatures (-25°C) exhibited the lowest GF among all the temperatures. Nevertheless, it still achieved a high coefficient of determination (R^2). As the temperature increased, the FCR rose. However, the strains of the samples at higher temperatures also increased. The combined effects of increasing FCR and strains lead to a decrease in the GF for the samples at 50℃ and 75℃ compared to those under room temperature (see **Figure 7.11**). Nonetheless, it's noteworthy that all samples exhibit exceptional linearity, with R^2 value of 0.99.

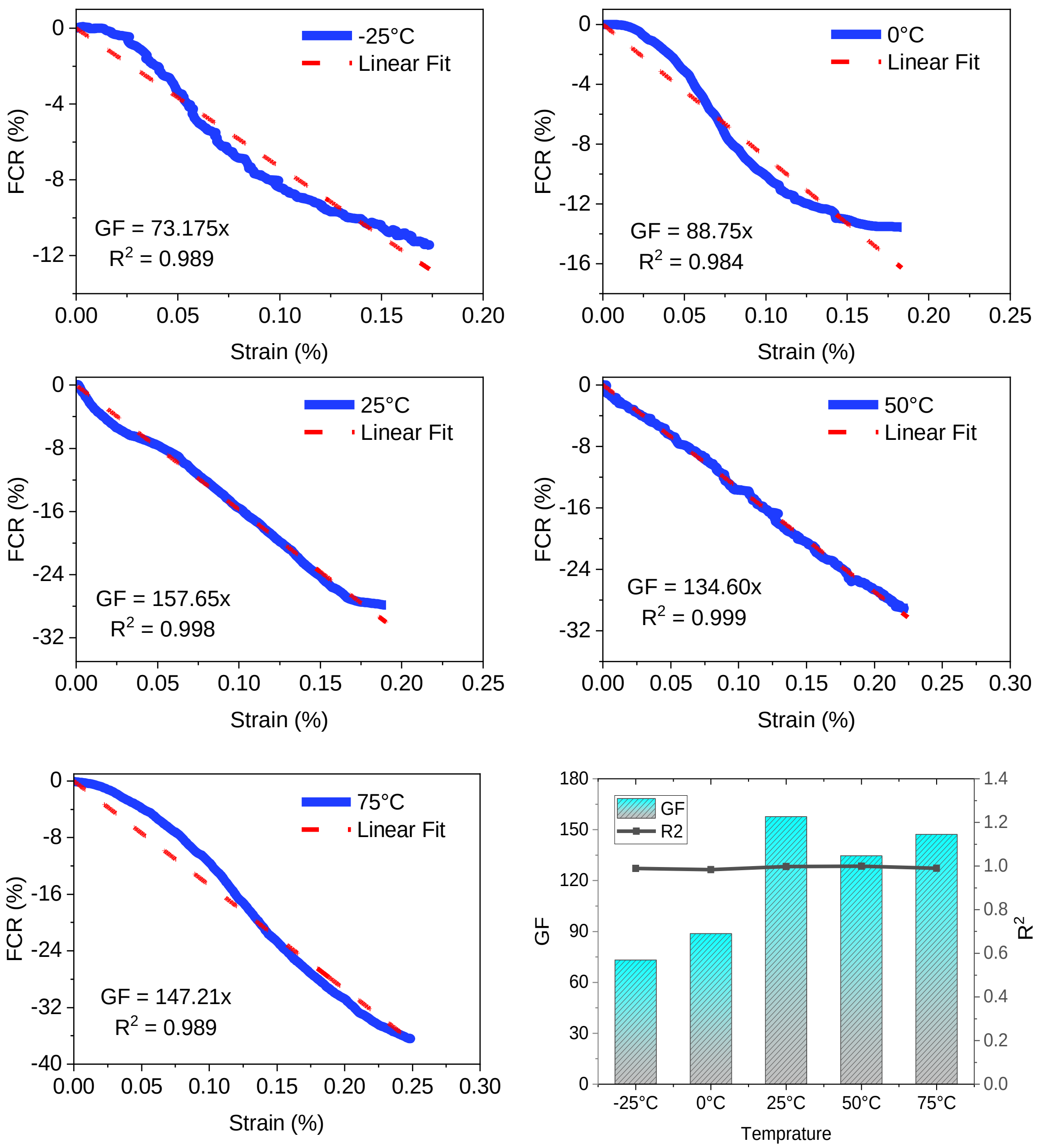

Figure 7.11. Experimental and fitting curves (FCR vs. strain) and the gauge factor of 1.40nCB specimens during monotonic compressive at different temperature ranges from -25℃ to 75℃.

7.4.5.3 Effect of Accelerated Exposure

The 1.40nCB samples were further explored for piezoresistive behaviour after exposure to a sea-salt solution for 90 days. The samples were tested for repeatability (cyclic loading response) and sensitivity (monotonic loading response). The samples were air-dried for one day after taking out from the exposure unit. The samples were tested at room temperature after being taken from the exposed environment. It can be seen from **Figure 7.12** that the cyclic response of the FCR corresponding to the stress-strain is precisely synchronised. It can be observed from the results that the samples after sea-salt solution exposure had lower strain sensitivity than the samples at room temperature with a high R^2 value.

Conversely, it is stated that exposure to seawater could lead to higher conductivity due to the high number of ions, such as Na^+, Mg^{2+}, and Cl^-, which increased the ionic activity and concentration of the pore solution (Dong et al., 2022; Montanari et al., 2019; Snyder et al., 2003). However, the microstructure deterioration and crack formation, which can be seen from the microstructure analysis, led to increasing FCR behaviour. The FCR response on each cycle has an irreversibly increasing behaviour corresponding to its stresses and strains. The fluctuation and noise in signals are also observed. The reason for these fluctuations would be a polarization effect from the pore solutions, where movements of ions occur in the electric field until reaching the electrical potential balance (Hong et al., 2018). Additionally, the interaction of nearby pore solutions during loading may lead to increased instability in the curve (Dong et al., 2019). However, the irreversible increasing behaviour may be attributed to the microstructure changes of the matrix, where the seawater and sea-sand can cause the formation of secondary hydration products and microcracks. As evident from the SEM micrographs and the MIP results, the higher porosity indicates the formation of the microcracks due to the volumetric expansion of the matrix, while the microstructure is directly linked to the conductive network.

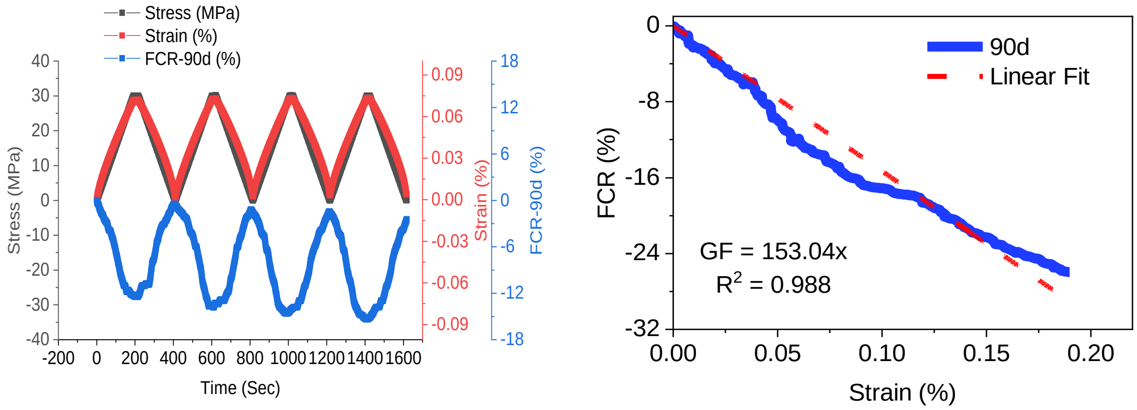

Figure 7.12. Piezoresistive behaviour of 1.40nCB specimens at seawater exposure for 90 days. (a) Cyclic compressive loading. (b) Monotonic compressive loading.

7.5 Summary and Conclusions

The study presented in this chapter represents a continuation of the study presented in Chapter 6, which successfully developed an ultra-high-performance self-sensing concrete (UHPSSC) by incorporating a cost-effective nanocarbon black (nCB) at a minimal dosage of 1.40%. A comprehensive investigation was conducted, encompassing mechanical properties under various curing conditions and exposure durations, as well as the analysis of microstructure. Furthermore, the impact of temperature variations and sea-salt solution exposure on the piezoresistive properties was explored to gain insights into the sensitivity and reliability of the self-sensing capabilities of nCB-UHPSSC. The following conclusions have been drawn from this study:

1. The compressive strength of the samples cured in normal water was higher than those cured in seawater for both UHPSSC and 1.40nCB. However, after exposed to sea-salt solution for up to 90 days, the compressive strength decreased in both UHPSSC and 1.40nCB due to the formation of secondary products and the volumetric expansion. It is worth noting that the reduction ratio of compressive strength was lower for 1.40nCB compared to UHPSSC.
2. The resistivity of the samples decreased with rising temperature, and its response was well-synchronized with the corresponding stresses and strains under all conditions. However, at elevated temperatures, the strain sensitivity initially decreased before a subsequently increase compared to that at the ambient temperature. In contrast, the strain sensitivity was reduced at freezing temperatures than at the ambient temperature and continued to decrease as the temperature dropped further.

3. After 90-day exposure to sea-salt solution, the sensitivity response to applied strain decreased. Nevertheless, the high coefficient of determination ($R^2 > 0.98$) demonstrated that the linearity of the responses was still strong.

The findings of this study will offer decisive insights for optimizing the design and performance of the nCB-UHPSSC composite. These insights will facilitate the reliable and durable application of nCB-UHPSSC in various civil engineering projects.

Chapter 8.

Conclusions and Future Work

8.1 Summary and Conclusions

This thesis has presented a comprehensive study on the development of a new class of ultra-high-performance (UHPC) with strain-sensing capability by incorporation of cost-effective nanocarbon black (nCB), referred to as "nCB-UHPC". A suitable nCB was first determined after systematic investigations of the mechanical and piezoresistive properties of cementitious composites using different structures of nCB, noting that the structure of nCB is the crucial factor influencing the piezoresistive behaviour of the system. The suitable nCB identified was then utilised to develop nCB-based UHPC. A comprehensive experimental program was constituted with a conductive matrix approach. Due to the low water-binder ratio of UHPC, it is not easy to produce the UHPC by incorporation of nanoparticles. Therefore, several preliminary investigations with different approaches were designed and tested. As a result, a new mix design for nCB-UHPC was formulated, which has desirable fresh and hardened properties. The study examined the mechanical properties, microstructure, and piezoresistive behaviour of nCB-UHPC, including aspects such as percolation, repeatability, and sensitivity.

Moreover, the performance and serviceability of the nCB-UHPC at different curing and environmental conditions were investigated. Long-term exposure to aggressive environments and their effects on the microstructure and mechanical properties were examined. Considering the field environment, the effects of different moisture contents and exposure to high salinity solution on the piezoresistive behaviour were thoroughly investigated to establish a relationship between the working environment and strain sensitivity.

Furthermore, nCB-based ultra-high-performance seawater sea-sand concrete (UHPSSC) with self-sensing capabilities (i.e., nCB-UHPSSC) was developed, considering the many benefits that seawater sea-sand UHPC offers including significant environmental and sustainability benefits and reduced carbon footprints, especially for marine infrastructure. In addition, it is worth noting that seawater and sea-sand may contribute to the conductivity due to the high number of dissolved ions. The mix designs with different concentrations of nCB were formulated and tested to investigate its effects on the properties of the material, including mechanical, microstructure and piezoresistive behaviour. With highly promising findings on the developed nCB-UHPSSC, the PhD study further assessed the durability performance of the new material for practical applications. nCB-UHPSSC samples were investigated under different curing conditions and exposure conditions, as well as freezing and elevated temperatures and the effects of these conditions on the piezoresistive behaviour of the nCB-UHPSSC were studied. Through comprehensive investigations, this PhD study has provided significant insights into the effects of different scenarios on self-sensing properties and shed light on developing strategies to mitigate potential inaccuracies caused by environmental variations.

The specified and brief conclusions of each chapter are given below:

1. The PhD study explored three different structures of the nCB with various concentrations to optimise the performance and application. It was found that the compressive strength of all the nCBs showed similar trends with minor differences: initially, the compressive strength increased with the nCB content, and it then decreased. Concerning the piezoresistive behaviour, a high-structure nCB showed a

very low and distinct percolation zone compared to the other nCBs due to its branched structure. The lower percolation threshold is incredibly beneficial for achieving desirable mechanical properties and piezoresistive behaviour at a low cost for a field-deployable solution. All three nCBs showed good strain sensitivity, high repeatability and precisely synchronised behaviour to the corresponding stresses and strains. The high-structure nCB demonstrated the highest strain sensitivity, which is several times higher than conventional strain sensors.

2. The high-structure nCB was then utilised to develop nCB-UHPC, which was investigated for its fresh and hardened properties. It was demonstrated that the flowability and compressive strength generally decreased with increasing nCB content. The strength of nCB-UHPC specimens subjected to 28-day normal water immersion curing was higher than their counterparts subjected to one-day heat curing at 90℃ ± 1℃ due to additional water provided by immersion curing. The percolation zone was found to be between 0.50% - 1.50% nCB, which is significantly lower than those reported in the existing studies. Moreover, the repeatability with highly precise synchronization and excellent strain sensitivity (>130) with a coefficient of determination > 0.99 was achieved at the percolation threshold (1.50nCB-UHPC). On the other hand, the density of the samples decreased with the increase of nCB, which could be one of the most significant advantages along with sensing capability. The combination of lightweight properties and the built-in sensing capabilities of nCB-UHPC makes it an ideal choice for real-time monitoring of construction projects.
3. Furthermore, 1.50-nCB-UHPC was investigated for the durability of self-sensing behaviour under different working and environmental conditions. The results indicate that the mechanical properties of nCB-UHPC were improved by prolonged curing

duration and dry curing at 105°C due to the accelerated hydration activity at elevated temperatures. However, exposure to high salinity sea-salt solution for up to 180 days decreased the mechanical properties due to the formation of cracks by secondary hydration products. A relationship between the moisture content and the strain sensitivity has been established, which shows that strain sensitivity decreased with the increase of moisture content due to the contact resistance of the nCB particles by moisture content. Exposure to the sea-salt solution, however, increased strain sensitivity with fully saturated samples due to the mobility of a high number of ions from high-salinity sea-salt solutions. This is an interesting finding in the case of marine construction.

4. nCB-UHPSSC has been successfully developed using seawater and sea-sand and nCB fillers. It concludes that using seawater sea-sand with the addition of nCB led to decreases in flowability and the compressive strength of UHPSSC after 28 days of curing. Interestingly, the piezoresistivity was observed in plain concrete (without nCB) in the saturated state, which is attributed to high dissolved ions in seawater. The highest strain sensitivity of the nCB-UHPSSC composite was achieved at 1.40% of nCB, which is the percolation threshold determined for the nCB-UHPSSC matrix in both saturated and dry samples. Additionally, the strain sensitivity of saturated samples was 18% higher than that of the dried samples, indicating that dissolved ions from seawater contribute to the additional sensitivity.
5. The UHPSSC with 1.40% nCB were further investigated for the effects of various curing and working conditions on its mechanical and piezoresistive properties. The results demonstrate that the compressive strength of the samples cured in normal water conditions (NWC) was higher than that of samples cured in seawater conditions

(SWC) for both plain UHPSSC and 1.40nCB. However, exposure to sea-salt solution for up to 90 days decreased the compressive strength compared to 28 days NWC, attributed to the formation of secondary products and volumetric expansion. Notably, the reduction ratio of compressive strength was lower in 1.40nCB compared to plain UHPSSC. Furthermore, the study reveals that the FCR increases with rising temperature, exhibiting a well-synchronized relationship with stresses and strains under all tested conditions. However, the strain sensitivity at elevated temperatures initially decreased with the temperature and then increased, reflecting the increasing strain response with temperature. Additionally, the sensitivity at freezing temperatures and exposure to sea-salt solution decreases relative to that at the ambient temperature.

With their excellent properties summarized above, it is evident that the two types of newly developed UHPCs (nCB-UHPC and nCB-UHPSSC) in this study have great potential for practical applications serving as both a structural material and a health monitoring measure. The low percolation zone of nCB in the developed UHPC leads to reduced material costs and is incredibly beneficial for ease of implementation, while its high strain sensitivity is an essential advantage for strain-sensing purposes. The durability parameters examined also show very encouraging and excellent results. Therefore, the new materials could be an appropriate solution for concrete structures, especially for those in harsh environments such as marine and coastal structures.

8.2 Recommendations for Future Work

Smart cementitious composites (SSC) have been developed for more than three decades. Different piezoresistive materials and matrix have been utilized to improve the sensitivity and repeatability. While the nCB-UHPC and nCB-UHPSSC developed in this PhD study represent a significant advancement in this area, to make it a practical and field-deployable solution, some potential fields of studies are recommended for future work, as elaborated.

1. Most of the available literature shows the development of new SCCs, but there is a lack of studies in terms of their durability and serviceability. It could be a magnificent contribution to focus now on the durability and serviceability of the SCC so that it could step up for field applications. To achieve this, the pilot application of nCB-UHPC in some small-scale projects may be first explored.
2. With the vision of carbon neutrality by 2050, incorporating geopolymers into nCB-UHPC would be an attractive approach that has the potential to further enhance the performance and viability of these strain-sensing materials. As an alternative to traditional Portland cement-based matrices, geopolymers offer several advantages, including improved durability, sustainability, and being environmentally friendly. Geopolymers can facilitate the movement of alkaline ions due to their alkali-activated nature, which creates a highly alkaline environment that enhances the mobility of alkaline ions (like Na^+ and K^+) within the geopolymer matrix. The high concentration of these ions promotes their ionic movement and allows the material to respond more effectively to mechanical stress. The most important is its inherent electrical properties, along with its compatibility with piezoresistive additives, which may lead to enhanced strain-sensing capabilities, improved signal stability, and cost-effectiveness and environmental friendliness in the applications of nCB-UHPC.
3. Nanocarbon black has been used in energy storage devices like batteries and superconductors for many years. With the rise of electric vehicles (EVs), the need for efficient and convenient charging infrastructure has become increasingly important. The concept of utilizing the road system itself as a means of energy storage and

charging for EVs holds great potential. Integrating nCB-based composites into the road infrastructure may revolutionise the road system by generating energy for vehicles and storing it for later use.

4. Conventional sensors employ a wireless system and mobile APP to monitor the structure's health in real-time. SCCs typically employed a wiring system to measure the response of the structure. It could be a revolution in SCC to produce a wireless system that can sense the response of the structure.
5. The incorporation of steel fibres into UHPC has significantly improved its mechanical properties, including compressive and flexural strength, as well as its energy absorption capacity. Additionally, steel fibres enhance the material's electrical conductivity, potentially impacting its piezoresistive characteristics by creating a conductive network within the microstructure. Therefore, integrating steel fibres into nCB-based UHPC may lead to distinct piezoresistive properties, which need further research.

References

Abdulkareem, O. M., Fraj, A. B., Bouasker, M., Khouchaf, L., & Khelidj, A. (2021). Microstructural investigation of slag-blended UHPC: The effects of slag content and chemical/thermal activation. *Construction and Building Materials*, *292*, 123455.

Adresi, M., Hassani, A., Tulliani, J.-M., Lacidogna, G., & Antonaci, P. (2017). A study of the main factors affecting the performance of self-sensing concrete. *Advances in Cement Research, 29*(5), 216-226.

Adresi, M., & Pakhirehzan, F. (2023). Evaluating the performance of Self-Sensing concrete sensors under temperature and moisture variations-a review. *Construction and Building Materials, 404*, 132923.

Ahlborn, T. M., Harris, D. K., Misson, D. L., & Peuse, E. J. (2011). Characterization of strength and durability of ultra-high-performance concrete under variable curing conditions. *Transportation research record, 2251*(1), 68-75.

Ahmad, M. R., Das, C. S., Khan, M., & Dai, J.-G. (2023). Development of low-carbon alkali-activated materials solely activated by flue gas residues (FGR) waste from incineration plants. *Journal of Cleaner Production, 397*, 136597.

Ahmad, S., Hakeem, I., & Azad, A. K. (2015). Effect of curing, fibre content and exposures on compressive strength and elasticity of UHPC. *Advances in Cement Research, 27*(4), 233-239.

Ahmed, S., Hussain, A., Hussain, Z., Pu, Z., Ostrowski, K. A., & Walczak, R. (2021). Effect of carbon black and hybrid steel-polypropylene fiber on the mechanical and self-sensing characteristics of concrete considering different coarse aggregates' sizes. *Materials, 14*(23), 7455.

Al-Dahawi, A., Ozturk, O., Emami, F., Yildirim, G., & Sahmaran, M. (2016). Effect of mixing methods on the electrical properties of cementitious composites incorporating different carbon-based materials. *Construction and Building Materials, 104*, 160-168. doi:10.1016/j.conbuildmat.2015.12.072

Al-Dahawi, A., Öztürk, O., Emami, F., Yıldırım, G., & Şahmaran, M. (2016). Effect of mixing methods on the electrical properties of cementitious composites incorporating different carbon-based materials. *Construction and Building Materials, 104*, 160-168. doi:10.1016/j.conbuildmat.2015.12.072

Ali, H. A., Sun, K., Xuan, D., Lu, J.-X., Cyr, M., & Poon, C. S. (2023). Recycling of high-volume waste glass powder in alkali-activated materials: An efflorescence mitigation strategy. *Journal of Building Engineering, 65*, 105756.

Amjadi, M., Kyung, K. U., Park, I., & Sitti, M. (2016). Stretchable, Skin-Mountable, and Wearable Strain Sensors and Their Potential Applications: A Review. *Advanced Functional Materials, 26*(11), 1678-1698. doi:10.1002/adfm.201504755

Andrawes, B., & Chan, L. Y. (2012). Compression and tension stress-sensing of carbon nanotube-reinforced cement. *Magazine of Concrete Research, 64*(3), 253-258. doi:10.1680/macr.10.00182

Andreasen, A. (1930). Ueber die Beziehung zwischen Kornabstufung und Zwischenraum in Produkten aus losen Körnern (mit einigen Experimenten). *Kolloid-Zeitschrift, 50*, 217-228.

Antonov, J., Seidov, D., Boyer, T., Locarnini, R., Mishonov, A., Garcia, H., . . . Johnson, D. (2010). *World Ocean Atlas 2009 Volume 2: Salinity, NOAA Atlas NESDIS 69.* Ed. S. Levitus.) 184 pp.(US Government Printing Office: Washington, DC),

Armstrong, M. (March, 2024). Where Water Stress Will Be Highest by 2050. *https://www.statista.com/chart/26140/water-stress-projections-global/*.

ASTM, C.-. (2020). Standard Test Method for Measurement of Rate of Absorption of Water by Hydraulic-Cement Concretes. *ASTM International*.

Azenha, M., Gabrijel, I., Schlicke, D., Kanstad, T., & Jensen, O. M. (2016). *Service Life of Cement-Based Materials and Structures* (Vol. 1).

Azhari, F. (2008). *Cement-based sensors for structural health monitoring.* University of British Columbia,

Azhari, F., & Banthia, N. (2012). Cement-based sensors with carbon fibers and carbon nanotubes for piezoresistive sensing. *Cement and Concrete Composites, 34*(7), 866-873.

Badot, J. C., Ligneel, É., Dubrunfaut, O., Guyomard, D., & Lestriez, B. (2009). A multiscale description of the electronic transport within the hierarchical architecture of a composite electrode for lithium batteries. *Advanced Functional Materials, 19*(17), 2749-2758.

Baeza, F. J., Galao, O., Zornoza, E., & Garcés, P. (2013). Multifunctional cement composites strain and damage sensors applied on reinforced concrete (RC) structural elements. *Materials, 6*(3), 841-855.

Bajaber, M., & Hakeem, I. (2021). UHPC evolution, development, and utilization in construction: A review. *Journal of Materials Research and Technology, 10*, 1058-1074.

Banthia, N., Djeridane, S., & Pigeon, M. (1992). Electrical resistivity of carbon and steel micro-fiber reinforced cements. *Cement and Concrete Research, 22*(5), 804-814.

Baroghel-Bouny, V., Wang, X., Thiery, M., Saillio, M., & Barberon, F. (2012). Prediction of chloride binding isotherms of cementitious materials by analytical model or numerical inverse analysis. *Cement and Concrete Research, 42*(9), 1207-1224.

Belli, A., Mobili, A., Bellezze, T., Tittarelli, F., & Cachim, P. (2018). Evaluating the self-sensing ability of cement mortars manufactured with graphene nanoplatelets, virgin or recycled carbon fibers through piezoresistivity tests. *Sustainability, 10*(11), 4013.

Benezet, J., & Benhassaine, A. (1999). The influence of particle size on the pozzolanic reactivity of quartz powder. *Powder Technology, 103*(1), 26-29.

Beushausen, H., & Luco, L. F. (2016). Performance-based specifications and control of concrete durability. *RILEM TC*, 66-72.

Birnin-Yauri, U., & Glasser, F. (1998). Friedel's salt, Ca2Al (OH) 6 (Cl, OH)· 2H2O: its solid solutions and their role in chloride binding. *Cement and Concrete Research, 28*(12), 1713-1723.

Bontea, D.-M., Chung, D., & Lee, G. (2000). Damage in carbon fiber-reinforced concrete, monitored by electrical resistance measurement. *Cement and Concrete Research, 30*(4), 651-659.

Brand, A. S., & Roesler, J. R. (2015). Steel furnace slag aggregate expansion and hardened concrete properties. *Cement and Concrete Composites, 60*, 1-9.

C109/C109M-21, A. (2021). Standard Test Method for Compressive Strength of Hydraulic Cement Mortars (Using 2-in. or [50 mm] Cube Specimens). *ASTM International*. doi:10.1520/c0109_c0109m-20b

C230/C230M-21, A. (2021). Standard Specification for Flow Table for Use in Tests of Hydraulic Cement. *ASTM International*, 4-9. doi:10.1520/C0230

C1437-20, A. (2020). Standard test method for flow of hydraulic cement mortar. *ASTM International*. doi:10.1520/C1437-20

C1585-20, A. (2020). Standard Test Method for Measurement of Rate of Absorption of Water by Hydraulic-Cement Concretes. *ASTM International*.

C1856/C1856M-17, A. (2017). Standard Practice for Fabricating and Testing Specimens of Ultra-High Performance Concrete. *ASTM International*, 4-4. doi:10.1520/C1856

Cadiou, F., Etiemble, A., Douillard, T., Willot, F., Valentin, O., Badot, J.-C., . . . Maire, E. (2019). Numerical prediction of multiscale electronic conductivity of lithium-ion battery positive electrodes. *Journal of The Electrochemical Society, 166*(8), A1692.

Cai, H., & Liu, X. (1998). Freeze-thaw durability of concrete: ice formation process in pores. *Cement and Concrete Research, 28*(9), 1281-1287.

Cai, W. (2017). *Effect of particle packing on flow property and strength of concrete mortar*. Iowa State University,

Cao, F., Miao, M., & Yan, P. (2018). Hydration characteristics and expansive mechanism of MgO expansive agents. *Construction and Building Materials, 183*, 234-242.

Cao, J., & Chung, D. (2002). Damage evolution during freeze–thaw cycling of cement mortar, studied by electrical resistivity measurement. *Cement and Concrete Research, 32*(10), 1657-1661.

Catalá, G., Ramos-Fernández, E., Zornoza, E., Andión, L. G., & Garcés, P. (2011). Influence of the oxidation process of carbon material on the mechanical properties of cement mortars. *Journal of Materials in Civil Engineering, 23*(3), 321-329.

Celzard, A., McRae, E., Deleuze, C., & Dufort, M. (1996). Critical concentration in percolating systems containing a high-aspect-ratio filler. *Physical Review B - Condensed Matter and Materials Physics, 53*(10), 6209-6214. doi:10.1103/PhysRevB.53.6209

Chang, C., Song, G., Gao, D., & Mo, Y. (2013). Temperature and mixing effects on electrical resistivity of carbon fiber enhanced concrete. *Smart Materials and Structures, 22*(3), 035021.

Chanut, N., Stefaniuk, D., Weaver, J. C., Zhu, Y., Shao-Horn, Y., Masic, A., & Ulm, F.-J. (2023). Carbon–cement supercapacitors as a scalable bulk energy storage solution. *Proceedings of the National Academy of Sciences, 120*(32), e2304318120.

Chen, B., Wu, K., & Yao, W. (2004). Conductivity of carbon fiber reinforced cement-based composites. *Cement and Concrete Composites, 26*(4), 291-297. doi:10.1016/S0958-9465(02)00138-5

Chen, J., Cui, X., Sui, K., Zhu, Y., & Jiang, W. (2017). Balance the electrical properties and mechanical properties of carbon black filled immiscible polymer blends with a double percolation structure. *Composites Science and Technology, 140,* 99-105. doi:10.1016/j.compscitech.2016.12.029

Chen, J., Hou, Z. F., Yu, H. C., & Gao, L. (2012). *Research on the Double Yellow Lines Monitoring System Based on Pressure-Sensitivity of Carbon Fiber Reinforced Concrete.* Paper presented at the Applied Mechanics and Materials.

Chen, P.-W., & Chung, D. (1995). Improving the electrical conductivity of composites comprised of short conducting fibers in a nonconducting matrix: The addition of a nonconducting particulate filler. *Journal of Electronic Materials, 24*(1), 47-51.

Chen, P.-W., & Chung, D. (1996). Low-drying-shrinkage concrete containing carbon fibers. *Composites Part B: Engineering, 27*(3-4), 269-274.

Chen, P. W., & Chung, D. D. (1993). Carbon fiber reinforced concrete for smart structures capable of non-destructive flaw detection. *Smart Materials and Structures, 2*(1), 22-30. doi:10.1088/0964-1726/2/1/004

Chiarello, M., & Zinno, R. (2005). Electrical conductivity of self-monitoring CFRC. *Cement and Concrete Composites, 27*(4), 463-469.

Choi, H., Choi, S., & Cha, H. (2008). Structural Health Monitoring system based on strain gauge enabled wireless sensor nodes. *Proceedings of INSS 2008 - 5th International Conference on Networked Sensing Systems*, 211-214. doi:10.1109/INSS.2008.4610888

Chong, K. P., Carino, N. J., & Washer, G. (2003). Health monitoring of civil infrastructures. *Smart Materials and Structures, 12*(3), 483-493. doi:Doi 10.1088/0964-1726/12/3/320

Chu, H.-y., & Chen, J.-k. (2016). The experimental study on the correlation of resistivity and damage for conductive concrete. *Cement and Concrete Composites, 67*, 12-19.

Chung, D., & Xi, X. (2023). A review of cement-based materials as electroceramics. *Ceramics International*.

Chung, D. D. L. (2002). Piezoresistive cement-based materials for strain sensing. *Journal of Intelligent Material Systems and Structures, 13*(9), 599-609. doi:10.1106/104538902031861

Chung, D. D. L. (2005). Dispersion of Short Fibers in Cement. *Journal of Materials in Civil Engineering, 17*(4), 379-383. doi:10.1061/(ASCE)0899-1561(2005)17:4(379)

Chung, D. D. L. (2018). *Multifunctional cement-based materials*: CRC Press.

Chung, D. D. L. (2020). A critical review of piezoresistivity and its application in electrical-resistance-based strain sensing. *Journal of materials science, 55*(32), 15367-15396. doi:10.1007/s10853-020-05099-z

D2414-21, A. (2021). Standard test method for carbon black—Oil absorption number (OAN). *ASTM International*.

D'Alessandro, A., Rallini, M., Ubertini, F., Materazzi, A. L., & Kenny, J. M. (2016). Investigations on scalable fabrication procedures for self-sensing carbon nanotube cement-matrix composites for SHM applications. *Cement and Concrete Composites, 65*, 200-213. doi:10.1016/j.cemconcomp.2015.11.001

D'Alessandro, A., Ubertini, F., Laflamme, S., & Materazzi, A. L. (2016). Towards smart concrete for smart cities: Recent results and future application of strain-sensing nanocomposites. *Journal of Smart Cities (Transferred), 1*(1).

D'Alessandro, A., Ubertini, F., Materazzi, A. L., Laflamme, S., & Porfiri, M. (2015). Electromechanical modelling of a new class of nanocomposite cement-based sensors for structural health monitoring. *Structural Health Monitoring, 14*(2), 137-147.

Dai, Y., Sun, M., Liu, C., & Li, Z. (2010). Electromagnetic wave absorbing characteristics of carbon black cement-based composites. *Cement and Concrete Composites, 32*(7), 508-513. doi:10.1016/j.cemconcomp.2010.03.009

Danoglidis, P. A., Konsta-Gdoutos, M. S., Gdoutos, E. E., & Shah, S. P. (2016). Strength, energy absorption capability and self-sensing properties of multifunctional carbon nanotube reinforced mortars. *Construction and Building Materials, 120*, 265-274. doi:10.1016/j.conbuildmat.2016.05.049

De Weerdt, K., Justnes, H., & Geiker, M. R. (2014). Changes in the phase assemblage of concrete exposed to sea water. *Cement and Concrete Composites, 47*, 53-63.

Dehghani, A., & Aslani, F. (2021). Piezoresistive sensing of cementitious composites reinforced with shape memory alloy, steel, and carbon fibres. *Construction and Building Materials, 267*, 121046.

Dehghanpour, H., & Yilmaz, K. (2020). Investigation of specimen size, geometry and temperature effects on resistivity of electrically conductive concretes. *Construction and Building Materials, 250*, 118864.

Demircilioğlu, E., Teomete, E., Schlangen, E., & Baeza, F. J. (2019). Temperature and moisture effects on electrical resistance and strain sensitivity of smart concrete. *Construction and Building Materials, 224*, 420-427. doi:10.1016/j.conbuildmat.2019.07.091

Dickson, A. G., & Goyet, C. (1994). *Handbook of methods for the analysis of the various parameters of the carbon dioxide system in sea water. Version 2*. Retrieved from

Ding, S., Dong, S., Ashour, A., & Han, B. (2019). Development of sensing concrete: Principles, properties and its applications. *Journal of applied physics, 126*(24).

Ding, S., Ruan, Y., Yu, X., Han, B., & Ni, Y.-Q. (2019). Self-monitoring of smart concrete column incorporating CNT/NCB composite fillers modified cementitious sensors. *Construction and Building Materials, 201*, 127-137.

Ding, S., Xiang, Y., Ni, Y.-Q., Thakur, V. K., Wang, X., Han, B., & Ou, J. (2022). In-situ synthesizing carbon nanotubes on cement to develop self-sensing cementitious composites for smart high-speed rail infrastructures. *Nano Today, 43*, 101438.

Ding, S., Xu, C., Ni, Y.-Q., & Han, B. (2021). Extracting piezoresistive response of self-sensing cementitious composites under temperature effect via Bayesian blind source separation. *Smart Materials and Structures, 30*(6), 065010.

Ding, Y., Chen, Z., Han, Z., Zhang, Y., & Pacheco-torgal, F. (2013). Nano-carbon black and carbon fiber as conductive materials for the diagnosing of the damage of concrete beam. *Construction and Building Materials, 43*, 233-241. doi:10.1016/j.conbuildmat.2013.02.010

Ding, Y., Han, Z., Zhang, Y., & Aguiar, J. (2016). Concrete with triphasic conductive materials for self-monitoring of cracking development subjected to flexure. *Composite Structures, 138*, 184-191.

Ding, Y., Han, Z., Zhang, Y., & Azevedo, C. (2012). *Hybrid Use of Steel- and Carbon-Fiber Reinforced Concrete for Monitoring of Crack Behavior.* Paper presented at the European Conference on Composite Materials.

Ding, Y., Liu, G., Hussain, A., Pacheco-Torgal, F., & Zhang, Y. (2019). Effect of steel fiber and carbon black on the self-sensing ability of concrete cracks under bending. *Construction and Building Materials, 207*, 630-639. doi:10.1016/j.conbuildmat.2019.02.160

Ding, Y. N., Chen, Z. P., Han, Z. B., Zhang, Y. L., & Pacheco-Torgal, F. (2013). Nano-carbon black and carbon fiber as conductive materials for the diagnosing of the damage of concrete beam. *Construction and Building Materials, 43*, 233-241. doi:10.1016/j.conbuildmat.2013.02.010

Ding, Y. N., Liu, G. J., Hussain, A., Pacheco-Torgal, F., & Zhang, Y. L. (2019). Effect of steel fiber and carbon black on the self-sensing ability of concrete cracks under bending. *Construction and Building Materials, 207*, 630-639. doi:10.1016/j.conbuildmat.2019.02.160

Dobias, D., Pernicova, R., & Mandlik, T. (2016). *Water transport properties and depth of chloride penetration in ultra high performance concrete.* Paper presented at the Key Engineering Materials.

Dong, S., Dong, X., Ashour, A., Han, B., & Ou, J. (2020). Fracture and self-sensing characteristics of super-fine stainless wire reinforced reactive powder concrete. *Cement and Concrete Composites, 105*, 103427.

Dong, S., Han, B., Ou, J., Li, Z., Han, L., & Yu, X. (2016). Electrically conductive behaviors and mechanisms of short-cut super-fine stainless wire reinforced reactive powder concrete. *Cement and Concrete Composites, 72*, 48-65.

Dong, S., Ouyang, X., Yoo, D.-Y., & Han, B. (2024). Influence of early thermal curing regimes on properties of ultra-high performance concrete: A review. *Journal of Building Engineering*, 110494.

Dong, W., Li, W., Guo, Y., Qu, F., Wang, K., & Sheng, D. (2022). Piezoresistive performance of hydrophobic cement-based sensors under moisture and chloride-rich environments. *Cement and Concrete Composites, 126*, 104379.

Dong, W., Li, W., Lu, N., Qu, F., Vessalas, K., & Sheng, D. (2019). Piezoresistive behaviours of cement-based sensor with carbon black subjected to various temperature and water content. *Composites Part B: Engineering, 178*, 107488.

Dong, W., Li, W., Shen, L., & Sheng, D. (2019). Piezoresistive behaviours of carbon black cement-based sensors with layer-distributed conductive rubber fibres. *Materials & design, 182*, 108012.

Dong, W., Li, W., Shen, L., & Sheng, D. (2019). Piezoresistive behaviours of carbon black cement-based sensors with layer-distributed conductive rubber fibres. *Materials & Design, 182*. doi:10.1016/j.matdes.2019.108012

Dong, W., Li, W., Tao, Z., & Wang, K. (2019). Piezoresistive properties of cement-based sensors: Review and perspective. *Construction and Building Materials, 203*, 146-163.

Dong, W., Li, W., Wang, K., Guo, Y., Sheng, D., & Shah, S. P. (2020). Piezoresistivity enhancement of functional carbon black filled cement-based sensor using polypropylene fibre. *Powder Technology, 373*, 184-194. doi:10.1016/j.powtec.2020.06.029

Dou, Y., Gu, H., Sun, S., Yao, W., & Guan, D. (2022). Synthesis of a grape-like conductive carbon black/Ag hybrid as the conductive filler for soft silicone rubber. *RSC advances, 12*(2), 1184-1193.

Du, G., Bu, L., & Yang, D. (2022). Experimental study and numerical simulation on the flexural performance of section steel beams strengthened by wrapping reinforced RPC under secondary load. *Engineering Structures, 270*, 114816. doi:https://doi.org/10.1016/j.engstruct.2022.114816

Du, J., Meng, W., Khayat, K. H., Bao, Y., Guo, P., Lyu, Z., . . . Wang, H. (2021). New development of ultra-high-performance concrete (UHPC). *Composites Part B: Engineering, 224*, 109220.

Ebead, U., Lau, D., Lollini, F., Nanni, A., Suraneni, P., & Yu, T. (2022). A review of recent advances in the science and technology of seawater-mixed concrete. *Cement and Concrete Research, 152*, 106666.

El-Reedy, M. (2007). *Steel-reinforced concrete structures: Assessment and repair of corrosion*: CRC press.

Elango, K., Sanfeer, J., Gopi, R., Shalini, A., Saravanakumar, R., & Prabhu, L. (2021). Properties of light weight concrete–a state of the art review. *Materials Today: Proceedings, 46*, 4059-4062.

Elseady, A. A., Zhuge, Y., Ma, X., Chow, C. W., Lee, I., Zeng, J., & Gorjian, N. (2024). Development of self-sensing cementitious composites by incorporating a two-dimensional carbon-fibre textile network for structural health monitoring. *Construction and Building Materials, 415*, 135049.

Endo, M., Noguchi, T., Ito, M., Takeuchi, K., Hayashi, T., Kim, Y. A., . . . Dresselhaus, M. S. (2008). Extreme‐Performance Rubber Nanocomposites for Probing and Excavating Deep Oil Resources Using Multi‐Walled Carbon Nanotubes. *Advanced Functional Materials, 18*(21), 3403-3409.

Fehervari, A., MacLeod, A. J. N., Garcez, E. O., Aldridge, L., Gates, W. P., Yang, Y., & Collins, F. (2020). On the mechanisms for improved strengths of carbon nanofiber-enriched mortars. *Cement and Concrete Research, 136*, 106178.

Feng, J., & Chan, C. m. (2003). Effects of strain and temperature on the electrical properties of carbon black - filled alternating copolymer of ethylene - tetrafluoroethylene composites. *Polymer Engineering & Science, 43*(5), 1064-1070.

Feng, P., Li, Z., Zhang, S., & Yang, J.-Q. (2022). Steel slag aggregate concrete filled-in FRP tubes: Volume expansion effect and axial compressive behaviour. *Construction and Building Materials, 318*, 125961.

Fennis, S. A., & Walraven, J. C. (2012). Using particle packing technology for sustainable concrete mixture design. *Heron, 57 (2012) 2*.

Fernandes, V. A., Purnell, P., Still, G. T., & Thomas, T. H. (2007). The effect of clay content in sands used for cementitious materials in developing countries. *Cement and Concrete Research, 37*(5), 751-758. doi:10.1016/j.cemconres.2006.10.016

Fu, X., & Chung, D. (1997). Effect of curing age on the self-monitoring behavior of carbon fiber reinforced mortar. *Cement and Concrete Research, 27*(9), 1313-1318.

Fulham-Lebrasseur, R., Sorelli, L., & Conciatori, D. (2020). Development of electrically conductive concrete and mortars with hybrid conductive inclusions. *Construction and Building Materials, 237*, 117470.

Funk, J. E., & Dinger, D. R. (2013). *Predictive process control of crowded particulate suspensions: applied to ceramic manufacturing*: Springer Science & Business Media.

Gagg, C. R. (2014). Cement and concrete as an engineering material: An historic appraisal and case study analysis. *Engineering Failure Analysis, 40*, 114-140.

Gapparov, A., & Isakova, M. (2023). *Study on the characteristics of water resources through electrical conductivity: A case study of Uzbekistan.* Paper presented at the IOP Conference Series: Earth and Environmental Science.

Georgousis, G., Roumpos, K., Kontou, E., Kyritsis, A., Pissis, P., Koutsoumpis, S., . . . Omastová, M. (2017). Strain and damage monitoring in SBR nanocomposites under cyclic loading. *Composites Part B: Engineering, 131*, 50-61.

Gnanamuthu, R. M., & Lee, C. W. (2011). Electrochemical properties of Super P carbon black as an anode active material for lithium-ion batteries. *Materials Chemistry and Physics, 130*(3), 831-834. doi:10.1016/j.matchemphys.2011.08.060

Gupta, S., Gonzalez, J. G., & Loh, K. J. (2017). Self-sensing concrete enabled by nano-engineered cement-aggregate interfaces. *Structural Health Monitoring, 16*(3), 309-323.

Hamada, H., Alattar, A., Tayeh, B., Yahaya, F., & Almeshal, I. (2022). Influence of different curing methods on the compressive strength of ultra-high-performance concrete: A comprehensive review. *Case Studies in Construction Materials, 17*, e01390. doi:https://doi.org/10.1016/j.cscm.2022.e01390

Han, B., Ding, S., Wang, J., & Ou, J. (2019). *Nano-engineered cementitious composites: principles and practices*: Springer.

Han, B., Ding, S., Wang, J., Ou, J., Han, B., Ding, S., . . . Ou, J. (2019). Electrostatic Self-Assembled Carbon Nanotube/Nano-Carbon Black Fillers-Engineered Cementitious Composites. *Nano-Engineered Cementitious Composites: Principles and Practices*, 665-707.

Han, B., Ding, S., & Yu, X. (2015). Intrinsic self-sensing concrete and structures: A review. *Measurement: Journal of the International Measurement Confederation, 59*, 110-128. doi:10.1016/j.measurement.2014.09.048

Han, B., & Ou, J. (2007). Embedded piezoresistive cement-based stress/strain sensor. *Sensors and Actuators A: Physical, 138*(2), 294-298.

Han, B., Sun, S., Ding, S., Zhang, L., Yu, X., & Ou, J. (2015). Review of nanocarbon-engineered multifunctional cementitious composites. *Composites Part A: Applied Science and Manufacturing, 70*, 69-81.

Han, B., Yang, Z., Shi, X., & Yu, X. (2013). Transport properties of carbon-nanotube/cement composites. *Journal of Materials Engineering and Performance, 22,* 184-189.

Han, B., Yu, X., & Kwon, E. (2009). A self-sensing carbon nanotube/cement composite for traffic monitoring. *Nanotechnology, 20*(44), 445501.

Han, B., Yu, X., Kwon, E., & Ou, J. (2012). Effects of CNT concentration level and water/cement ratio on the piezoresistivity of CNT/cement composites. *Journal of Composite Materials, 46*(1), 19-25.

Han, B., Yu, X., & Ou, J. (2014). *Self-sensing concrete in smart structures*: Butterworth-Heinemann.

Han, B., Zhang, K., Burnham, T., Kwon, E., & Yu, X. (2012). Integration and road tests of a self-sensing CNT concrete pavement system for traffic detection. *Smart Materials and Structures, 22*(1), 015020.

Han, B., Zhang, K., Yu, X., Kwon, E., & Ou, J. (2012). Fabrication of piezoresistive CNT/CNF cementitious composites with superplasticizer as dispersant. *Journal of Materials in Civil Engineering, 24*(6), 658-665.

Han, B., Zhang, L., & Ou, J. (2010). Influence of water content on conductivity and piezoresistivity of cement-based material with both carbon fiber and carbon black.

Journal of Wuhan University of Technology-Mater. Sci. Ed., 25(1), 147-151. doi:10.1007/s11595-010-1147-z

Han, B., Zhang, L., & Ou, J. (2017). *Smart and multifunctional concrete toward sustainable infrastructures*: Springer.

Han, B., Zhang, L., Sun, S., Yu, X., Dong, X., Wu, T., & Ou, J. (2015). Electrostatic self-assembled carbon nanotube/nano carbon black composite fillers reinforced cement-based materials with multifunctionality. *Composites Part A: Applied Science and Manufacturing, 79*, 103-115. doi:10.1016/j.compositesa.2015.09.016

Han, B., Zhang, L., Zeng, S., Dong, S., Yu, X., Yang, R., & Ou, J. (2017). Nano-core effect in nano-engineered cementitious composites. *Composites Part A: Applied Science and Manufacturing, 95*, 100-109.

Han, B. G., Ding, S. Q., & Yu, X. (2015). Intrinsic self-sensing concrete and structures: A review. *Measurement, 59*, 110-128. doi:10.1016/j.measurement.2014.09.048

Han, B. G., Zhang, L. Q., Sun, S. W., Yu, X., Dong, X. F., Wu, T. J., & Ou, J. P. (2015). Electrostatic self-assembled carbon nanotube/nano carbon black composite fillers reinforced cement-based materials with multifunctionality. *Composites Part a-Applied Science and Manufacturing, 79*, 103-115. doi:10.1016/j.compositesa.2015.09.016

Han, J., Pan, J., Cai, J., & Li, X. (2020). A review on carbon-based self-sensing cementitious composites. *Construction and Building Materials, 265*, 120764.

Haque, M., Al-Khaiat, H., & Kayali, O. (2004). Strength and durability of lightweight concrete. *Cement and Concrete Composites, 26*(4), 307-314.

Hartley, P., & Parfitt, G. (1985). Dispersion of powders in liquids. 1. The contribution of the van der Waals force to the cohesiveness of carbon black powders. *Langmuir, 1*(6), 651-657.

Hartley, P., Parfitt, G., & Pollack, L. (1985). The role of the van der Waals force in the agglomeration of powders containing submicron particles. *Powder Technology, 42*(1), 35-46.

Hayat, U., Kai, M.-F., Hu-Bao, A., Liew, J.-X., & Dai, J.-G. (2024). Atomic-level investigation into the transport of NaCl solution in porous cement paste: The effects of pore size and temperature. *Journal of Building Engineering*, 108976.

He, Z.-h., Han, X.-d., Zhang, M.-y., Yuan, Q., Shi, J.-y., & Zhan, P.-m. (2022). A novel development of green UHPC containing waste concrete powder derived from construction and demolition waste. *Powder Technology, 398*, 117075.

He, Z., Li, W., Salehi, H., Zhang, H., Zhou, H., & Jiao, P. (2022). Integrated structural health monitoring in bridge engineering. *Automation in Construction, 136*, 104168.

Hiremath, P. N., & Yaragal, S. C. (2017). Effect of different curing regimes and durations on early strength development of reactive powder concrete. *Construction and Building Materials, 154*, 72-87.

Hoheneder, J., Flores-Vivian, I., Lin, Z., Zilberman, P., & Sobolev, K. (2015). The performance of stress-sensing smart fiber reinforced composites in moist and sodium chloride environments. *Composites Part B: Engineering, 73*, 89-95.

Hong, C., Li, Q., Zhuang, Z., Xie, H., & Xu, S. (2024). Electrical and piezoresistive properties of ultra-high toughness cementitious composite incorporating multi-walled carbon nanotubes: Testing, analyzing, and phenomenological modeling. *Cement and Concrete Composites*, 105757.

Hong, Y., Li, Z., Qiao, G., Ou, J., & Cheng, W. (2018). Pressure sensitivity of multiscale carbon-admixtures–enhanced cement-based composites. *Nanomaterials and Nanotechnology, 8*, 1847980418793529. doi:10.1177/1847980418793529

Hou, T.-C., & Lynch, J. P. (2005). Conductivity-based strain monitoring and damage characterization of fiber reinforced cementitious structural components. *Proc. of SPIE Vol.*(May 2005), 419-429. doi:10.1117/12.599955

Huang, Y., Li, H., & Qian, S. (2018). Self-sensing properties of Engineered Cementitious Composites. *Construction and Building Materials, 174*(June), 253-262. doi:10.1016/j.conbuildmat.2018.04.129

Hussain, A., Ding, Y., Liu, G., & Naqi, A. (2019). Study on self-monitoring of multiple cracked concrete beams with multiphase conductive materials subjected to bending. *Smart Materials and Structures, 28*(9), 095003.

Hussain, A., Xiang, Y., Yu, T., & Zou, F. (2022). Nanocarbon black-based ultra-high-performance concrete (UHPC) with self-strain sensing capability. *Construction and Building Materials, 359*, 129496.

Hussain, A., Yu, T., & Zou, F. (2023). Development of Nanocarbon Black-enabled Self-strain Sensing Ultra-high-performance Cementitious Composites. *STRUCTURAL HEALTH MONITORING 2023*.

Hussain, A., Yu, T., & Zou, F. (2024). Nanocarbon black based ultra-high-performance seawater sea-sand concrete (UHPSSC) with self-strain sensing capability. *Cement and Concrete Composites*, 105895.

Hussain, Z., Pu, Z., Hussain, A., Ahmed, S., Shah, A. U., Ali, A., & Ali, A. (2022). Effect of fiber dosage on water permeability using a newly designed apparatus and crack monitoring of steel fiber–reinforced concrete under direct tensile loading. *Structural Health Monitoring, 21*(5), 2083-2096.

Imbabi, M. S., Carrigan, C., & McKenna, S. (2012). Trends and developments in green cement and concrete technology. *International Journal of Sustainable Built Environment, 1*(2), 194-216.

Islam, M., Rojas, E., Bergey, D., Johnson, A., & Yodh, A. (2003). High weight fraction surfactant solubilization of single-wall carbon nanotubes in water. *Nano letters, 3*(2), 269-273.

Ismail, K. M., Fathi, M. S., & Manaf, N. (2004). Study of lightweight concrete behaviour. *Universiti Teknologi Malaysia*.

Jackson, E. M., Laibinis, P. E., Collins, W. E., Ueda, A., Wingard, C. D., & Penn, B. (2016). Development and thermal properties of carbon nanotube-polymer composites. *Composites Part B: Engineering, 89*, 362-373. doi:10.1016/j.compositesb.2015.12.018

Jahanbakhsh, H., Karimi, M. M., Jahangiri, B., & Nejad, F. M. (2018). Induction heating and healing of carbon black modified asphalt concrete under microwave radiation. *Construction and Building Materials, 174*, 656-666. doi:10.1016/j.conbuildmat.2018.04.002

Jiang, S., Zhang, L., Zhou, D., Han, B., Cui, X., Ouyang, J., & Yu, X. (2017). Comparison of compressive strength and electrical resistivity of cementitious composites with different nano- and micro-fillers. *Archives of Civil and Mechanical Engineering, 18*(1), 60-68. doi:10.1016/j.acme.2017.05.010

Kang, M., Kang, M.-C., Yonis, A., Vashistha, P., & Pyo, S. (2024). Effect of steel slag on the mechanical properties and self-sensing capability of ultra-high performance concrete (UHPC). *Developments in the Built Environment, 17*, 100342.

Karadumpa, C. S., & Pancharathi, R. K. (2021). Influence of Particle Packing Theories on Strength and Microstructure Properties of Composite Cement–Based Mortars. *Journal of Materials in Civil Engineering, 33*(10), 04021267. doi:10.1061/(asce)mt.1943-5533.0003848

Kashif Ur Rehman, S., Ibrahim, Z., Memon, S. A., Aunkor, M. T. H., Faisal Javed, M., Mehmood, K., & Shah, S. M. A. (2018). Influence of graphene nanosheets on rheology, microstructure, strength development and self-sensing properties of cement based composites. *Sustainability, 10*(3), 822.

Kaushik, S., & Islam, S. (1995). Suitability of sea water for mixing structural concrete exposed to a marine environment. *Cement and Concrete Composites*, *17*(3), 177-185.

Kersey, A. D. (1996). A review of recent developments in fiber optic sensor technology. *Optical Fiber Technology, 2*(3), 291-317. doi:10.1006/ofte.1996.0036

Khan, M., Cao, M., Hussain, A., & Chu, S. (2021). Effect of silica-fume content on performance of CaCO3 whisker and basalt fiber at matrix interface in cement-based composites. *Construction and Building Materials*, *300*, 124046.

Khan, M., Kai, M., Ahmad, M. R., Lao, J., & Dai, J.-G. (2023). Fire Performance of Fiber-reinforced Ultra-High-Performance Concrete: A state-of-the-art review. *Journal of Asian Concrete Federation, 9*(1), 65-102.

Kim, M. K., Kim, D. J., & An, Y.-K. (2018). Electro-mechanical self-sensing response of ultra-high-performance fiber-reinforced concrete in tension. *Composites Part B: Engineering, 134*, 254-264.

Kong, Q., Robert, R., Silva, P., & Mo, Y. (2016). Cyclic Crack Monitoring of a Reinforced Concrete Column under Simulated Pseudo-Dynamic Loading Using Piezoceramic-Based Smart Aggregates. *Applied Sciences, 6*(11). doi:10.3390/app6110341

Konsta-Gdoutos, M. S., Metaxa, Z. S., & Shah, S. P. (2010). Highly dispersed carbon nanotube reinforced cement based materials. *Cement and Concrete Research, 40*(7), 1052-1059.

Kovacs, J. Z., Velagala, B. S., Schulte, K., & Bauhofer, W. (2007). Two percolation thresholds in carbon nanotube epoxy composites. *Composites Science and Technology, 67*(5), 922-928. doi:10.1016/j.compscitech.2006.02.037

Lau, A. K.-T., & Hui, D. (2002). The revolutionary creation of new advanced materials—carbon nanotube composites. *Composites Part B: Engineering, 33*(4), 263-277. doi:10.1016/s1359-8368(02)00012-4

Le, H. V., Dao, P. L., Nguyen, S. D., Ngo, T. T., Tran, N. T., Nguyen, D. L., & Kim, D. J. (2023). Improvement of the stress sensing ability of ultra-high-performance concrete using short steel fibers and steel slag aggregates under high compression. *Sensors and Actuators A: Physical, 362*, 114616.

Le, H. V., Kim, M. K., Kim, D. J., & Park, J. (2021). Electrical properties of smart ultra-high performance concrete under various temperatures, humidities, and age of concrete. *Cement and Concrete Composites, 118*, 103979.

Lee, S. H., Kim, S., & Yoo, D.-Y. (2018). Hybrid effects of steel fiber and carbon nanotube on self-sensing capability of ultra-high-performance concrete. *Construction and Building Materials, 185*, 530-544.

Lee, S. H., Kim, S., & Yoo, D. Y. (2018). Hybrid effects of steel fiber and carbon nanotube on self-sensing capability of ultra-high-performance concrete. *Construction and Building Materials, 185*, 530-544. doi:10.1016/j.conbuildmat.2018.07.071

Lee, S. Y., Le, H. V., & Kim, D. J. (2019). Self-stress sensing smart concrete containing fine steel slag aggregates and steel fibers under high compressive stress. *Construction and Building Materials, 220*, 149-160. doi:10.1016/j.conbuildmat.2019.05.197

Leong, C.-K., Aoyagi, Y., & Chung, D. (2006). Carbon black pastes as coatings for improving thermal gap-filling materials. *Carbon, 44*(3), 435-440.

Leong, C.-K., & Chung, D. D. L. (2003). Carbon black dispersions as thermal pastes that surpass solder in providing high thermal contact conductance. *Carbon, 41*(13), 2459-2469.

Leong, C.-K., & Chung, D. D. L. (2004). Carbon black dispersions and carbon–silver combinations as thermal pastes that surpass commercial silver and ceramic pastes in providing high thermal contact conductance. *Carbon, 42*(11), 2323-2327. doi:10.1016/j.carbon.2004.05.013

Li, C. (2021). Chloride permeability and chloride binding capacity of nano-modified concrete. *Journal of Building Engineering, 41*, 102419.

Li, G. Y., Wang, P. M., & Zhao, X. (2007). Pressure-sensitive properties and microstructure of carbon nanotube reinforced cement composites. *Cement and Concrete Composites, 29*(5), 377-382.

Li, H., Xiao, H.-g., & Ou, J.-p. (2006). Effect of compressive strain on electrical resistivity of carbon black-filled cement-based composites. *Cement and Concrete Composites, 28*(9), 824-828.

Li, H., Xiao, H., & Ou, J. (2008). Electrical property of cement-based composites filled with carbon black under long-term wet and loading condition. *Composites Science and Technology*, *68*(9), 2114-2119. doi:10.1016/j.compscitech.2008.03.007

Li, H., Xiao, H. G., & Ou, J. P. (2006). Effect of compressive strain on electrical resistivity of carbon black-filled cement-based composites. *Cement & Concrete Composites, 28*(9), 824-828. doi:10.1016/j.cemconcomp.2006.05.004

Li, H., Xiao, H. g., & Ou, J. p. (2006). Effect of compressive strain on electrical resistivity of carbon black-filled cement-based composites. *Cement and Concrete Composites, 28*(9), 824-828. doi:10.1016/j.cemconcomp.2006.05.004

Li, H., Xiao, H. G., & Ou, J. P. (2008). Electrical property of cement-based composites filled with carbon black under long-term wet and loading condition. *Composites Science and Technology*, *68*(9), 2114-2119. doi:10.1016/j.compscitech.2008.03.007

Li, J., Wu, Z., Shi, C., Yuan, Q., & Zhang, Z. (2020). Durability of ultra-high performance concrete–A review. *Construction and Building Materials, 255*, 119296.

Li, P., Li, W., Yu, T., Qu, F., & Tam, V. W. (2020). Investigation on early-age hydration, mechanical properties and microstructure of seawater sea sand cement mortar. *Construction and Building Materials, 249*, 118776.

Li, W., Dong, W., Shen, L., Castel, A., & Shah, S. P. (2020). Conductivity and piezoresistivity of nano-carbon black (NCB) enhanced functional cement-based sensors using polypropylene fibres. *Materials Letters, 270*, 127736.

Li, W., Guo, Y., Zhang, X., Dong, W., Li, X., Yu, T., & Wang, K. (2024). Development of self-sensing ultra-high-performance concrete using hybrid carbon black and carbon nanofibers. *Cement and Concrete Composites*, 105466.

Li, W., Guo, Y., Zhang, X., Dong, W., Li, X., Yu, T., & Wang, K. (2024). Development of self-sensing ultra-high-performance concrete using hybrid carbon black and carbon nanofibers. *Cement and Concrete Composites, 148*, 105466.

Li, X., Wang, L., Liu, Y., Li, W., Dong, B., & Duan, W. H. (2018). Dispersion of graphene oxide agglomerates in cement paste and its effects on electrical resistivity and flexural strength. *Cement and Concrete Composites, 92*, 145-154.

Lin, C., & Chung, D. (2007). Effect of carbon black structure on the effectiveness of carbon black thermal interface pastes. *Carbon, 45*(15), 2922-2931.

Lin, V. W. J., Li, M., Lynch, J. P., & Li, V. C. (2011). Mechanical and electrical characterization of self-sensing carbon black ECC. *798316*(April 2011), 798316-798316. doi:10.1117/12.880178

Lipscomb, I. P., Weaver, P. M., Swingler, J., & McBride, J. W. (2009). The effect of relative humidity, temperature and electrical field on leakage currents in piezo-ceramic actuators under dc bias. *Sensors and Actuators a-Physical, 151*(2), 179-186. doi:10.1016/j.sna.2009.01.017

Liu, L., Xu, J., Yin, T., Wang, Y., & Chu, H. (2022). Improving electrical and piezoresistive properties of cement-based composites by combined addition of nano carbon black and nickel nanofiber. *Journal of Building Engineering, 51*, 104312.

Liu, Q., Xu, Q., Yu, Q., Gao, R., & Tong, T. (2016). Experimental investigation on mechanical and piezoresistive properties of cementitious materials containing graphene and graphene oxide nanoplatelets. *Construction and Building Materials, 127*, 565-576.

Lu, J.-X. (2023). Recent advances in high strength lightweight concrete: From development strategies to practical applications. *Construction and Building Materials, 400*, 132905.

Lu, J.-X., Ali, H. A., Jiang, Y., Guan, X., Shen, P., Chen, P., & Poon, C. S. (2022). A novel high-performance lightweight concrete prepared with glass-uhpc and lightweight microspheres: Towards energy conservation in buildings. *Composites Part B: Engineering, 247*, 110295.

Lu, J.-X., Shen, P., Ali, H. A., & Poon, C. S. (2021). Development of high performance lightweight concrete using ultra high performance cementitious composite and different lightweight aggregates. *Cement and Concrete Composites, 124,* 104277.

Lu, J.-X., Shen, P., Sun, Y., & Poon, C. S. (2022). Strategy for preventing explosive spalling and enhancing material efficiency of lightweight ultra high-performance concrete. *Cement and Concrete Research, 158*, 106842.

Lu, J.-X., Shen, P., Zheng, H., Ali, H. A., & Poon, C. S. (2021). Development and characteristics of ultra high-performance lightweight cementitious composites (UHP-LCCs). *Cement and Concrete Research, 145*, 106462.

Lubelli, B., Van Hees, R., Huinink, H., & Groot, C. (2006). Irreversible dilation of NaCl contaminated lime–cement mortar due to crystallization cycles. *Cement and Concrete Research, 36*(4), 678-687.

Luheng, W., Tianhuai, D., & Peng, W. (2009). Influence of carbon black concentration on piezoresistivity for carbon-black-filled silicone rubber composite. *Carbon, 47*(14), 3151-3157. doi:10.1016/j.carbon.2009.06.050

Luo, J. L., Duan, Z. D., Zhao, T. J., & Li, Q. Y. (2010). Self-Sensing Property of Cementitious Nanocomposites Hybrid with Nanophase Carbon Nanotube and Carbon Black. *Advanced Materials Research, 143-144*, 644-647.

Materazzi, A. L., Ubertini, F., & D'Alessandro, A. (2013). Carbon nanotube cement-based transducers for dynamic sensing of strain. *Cement and Concrete Composites, 37*, 2-11.

Matos, A. M., Nunes, S., Costa, C., & Aguiar, J. L. B. (2021). Durability of an UHPC containing spent equilibrium catalyst. *Construction and Building Materials, 305*, 124681.

Meehan, D. G., Wang, S., & Chung, D. (2010). Electrical-resistance-based sensing of impact damage in carbon fiber reinforced cement-based materials. *Journal of Intelligent Material Systems and Structures, 21*(1), 83-105.

Mendoza, O., Sierra, G., & Tobón, J. I. (2013). Influence of super plasticizer and Ca(OH)2 on the stability of functionalized multi-walled carbon nanotubes dispersions for cement composites applications. *Construction and Building Materials, 47*, 771-778. doi:10.1016/j.conbuildmat.2013.05.100

Meng, W., & Khayat, K. H. (2016). Mechanical properties of ultra-high-performance concrete enhanced with graphite nanoplatelets and carbon nanofibers. *Composites Part B: Engineering, 107*, 113-122.

Miller, S. A., Horvath, A., & Monteiro, P. J. (2018). Impacts of booming concrete production on water resources worldwide. *Nature Sustainability, 1*(1), 69-76.

Milone, G., Vlachakis, C., Tulliani, J.-M., & Al-Tabbaa, A. (2024). Strain Monitoring of Concrete Using Carbon Black-Based Smart Coatings. *Materials, 17*(7), 1577.

Mohamad, N., Muthusamy, K., Embong, R., Kusbiantoro, A., & Hashim, M. H. (2022). Environmental impact of cement production and Solutions: A review. *Materials Today: Proceedings, 48*, 741-746.

Montanari, L., Suraneni, P., Tsui-Chang, M., Khatibmasjedi, M., Ebead, U., Weiss, J., & Nanni, A. (2019). Hydration, pore solution, and porosity of cementitious pastes made with seawater. *Journal of Materials in Civil Engineering, 31*(8), 04019154.

Monteiro, A. O., Cachim, P. B., & Costa, P. M. F. J. (2015). Electrical Properties of Cement-based Composites Containing Carbon Black Particles. *Materials Today: Proceedings, 2*(1), 193-199. doi:10.1016/j.matpr.2015.04.021

Monteiro, A. O., Cachim, P. B., & Costa, P. M. F. J. (2017). Self-sensing piezoresistive cement composite loaded with carbon black particles. *Cement and Concrete Composites, 81*, 59-65. doi:10.1016/j.cemconcomp.2017.04.009

Monteiro, A. O., Cachim, P. B., & Costa, P. M. F. J. (2017). Self-sensing piezoresistive cement composite loaded with carbon black particles. *Cement & Concrete Composites, 81*, 59-65. doi:10.1016/j.cemconcomp.2017.04.009

Monteiro, A. O., Loredo, A., Costa, P. M. F. J., Oeser, M., & Cachim, P. B. (2017). A pressure-sensitive carbon black cement composite for traffic monitoring. *Construction and Building Materials, 154*, 1079-1086. doi:10.1016/j.conbuildmat.2017.08.053

Mosavinejad, S. G., Barandoust, J., Ghanizadeh, A., & Sigari, M. (2018). Crack detection of a HPCFRCC thin plate using electrical resistivity method. *Construction and Building Materials, 193*, 255-267.

Moyo, P., Brownjohn, J. M. W., Suresh, R., & Tjin, S. C. (2005). Development of fiber Bragg grating sensors for monitoring civil infrastructure. *Engineering Structures, 27*(12), 1828-1834. doi:10.1016/j.engstruct.2005.04.023

Nalon, G. H., Ribeiro, J. C. L., de Araújo, E. N. D., Pedroti, L. G., de Carvalho, J. M. F., Santos, R. F., & Aparecido-Ferreira, A. (2020). Effects of different kinds of carbon black nanoparticles on the piezoresistive and mechanical properties of cement-based composites. *Journal of Building Engineering, 32*, 101724.

Naqi, A., Abbas, N., Zahra, N., Hussain, A., & Shabbir, S. Q. (2019). Effect of multi-walled carbon nanotubes (MWCNTs) on the strength development of cementitious materials. *Journal of Materials Research and Technology, 8*(1), 1203-1211.

Naqi, A., & Jang, J. G. (2019). Recent progress in green cement technology utilizing low-carbon emission fuels and raw materials: A review. *Sustainability, 11*(2), 537.

Nguyen, D. L., Song, J., Manathamsombat, C., & Kim, D. J. (2015). Comparative electromechanical damage-sensing behaviors of six strain-hardening steel fiber-reinforced cementitious composites under direct tension. *Composites Part B: Engineering, 69*, 159-168.

Nishida, T., Otsuki, N., Ohara, H., Garba-Say, Z. M., & Nagata, T. (2015). Some considerations for applicability of seawater as mixing water in concrete. *Journal of Materials in Civil Engineering, 27*(7), B4014004.

Orellan, J., Escadeillas, G., & Arliguie, G. (2004). Electrochemical chloride extraction: efficiency and side effects. *Cement and Concrete Research, 34*(2), 227-234.

Organization, W. H., & Fund, U. N. C. s. (2022). *State of the world's drinking water: an urgent call to action to accelerate progress on ensuring safe drinking water for all*: World Health Organization.

Orie, O., & Ojaruega, A. (2015). Experimental evaluation of alternative mix water for concrete: Case study of seawater and laboratory brine. *Nigerian Journal of Technology, 34*(3), 467-471.

Ou, J. (2006). *Research and practice of intelligent sensing technologies in civil structural health monitoring in the mainland of China.* Paper presented at the Nondestructive Evaluation and Health Monitoring of Aerospace Materials, Composites, and Civil Infrastructure V.

Ou, J., & Han, B. (2009). Piezoresistive cement-based strain sensors and self-sensing concrete components. *Journal of Intelligent Material Systems and Structures, 20*(3), 329-336. doi:10.1177/1045389X08094190

Ozbulut, O. E., Jiang, Z., & Harris, D. K. (2018). Exploring scalable fabrication of self-sensing cementitious composites with graphene nanoplatelets. *Smart Materials and Structures, 27*(11), 115029.

Pan, D., Yaseen, S. A., Chen, K., Niu, D., Leung, C. K. Y., & Li, Z. (2021). Study of the influence of seawater and sea sand on the mechanical and microstructural properties of concrete. *Journal of Building Engineering, 42,* 103006.

Pantea, D., Darmstadt, H., Kaliaguine, S., & Roy, C. (2003). Electrical conductivity of conductive carbon blacks: influence of surface chemistry and topology. *Applied Surface Science, 217*(1-4), 181-193. doi:10.1016/s0169-4332(03)00550-6

Parvaneh, V., & Khiabani, S. H. (2019). Mechanical and piezoresistive properties of self-sensing smart concretes reinforced by carbon nanotubes. *Mechanics of Advanced Materials and Structures*, *26*(11), 993-1000.

Qiao, C., Suraneni, P., & Weiss, J. (2018). Damage in cement pastes exposed to NaCl solutions. *Construction and Building Materials, 171*, 120-127.

Qing, Y., Zenan, Z., Li, S., & Rongshen, C. (2006). A comparative study on the pozzolanic activity between nano-SiO 2 and silica fume. *Journal of Wuhan University of Technology-Mater. Sci. Ed., 21*, 153-157.

Qiu, L., Dong, S., Yu, X., & Han, B. (2021). Self-sensing ultra-high performance concrete for in-situ monitoring. *Sensors and Actuators A: Physical, 331*, 113049.

Qureshi, T. S., & Panesar, D. K. (2020). Nano reinforced cement paste composite with functionalized graphene and pristine graphene nanoplatelets. *Composites Part B: Engineering, 197*, 108063.

Ragalwar, K., Heard, W. F., Williams, B. A., & Ranade, R. (2020). Significance of the particle size distribution modulus for strain-hardening-ultra-high performance concrete (SH-UHPC) matrix design. *Construction and Building Materials, 234*, 117423.

Rajabipour, F., & Weiss, J. (2007). Electrical conductivity of drying cement paste. *Materials and Structures, 40*, 1143-1160.

Ralli, Z. G., Akhtarian, S., Pantazopoulou, S. J., & Perry, V. (2023). Self-sensing nano-engineered ultra-high performance concrete (UHPC) under tension. *Advances in Structural Engineering*, 13694332231213457.

Rehman, S. K. U., Ibrahim, Z., Memon, S. A., Javed, M. F., & Khushnood, R. A. (2017). A sustainable graphene based cement composite. *Sustainability, 9*(7), 1229.

Reza, F., Batson, G. B., Yamamuro, J. A., & Lee, J. S. (2003). Resistance changes during compression of carbon fiber cement composites. *Journal of Materials in Civil Engineering, 15*(5), 476-483.

Reza, F., Yamamuro, J. A., & Batson, G. B. (2004). Electrical resistance change in compact tension specimens of carbon fiber cement composites. *Cement and Concrete Composites, 26*(7), 873-881.

Rhee, I., Lee, J. S., Kim, Y. A., Kim, J. H., & Kim, J. H. (2016). Electrically conductive cement mortar: Incorporating rice husk-derived high-surface-area graphene. *Construction and Building Materials, 125*, 632-642.

Robins, P., Austin, S., Chandler, J., & Jones, P. (2001). Flexural strain and crack width measurement of steel-fibre-reinforced concrete by optical grid and electrical gauge methods. *Cement and Concrete Research, 31*(5), 719-729. doi:10.1016/S0008-8846(01)00465-3

Rocha, C. A. A., Cordeiro, G. C., & Toledo Filho, R. D. (2015). Use of thermal analysis to determine the hydration products of oil well cement pastes containing NaCl and KCl. *Journal of Thermal Analysis and Calorimetry, 122*, 1279-1288.

Ruan, Y., Han, B., Wang, D., Zhang, W., & Yu, X. (2018). Electrical properties of carbon nanotubes filled cementitious composites. *Materials Research Express, 5*(10), 105704.

Rwei, S.-P., Ku, F.-H., & Cheng, K.-C. (2002). Dispersion of carbon black in a continuous phase: Electrical, rheological, and morphological studies. *Colloid and Polymer Science*, *280*, 1110-1115.

Saar, M. O., & Manga, M. (2002). Continuum percolation for randomly oriented soft-core prisms. *Physical Review E - Statistical Physics, Plasmas, Fluids, and Related Interdisciplinary Topics, 65*(5), 6-6. doi:10.1103/PhysRevE.65.056131

Sánchez-González, J., Macías-García, A., Alexandre-Franco, M. F., & Gómez-Serrano, V. (2005). Electrical conductivity of carbon blacks under compression. *Carbon, 43*(4), 741-747. doi:10.1016/j.carbon.2004.10.045

Sasmal, S., Ravivarman, N., Sindu, B., & Vignesh, K. (2017). Electrical conductivity and piezo-resistive characteristics of CNT and CNF incorporated cementitious nanocomposites under static and dynamic loading. *Composites Part A: Applied Science and Manufacturing, 100*, 227-243.

Sassani, A., Arabzadeh, A., Ceylan, H., Kim, S., Sadati, S. M. S., Gopalakrishnan, K., . . . Abdualla, H. (2018). Carbon fiber-based electrically conductive concrete for salt-free deicing of pavements. *Journal of Cleaner Production, 203*, 799-809. doi:10.1016/j.jclepro.2018.08.315

Saxena, S., & Baghban, M. H. (2023). Seawater concrete: A critical review and future prospects. *Developments in the Built Environment*, 100257.

Seo, J., Jang, D., Yang, B., Yoon, H. N., Jang, J. G., Park, S., & Lee, H.-K. (2022). Material characterization and piezoresistive sensing capability assessment of thin-walled CNT-embedded ultra-high performance concrete. *Cement and Concrete Composites, 134*, 104808.

Shah, S. P., Konsta-Gdoutos, M. S., Metaxa, Z. S., & Mondal, P. (2009). Nanoscale Modification of Cementitious Materials. In (pp. 125-130): Springer Berlin Heidelberg.

Shen, P., Lu, L., He, Y., Wang, F., & Hu, S. (2019). The effect of curing regimes on the mechanical properties, nano-mechanical properties and microstructure of ultra-high performance concrete. *Cement and Concrete Research, 118*, 1-13.

Shi, C., Wu, Z., Xiao, J., Wang, D., Huang, Z., & Fang, Z. (2015). A review on ultra high performance concrete: Part I. Raw materials and mixture design. *Construction and Building Materials, 101*, 741-751.

Shi, L., Lu, Y., & Bai, Y. (2017). Mechanical and Electrical Characterisation of Steel Fiber and Carbon Black Engineered Cementitious Composites. *Procedia Engineering, 188*, 325-332. doi:10.1016/j.proeng.2017.04.491

Shi, Z., Hua, L., Lu, Y., Shen, D., & Huang, D. (2024). Investigation of carbon black nanoparticle modified cementitious composites for sensing dynamic vibro-acousto signals. *Measurement*, 115231.

Sikarwar, S., & Yadav, B. C. (2015). Opto-electronic humidity sensor: A review. *Sensors and Actuators a-Physical, 233*, 54-70. doi:10.1016/j.sna.2015.05.007

Simmons, J. G. (1963). Generalized formula for the electric tunnel effect between similar electrodes separated by a thin insulating film. *Journal of applied physics, 34*(6), 1793-1803.

Snyder, K. A., Feng, X., Keen, B., & Mason, T. (2003). Estimating the electrical conductivity of cement paste pore solutions from OH−, K+ and Na+ concentrations. *Cement and Concrete Research, 33*(6), 793-798.

Soboleva, T., Zhao, X., Malek, K., Xie, Z., Navessin, T., & Holdcroft, S. (2010). On the micro-, meso-, and macroporous structures of polymer electrolyte membrane fuel cell catalyst layers. *ACS applied materials & interfaces, 2*(2), 375-384.

Soliman, N. A., Chanut, N., Deman, V., Lallas, Z., & Ulm, F.-J. (2020). Electric energy dissipation and electric tortuosity in electron conductive cement-based materials. *Physical Review Materials, 4*(12), 125401.

Soliman, N. A., & Tagnit-Hamou, A. (2017). Using Particle Packing and Statistical Approach to Optimize Eco-Efficient Ultra-High-Performance Concrete. *ACI Materials Journal, 114*(6), 847-858. doi:10.14359/51701001

Song, F., Chen, Q., & Zheng, Q. (2023). Multifunctional ultra-high performance fibre-reinforced concrete with integrated self-sensing and repair capabilities towards in-situ structure monitoring. *Composite Structures, 321*, 117240.

Spahr, M. E., Gilardi, R., & Bonacchi, D. (2017). Carbon Black for Electrically Conductive Polymer Applications. In (pp. 375-400): Springer International Publishing.

Spragg, R., Bu, Y., Snyder, K., Bentz, D., & Weiss, J. (2013). Electrical testing of cement-based materials: Role of testing techniques, sample conditioning, and accelerated curing.

Sun, J., Zhang, W., Zhang, J., & Hou, D. (2021). Molecular dynamics study the structure, bonding, dynamic and mechanical properties of calcium silicate hydrate with ultra-confined water: Effects of nanopore size. *Construction and Building Materials, 280*, 122477.

Sun, S., Ding, S., Han, B., Dong, S., Yu, X., Zhou, D., & Ou, J. (2017). Multi-layer graphene-engineered cementitious composites with multifunctionality/intelligence. *Composites Part B: Engineering, 129*, 221-232. doi:10.1016/j.compositesb.2017.07.063

Sun, S., Han, B., Jiang, S., Yu, X., Wang, Y., Li, H., & Ou, J. (2017). Nano graphite platelets-enabled piezoresistive cementitious composites for structural health monitoring. *Construction and Building Materials, 136*, 314-328.

Taha, S. T. S. (2020). *Effect of nano Cellulose and nano carbon black on cement paste microstructure.* Massachusetts Institute of Technology,

Taheri, S. (2019). A review on five key sensors for monitoring of concrete structures. *Construction and Building Materials, 204*, 492-509. doi:10.1016/j.conbuildmat.2019.01.172

Tavares, L. R. C., Junior, J. F. T., Costa, L. M., da Silva Bezerra, A. C., Cetlin, P. R., & Aguilar, M. T. P. (2020). Influence of quartz powder and silica fume on the performance of Portland cement. *Scientific reports, 10*(1), 21461.

Taylor, H., Famy, C., & Scrivener, K. (2001). Delayed ettringite formation. *Cement and Concrete Research, 31*(5), 683-693.

Teng, J.-G., Xiang, Y., Yu, T., & Fang, Z. (2019). Development and mechanical behaviour of ultra-high-performance seawater sea-sand concrete. *Advances in Structural Engineering, 22*(14), 3100-3120.

Teng, J. (2014). *Performance enhancement of structures through the use of fibre-reinforced polymer (FRP) composites.* Paper presented at the Proceedings of the 23rd Australasian Conference on the Mechanics of Structures and Materials (ACMSM23), Lismore, NSW, Australia.

Teng, J., Yu, T., Dai, J., & Chen, G. (2011). *FRP composites in new construction: current status and opportunities.* Paper presented at the Proceedings of 7th National Conference on FRP Composites in Infrastructure (Supplementary Issue of Industrial Construction), keynote presentation, Hangzhou, China.

Teng, J. G., Xiang, Y., Yu, T., & Fang, Z. (2019). Development and mechanical behaviour of ultra-high-performance seawater sea-sand concrete. *Advances in Structural Engineering, 22*(14), 3100-3120.

Teomete, E. (2016). The effect of temperature and moisture on electrical resistance, strain sensitivity and crack sensitivity of steel fiber reinforced smart cement composite. *Smart Materials and Structures, 25*(7), 075024.

Tian, Z., Li, Y., Zheng, J., & Wang, S. (2019). A state-of-the-art on self-sensing concrete: Materials, fabrication and properties. *Composites Part B: Engineering, 177*, 107437.

Ting, M. Z. Y., Wong, K. S., Rahman, M. E., & Meheron, S. J. (2021). Deterioration of marine concrete exposed to wetting-drying action. *Journal of Cleaner Production, 278*, 123383.

Ubertini, F., Materazzi, A. L., D'Alessandro, A., & Laflamme, S. (2014). Natural frequencies identification of a reinforced concrete beam using carbon nanotube cement-based sensors. *Engineering Structures, 60*, 265-275.

Ukpata, J. O., Ewa, D. E., Liwhuliwhe, J. U., Alaneme, G. U., & Obeten, K. E. (2023). Effects of elevated temperatures on the mechanical properties of laterized concrete. *Scientific reports, 13*(1), 18358.

UNEP. (2022). *Sand and sustainability: 10 strategic recommendations to avert a crisis*. Retrieved from United Nations Environment Programme, Geneva, Switzerland:

Vafaei, D., Hassanli, R., Ma, X., Duan, J., & Zhuge, Y. (2021). Sorptivity and mechanical properties of fiber-reinforced concrete made with seawater and dredged sea-sand. *Construction and Building Materials, 270*, 121436.

Vafaei, D., Ma, X., Hassanli, R., & Zhuge, Y. (2021). *Effects of seawater and sea-sand on concrete properties: A review paper.* Paper presented at the EASEC16: Proceedings of The 16th East Asian-Pacific Conference on Structural Engineering and Construction, 2019.

Vande Voort, T. L., Suleiman, M. T., & Sritharan, S. (2008). *Design and performance verification of UHPC piles for deep foundations*. Retrieved from

Vlachakis, C., Perry, M., & Biondi, L. (2020). Self-sensing alkali-activated materials: A review. *Minerals, 10*(10), 885.

Wang, H., Gao, X., & Liu, J. (2018). Effects of salt freeze-thaw cycles and cyclic loading on the piezoresistive properties of carbon nanofibers mortar. *Construction and Building Materials, 177*, 192-201.

Wang, H., Zhang, A., Zhang, L., Wang, Q., Yang, X.-h., Gao, X., & Shi, F. (2020). Electrical and piezoresistive properties of carbon nanofiber cement mortar under different temperatures and water contents. *Construction and Building Materials, 265*, 120740.

Wang, J., Zhou, T., Xu, D., Zhou, Z., Du, P., Xie, N., . . . Liu, Y. (2018). Effect of nano-silica on the efflorescence of waste based alkali-activated inorganic binder. *Construction and Building Materials, 167*, 381-390.

Wang, Q., Yan, P., Yang, J., & Zhang, B. (2013). Influence of steel slag on mechanical properties and durability of concrete. *Construction and Building Materials, 47*, 1414-1420.

Wang, S., Luo, J., Yuan, L., Chen, M., Ma, W., Sun, P., & Sun, S. (2020). Promoting Oxygen Electrochemical Reduction to Hydrogen Peroxide through Fabricating Hierarchical Pores. *Authorea Preprints*.

Wang, X., Wu, D., Hou, D., Yu, R., Geng, Q., Wang, P., . . . Li, X. (2022). The unification of light weight and ultra-high strength in LWC: A new homogeneity enhancement approach. *Construction and Building Materials, 315*, 125647. doi:https://doi.org/10.1016/j.conbuildmat.2021.125647

Wang, Y., Wang, Y., Wan, B., Han, B., Cai, G., & Li, Z. (2018). Properties and mechanisms of self-sensing carbon nano fi bers / epoxy composites for structural health monitoring. *Composite Structures, 200*(April), 669-678. doi:10.1016/j.compstruct.2018.05.151

Wegian, F. M. (2010). Effect of seawater for mixing and curing on structural concrete. *The IES Journal Part A: Civil & Structural Engineering, 3*(4), 235-243.

Wen, S., & Chung, D. (2003). A comparative study of steel-and carbon-fibre cement as piezoresistive strain sensors. *Advances in Cement Research, 15*(3), 119-128.

Wen, S., & Chung, D. (2007). Electrical-resistance-based damage self-sensing in carbon fiber reinforced cement. *Carbon, 45*(4), 710-716.

Wen, S., & Chung, D. (2007). Partial replacement of carbon fiber by carbon black in multifunctional cement–matrix composites. *Carbon, 45*(3), 505-513.

Wen, S., & Chung, D. (2008). Effect of moisture on piezoresistivity of carbon fiber-reinforced cement paste. *ACI Materials Journal, 105*(3), 274.

Wen, S., & Chung, D. D. L. (2001). Defect dynamics of cement paste under repeated compression studied by electrical resistivity measurement. *Cement and Concrete Research, 31*(10), 1515-1518. doi:10.1016/S0008-8846(01)00604-4

Wen, S., & Chung, D. D. L. (2006). Spatially resolved self-sensing of strain and damage in carbon fiber cement. *Journal of materials science, 41*(15), 4823-4831. doi:10.1007/s10853-006-0028-5

Wen, S., & Chung, D. D. L. (2007). Partial replacement of carbon fiber by carbon black in multifunctional cement–matrix composites. *Carbon, 45*(3), 505-513. doi:10.1016/j.carbon.2006.10.024

Wen, S., & Chung, D. D. L. (2008). Effect of moisture on piezoresistivity of carbon fiber-reinforced cement paste. *ACI Materials Journal, 105*(3), 274-280.

Wen, S., Wang, S., & Chung, D. (1999). Carbon fiber structural composites as thermistors. *Sensors and Actuators A: Physical, 78*(2-3), 180-188.

WHO, U., World Bank. (2022). *State of the world's drinking water: an urgent call to action to accelerate progress on ensuring safe drinking water for all* (9240060804). Retrieved from Geneva:

Wille, K., & Boisvert-Cotulio, C. (2015). Material efficiency in the design of ultra-high performance concrete. *Construction and Building Materials, 86*, 33-43. doi:10.1016/j.conbuildmat.2015.03.087

Wille, K., Naaman, A. E., & Parra-Montesinos, G. J. (2011). Ultra-High Performance Concrete with Compressive Strength Exceeding 150 MPa (22 ksi): A Simpler Way. *ACI Materials Journal, 108*(1).

Wong, H. H. C., & Kwan, A. K. H. (2008). Packing density of cementitious materials: part 1—measurement using a wet packing method. *Materials and Structures, 41*(4), 689-701. doi:10.1617/s11527-007-9274-5

Wu, N., Ji, T., Huang, P., Fu, T., Zheng, X., & Xu, Q. (2022). Use of sugar cane bagasse ash in ultra-high performance concrete (UHPC) as cement replacement. *Construction and Building Materials, 317*, 125881. doi:https://doi.org/10.1016/j.conbuildmat.2021.125881

Wu, S., Mo, L., Shui, Z., & Chen, Z. (2005). Investigation of the conductivity of asphalt concrete containing conductive fillers. *Carbon, 43*(7), 1358-1363.

Wu, S. P., Mo, L. T., Shui, Z. H., & Chen, Z. (2005). Investigation of the conductivity of asphalt concrete containing conductive fillers. *Carbon, 43*(7), 1358-1363. doi:10.1016/j.carbon.2004.12.033

Wu, Z., Wong, H., & Buenfeld, N. (2017). Transport properties of concrete after drying-wetting regimes to elucidate the effects of moisture content, hysteresis and microcracking. *Cement and Concrete Research, 98*, 136-154.

Wu, Z., Wong, H. S., & Buenfeld, N. R. (2017). Transport properties of concrete after drying-wetting regimes to elucidate the effects of moisture content, hysteresis and microcracking. *Cement and Concrete Research, 98*, 136-154. doi:10.1016/j.cemconres.2017.04.006

Wu, Z. M., Shi, C. J., Khayat, K. H., & Wan, S. (2016). Effects of different nanomaterials on hardening and performance of ultra-high strength concrete (UHSC). *Cement and Concrete Composites, 70,* 24-34. doi:10.1016/j.cemconcomp.2016.03.003

Xi, X., & Chung, D. (2020). Deviceless cement-based structures as energy sources that enable structural self-powering. *Applied Energy, 280*, 115916.

Xi, X., Ozturk, M., & Chung, D. D. L. (2022). DC electric polarization of cured cement paste being unexpectedly hindered by free water. *Journal of the American Ceramic Society, 105*(2), 1074-1082.

Xiao, H., Li, H., & Ou, J. (2010). Modeling of piezoresistivity of carbon black filled cement-based composites under multi-axial strain. *Sensors and Actuators A: Physical, 160*(1-2), 87-93.

Xie, P., Gu, P., & Beaudoin, J. J. (1996). Electrical percolation phenomena in cement composites containing conductive fibres. *Journal of materials science, 31*, 4093-4097.

Xu, J., Zhong, W., & Yao, W. (2010). Modeling of conductivity in carbon fiber-reinforced cement-based composite. *Journal of materials science, 45*, 3538-3546.

Yang, C. Q., Wu, Z. S., & Huang, H. (2007). Electrical properties of different types of carbon fiber reinforced plastics (CFRPs) and hybrid CFRPs. *Carbon, 45*(15), 3027-3035. doi:10.1016/j.carbon.2007.09.001

Yang, S., Han, M., Chen, X., Song, J., & Yang, J. (2022). Influence of sulfate crystallization on bond-slip behavior between deformed rebar and concrete subjected to combined actions of dry-wet cycle and freeze-thaw cycle. *Construction and Building Materials, 345*, 128368.

Yao, Y., Zhang, Z., Liu, H., Zhuge, Y., & Zhang, D. (2022). A new in-situ growth strategy to achieve high performance graphene-based cement material. *Construction and Building Materials, 335*, 127451.

Yazıcı, H., Deniz, E., & Baradan, B. (2013). The effect of autoclave pressure, temperature and duration time on mechanical properties of reactive powder concrete. *Construction and Building Materials, 42*, 53-63.

Yoo, D.-Y., Kim, S., & Lee, S. H. (2018). Self-sensing capability of ultra-high-performance concrete containing steel fibers and carbon nanotubes under tension. *Sensors and Actuators A: Physical, 276*, 125-136.

Yoo, D.-Y., You, I., & Lee, S.-J. (2017). Electrical properties of cement-based composites with carbon nanotubes, graphene, and graphite nanofibers. *Sensors, 17*(5), 1064.

Yoo, D.-Y., You, I., & Lee, S.-J. (2018). Electrical and piezoresistive sensing capacities of cement paste with multi-walled carbon nanotubes. *Archives of Civil and Mechanical Engineering, 18*(2), 371-384.

Yoo, D.-Y., You, I., Youn, H., & Lee, S.-J. (2018). Electrical and piezoresistive properties of cement composites with carbon nanomaterials. *Journal of Composite Materials, 52*(24), 3325-3340.

Yoo, D.-Y., You, I., Zi, G., & Lee, S.-J. (2019). Effects of carbon nanomaterial type and amount on self-sensing capacity of cement paste. *Measurement, 134*, 750-761. doi:10.1016/j.measurement.2018.11.024

You, I., Yoo, D. Y., Kim, S., Kim, M. J., & Zi, G. (2017). Electrical and Self-Sensing Properties of Ultra-High-Performance Fiber-Reinforced Concrete with Carbon Nanotubes. *Sensors (Basel), 17*(11). doi:10.3390/s17112481

Youngs, I. J. (2003). A geometric percolation model for non-spherical excluded volumes. *Journal of Physics D: Applied Physics, 36*(6), 738-738. doi:10.1016/j.cemconres.2009.08.020

Younis, A., Ebead, U., Suraneni, P., & Nanni, A. (2018). Fresh and hardened properties of seawater-mixed concrete. *Construction and Building Materials, 190*, 276-286.

Youssry, M., Madec, L., Soudan, P., Cerbelaud, M., Guyomard, D., & Lestriez, B. (2013). Non-aqueous carbon black suspensions for lithium-based redox flow batteries: rheology and simultaneous rheo-electrical behavior. *Phys Chem Chem Phys, 15*(34), 14476-14486. doi:10.1039/c3cp51371h

Zeng, J.-J., Liao, J., Zhuge, Y., Guo, Y.-C., Zhou, J.-K., Huang, Z.-H., & Zhang, L. (2022). Bond behavior between GFRP bars and seawater sea-sand fiber-reinforced ultra-high strength concrete. *Engineering Structures, 254,* 113787.

Zhang, J., Liu, H., Liu, G., Wang, X., Geng, J., Wang, Q., & Hussain, A. (2023). Influence on mechanical properties and microstructure analysis of hybrid fiber recycled aggregate concrete after exposure to elevated temperature. *Journal of Adhesion Science and Technology, 37*(16), 2328-2347.

Zhang, J., Yu, R., Shui, Z., & Liu, K. (2022). Hydration kinetics and microstructure development of Ultra-High Performance Concrete (UHPC) subjected to microwave pre-curing. *Cement and Concrete Composites, 129,* 104484.

Zhang, J., Zhuge, Y., & Liu, Y. (2024). Fracture Properties of Nanofiber Reinforced Cementitious Material: A Review. *Case Studies in Construction Materials,* e03371.

Zhang, K., Han, B., & Yu, X. (2011). Nickel particle based electrical resistance heating cementitious composites. *Cold Regions Science and Technology, 69*(1), 64-69. doi:10.1016/j.coldregions.2011.07.002

Zhang, L., Ding, S., Han, B., Yu, X., & Ni, Y.-Q. (2019). Effect of water content on the piezoresistive property of smart cement-based materials with carbon nanotube/nanocarbon black composite filler. *Composites Part A: Applied Science and Manufacturing, 119*, 8-20.

Zhang, L., Ding, S., Li, L., Dong, S., Wang, D., Yu, X., & Han, B. (2018). Effect of characteristics of assembly unit of CNT/NCB composite fillers on properties of smart cement-based materials. *Composites Part A: Applied Science and Manufacturing, 109*, 303-320.

Zhang, L. Q., Ding, S. Q., Li, L. W., Dong, S. F., Wang, D. N., Yu, X., & Han, B. G. (2018). Effect of characteristics of assembly unit of CNT/NCB composite fillers on properties of smart cement-based materials. *Composites Part A: Applied Science and Manufacturing, 109*, 303-320. doi:10.1016/j.compositesa.2018.03.020

Zhang, Q., Luan, C., Yu, C., Huang, Y., & Zhou, Z. (2022). Mechanisms of carbon black in multifunctional cement matrix: Hydration and microstructure perspectives. *Construction and Building Materials, 346*, 128455.

Zhang, Y., Sun, Y., Shen, P., Lu, J., Cai, Y., & Poon, C. S. (2022). Physicochemical investigation of Portland cement pastes prepared and cured with seawater. *Materials and Structures, 55*(6), 150.

Zhao, J., Bao, T., Chen, S., & Kundu, T. (2016). Smart aggregate-piezoceramic patch combination for health monitoring of concrete structures. *Journal of sensors, 2016*.

Zhao, X., Li, H., Du, D., & Wang, J. (2008). *Concrete structure monitoring based on built-in piezoelectric ceramic transducers.* Paper presented at the Sensors and Smart Structures Technologies for Civil, Mechanical, and Aerospace Systems 2008.

Zhao, Y., Hu, X., Shi, C., Zhang, Z., & Zhu, D. (2021). A review on seawater sea-sand concrete: Mixture proportion, hydration, microstructure and properties. *Construction and Building Materials, 295*, 123602.

Zhong, R., & Wille, K. (2015). Material design and characterization of high performance pervious concrete. *Construction and Building Materials, 98,* 51-60.

Zhu, B., Liu, H., Liu, G., Hussain, A., Zhang, X., & Wang, X. (2021). Bond behavior between BFRP bars and hybrid fiber recycled aggregate concrete after high temperature. *Journal of Renewable Materials, 9*(3), 507-521.